

Analysis of Smart Transformer features for electric distribution

Dissertation

zur Erlangung des akademischen Grades
Doktor der Ingenieurwissenschaften
(Dr.-Ing.)
Technische Fakultät
der Christian-Albrechts-Universität zu Kiel
vorgelegt von

M. Sc. Giovanni De Carne

Kiel
2017

Erklärung

Ich erkläre an Eides statt, dass ich die Dissertation zum Thema:

Analysis of Smart Transformer features for electric distribution

abgesehen von der Betreuung durch Herrn Prof. Marco Liserre selbstständig und ohne Hilfe angefertigt habe und bisher weder ganz noch zum Teil an einer anderen Stelle im Rahmen eines Prüfungsverfahrens vorgelegt, veröffentlicht oder zur Veröffentlichung eingereicht habe. Weiterhin versichere ich hiermit, dass ich die vorliegende Arbeit unter Einhaltung der Regeln guter wissenschaftlicher Praxis der Deutschen Forschungsgemeinschaft angefertigt habe und alle von anderen Autoren wörtlich übernommenen Stellen wie auch die sich an die Gedankengänge anderer Autoren eng anlehrenden Ausführungen meiner Arbeit besonders gekennzeichnet und die entsprechenden Quellen angegeben sind

Kiel, den 18. Oktober 2017

Giovanni De Carne

1. Gutachter:	Prof. Marco Liserre, Ph.D.
2. Gutachter:	Prof. Dr.-Ing. Christian Rehtanz
3. Gutachter:	Prof. A. P. Meliopoulos, Ph.D.
Datum der mündlichen Prüfung:	23.02.2018

To my brother Roberto

Acknowledgment

As first, I would like to thank my doctoral supervisor and mentor Prof. Marco Liserre for the opportunities received during my doctorate. He always gave me insightful suggestions and comments, teaching me how to carry out a successful research. I will personally make treasure of his precious suggestions in my future career.

I would like to thank Prof. Christian Rehtanz and Prof. Sakis Meliopoulos for reviewing my thesis and for the interesting points arisen during my defense. A thanks goes to Prof. Meliopoulos for hosting me for two months in his lab at Georgia Tech.

A special thank goes to two people always available to back me up during my doctorate: my "unofficial" menthor, Prof. Costas Vournas, who always gave me important feedback and suggestions, and helped me to grow in the power systems direction; and prof. Giampaolo Buticchi, who shared with me these last years of research in Germany, as colleague, mentor and friend.

I would like to thank all the colleagues at the Chair of Power Electronics that shared my research path and supported my scientific growth. I could not list all of them here, but I would like to especially mention Dr.-Ing. Markus Andresen, for the help given in adapting to a new environment, such as the German research system; and Dr. Zhixiang Zou, for being always available to reply my questions and doubts. Furthermore, I would like to thank Prof. Massimo La Scala and Prof. Sergio Bruno, for introducing me in the research world, when I was still a master student at the Politecnico di Bari.

A huge thank goes to my family, that has always believed in me and never gave up in supporting my studies and efforts. Their encouragements gave me the possibility to reach this goal, otherwise not possible. A personal thank is for Julia, that has been always at my side during these last months of preparation for the defense and encourages me in any decisions I may take.

Kiel, February 2018

Giovanni De Carne

Deutsch Kurzfassung der Arbeit

Das elektrische Verteilnetz erlebt infolge der Integration neuer Erzeugungseinheiten, wie Erneuerbare Energien, und neuer Lasten, wie Elektrofahrzeuge, eine tiefgreifende Veränderung. Diese neuen Akteure haben Auswirkungen auf das Verteilnetzmanagement, sowohl durch die Einführung einer höheren Variabilität des Energiebedarfs und eines daraus resultierenden Leistungsungleichgewichts als auch durch Rückleistung mit gesteigerten Überspannungszuständen im Fall hoher Energieerzeugung und niedrigem Leistungsverbrauch oder durch Kabel- und Transformatorüberlastung im Fall niedriger Energieerzeugung und hohem Leistungsverbrauch und ebenfalls durch eine verringerte Systemträgheit aufgrund der leistungselektronik-basierten Verbindungen der Einheiten. Der Smart Transformer (ST) ermöglicht das Verteilnetzmanagement und hat dabei drei Hauptaufgaben: Spannungsanpassung von Mittel- auf Niederspannungsnetzen, Verteilnetzmanagement unter Berücksichtigung obengenannter Probleme und die Bereitstellung von Netzdienstleistungen für das Stromnetz. Aufgrund dessen kann der ST nicht wie ein klassischer Solid-State-Transformator entwickelt werden. Diese Arbeit beschreibt im Detail die Regelkreise und -einstellung des ST unter Beachtung der Netzdienstleistungen, die bereitgestellt werden müssen. Da der ST aus vielen unterschiedlichen Komponenten und Regelkreisen besteht, kann eine detaillierte Simulation des ST in großen und komplexen Netzen zu einem großen Rechenaufwand und in der Folge zu einer Über- oder Unterschätzung der Leistungsfähigkeit des ST führen. Somit sind experimentelle Ergebnisse zwingend erforderlich, um die Effektivität der ST Regelung zu verifizieren. In dieser Arbeit werden drei mögliche Versuchsanordnungen vorgestellt: Mikronetz, Control- und Power-Hardware-In-the-Loop. Der ST ermöglicht die direkte Regelung der Spannungsform im ST-gespeisten Netz durch eine Anpassung der Spannungsamplitude und Frequenz. Dadurch wird eine Interaktion mit spannungssensitiven Lasten und droop-geregelten Erzeugern ermöglicht, um so den Leistungsbedarf des ST-gespeisten Netzes anzupassen. Durch Nutzung dieser Regelung kann der ST Netzdienstleistungen bereitstellen. Die Qualität der Dienstleistungen kann gesteigert werden, indem die Leistungssensitivität des Netzes gegenüber Spannung und Frequenz identifiziert wird. Der ST führt die Identifizierung der Leistungssensitivität des Netzes unter Verwendung kontrollierter Variationen der Spannungsamplitude und der Frequenz in Echtzeit durch. Unter Verwendung dieser Information kann sich der ST in Überlastsituationen oder bei Vorliegen von Konstantleistungslasten selbst schützen; eine Spannungsvariation ohne Kenntnis der Lasteigenschaften kann die Überlastsituationen verschärfen anstatt diese abzuschwächen. Die Identifizierung der Leistungssensitivität ermöglicht die Bereitstellung neuer Systemdienstleistungen für das Verteil- und Übertragungsnetz. Die Möglichkeit, den Lastbedarf dynamisch anzupassen, macht die Nutzung von Lastabwurfstrategien vermeidbar und erlaubt es diese in eine weiche Lastabsenkung umzuwandeln, wobei die Spannung variiert wird, um den Lastbedarf zu reduzieren. Die Lastformung wird auch zur Unterstützung der Frequenzregelung im Hochspannungsnetz während großer Frequenzänderungen genutzt. Sie verbessert die Dynamik des Systems und unterstützt die Leistungsrampen der Erzeuger.

English Summary

The distribution grid is undergoing deep changes created by the integration of new generation resources, such as renewables, and new loads, like electric vehicles. These new actors impact on the distribution grid management, introducing 1) higher variability of the grid power demand and subsequent power unbalance, 2) reverse power flow with increased over-voltage conditions in case of high power production and low power consumption, cables and transformer overload in case of low power production and high power consumption, and 3) decreased system inertia, due to the power electronics-connection of the resources.

The Smart Transformer (ST) enables the management of the distribution grid, absolving three main tasks: 1) adapting the voltage level from medium to low voltage grids; 2) managing the distribution grid during the aforementioned issues; and 3) offering higher controllability of distribution and transmission grid. Due to these tasks, the ST cannot be designed as a classical Solid State Transformer or Power Electronics Transformer. This work describes in details the ST controllers and their tuning, taking into account the services to be provided.

Being composed of many components and controllers, the ST detailed simulation in large and complex grids can lead to large computational efforts and over- or underestimation of its performances. Thus, experimental results are needed to verify the effectiveness of ST controls. In this work, three possible experimental setups are presented, that are the microgrid, Control-Hardware-In-Loop, and Power-Hardware-In-Loop setups, highlighting their advantages and limitations.

The ST enables the direct control of the voltage waveform in the ST-fed grid, varying the voltage amplitude and frequency. This allows to interact with the voltage-sensitive loads power consumption and droop controlled-generators in order to shape the power consumption of the ST-fed grid. Applying this control the ST can offer services to the grid, like limiting the reverse power flow in the medium voltage grid, or managing its overload conditions.

The accuracy of these services can be increased if the identification of the grid power sensitivity to voltage and frequency is carried out. The ST, applying a controlled voltage amplitude and frequency variation, performs the on-line load sensitivity identification and evaluates in real time the grid sensitivity. Employing this information, the ST can protect itself during overload conditions in presence of constant power loads: varying the voltage without knowing the load nature can lead to worsen the overload conditions instead to relieve them (e.g., mistaking constant power for constant impedance load).

This identification enables the offer of new ancillary services to the distribution and transmission grids. The possibility to dynamically shape the load consumption avoids the use of firm load shedding strategies, converting them in a "soft load reduction", where the voltage is varied to reduce the load power consumption. No customers is disconnected in the process, on the opposite of the load shedding approach. The load shaping capability is employed also for supporting the frequency regulation in the HV grid during large frequency variations. It improves the response dynamic of the system and support the generators power ramp.

Contents

Used symbols and abbreviations	III
0 Introduction	1
1 Impact of the distributed generation and electric vehicles in the distribution grid	6
1.1 Grid issues	7
1.2 Solutions proposed in literature	13
1.3 Examples of solution scenarios	17
1.4 Conclusion	23
2 The Smart Transformer	26
2.1 Power Electronics Transformer: past and recent developments	27
2.2 ST control: provision of services for the distribution grid	29
2.3 MV converter	33
2.3.1 Control of MV converter	39
2.4 DC/DC transformation stage	49
2.4.1 Dual Active Bridge	50
2.4.2 Series Resonant Converter	53
2.5 LV converter	58
2.5.1 Control of the LV converter	60
2.6 Conclusions	67
3 Experimental validation of ST services: laboratory test descriptions	68
3.1 Microgrid setup	69
3.2 Control Hardware In Loop evaluation	73
3.3 Power Hardware In Loop evaluation	75
3.3.1 Current-type PHIL evaluation setup	75
3.4 Conclusions	92
4 On-line load sensitivity evaluation	95
4.1 Representation of voltage and frequency dependency of loads	96
4.2 Load Sensitivity to voltage and frequency	99
4.2.1 Load sensitivity evaluation methodologies	102
4.3 On-Line Load sensitivity Identification algorithm	105
4.3.1 Effect of DG power injection in voltage sensitivity values	108
4.4 Simulation results	109
4.5 CHIL validation of On-Line Load sensitivity Identification	110
4.6 Experimental validation of DER impact on sensitivity evaluation	116
4.6.1 Load sensitivity accuracy in case of ST low power conditions	118
4.7 Conclusions	119
5 Voltage/frequency control of a ST-fed grid: distribution grid services	122
5.1 Reverse power flow control in distribution grids	124
5.2 ST overload limitation control	139
5.3 Sensitivity-based ST Overload Control	146
5.4 Control of variable-frequency ST-fed grid	149
5.5 Conclusions	159

6	Voltage control of ST-fed grid: transmission grid services	161
6.1	On-Line Load sensitivity Identification and Control	162
6.2	ST transmission grid frequency regulation	166
6.3	Power Hardware In Loop evaluation	171
6.4	Conclusions	177
7	Summary, conclusion and future research	179
7.1	Summary and conclusion	179
7.2	Research contribution	181
7.3	Future Research	182
8	References	183
9	Attachments	196
9.1	Journal publications related to this thesis	196
9.2	Conference publications related to this thesis	196
9.3	Candidate resume	198

Used symbols and abbreviations

General Symbols

General Symbols

$u(t), u$	Time-variant variable
\tilde{u}	Oscillating component
\bar{u}	Phasor
\dot{u}	Complex number
U	Constant value
Δ	Variation
(s)	Laplace domain operator
(t)	Time domain operator
(z^{-1})	Discrete domain operator

Superscripts

*	Reference
h	Harmonic
i	i -th component
th	Order

Subscripts

0	Nominal value
1,...,6	PWM switching signals
α, β	$\alpha \beta$ components
a,b,c	Phase a,b,c
base	Base value for power, voltage, and current
dab	Dual active bridge
d,q	Components rotating dq-frame
dc	Direct current
diff	Differential
H	High voltage
L	Low voltage
M	Medium voltage
min	Minimum
max	Maximum
pk – pk	Peak-to-peak value

src Series resonant converter

Special symbols

α	Vectorial rotational element
χ	Active power sensitivity to voltage
δ	Reactive power sensitivity to voltage
ε	Reactive power sensitivity to frequency
ε_{pd}	Phase oscillator error
λ	Requested load variation
φ	Phase shift between the primary and secondary voltages in the HF transformer
ϕ	PLL reference voltage angle
ϕ'	PLL feedback voltage angle
ϕ_{cf}	PLL crossover frequency
γ	Active power sensitivity to frequency
θ	Rotational angle
ψ	Maximum phase margin, dc voltage loop, MV converter
Ψ	PLL phase angle
ω	Grid angular frequency
ω_c	Angular frequency center of VCO
ω_r	Angular frequency of HV grid
$\cos\phi$	Power factor
d	Phase shift ratio, DAB controller
d_1	Current disturb signal
del_{RTDS}	RTDS delay transfer function
del_{ST}	Smart Transformer delay transfer function
f	Grid frequency
f_0	Resonant frequency, SRC converter
f_{BW}	Controller bandwidth
f_s	Switching frequency
i_0	Disturbance current signal, LV converter
$i_{\alpha\beta M}$	Medium voltage $\alpha\beta$ -frame current
i_{ac}	AC current contribution of MMC legs
i_c	Current flowing in the filter capacitor, LV converter
i_{CL}	Current flowing in the LV DC-link capacitor
i_d	Medium voltage line current d-component
\bar{i}_d	Medium voltage line current d-component, constant component
\tilde{i}_d	Medium voltage line current d-component, oscillating component
i_{dab}	Current flowing in the HF transformer circuit, DAB converter
i_{dcL}	Current flowing in the LV DC-link
i_g	ST-fed grid current

i_L	Low voltage line current over the filter inductor
i_{load}	Load impedance line current
i_{max}	Maximum allowable current for ST
i_M	Medium voltage line current over the filter inductor
i_n	MMC lower leg current
i_p	MMC upper leg current
i_{src}	Current flowing in the HF transformer circuit, SRC converter
i_q	Medium voltage line current q-component
i_{ratio}	Current ration between software and hardware in PHIL evaluation
k_i	PLL low pass filter integral gain
k_p	PLL low pass filter proportional gain
k_{pd}	PLL phase detector proportional gain
k_{vco}	PLL voltage-controlled oscillator proportional gain
m	Harmonic order for CRC controller, FORC
m_{abc}	Modulation signal for phase a,b,c
n	Winding ratio, HF transformer
p	Medium voltage instantaneous power
q	Medium voltage reactive power
t_c	Evaluation time window, OLLI algorithm
t_d	Algorithm's start delay, OLLI algorithm
t_s	Steady state time window, OLLI algorithm
u_L	Line-to-ground voltage before the converter filter, LV converter
u_M	Line-to-ground voltage before the converter filter, MV converter
v_0	Nominal voltage
v_1	Primary side High Frequency transformer voltage
v_2	Secondary side High Frequency transformer voltage
$v_{\alpha\beta M}$	Medium voltage $\alpha\beta$ -frame voltage
v_{dcL}	Low voltage DC voltage
v_{dcM}	Medium voltage DC voltage
v_{dqM}	Medium voltage dq-frame voltage
v_{diff}	MMC differential voltage
v_g	ST-fed grid voltage
v_{lf}	Output PLL low pass filter
v_L	Low voltage phase-to-ground voltage
v_M	Medium voltage phase-to-ground voltage
v_n	MMC lower leg voltage
v_p	MMC upper leg voltage
A_k	Lagrange coefficient, FORC
BW_{ST}	ST controller bandwidth, FORC
C_{dcL}	Low voltage DC capacitance
C_{dcM}	Medium voltage DC capacitance
C_L	Low voltage filter capacitance
C_r	Resonant capacitance, SRC converter

D	Disturbance signal, FORC
D_L	Load damping factor
E	Control error, FORC
F	Small fractional order, FORC
F_{HP}	Turbine high pressure fractional power
$Flag_f$	Activation flag of real time frequency controller
$Flag_I$	Activation flag of overload controller
$Flag_P$	Activation flag of soft load reduction controller
G_c	Feedback controller transfer function, FORC
G_d	delay computation transfer function, FORC
G_f	Output filter transfer function, FORC
I	Current measured for sensitivity calculation
I_0	Initial current measured for sensitivity calculation
I_{sec}	ST current security threshold
K_{dab}	Equivalent gain DAB controller
K_{dr}	ST droop coefficient, RTFR controller
K_{drV}	Voltage/reactive current droop gain, MV converter
K_h	Harmonic resonant gain, LV converter
K_i	Current sensitivity to voltage
K_{icc}	Integral gain, current loop, DER converter
K_{idcM}	Integral gain, dc voltage loop, MV converter
K_{iM}	Integral gain, current loop, MV converter
K_{iPA}	Integral gain, current loop, power amplifier
K_I	DG P/f droop coefficient
K_{forc}	ST FORC controller proportional gain
$K_{forc,cc}$	DER FORC controller proportional gain
K_{fp}	Active power frequency linear coefficient, exponential load model
K_{fq}	Reactive power frequency linear coefficient, exponential load model
K_p	Active power voltage exponential coefficient, exponential load model
$K_{p,L}$	Active power voltage exponential coefficient, exponential load model, only passive load
K_{pcc}	Proportional gain, current loop, DER converter
K_{pdcM}	Proportional gain, dc voltage loop, MV converter
K_{pi}	Proportional gain, current loop, LV converter
K_{pM}	Proportional gain, current loop, MV converter
K_{pPA}	Proportional gain, current loop, power amplifier
K_{pv}	Proportional gain, voltage loop, LV converter
K_q	Reactive power voltage exponential coefficient, exponential load model
K_{rM}	Integral gain, harmonic controller, current loop, MV converter
K_{rPA}	Resonant gain, current loop, power amplifier
K_{rv}	Resonant gain, voltage loop, LV converter
K_{ST}	ST integration factor in the grid
L_{dc}	LV DC link inductance, SRC converter
L_{DER}	DER inductance

L_L	Low voltage filter inductance
L_{load}	Low voltage load inductance
L_M	Medium voltage filter inductance
L_{PA}	Power amplifier filter impedance
L_r	Leakage inductance, DAB converter
M_I	Machine inertia
N	Fractional order, FORC
N_i	Fractional order integer part, FORC
P_0	Nominal active power
P_1	Active power share in ZIP model, constant impedance
P_2	Active power share in ZIP model, constant current
P_3	Active power share in ZIP model, constant power
$Pade^i$	i-th Pade order transfer function
P_{cell}	CHB rated power, single cell
P_{CHB}	CHB rated power
P_{dc}	DC link power
P_e	HV grid electrical power
P_g	DG active power
P_L	ST-fed grid active power, only passive load
P_m	Generator mechanical power
P_{max}	Maximum power transfer in DC/DC converter
P_{min}	Minimum power transfer in DC/DC converter
P_{set}	Desired active power, RSCAD load model
P_{ST}	ST total power contribution in the HV grid
PLL_{bw}	PLL bandwidth
Q_0	Nominal reactive power
Q_1	Reactive power share in ZIP model, constant impedance
Q_2	Reactive power share in ZIP model, constant current
Q_3	Reactive power share in ZIP model, constant power
Q_{set}	Desired reactive power, RSCAD load model
R	Reference input, FORC
R_d	Damping resistance LV DC link
R_{dC}	LV DC-link resistance, SRC converter
R_{dL}	Damping resistance filter capacitor, LV converter
R_{harm}	Medium voltage rectifier load resistance
R_{load}	Low voltage load resistance
R_G	Governor droop characteristic
R_L	Low voltage filter resistance
R_M	Medium voltage filter resistance
R_{PA}	Power amplifier filter resistance
R_r	HF transformer resistance, DAB converter
S	Apparent power
S_0	Nominal apparent power

S_i	Switching element (i-th)
S_n	MMC switching function lower leg
S_p	MMC switching function upper leg
T_c	Time step
T_s	Sampling frequency
T_{ST}	Smart Transformer time step
T_{dab}	Equivalent DAB time constant
T_0	Resonance time-step, SRC converter
T_{dq}	Transformation matrix dq-frame
T_x	Equivalent time constant current loop, MV converter
T_{CH}	Main inlet volume time constant
T_G	Governor dynamic time constant
T_{RH}	Reheater time constant
Y	System output, FORC
Z_0	Resonant impedance, SRC converter
Z_f	ST filter impedance, FORC
Z_{ff}	DER filter impedance, FORC
Z_g	Ground connection impedance, LV converter
Z_l	ST-side line impedance, FORC
Z_{ll}	DER-side line impedance, FORC
Z_n	Neutral connection impedance, LV converter
Z_L	Constant impedance load

Abkürzungen

ACER	Agency for the Cooperation of Energy Regulators
BESS	Battery Energy Storage System
CEI	Comitato Elettrotecnico Italiano
CHB	Cascaded Half Bridge
CHIL	Control-Hardware-In-Loop
CIGRE	Conseil International des Grands Réseaux Électriques
CRC	Conventional Repetitive Control
CSC	Current Source Converter
CVR	Conservation Voltage Reduction
DAB	Dual Active Bridge
DC	Direct Current
DCM	Discontinuous Conduction Mode
DDC	Dynamic Demand Control
DER	Distributed Energy Resources
DFIG	Doubly Fed Induction Generator
DFR	Digital Fault Recorder

DFT	Discrete Fourier Transformation
DG	Distributed Generation
DLC	Direct Load Control
DSM	Demand Side Management
DSO	Distribution System Operator
DVR	Dynamic Voltage Restorer
ENTSO-E	European Network of Transmission System Operators for Electricity
EV	Electric Vehicle
FCEV	Fast Charging Electric Vehicle
FIT	Feed-In-Tariff
FORC	Fractional-Order Repetitive Control
GTAI	Gigabit Transceiver Analog Input
GTAO	Gigabit Transceiver Analog Output
GTDI	Gigabit Transceiver Digital Input
GTDO	Gigabit Transceiver Digital Output
HuT	Hardware under Test
HV	High Voltage
IGBT	Insulated Gate Bipolar Transistor
ILM	Interruptible Load Management
IMP	Internal Model Principle
KCL	Kirchhoff Current Law
KVL	Kirchhoff Voltage Law
LF	Low-pass Filter
LTC	Load Tap Changer
LV	Low Voltage
MMC	Multilevel Modular Converter
MV	Medium Voltage
NPC	Neutral Point Clamped
OLLI	On-Line Load sensitivity Identification
OVC	Overload Control
PCC	Point of Common Coupling
PD	Phase Detector
PD-PWM	Phase Disposition PWM
PET	Power Electronics Transformer
PHIL	Power-Hardware-In-Loop
PI	Proportional-Integral
PLL	Phase Locked Loop
PMU	Phasor Measurement Units
PR	Proportional-Resonant
PV	Photovoltaic
PWM	Pulse Width Modulation
RES	Renewable Energy Resource
ROCOF	Rate Of Change Of Frequency

RPFL	Reverse Power Flow Limitation
RTFR	Real Time Frequency Regulation
RTDS	Real Time Digital Simulator
SLR	Soft Load Reduction
SOC	State Of Charge
SOGI	Second-Order General Integrator
SRC	Series Resonant Converter
SST	Solid State Transformer
STATCOM	Static synchronous compensator
SVC	Static VAR compensator
THD	Total Harmonic Distortion
TSO	Transmission System Operator
VCO	Voltage-Controlled Oscillator
VSC	Voltage Source Converter
VSG	Virtual Synchronous Generator
WTS	Wind Turbine Systems
ZIP	Impedance, current, and power load

0 Introduction

This work has been carried out in the European Research Council (ERC) Consolidator Grant "The Highly Efficient And Reliable smart Transformer - HEART", under the Task 1.1 of the project: "Analysis of ST features for electric distribution". The planned goal in this task is to identify all the features of the ST at the system level, where each feature has to be selectable and thus easily studied both individually and in interaction with the others. Two milestones have been set in Task 1.1:

- *M 1.1* Report regarding the identification the features for the ST that can have a significant impact on the distribution system hosting capacity and reliability.
- *M 1.2* Report for external review and publications concerning the most critical operation modes for the ST reliability.

The task 1.1 and the relative milestones have been fulfilled by means of publications in conferences and international peer-reviewed journals, published under the HEART project acknowledgment. These publications are the backbone of this work, and, in the following, they have been connected to the relative sections of this thesis.

This section aims to motivate the need for a Smart Transformer (ST) to provide ancillary services to the distribution and transmission grid, and to formulate the research proposal of the thesis. The thesis structure is depicted, making reference with the author publications in each chapter.

Motivation for ST provision of ancillary services

The distribution grids are undergoing several changes due to the introduction of new energy actors, such as distributed generation (DG), mainly renewable-based. The main feature of these resources, is to extract energy from natural resources (e.g., wind, solar irradiation, tide movements) to produce electrical energy. Several of these resources can vary their size from hundreds of Watt to several MWs (e.g., photovoltaic and wind turbines), that can be adapted to the grid level and power transfer capability. This implies a "zero-cost" energy production, spread geographically over the grid, where electricity is produced if the resource is available. This leads to two effects: the energy production is variable in the time and not scheduled, and the position of each generator cannot be decided during the grid planning, like the large power plants, but it is left to the single customer investment.

The generation power variability in the distribution grid can have beneficial effects for the grid, like grid congestion relief and voltage support during peak load consumption, and grid infrastructure upgrade deferral. However, this is valid only if the generation share in the distribution grid is limited. If the distributed generators are massively integrated, it may represent a challenge for the grid management: the voltage increase and reverse power flow during

low load consumption and high power production; imbalances caused by single-phase generation (e.g., photovoltaics); decrease of system inertia due to power electronics-connection to the grid; grid protection system coordination failure and higher fault current.

Solutions at device level have been proposed, like the installation of voltage regulators such as capacitor banks, on-load tap changer transformers, and power electronics-based devices (STATCOM, static VAR compensator, DG converters), to manage the grid voltage under high energy production variability. However, each of this solution targets a specific problem and they cannot offer a general solution for the grid management (e.g., the STATCOM can regulate the voltage and grid imbalances, but it cannot influence the lower grid inertia). At system level, more systematic solutions have been proposed, such as microgrids, multi-carrier energy systems, and demand management, where the resources in the grid are coordinated in order to improve with the grid management under high penetration of renewables. Common characteristic of these approaches is the use of a communication infrastructure to exchange data and control signals in the grid.

The Smart Transformer, a power electronics-based MV/LV transformer, is an actuator of system level strategies, with advanced control and communication capability, that targets the grid challenges. The ST does not aim simply to substitute the conventional iron transformer everywhere in the distribution grid, but to replace it where it can contribute to the grid management and offer ancillary services. On the opposite of the already existing concepts of Solid State Transformer (SST) and Power Electronics Transformer (PET), the ST has to be designed and controlled to deal with the grid issues, where the SST and PET focus more on the hardware aspects (e.g., weight and size reduction).

Motivation for Power-Hardware-In-Loop evaluation

The hardware and its controllers validation has to be performed in laboratory environment, due to the necessity to evaluate the performances in real time. Small grid setups can be created in lab for hardware testing. This can be a suitable choice for verifying the hardware performances in case of distributed generation, where the grid can be emulated with its Thevenin equivalent. However, in case of Smart Transformer applications this may limit to show the ST impact in the ST-fed grid, due to the oversimplified lab setup. A certain control action (e.g., voltage variation) can have different effects in the grid, varying in case of long lines, depending on the appliances connected, such as loads or generators, and on their power sensitivity to the control action. The Power-Hardware-In-Loop (PHIL) offers the possibility to test the hardware in realistic grid conditions, emulated in a Real Time Digital Simulator (RTDS). The grid simulated in RTDS is interfaced with the hardware under test, in this case the ST, by means of a power interface (e.g., a linear power amplifier), that reproduces the grid behavior in the hardware side. In the particular case of the ST, the power amplifier need to control its current output, in order to reproduce the current flowing in the ST-fed grid.

The advantages of the PHIL are several: possibility to emulate realistic grid condition, also with recorded data; flexibility in varying the test conditions; higher test safety conditions,

due to the reduced number of hardware components; possibility to repeat tests indefinitely and without impacting on the real distribution grid (e.g., faults conditions can be emulated without involving the distribution grid where the lab is connected). However, the PHIL needs to be tuned in order to have stable behavior and reproduce accurately the grid conditions in the hardware side. Interfacing several components controllers (hardware under test, grid emulated in the RTDS and power amplifier) can create unstable conditions in the loop or they can decrease its accuracy. Its tuning and choice of interfacing components (e.g., power interface inductor) have to take in account these stability and accuracy issue, together with the need to reproduce in hardware a determined class of phenomena (e.g., harmonics or fast transients).

Research proposal

This thesis aims to work on three different targets:

Target 1: Modeling of the Smart Transformer for power system studies

The first objective is to model the Smart Transformer hardware in software environment, with the proper tuning of its controllers. The outcome of this task is a ST average model that has to be employed for large scale power system studies.

Target 2: Investigation on ST features to optimize the distribution grid operations

The second research objective is to investigate the ST control features and the respective services that can be offered to the distribution grid. A higher cost of the components with respect to the conventional iron transformer must be justified by means of the provision of additional services, that are not available with the standard solutions. To address this task, the ST capability to influence the ST-fed grid through voltage and frequency control should be exploited.

Target 3: ST features evaluation by means of a Real Time Digital Simulator

The third research objective regards the evaluation of ST features by means of Real Time Digital Simulator (RTDS). To verify the effectiveness of the ST advanced control features, the ST must be tested in realistic grid scenarios, including several loads, generators and lines. These conditions are difficult to realize in lab, due to the limited available space. A Power-Hardware-In-Loop setup has to be considered as possibility to verify the ST features, interconnecting the ST hardware with a large grid simulated in RTDS. Loop stability and accuracy issues must be addressed in order to obtain realistic grid conditions.

Structure of the thesis

This thesis is structured in 6 Chapters, as described in Figure 0.1, where the publications are associated to the respective sections:

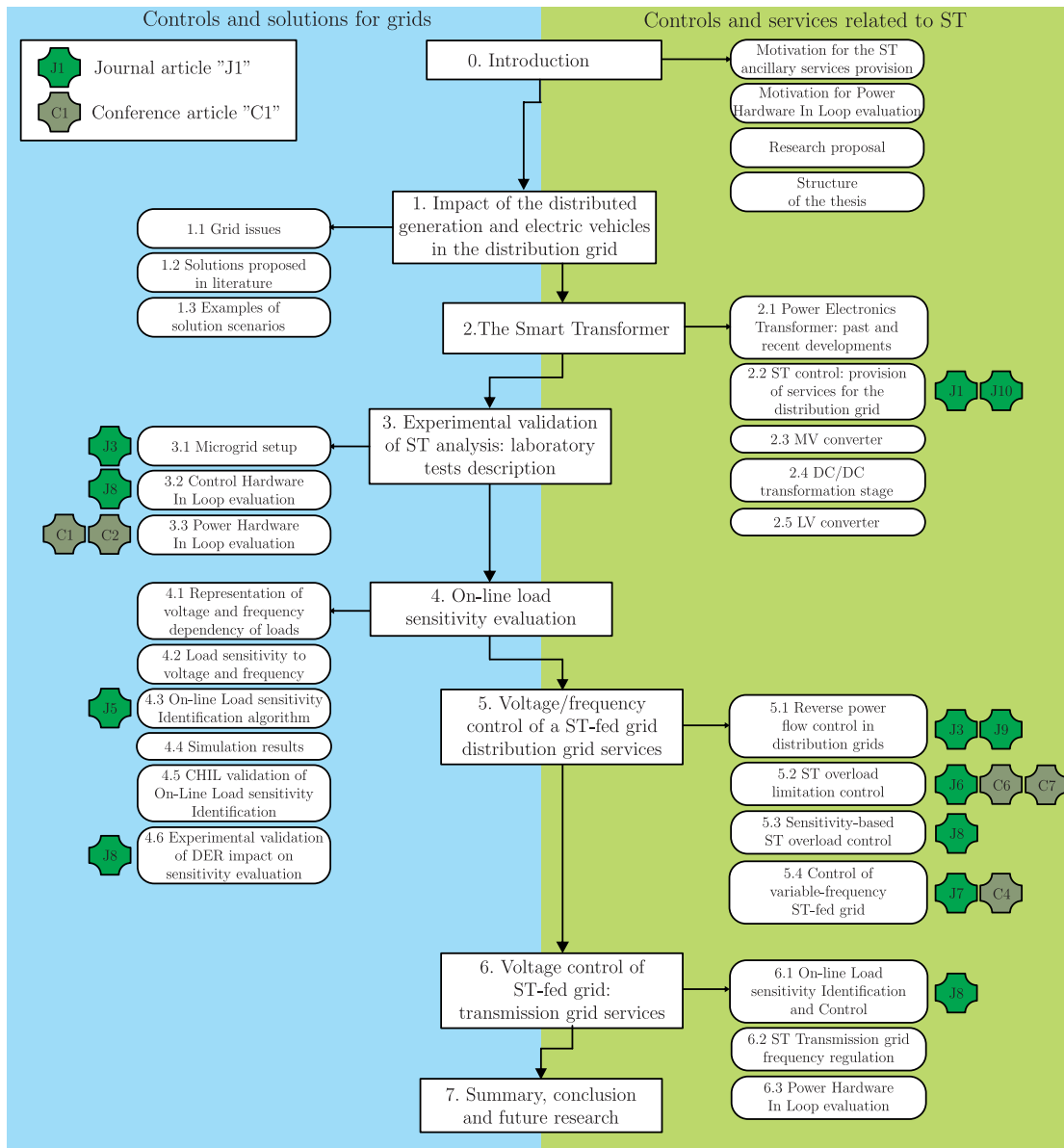


Figure 0.1: Structure of the thesis and related publications.

- Chapter 1 gives an overview on the issues created by the increasing penetration of distributed generation and resources in the distribution grid. Practical solutions, as well as system-level solutions are described.
- Chapter 2 introduces the concept of Smart Transformer and describes its modeling and basic features. The tuning procedures of each ST stage is depicted, with particular insights in the basic services that the ST offers (e.g., disturbance rejection, harmonic compensation).
- Chapter 3 describes the different experimental procedure for ST applications in validating its controllers. Three approaches are considered: "pure hardware" evaluation, by means of a microgrid setup; "external controller" evaluation by means of Control-Hardware-In-Loop (CHIL); "hybrid solution", the Power-Hardware-In-Loop (PHIL), where hardware and software are combined to obtain the advantages from both.

4. Chapter 4 depicts the ST advanced feature of the On-Line Load sensitivity Identification, that allows the real time evaluation of the active and reactive power sensitivity to voltage and frequency of the ST-fed load.
5. Chapter 5 explores the advanced possibility that the ST offers to shape the load consumption and generators production in the ST-fed grid, by means of a voltage and frequency control. Services, like the ST overload control and the reverse power flow limitation, can be offered to increase the controllability of the grid.
6. Chapter 6 analyzes the possibility to combine the ST-fed grid voltage control presented in Chapter 5, with the On-Line Load sensitivity Identification control in Chapter 4, to offer real time frequency regulation service to the HV grid. The enabling feature to control the ST-fed load transform the ST in a controllable resource that can provide services to the high and medium voltage grids.

Assignment of publications to the section of this thesis

The publications included in this work are distributed in the chapters in the following. A complete list of publications is given as attachment in the Chapter 9.1 and 9.2.

- Chapter 2 addresses the ST concept and its control considered in [J10]. Considerations on the ST grid-tailored sizing derive from [J1].
- Chapter 3 describes the microgrid [J3][J6][J7][J9], Control-Hardware-In-Loop [J8], and Power-Hardware-In-Loop [C2][C3] setups, employed in this work and respective publications.
- Chapter 4 analyzes the on-line load sensitivity identification, depicted in [J5].
- Chapter 5 includes the controller applications described in [J3][J9] (reverse power flow limitation control), [J6][C6][C7] (ST overload control), and [J7][C4] (fractional-order repetitive control).
- Chapter 6 depicts the sensitivity-based load control, applied in the case of the soft load reduction explored in [J8].

1 Impact of the distributed generation and electric vehicles in the distribution grid

The current distribution grid is currently under transformation. New actors, such as DG, or Distributed Energy Resources (DERs), and Electric Vehicles (EVs) in the near future, play an increasing role in the electrical power system. To define the concept of DG, the definition of distributed generation in [1] can be used: the DG consist of any generator of limited size (roughly 10 MW or less) that is interconnected at the substation, distribution feeder or customer level. In the DG category fall several technologies: photovoltaics, wind turbines, fuel cells, small and micro-turbines, and internal combustion engines. The DG, producing energy near the load consumption, provides several benefits to the distribution and transmission grid [1]:

- "system support benefit", like voltage support and improved power quality;
- loss reduction;
- transmission and distribution capacity release;
- deferral of new or upgraded transmission and distribution infrastructure;
- improved utility system reliability.

However, these generators create new challenges in the grid management. Originally, the distribution grid has been thought as a radial system, with the energy flowing from the main grid or bulk power system, where the production takes place, toward the low and medium voltage grids, where the consumers are connected. With the integration of small generators in the lower voltage level grids, the load energy consumption is being satisfied locally. Although a limited amount of generators provided benefits sharing the power production with the main grid, the DG penetration increase creates new control challenges to the distribution grid [1, 2, 3, 4, 5, 6]:

- voltage limit violations;
- greater demand variability;
- cables and transformer overload;
- decreased system inertia;
- reverse power flow;
- protection system coordination;
- higher fault current;
- grid losses;

Although all these issues are all to be considered for a proper grid management, this work concentrates the focus mainly on the first 5 issues. At first, the grid issues are explained and their impact on the distribution grid described. Following, the current solutions proposed in literature to solve the grid issues are given. Eventually, several system level scenarios are depicted to achieve full controllability of the grid and thus manage the high integration of DG.

1.1 Grid issues

Steady-state voltage and current limits violations

The integration of the DERs has to respect the limits of the distribution grid, mainly regarding the voltage amplitude value. The Distribution System Operators (DSOs) suggest to operate within range 0.90-1.05 p.u. of the rated voltage value: lower voltage may lead to bad functioning of the appliances and higher voltage level may provoke irreversible damages to the connected devices. Among the DERs, the EV represents a breakthrough technology in the automotive field. However, no dedicated infrastructure actually exists and integrating these new loads in the grid will have an impact on the grid management in the near future. The high power request coming from the EVs charging stations causes a high voltage drop along the lines violating the lower voltage limits [7], as shown in Figure 1.1a. The DG, if installed extensively in the distribution grid, impacts strongly on the voltage profile [8][9]. As shown in Figure 1.1b and demonstrated in [9], a very limited amount of photovoltaic (PV) energy production is enough to violate the upper voltage limits in critical buses. If the PV is placed in a high voltage sensitive bus (e.g., end of the feeder), the PV integration is limited to 35 % or less than the total load. On the opposite side, new loads, like the EVs, may create management issues in the distribution grid, mostly regarding the voltage profile in the grid and the transformer overload. The uncoordinated EV charging can impact heavily on the grid: when the load request is high, the additional power request from EVs can lower the voltage below the lower voltage limit. It occurs also in case of relatively low EVs concentration and slow battery charging [10]. As proved in [11] in a MV grid, the 30 % of EV integration is sufficient for exceeding the lower voltage limit, despite the action of the substation Load Tap Changer (LTC) transformer that reaches its tap limits.

The transformer may be not able to carry the power requested without overloading [12], reducing its lifetime [13]. Its overload capability depends on the component with the highest temperature (hot spot), and short term overload conditions are permitted for few hours per day, without affecting their planned lifetime [14][4]. The transformer overload is an important aspect to be considered when planning an EV charging stations installation. As noted in [15], in US the presence of an EV is equivalent to another household load, thus it increases the possibility of transformer overload. This concept is also recurring in [16], showing the increasing of the power consumption for each household with uncontrolled charging (Figure 1.2). Also in case of limited integration of EVs, the transformer overloads more frequently than the passive load case [16]. In a possible initial implementation scenario,

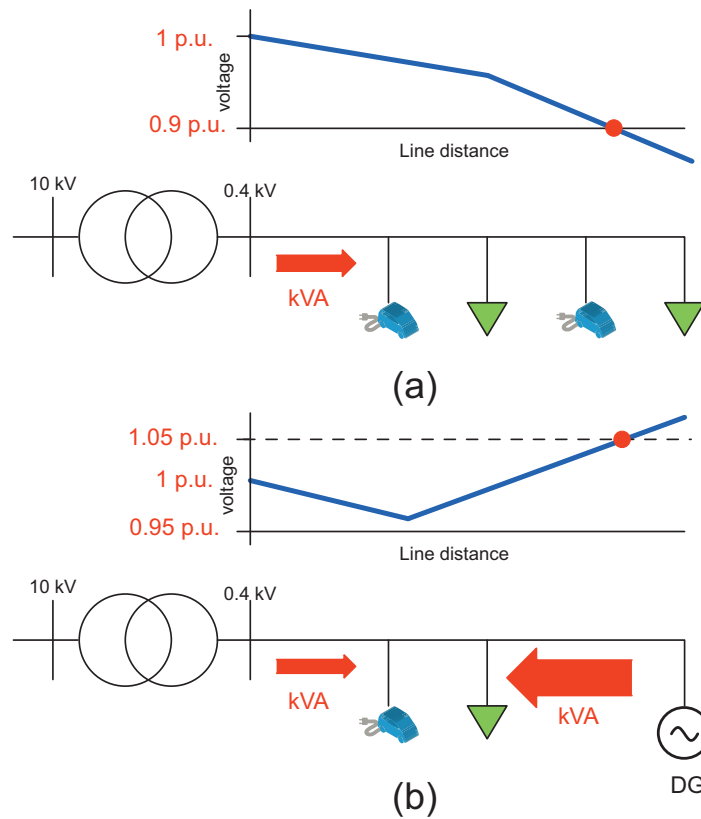


Figure 1.1: Voltage violations cases: (a) high load demand (e.g., EV charging station integration), (b) high DG energy production (e.g., PV power plants integration).

where the infrastructure is not deeply developed for hosting these new loads, the overload conditions can occur up to 40 % of the cases.

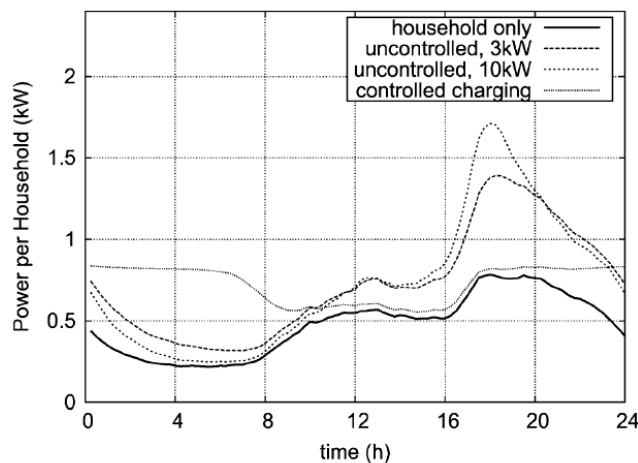


Figure 1.2: Impact of the uncontrolled EV charging per household [16].

The unbalanced voltage conditions in distribution grid derives from the presence of single-phase DG, and not balanced load distribution in the grid (e.g., domestic load and EV slow charging stations). As suggested by the IEEE 1159 standard, the voltage imbalance in steady state should be contained within 2 % of the nominal voltage. However, the integration of

small single-phase PV power plants in the LV grid can affect the voltage waveform balancing [17]. Depending on the installation distance of the PVs from the substation, the impact on the voltage unbalance can vary significantly: the outcomes of an investigation with over 10000 scenarios and PV power variable between 1 kW and 5 kW in [17] shows that the unbalanced power injection creates an average violation of the $2\% \pm 0.5\%$ voltage unbalance limit (ratio between voltage inverse and direct sequence) if the PV plants are installed at the end of the feeder (Figure 1.3a). There is indeed a much higher probability that the voltage unbalance violation occurs if the PV is located at the end of the feeder than at the beginning (median of 1.8% instead of 0.61% in Figure 1.3b). The scenario in [18] describes a case where the integration of EVs reaches high level in the LV grid. Investigating the voltage unbalance level during a long period, many violations of the limit imposed by the [19] are found, mostly in case of uncoordinated EVs charging.

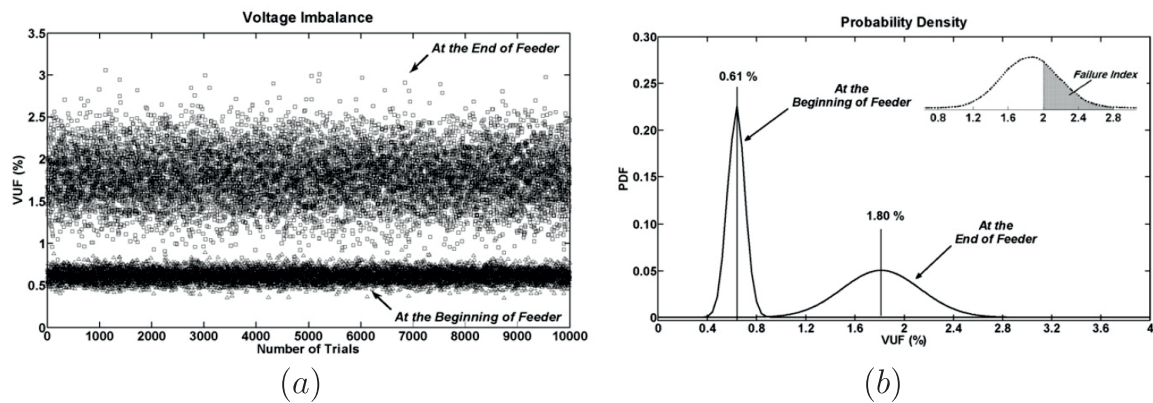


Figure 1.3: Impact of the uncontrolled EV charging per household [17].

As explained in [20, 21, 22], the unbalanced voltage conditions impacts heavily on the motors (heating increase, torque pulsation, and reduction of lifespan). Wind turbines, interfacing the grid with particular converter configurations, can result be affected by unbalanced voltage conditions as well, mainly if not asynchronously-connected with the main grid. In [23] is described that the voltage unbalances affects the DC capacitors of the Doubly Fed Induction Generators (DFIGs): the presence of the inverse sequence creates a 2^{nd} harmonic oscillation on the DC link, decreasing the capacitors' lifespan and reliability.

Effects of high power variability in the grid

Nowadays, intermittent generation, like PVs or Wind Turbine Systems (WTSs), are characterized by quick variations of the active power injection, and consequentially quick voltage variations [24]. If the load power profile can be considered constant or with smooth variation in the short term, the power variability of the DG can impact heavily on the net load profile Figure 1.4.

In case of photovoltaic power plants, the different irradiation along the day causes voltage drops [25], leading the system in unacceptable operating conditions. The outcome is a fast voltage variation in the range of 3%-4% in case of a cloud obscures the solar irradiation

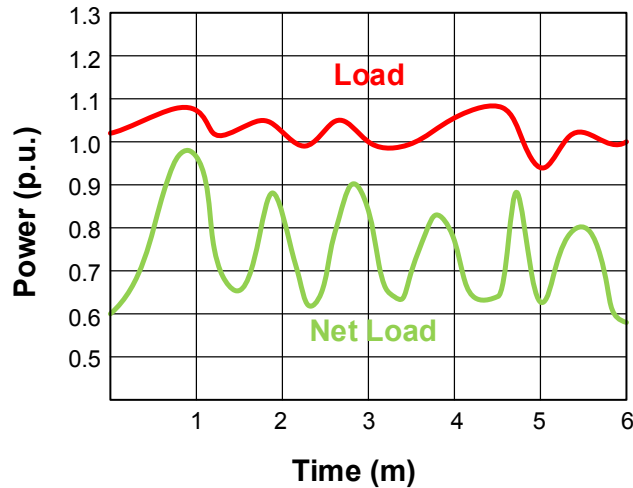


Figure 1.4: Effect on the fast power variation of DG on the grid net load.

on the PV plant. This value can exceed the limit of fast voltage variation imposed by distribution operators. In Germany, the maximum voltage variation caused by the connection / disconnection of a generator is limited to 2% [26]. Thus, conditions of 3%-4% described before are considered not acceptable for German standards.

In case of high penetration of renewables, in particular PV power plants (40% of the nominal load), the fast variations of the power injection in a heavily loaded grid may generate voltage instability [27]. The passing clouds can cause a local low voltage conditions, that can affect the connected induction motors. Lowering excessively the voltage brings the motors to stall, withdrawing higher current from the grid and worsening the voltage profile, till instability (Figure 1.5).

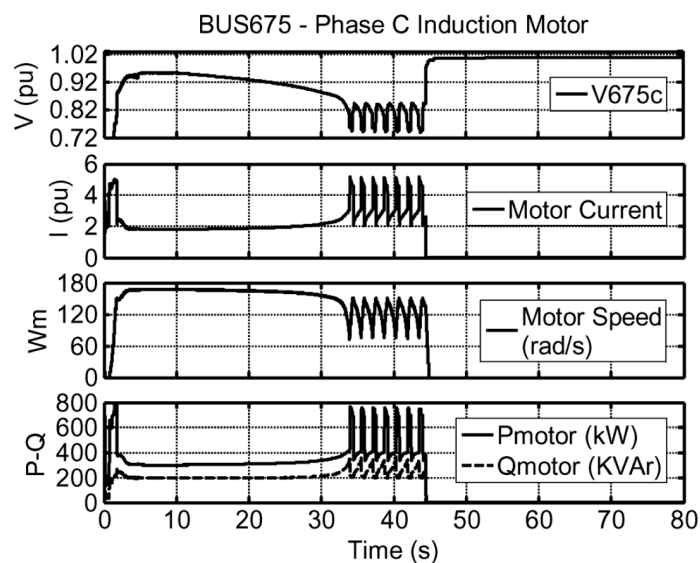


Figure 1.5: Effect on the fast power variation of PV (40% of the total load) on induction motor [27].

Decreased grid inertia

The DG, composed of small generators spread in the distribution grid, has lower inertia with respect to the large generators installed in the transmission system. If referred to renewables, these resources can be connected by means of power electronics converters, behaving as constant power generators. These generators features contribute to decrease the frequency response in the grid. This concept has been addressed in details in [5]. The impact of the converter-based DG on the frequency deviation and on the ROCOF has been analyzed varying the amount of DG installed. In Figure 1.6 the frequency response of the system to a loss of 10 % of generation capacity is described, considering different synchronous generators inertia. Increasing the amount of converter-based DG installed, the frequency deviation (Figure 1.6a) and the the Rate Of Change Of Frequency (ROCOF) (Figure 1.6b) during a perturbation increase, and only generators with high inertia ($H_{SG}=10$, that is the case of steam turbines) are able to keep the frequency deviation and ROCOF within the allowable range for high DG penetration (48.5 Hz and 1 Hz/s respectively, in case of 70 % DG penetration).

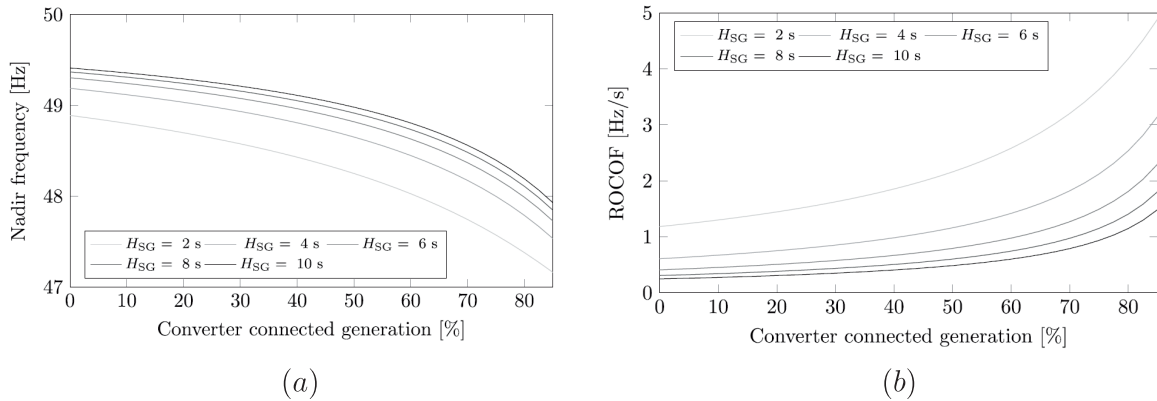


Figure 1.6: Decreased grid inertia with high converter-based DG penetration: (a) 12 % penetration (dark curve); (b) 30 % penetration (light curve) [5].

A practical case is the one of the isolated grids (e.g., islands), where the initial amount of inertia from the generator is not high, and it keeps deteriorating in case of high penetration of converter-based DG. In [28], two different scenarios of DG penetration in the Guadalupe island are considered: 12 % and 30 % of converter-based renewable power installed respectively, in case of disconnection of a non-renewable power plant. Two effects can be seen in Figure 1.7: the ROCOF decreases from -1.15 Hz/s to -1.33 Hz/s, and the frequency deviation increases in the second scenarios, leading to the activation of the automatic load shedding scheme (-10 % load at the 48.5 Hz threshold).

Reverse Power Flow

An issue affecting the distribution grids is the bidirectional power flow and the subsequent reversal at LV/MV substation level. The distribution grids, being radial, in case of high power production and low load demand, suffer of reverse power flow, that leads to a voltage increase

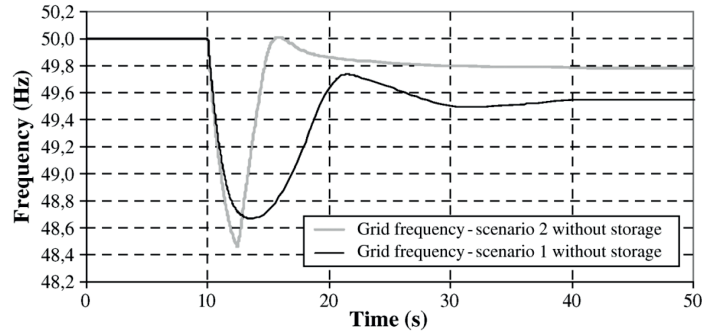


Figure 1.7: Decreased grid inertia with high converter-based DG penetration: (a) 12 % penetration (dark curve); (b) 30 % penetration (light curve) [28].

till the upper limits imposed by the distribution system operator (DSO) are reached [29, 2, 30]. Figure 1.8 shows schematically the effect of the reverse power flow in the distribution grid. If the amount of DG is limited (Figure 1.8a), the reverse power flow caused locally by DG supports the voltage profile to remain within the limits. However, in case of massive penetration of DG both in MV and LV grids (Figure 1.8b), the voltage amplitude can increase far above the limits imposed by the DSO.

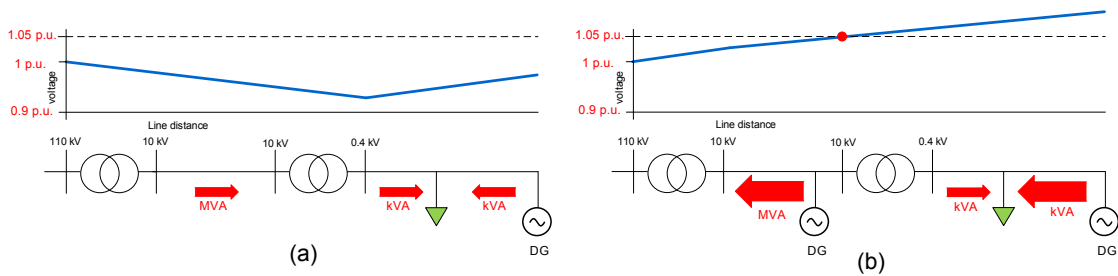


Figure 1.8: Effect on the voltage profile of DG in distribution grids: (a) moderate integration of DG, (b) high integration of DG and subsequent reverse power flow in MV grid.

Of particular concern is the widespread installation of photovoltaic systems in the LV grids. In the worst case scenarios, that is high PV generation / low load consumption, the power flow reverses in the feeder, violating the voltage upper limits [6]. As example, in Figure 1.9, the impact on a LV/MV transformer is shown in presence of high PV penetration. In a period of one day, during the central hours, the PV power injection is higher than the load consumption, leading to the power reversal in MV grid (Figure 1.9a). The voltage at the substation level, that in nominal condition is fixed to $230 V_{rms}$, increases till reaching the peak of $239 V_{rms}$ at noon, leading to over-voltage conditions in the downstream grid.

The MV/LV transformer with on-line LTC implemented have power transfer limitations in case of reverse power flow. LTC technologies with asymmetrical mechanical topologies (e.g. single resistor LTC [31]) have limited overload capability [30 ÷ 50 %]. Due to construction limitations, in case of reverse power flow, the transient current flowing in the tap-changer is higher than the designed one [32]. Limitations can occur also in the LTC control. If

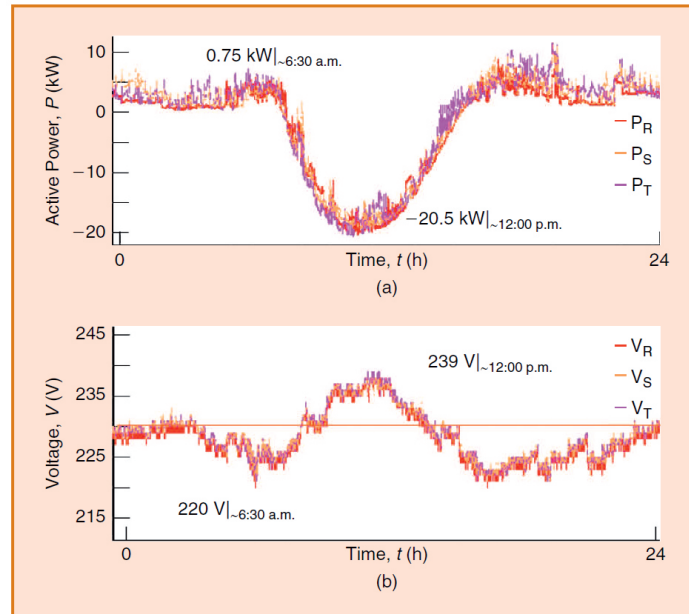


Figure 1.9: Reverse power flow conditions in a LV/MV transformer: (a) power flow; (b) voltage profile in LV transformer side [29].

the power reverse, the LTC tries to vary the tap-changer position to lower the voltage in the downstream grid. However, it has been proved in [33], that the minimum tap changers position can be reached in case of high power flow reversal, thus losing the voltage control in the LV grid.

1.2 Solutions proposed in literature

Voltage and current control in distribution grids

Actually, different solutions to the voltage limit violations have been implemented in the distribution grid. Electro-mechanical solutions, such as shunt capacitor banks and LTCs, have been employed in the early stage of voltage control. In the recent years, power electronics solutions, such as converter-based DG reactive power support [34] or Dynamic Voltage Restorer (DVR) and STATCOM, have been installed at the transmission and distribution grid level.

The first solution, that is the distributed implementation of capacitor banks in the distribution grid, although is the most cost-effective, can be applied only in case of passive grids, or with limited penetration of DG, where only under-voltage conditions occur. The capacitors, working in coordination with the transformer's LTC, are able to control the steady-state voltage profile near the nominal value [35]. However, they have limited effect in case of the fast voltage variations created by the renewables intermittent power injection [36].

The LTC solution controls the voltage profile changing the transformer ratio, thus modifying the voltage magnitude. LTCs, in general, allow for following properly the load trend in the network, mostly in stressed conditions and under the presence of DG (e.g., [37, 38, 39, 40]).

However, the LTC-based voltage control represents a centralized method and does not allow for a flexible control of the voltage in the different network buses. Furthermore, the number of LTC switches allowed per hour is restricted and the voltage range that can be controlled is limited [41]. The slow control actions during transients and the restricted number of step changes per hour may lead to transient under- or over-voltage conditions. Thus, these devices are not good candidates for dealing with the voltage control of active grids during transients, which is one of the main characteristics in case of high penetration of renewable energy resources such as PV.

The DG reactive power control represents a good solution to avoid over-voltages in the grid in case of high DG production [42]. It offers the possibility to provide reactive power to the loads locally, reducing the current flow and thus the grid losses; it increases the control flexibility, due to the presence of a large number of individual compensators; it enhances the reliability of the systems, not relying in large compensation systems, like large capacitor banks [36]. However, depending on the strategy adopted, this solution can have heavy drawbacks. If the converter goal is to minimize the distance of the bus voltage from the nominal one, the converter behaves like an inductor, absorbing reactive power. This leads to a higher request of inductive reactive power from the higher voltage level grids, increasing the losses and reducing the power transfer capability in the transmission system [34]. Coordinating properly the reactive power injection, this drawback can be overcome, leading to an energy-efficient optimization of the voltage profile.

To solve the voltage unbalance issue, power electronics-based devices can represent a solution in the distribution grid, in particular in customer-related applications (e.g., industrial plants). Dedicated solutions, such as STATCOM or DVR, can be installed to deal with the unbalance issues. In [43] the application of STATCOM to compensate voltage or current unbalances is proposed, considering Voltage Source Converter (VSC) and Current Source Converter (CSC) solutions. Both solutions have been proved to be effective in compensating voltage and current unbalances, with more advantages for CSCs in case of low rated converters. In opposition with shunt elements, like STATCOM or converter-based DG, the DVR are series elements controlling the voltage waveform amplitude and frequency in the installation point [44]. Depending on the line impedance, the DVR can fully attenuate or partially compensate any disturbance coming from the grid: unbalances, harmonics and voltage dips. Its control action limitations lie on the converter size and in the grid reactance. Cables with high resistance/reactance ratios may require high reactive power injection and thus high converter capacity.

High power variability reduction by means of storage

In order to compensate the high power variability caused by intermittent renewables, storage systems have been employed. A battery energy storage system (BESS) enables to reduce the power fluctuation at the connection point of the renewables with the distribution grid. In systems such as photovoltaic power plants, it helps to reduce the power output oscillations

during cloudy days [45]. The BESS shown in Figure 1.10, contributes to smooth the power variation, caused by partial shadowing of the PV plant.

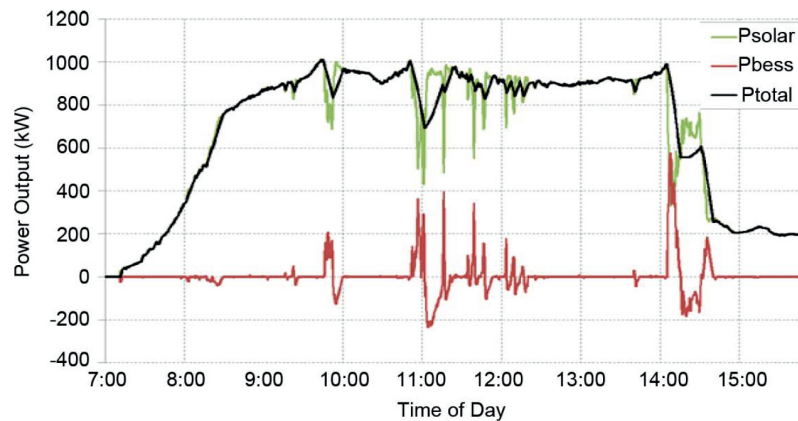


Figure 1.10: Reduction of PV power fluctuation at the connection point with the use of BESSs [45].

Combined wind-energy storage systems can be installed to target a flat power output of the wind plant or to provide dispatching services like conventional generators [46]. The wind output can be leveled, but the power rating of the batteries can be considerable (about 20-30 % of the wind farm installed capacity) to obtain dispatch profiles. Large wind power variation or too aggressive power target can lead to deplete the battery energy and to reduce their control capability [47].

Inertia dynamic support

Power electronics-based solutions offer the possibility to provide support with faster dynamics than the generators (milliseconds instead of seconds). This enhances the system rejection capability of disturbances, like faults, load and generator disconnection, and line tripping. This service can be provided under the form of dynamic support by means of energy storage, like ultracapacitor storage units [28]. As shown in Figure 1.11, the dynamic support acts in the first hundred of milliseconds in order to decrease the frequency deviation in the grid. Due to the limited energy stored in the ultracapacitor, the service is provided just for the first 15 s, time needed for the generators controller for increasing the power to restore the frequency.

An alternative to the employment of storage is to control the converter-based DG reproducing the dynamic properties of a real synchronous generator, in order to inherit the advantages in stability enhancement [48]. As an example of this concept the so-called "Virtual Synchronous Generator" (VSG) enables to adjust the DG active and reactive power depending on the grid frequency, emulating the behavior of a synchronous machine. The VSG can be composed of a converter-based DG equipped with storage and the VSG control mechanism.

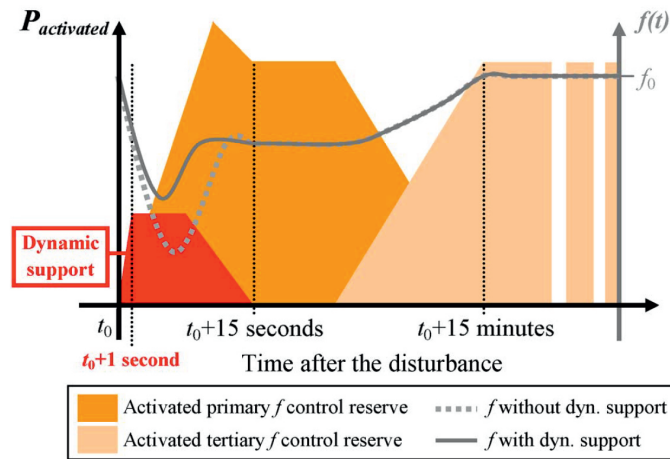


Figure 1.11: Effect of dynamic frequency support by means of ultracapacitor storage units [28].

Another possibility is to influence the load demand to provide frequency support. This concept goes under the name of Dynamic Demand Control (DDC), and involves the load controller to be responsive to a frequency change. In [49], a frequency dependent control of thermostatic loads (refrigerators) has been proposed to cope with the slow dynamic of spinning reserve to reduce the frequency variation during grid perturbation (e.g., loss of a large generator). In Figure 1.12 the response of the system to a loss of 1320 MW generator is shown in case of only spinning reserve available (light curve) and the integration of DDC (dark curve). The results show that the DDC is able to reduce the frequency variation during the generator loss event, from 49.4 Hz to 49.8 Hz.

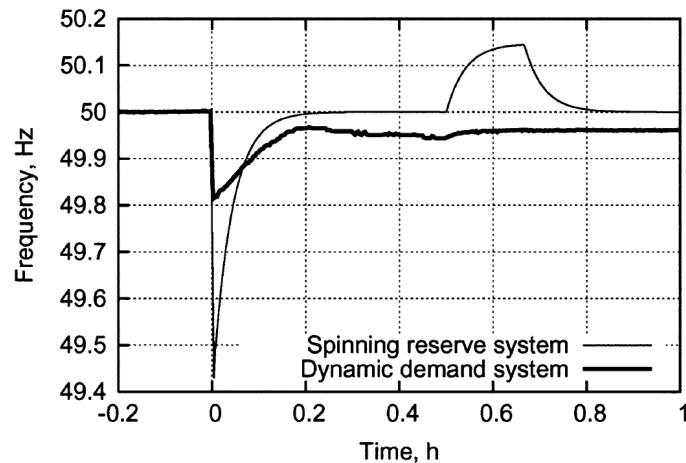


Figure 1.12: Effect of dynamic frequency support by means of dynamic demand system [49].

The last two approaches differ on their applicability in the current grid. The frequency support of DG can work mostly for downwards regulation (frequency increase and subsequent power reduction), with limitations for upwards regulation. Except for cases in which storage is present, the DG has to spare some power during normal operations (e.g., working at lower efficiency) in order to have spinning reserve during frequency changes. This corresponds to a waste of energy on the long term. On the other hand, requiring this support

from load can be easily achieved and it can work both upwards and downwards. Two limitations are present. The first one is the limited communication intelligence of these loads with central controllers. This technology will be largely implemented in the future, but it is not available currently. The second limitation lies on the re-bounce effect. Reducing the load consumption of controllable load (e.g., refrigerators) may require an higher consumption after the recover of normal conditions (e.g., refrigerators increase the power to cope with the higher temperature of the fridge chamber). This can lead to solve the frequency problem in the immediate, but it may present other problems, such lines and transformer overload, later.

Reverse power flow limitation

Actually there are no standard solutions to prevent the reverse power flow in MV grids. Control solution have been proposed to manage the grid energy and to limit the power flow reversal in the grid. Algorithm solutions as Demand Side Management and Optimal Power Scheduling have been proposed in literature. In the first case, a central controller varies the load demand by means of energy price signals, limiting the voltage rise during the peak hours of the PV production [50]. In the second case, the optimal power scheduling coordinates instead several devices (e.g., controllable loads, batteries, transformer tap changers, step voltage regulators, etc.) in order to keep under control the voltage profile during the PV intermittent power production [51, 52]. An applicative case is described in [53], where the controllable devices are the heat pump water heaters combined with BESSs and the reverse power flow is limited at customer level. The heaters power consumption is shaped by means of a communication infrastructure connecting the resources (heaters, batteries and PV) with a local centralized controller (always at customer level). If no control action is applied, the power injection in the grid reaches more than 2 kW in the PV production peak hours (Figure 1.13). Applying the power flow control, as soon as the power reverses, the batteries begin to charge and the heaters to increase their power consumption. The reverse power flow is thus limited to 0.75 kW. It can be noted in Figure 1.13, that the load control gives an additional degree of freedom to the system, while controlling only the battery, the reverse power flow is limited to 1 kW per household.

In extreme cases, the DSO may recur to remote disconnection of the DG plants. As reported in [54], power plants with power higher or equal to 100 kW connected in MV grids can be remotely disconnected by the DSO in case of need. Trivially, this implies a decrease of service quality offered by the DSO to the DG owners.

1.3 Examples of solution scenarios

The solutions presented in the previous section are customized for a certain category of problems. However, in the way of a "smarter" grid, more global and systematic approaches must be thought to manage the grid under high penetration of DG, mostly renewable-based

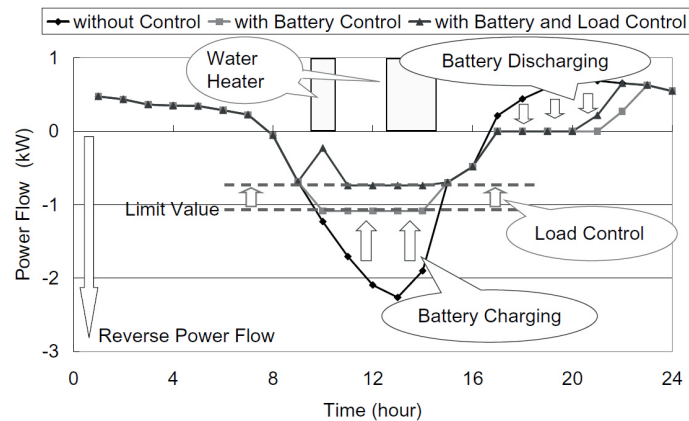


Figure 1.13: Effect of dynamic frequency support by means of dynamic demand system [53].

ones. In this section, 3 examples of system management scenarios are presented: demand management, microgrids, and multi-energy carriers systems. Each of these scenarios offers a different possibility to manage the energy in the grid, with the goal to increase the reliability of the system and the integration of DG.

Demand management

The ENTSO-E in [55] has underlined the importance on controlling the load to participate in the grid management, due to the large availability and distributed presence in the grid. Several mechanisms have been thought to make the load controllable and to involve it in the grid operations. The Demand Side Management (DSM) concept assumes the use of load as an additional degree of freedom for controlling the power volatility in the grid [56]. Although this concept is not entirely new (e.g., see applications of "conservation voltage reduction" for energy saving purposes [57]), the use of communication infrastructure and embedded systems makes it "smarter" with respect to the past. By means of market prices changes, the load power consumption can be influenced, without simply shifting it. If the power demand is simply shifted of few hours in order to avoid high demand in the power peaks, a "rebound effect" may occur. After avoiding the first power peak, the loads, trying to recover the energy as fast as possible, may create a second power peak [56]. This may just postpone the problem, without solving it entirely. Several services can be offered implementing the DSM: increase of energy efficiency, distributed spinning reserve, virtual storage, and demand shifting. It reduces the generation margin to be considered for system security [58], enabling the capability to control the load demand. Although the probability that an extreme event in need for severe load shedding occurs (e.g. faults) is very low, it is not foreseeable. To prevent local or national black-out the generation margin, under form of spinning reserve, must be always guaranteed, increasing the system costs. The load can perform the "spinning reserve" task, decreasing the consumption upon request of the Transmission System Operator (TSO).

BESSs can be considered part of the DSM as well. As shown in [59], the coordinated

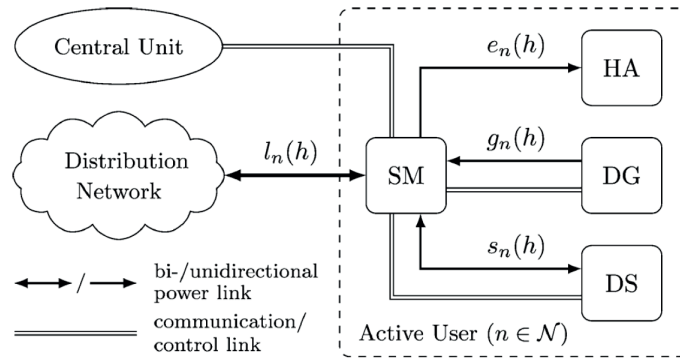


Figure 1.14: DSM management concept applied in [59]: *SM* Smart Meter; *HA* home appliances; *DG* distributed generation; *DS* distributed energy storage.

control of BESS, DG and home appliances allows to flatten the load consumption and the day-ahead market price for household loads. A smart meter (Figure 1.14) collects the power measurements from the DG and the energy storage, and interacting with a central controller unit, redistributes the power consumption of the active user (in this case an household load). The DSM in Figure 1.14, demonstrated that with a limited amount of active users willingly to participate to the DSM (24%), the peak-to-average value of the power can be leveled of 17.1% and the scheduled average price reduced of 16.5%.

Alternatively, the load consumption can be directly influence by a central controller using the Direct Load Control (DLC) approach [60]. The load consumption, composed of thermostatic controlled appliances, is managed by means of signals sent by the central controller, in order to reduce the load consumption in the peak hour, or upon request by the TSO. Using the DLC, spinning reserve services can be provided [61]. If the DLC is coordinated with a Interruptible Load Managements (ILM) system, the amount of controllable load can reach up to 10% of the total consumption. As depicted in Figure 1.15, the DLC and ILM can shape the load consumption below the system available capacity.

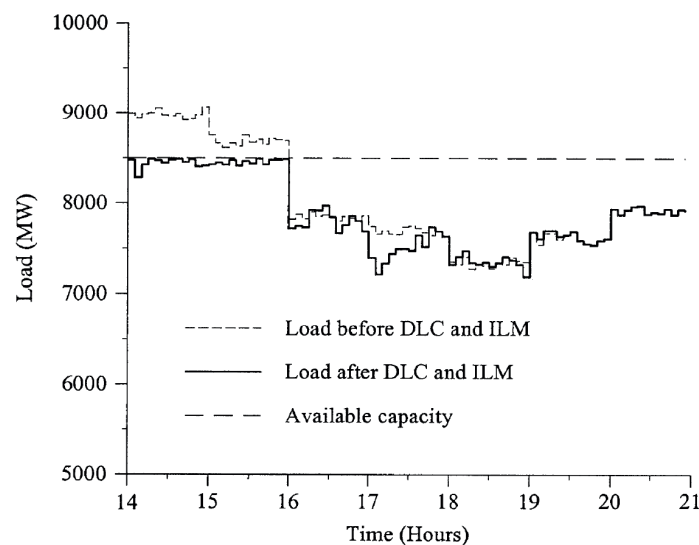


Figure 1.15: DLC and ILM reduction of load consumption to respect the system available capacity [61].

Currently, this method is limited by the lack of regulation involving the participation of load in the grid control. Suggestion and recommendations are coming from the European Union and the transmission system operators to let the load provide ancillary services, such as frequency control and "spinning reserve" [55], but they are not widely adopted. Moreover, the DSM and DLC assume the load controllability by means of control signals. This involves an advanced communication system that is currently not present in the distribution grid. Furthermore, the DSM adopting simpler communication systems, based on price signals, does not guarantee the system controllability, mainly for fast control actions, due to the lack of information on the load will on participating in the services market.

Microgrids

The Microgrid concept "assumes a cluster of loads and microsources operating as single controllable system that provides both power and heat to its local area" [62]. The aforementioned sources may consist of components like microturbines, PV panels, interconnection switches, communication infrastructure and batteries. The sources are controlled by means of the microgrid controller, that uses the resources status and local information to respond to any event occurring in the grid [63]. The microgrid control is based on the interaction among

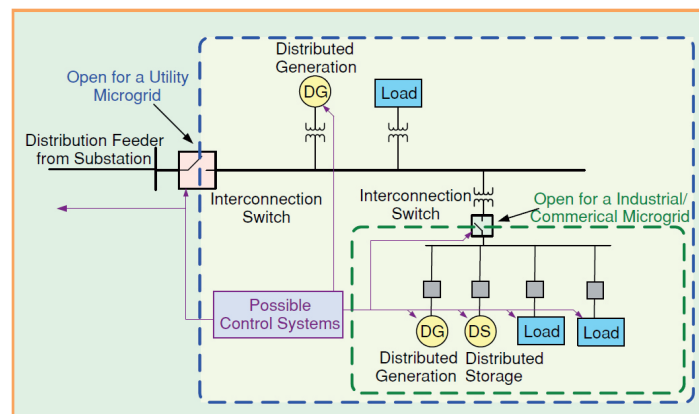


Figure 1.16: Microgrid concept [63].

resources. Each resource can be regulate following two control modes: Grid-Forming and Grid-Following [64].

- in the Grid-Forming control, the resource regulates the voltage waveform (amplitude, frequency and phase) at the point of common coupling (PCC) with the microgrid. This resource supplies the power to keep the power balance in the system, and thus, it must be of adequate capacity. This control enables the control of the microgrid in islanded mode, that is the control while the microgrid is disconnected from the main grid;
- the Grid-Following control regulates the active and reactive power injection of the resources. Depending on the control strategy, it can interact with the system varying the power output depending on the voltage amplitude and frequency values measured at his PCC with the grid, by means of droop controllers.

In order to manage many resources, mainly of different nature, a supervisory control is needed [64]: centralized control, distributed control, decentralized control, and hierarchical control [65].

- centralized controller allows to optimize the grid management by means of communication systems. The central control receives grid state at specified time intervals (e.g., 15 minutes) and, based on market prices, resources status and grid constraints, takes decisions for the following time interval, re-dispatching directly the resources. The control actuators can be classified in two categories:
 - central actuators, placed in a strategic point of the grid (e.g., substation or "weakest" bus), that apply the control action provided by the centralized controller.
 - distributed actuators, spread geographically in the grid, that contributes with a percentage of their capacity to the grid control. An example is the photovoltaic converter that reserves part of its ampacity to provide voltage support by means of reactive power, once received the power set-point from the centralized controller.
- decentralized controllers provides the maximum decision autonomy to the resources. Each resource take decisions in order to optimize its own operations, instead of the grid ones. This does not lead to a grid management optimization, however, an overall grid management improvement can be achieved.
- Hierarchical controllers imitates the behavior of transmission systems controllers [65]: a primary controller, based on droop methods, regulates voltage and frequency values by means of active and reactive power injection; the secondary control compensates the frequency and voltage error caused by droop characteristic in the primary controller; tertiary control regulates instead the power exchange with the external grid, allowing the creation of microgrid "clusters" and thus the control of more local microgrids.

In [63] several microgrid projects in US, Japan and Europe have been described, to show the capability of a microgrid to work autonomously and to optimize the local resources management. As example, the Hachinohe project is described in Figure 1.17, where the microgrid is constructed using a private distribution grid long more than 5 km, and it is composed of gas engines (three 170 kW systems), PV power plants (a large one of 50 kW, plus several small ones), and small wind turbines. The microgrid resources follows the load consumption in order to reduce the margin of error between supply and demand of less than 3 % for every six-minute interval. This enables the possibility to consider the microgrid as a dispatchable resource.

The microgrid concept has some intrinsic limits that must be considered. The communication-based microgrid solution, aiming for a fully-controllable grid, can see its control capability reduced in case of fail of the communication infrastructure. Moreover, the communication infrastructure may result complex and expensive, depending on the complexity of the control strategy. At the same time, a fully-decentralized grid results be sub-optimally controlled with respect to a centralized controller-based grid, due to the fact that each device does not take into account the neighbors action.

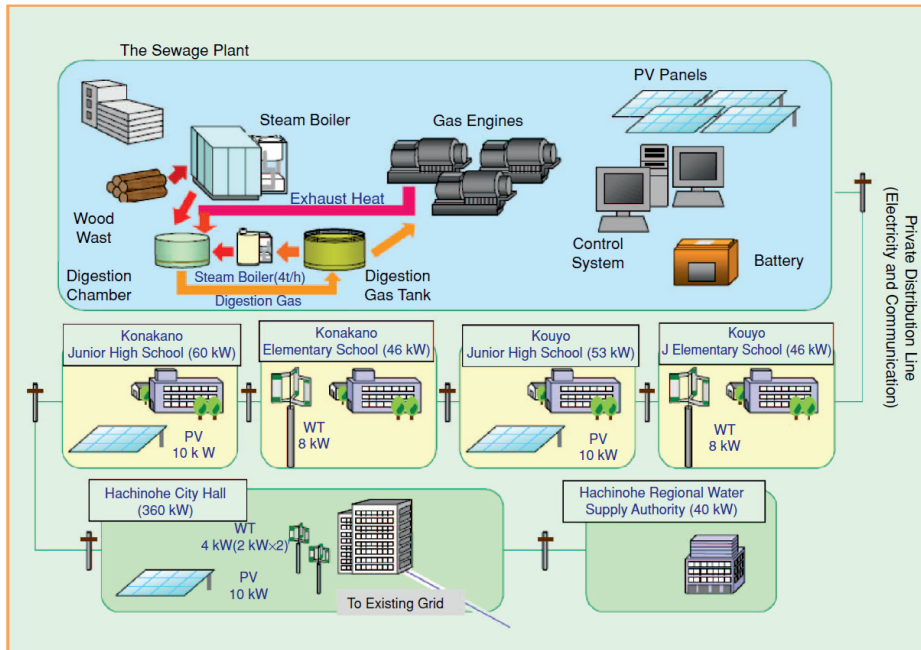


Figure 1.17: Hachinohe project showed in [63].

Multi-energy carriers systems

The multi-energy carriers system is a new concept developed in the last 10-15 years. It considers the possibility not to treat the different energy networks, such as gas, heat and electricity, as a set of independent problems, where each system is optimized without taking into account the interface points between the different energy layers [66]. It aims to design the future system as an interlaced grid, able to shift the energy from one layer to another one.

Following this idea, the concept of Energy Hub has been thought. The Energy Hub "is considered a unit where multiple energy carriers can be converted, conditioned, and stored. It represents an interface between different energy infrastructures and/or loads" [67]. The Energy Hub is a possible scenario of the energy system in 30 – 50 years, where the energy is delivered under different forms in order to optimize the system. The electrical, gas, and heating systems are interconnected and the energy is shifted from one layer to another one. The energy hub receives as input the resources as gas, electricity, district heat and wood chips, and produces as output electricity, heating and cooling (Figure 1.18). Within the hub, the energy is transformed and conditioned using technologies like combined heat and power plants, microturbines, power electronics-devices, storage. The internal components of the hub are interlaced, offering redundant path for supplying the output energies.

The application of a multi-energy carriers approach are several. It is possible to store energy under gas or heat form, and release it during electrical peak consumption times, by means of microturbines [66]. The power production is shifted from centralized to local, offering to the grid a redundant energy production system. A certain degree of flexibility and responsiveness is achievable in this way, increasing the reliability of the system at the same time. In [68]

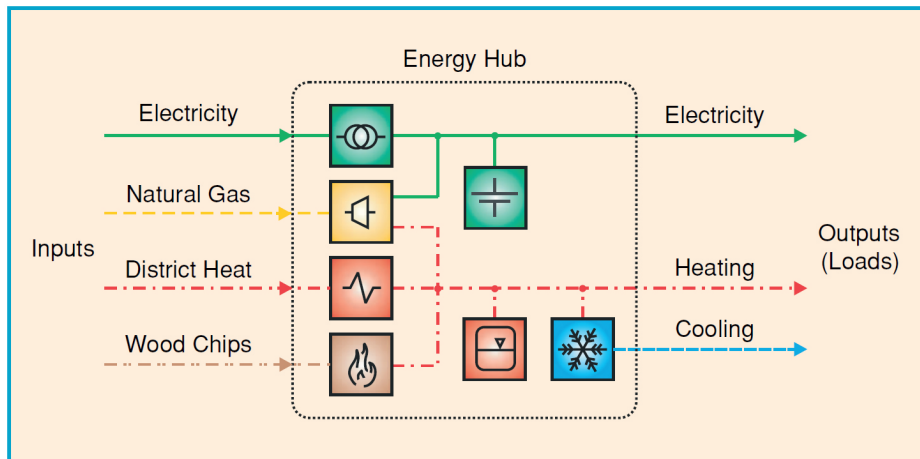


Figure 1.18: "Energy Hub" concept [67].

actors as thermostatic loads (e.g., refrigerators, heaters, conditioning systems) are included in the optimization problem, that takes in account objective function of different nature, such as energy cost, energy consumption, CO_2 emission costs, and peak load. Controlling the multi-energy carriers system by means of a centralized controller, it is possible to save up to 20% of energy costs and 50% of the peak demand for each household, maintaining the customer desired comfort levels (i.e., room temperature).

The current limit of this concept is in the involving several partners of different energy layers (electrical, heating and gas). It results particularly complex to coordinate them, mostly under the regulatory point of view, and simulation tools must be still be developed to analyze the interaction between energy layers. Several efforts in coordinating these systems have been done in literature [69], however the applications are still in the early stages.

1.4 Conclusion

This chapter aim is to briefly describe the most important challenges that the distribution grid must deal with under high penetration of distributed generation. Its focus is based on 3 main challenges:

- reverse power flow and voltage and current limit violations
- higher power variability
- decreased grid inertia

These challenges creates difficulties in the grid management, and in some cases (e.g., high voltage due to reverse power flow) can endanger the connected appliances. Several solutions have been proposed in the literature to solve these issues. The use of LTC and capacitor banks was the first adopted solution by the utilities to improve the voltage management in the grid. Following, power electronics solutions have been considered, installing new devices like STATCOM or DVR, or using the available resources, like the DG converters. The power electronics gives the possibility to support the voltage profile controlling the reactive power

injection. Furthermore, the integration of renewables increases the power variability, due to the intermittent energy production of these resources. If connected by means of power electronics converter, they contribute to decrease the system inertia, due to the faster control response with respect to the rotating machine-based generators. Storage systems can be employed to mitigate this higher power variability (e.g., batteries) and to increase the system inertia (e.g., ultracapacitors), compensating fast power variation or emulating the synchronous machine behaviors during system's perturbations.

At the end of this chapter, 3 possible grid management scenarios have been introduced: demand management, microgrids, and multi-energy carrier systems. Their goal is to make the system more reliable, while increasing the penetration of DG in the grid. The first system represents the possibility to see the load as controllable resource, and to manage the demand consumption varying the grid needs. Systems as demand side management or direct load control have been proposed to influence the load consumption. Both systems are directed by a central controller, connected by means of a communication infrastructure. If the central controller sends request to decrease the consumption by means of control or price signals, the load may be willingly to participate to the grid operations. This enables the possibility to offer fast power reserve, with the goal to provide "spinning reserve" services, to decrease the renewables power variability, and "increased inertia" services, to compensate the lower system inertia introduced by renewables. The microgrid concept aims to manage all the locally available resources in order to satisfy the local energy consumption. The resources are managed as a single controllable system by means of the microgrid controller. This solution gives 2 main advantages: it strengthens the grid local control, avoiding limit exceeding conditions (e.g., voltage and current), and increases the system reliability, providing energy to the local loads independently from the main grid conditions. In the last scenario, the main idea is to let interact all the energy layer presents in an area, such as natural gas, district heat and electrical networks, in order to convert, condition and store energy. Using different infrastructures offers redundant control of the grid and higher flexibility. Allowing to shift the energy among different energy layers, it gives the possibility to optimize the energy path in order to control optimally the grid (e.g., re-dispatching resources among layers).

The aforementioned solutions aim to solve a specific problem: microgrids and multi-energy carrier systems target an optimal management of the grid (e.g., controlling the voltage profile in the grid); demand management targets power reserve services, like the spinning reserve one. However, no one of these solutions offers a systematic approach to solve the grid issues: microgrids needs fast communication infrastructure for dealing with phenomena with fast transients (e.g., fast power variation of PV) or rely on decentralized control actions, that lead to a sub-optimal control solution; multi-energy carrier systems have slow response regarding fast transients, due to slower time constants of the coupled grids (e.g., heating or gas); demand management suffers of the impossibility to know a-priori the resources available to participate to the control action: if a load receives a new power set-point or a new price signal, it may not be willingly to participate to the service provision, limiting the control action effectiveness. As it will be seen in the next session, the Smart Transformer aims to fill the control gap left by these solutions, controlling the ST-fed grid as a whole

resource, in order to optimally manage the LV grid and to offer ancillary services to the MV and HV grids upon request from the DSO and TSO.

2 The Smart Transformer

The introductory chapter highlighted how the DG and mostly the renewable-based ones are characterized by high power injection variability and distributed presence in the distribution grid. These generation units vary their power output with short-term forecast possibilities and not simultaneously due to the different territory distribution. Thus, the grid has to deal with several challenges: voltage control, frequency stability, reverse power flow, greater demand variability, decreased system inertia, and protection systems coordination [1, 2, 70].

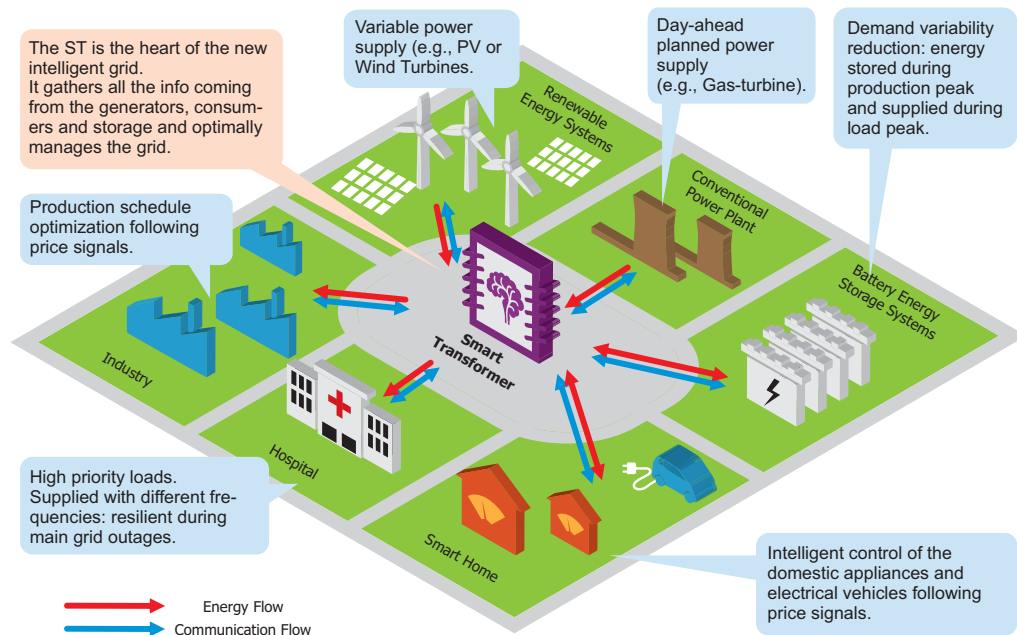


Figure 2.1: The Smart Transformer as central control point in the grid [J10].

The Smart Transformer represents an actuator of system level strategies that targets to solve the grid challenges. The ST is a power electronics-based transformer [J10] that aims not only to adapt the voltage from MV to LV grids, but to offer additional services to the grid, thanks to its advanced control features. The ST idea is to have a central point in the distribution grid, that, by means of communication infrastructure, enables the coordination of all the resources present in the grid (Figure 2.1), such as generators, industrial and residential loads, distributed generation, storage systems, etc. With respect to the solutions mentioned in the previous chapter, the ST has both the advantages of the centralized and decentralized approaches: for the LV grid, it is seen as a central control point where to send the info and the LV grid status is computed; for the MV grid, the ST is seen as a single resource (and not an aggregation of them) with the possibility to be controlled up to a certain extent. The ST, receiving the information from the grid, is able to optimize the grid management, and offer new services that were not possible to offer with the conventional transformer technology: reactive power support in MV grids, DC connectivity at both medium- and low-voltage level, and load control in LV side. Although several topology solutions can be adopted, the ST for grid applications chosen in this work is designed as a three-stage solution, with the isolation stage in the DC/DC converter. This solution enables the galvanic isolation between the two

grids, guaranteeing the LV appliances safety during abnormal conditions (e.g., faults), and at the same time enables DC connection possibilities both at MV and LV level. Other solutions can involve a conventional transformer plus a back-to-back solution, so moving the isolation stage out of the converter. This last solution, although simpler and with proven technology background, may limit the integration of large DC resources, such as EVs charging stations and batteries, or the connection of converter-based DG (e.g., photovoltaic).

2.1 Power Electronics Transformer: past and recent developments

The concept of Smart Transformer is not new, and it comes from the more generic definition of Power Electronics Transformer and Solid State Transformer. The first idea of PET can be found directly in 1968, when W. Mc Murray presented a patent regarding a DC transformer having a high frequency link, as shown in Figure 2.2. His goal was to adapt the input DC voltage with a different amplitude output by means of solid state switches and an electronic controls. In the 80s, Brook proposed an innovative transformer where the AC voltage adaptation was obtained by means of a high frequency link, with "a frequency very much larger than the input signal and then filtered to attenuate the high frequency component while passing the frequency of the AC input signal" [71]. The innovation of this last patent was in foreseeing a "voltage shaping" capability of the DC transformer, that moved the focus from the hardware configuration to the possible services that the PET could provide.

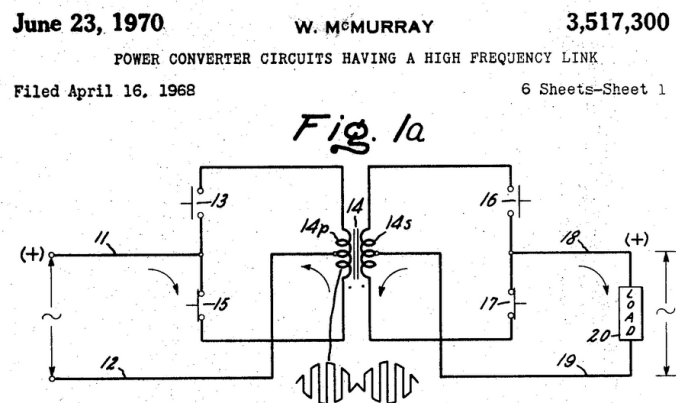


Figure 2.2: DC Transformer patented by W. Mc Murray [72].

The device technologies, when the patents of Brook and Mc Murray were proposed, was not developed enough to guarantee high efficiency and reduced weight and volume. With the introduction and the large-scale production of semiconductor devices, like Insulated-Gate Bipolar Transistor (IGBT), the PET started to be considered as valid alternative to the conventional iron-based transformer. The possibility to reduce weight and size represents an advantage in particular for traction applications. First PET transformers for traction applications have been proposed to increase the efficiency of the transformation stage [73, 74]. However, this application never break through the market and it remains still at experimental and prototype stages.

In the recent years, the PET, or SST, have been considered for replacing the conventional transformer in the MV/LV substations. Academic projects have been started to verify the applicability of the SST in the grid. The FREEDM center in US thought to the SST as link among loads, proposing the Energy Internet, where the energy is managed like information in internet [75]. Several prototypes, like the one in Figure 2.3 have been developed to demonstrate SST features in AC and DC microgrids [76].

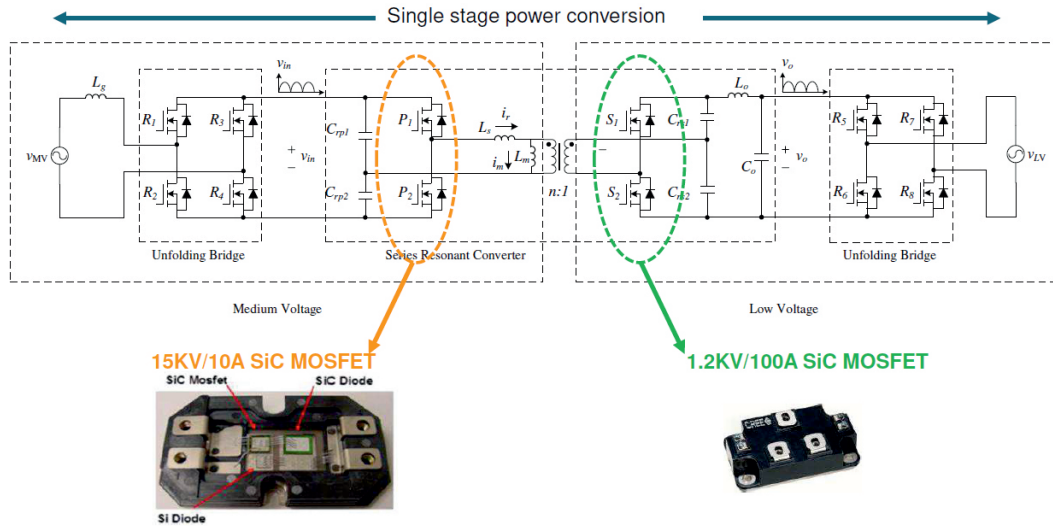


Figure 2.3: SST developed at the FREEDM center [77].

The SST has been thought to be a lower weight and size replacement of the conventional transformer in traction and grid applications. However, designing the SST for grid applications respecting the requirements of the traction field, can limit the SST provision of services to the grid. In the ST concept, instead, the hardware can be "tailored" to the grid [J1]. Single or double stage solutions have been proposed for the SST [78], in order to increase the transformer efficiency and reliability, decreasing the number of components. However, it does not allow or does limit the DC connection possibility in MV and LV DC stages. Furthermore, the goal to reduce the transformer size, weight and costs leads to downsize the SST to the maximum active power demand in LV grid. Some services that can be remunerated from the DSO, like reactive power injection in MV grid, can be limited due to the SST size constraints. In the ST view, the ST hardware must not be designed as a unique block, but each stage (MV, DC/DC, and LV) can be separately designed, to match the distribution grid needs [J1]. The LV and DC/DC converter sizes can be reduced with respect to the peak load case, thanks to the ST capability to shape the load consumption in the ST-fed grid (more details follow in the next chapters). The MV converter ampacity, instead, can be enlarged in order to increase the voltage support capability by means of reactive power injection. This "grid-tailored" approach, combined with the ST advance features, do allow the optimization of the grid services provision, keeping the hardware costs at the SST level [J1].

In the next section, the ST topologies and control are described, pointing out on the services that the ST can provide to the distribution and transmission grids. Applicative examples are provided to verify these new capabilities introduced by the ST and guidelines to the ST controllers tuning are provided.

2.2 ST control: provision of services for the distribution grid

The ST can act on three different levels as shown in Figure 2.4: on MV grid, on LV grid and on the DC grid (assumed as futuristic scenario). The three stages operations are interlaced. The MV converter controls the MV AC active current to maintain at the nominal value the MV DC link voltage. It can regulate the reactive power injection independently from the active power, remaining in the converter ampacity limits. The DC/DC converter transfers the power from the MV to the LV DC link in order to control the voltage in the LV DC link. The LV side converter controls the AC voltage waveform to be sinusoidal and balanced, and, upon request, it can shape the load consumption acting on voltage parameters (e.g., amplitude and frequency).

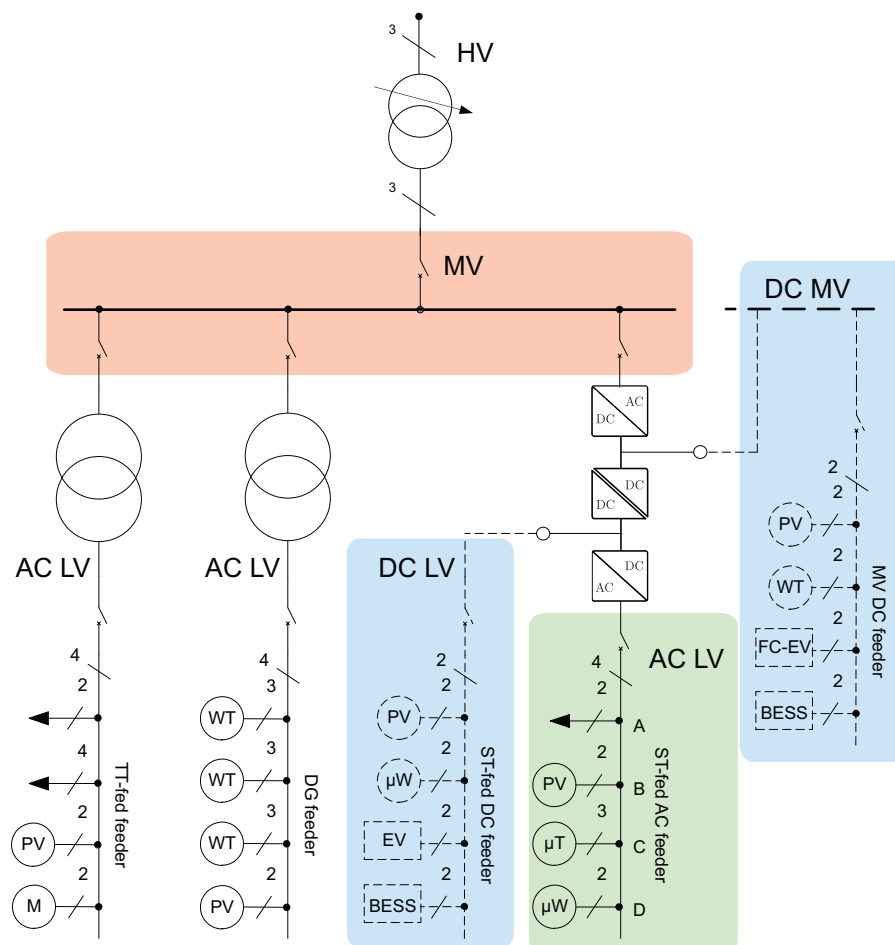


Figure 2.4: ST concept for providing services in distribution grid: load identification and control in LV grids (green area), active and reactive power support in MV grids (red area), enabled DC connectivity in MV and LV side (blue area).

In MV side (Figure 2.5) the ST has two controller layers: the first one composed of the MV DC link controller and the current controller, that absorb the current needed for guaranteeing the LV power demand; and the second one with a power controller, that aims to provide services to the MV grid, such as voltage support [C11], harmonic compensation and active

filtering. In the first control layer, the MV DC link controller sets the active current reference \tilde{i}_d^* to be sent to the current controller. The ST current controller absorbs the current to maintain the DC link voltage constant and thus to comply with the active power request from the load in the LV side plus the ST losses. The power controller in the second control layer operates both with active and reactive power. The outer power loop controller provides the reactive (i_q^*) and oscillating active current (\tilde{i}_d^*) references to the current controller reactive power support, to provide services like voltage and current control [C11], and harmonic compensation [79]. Reactive power and oscillating active power are defined as "non-active" powers, thus they are independent from the active power transfer from the MV to the LV side of the ST, as it can be noticed from (Figure 2.5). In the three stages-based ST technology, the two DC links decouple the AC power flow, leaving the active power flow as only link between the MV and LV grids. In section 3 a more detailed controller description is offered, with the controller implementation in practical cases, such as harmonic control and active filtering.

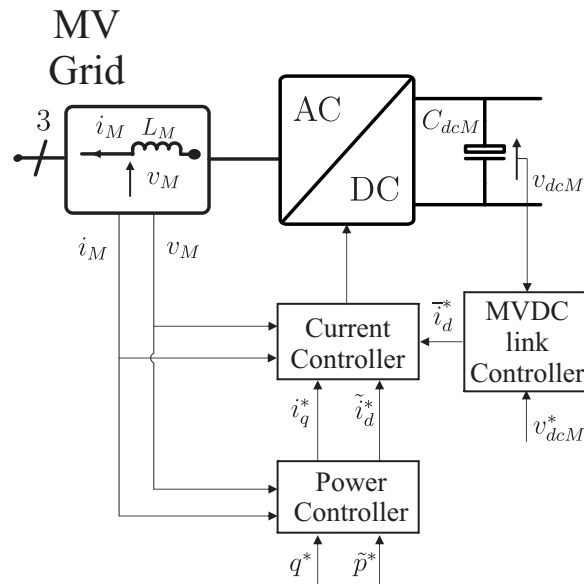


Figure 2.5: Smart Transformer MV converter control scheme.

As mentioned above, the ST creates a first interface of the AC grids with the future DC grids (Figure 2.4 blue box), both in the LV and MV level, by means of the DC/DC converter. The MV DC grids enables a new concept of distribution system, allowing the connection of MW-scale DC loads or generators, like PV and wind parks, large size BESS and Fast Charging Electric Vehicle stations (FCEV). The DC LV grid represents a valid alternative to the AC grids to host small DG and new loads, like EV and BESS. It can reduce the overall losses in the LV side, avoiding further AC/DC stages in the user side. The DC LV grid enables also the concept of Dual Microgrid Operation [80]: if controllable generators or BESS are installed in the DC grid, the ST can provide power to the LV grid also during disconnection of the MV grid, guaranteeing the respect of the power quality standard. The ST DC stage is characterized by two voltage levels: the MV DC link, controlled by the ST MV converter, and the LV DC link controlled by a DC/DC converter. The DC/DC converter technologies currently investigated for ST applications are the Dual Active Bridge (DAB)

and Series Resonant Converter (SRC). In the DAB technology (Figure 2.4), the LV DC link voltage v_{dcL} is controlled by means of a power flow controller, that regulates the active power flow from the MV to LV DC link, in order to maintain the LV DC link voltage constant. The SRC, instead, behaves as a DC transformer, adapting the LV DC voltage to the MV DC one. As described more in detail in section 4, these two technologies, DAB and SRC, are described, showing their control and disturbance rejection capability.

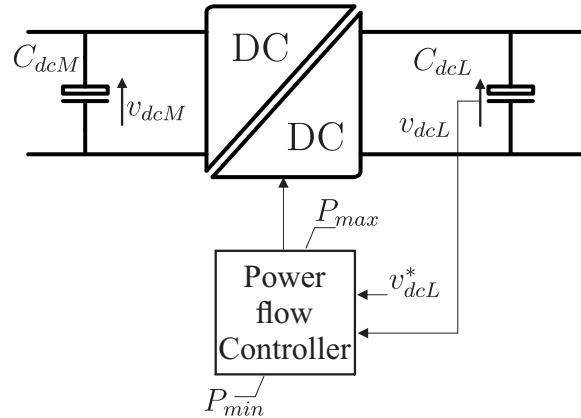


Figure 2.6: Smart Transformer DC/DC converter control scheme.

In LV side, the ST controls the voltage waveform in the ST-fed grid (Figure 2.7), where the ST can offer basic and advanced services. A basic service offered by the ST is to provide three-phase balanced voltage independently from the current waveforms [C8], that can be unbalanced or affected by harmonic content. The capability to modify the voltage magnitude and frequency, enables the possibility to interact with the local loads and generators in order to shape the LV grid power consumption. Possible advanced services that the ST can offer are the ST overload control (OVC) [J6], the Reverse Power Flow Limitation (RPFL) control [J9][J3], the On-Line Load sensitivity Identification (OLLI) [J5][J8], and Real Time Frequency Regulation (RTFR) control. In the first application the ST acts on the voltage frequency [C7], voltage amplitude [C6], or both of them [J6], to avoid the ST overload, during high load demand conditions. The RPFL control is a service offered to the MV grid, operating on the ST-fed grid frequency [J9][J3]. In case of power flow reversal from LV to MV grids due to high DG power production, the ST interacts with the local generators by means of a frequency increase to decrease their power injection, limiting the reverse power flow in the MV grid.

The accuracy of these services can be increased knowing the load power dependency to voltage and frequency. The ST enables the On-Line Load sensitivity Identification (OLLI) in order to analyze in real time the load active and reactive power sensitivity to voltage and frequency [J5]. The OLLI algorithm allows the ST to provide further services to the grid, shaping the load consumption in the ST-fed grid: the Soft Load Reduction (SLR), the transmission grid RTFR, and the sensitivity-based OVC [J8]. In case of request from the TSO or DSO during an emergency situation (faults, line overload, etc.), the SLR algorithm can decrease the power absorbed varying the voltage in the ST-fed grid, depending on the load voltage sensitivity. Similarly, the RTFR service allows to contribute to the transmission

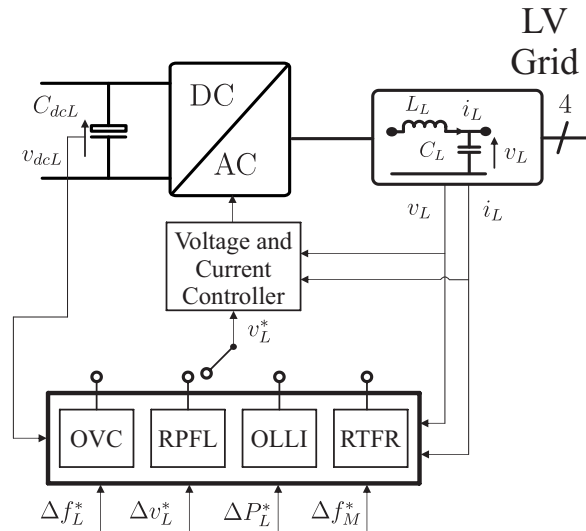


Figure 2.7: Smart Transformer LV converter control scheme.

grid frequency regulation, varying the load consumption in the ST-fed depending on the frequency value in HV grid. By means of OLLI algorithm, the ST applies the voltage variation to obtain the power variation requested for stabilizing the HV grid frequency. In case of constant power load behavior, a decrease of voltage in the LV grid causes a further increase of the line current and a worsening of the ST overload. The ST, with the sensitivity-based OVC, is able to avoid the overload condition, adapting the voltage set point depending on the load nature.

The overall ST control structure is shown in Figure 2.8, where the MV and LV converter are connected through the DC stage.

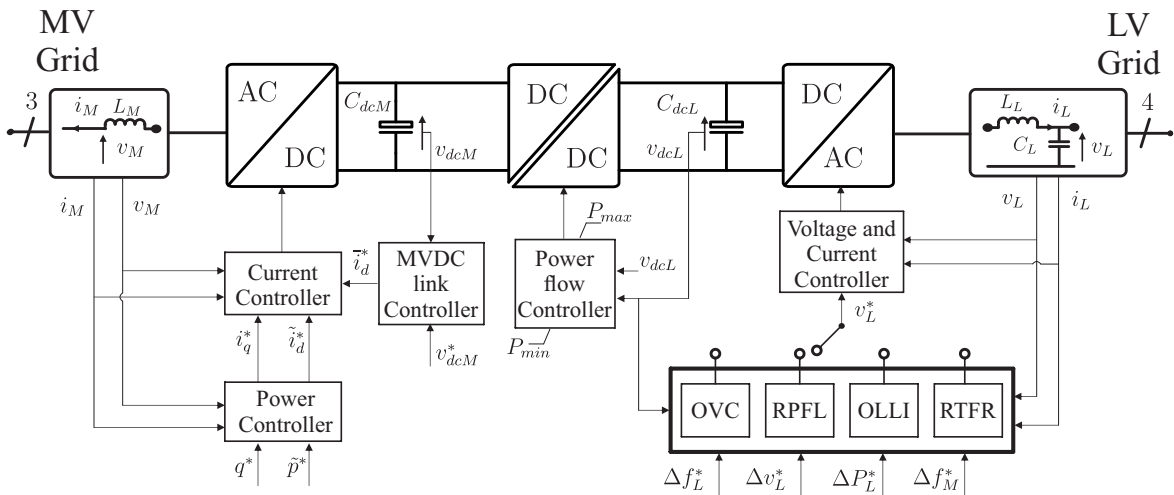


Figure 2.8: Smart Transformer control scheme.

This work structure idea is to go through all the services offered by the ST, starting from the basic controllers and features described in this chapter. In this Chapter, each ST converter stage topologies and controllers are analyzed in details, and tuning procedures are given. Basic application cases are provided, to verify the effectiveness of each proposed controller. In Chapter 4, the ST capability in evaluating the ST-fed grid power consumption dependency

on voltage and frequency is investigated, in order to provide real time information to the ancillary services controllers described in Chapters 5 and 6. To summarize, the aforementioned services are listed as follows:

Harmonic Compensation	}	Chapter 2
Active Filtering		
Power flow controller		
On line Load Identification (OLLI)	}	Chapter 4
ST overload controller (OVC)		
Reverse Power Flow Limitation (RPFL) controller	}	Chapter 5
Soft Load Reduction (SLR)		
Real Time Frequency Regulation (RTFR) of transmission grids	}	Chapter 6

2.3 MV converter

The MV converter can be realized following several topologies, that are linked to the necessity to work with higher voltage levels (10 kV and above) with low voltage components. Neutral Point Clamped (NPC) converters (Figure 2.9a), Multilevel Modular Converters (MMC) (Figure 2.9b), and Cascaded Half Bridge (CHB) converters (Figure 2.9c) are only few of different solutions offered for the ST MV side converter [J10].

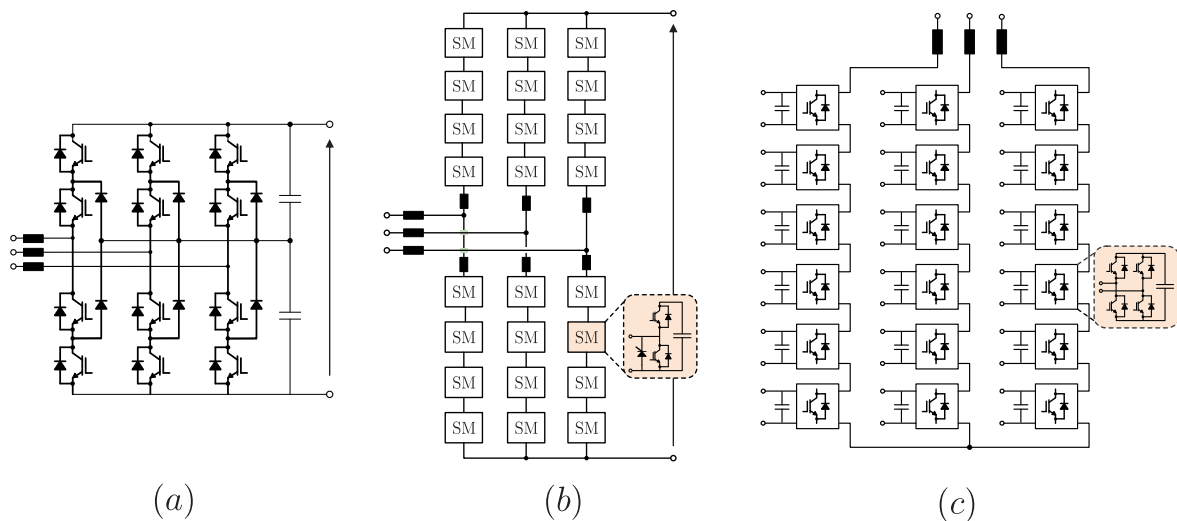


Figure 2.9: ST MV converter topologies considered: (a) Neutral Point Clamped converter, (b) Modular Multi-level Converter (MMC), (c) Cascaded Half-Bridge (CHB) converter.

The CHB solution has the advantage of using low voltage devices in series to reach the MV grid single-phase voltage amplitude. Each CHB cell has its own DC/DC converter. The main drawback is the absence of a common MV DC-link, that is a limit for connection of future MV DC grids. The MMC solution solves this drawback, offering the access to

a common MV DC-link, although its complex control structure and the use of bulky DC capacitor represents still an issue.

This work does not intend to discuss on the topologies comparison for the ST MV converter side, but more to analyze their modeling to be used in power system simulations. Although the aforementioned topologies are different in their realization, a simplified mathematical modeling can be represented as first with the equivalent model shown in Figure 2.10.

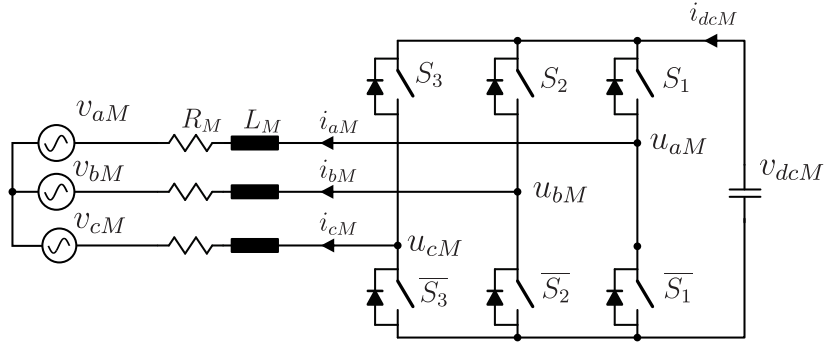


Figure 2.10: Circuitual scheme of the ST MV converter, general topology case.

This representation is valid for the NPC converter topology, however, for MMC and CHB converters the equivalent model should be adapted, as will be shown in the next sections in this chapter. In Figure 2.10, the MV converter is interfaced to the MV grid by means of a L filter in order to control the current needed for balancing the DC link stage.

Starting from this assumption, the Kirchhoff Voltage Laws (KVL) can be written as:

$$\begin{cases} u_{aM}(t) = L_M \frac{di_{aM}(t)}{dt} + R_M i_{aM}(t) + v_{aM}(t) \\ u_{bM}(t) = L_M \frac{di_{bM}(t)}{dt} + R_M i_{bM}(t) + v_{bM}(t) \\ u_{cM}(t) = L_M \frac{di_{cM}(t)}{dt} + R_M i_{cM}(t) + v_{cM}(t) \end{cases} \quad (2.1)$$

The equation system above can be represented vectorially, introducing the rotational element of the vector $\alpha = e^{j2\pi/3}$. Thus, the voltage vector can be expressed in terms of the three-phase voltages as:

$$\bar{u}_M(t) = \frac{2}{3} (u_{aM}(t) + \alpha \cdot u_{bM}(t) + \alpha^2 \cdot u_{cM}(t)) \quad (2.2)$$

Then, the converter KVL already expressed in (2.1) can be rewritten using (2.2) in a compact form as follow:

$$\bar{u}_M(t) = L_M \frac{d\bar{i}_M(t)}{dt} + R_M \bar{i}_M(t) + \bar{v}_M(t) \quad (2.3)$$

The (2.3) is a vectorial equation, that can be decomposed in three equations expressing the KVL of each phase. However, the MV grids are ungrounded, thus one phase is dependent from the other two. For this reason, the MV converter equations can be written in the dq

frame, reducing the system from 3 to 2 equations. The transformation matrix of the $p_{a,b,c}$ linking the abc variables and the new dq variables is:

$$\begin{bmatrix} u_{dM} \\ u_{qM} \end{bmatrix} = \begin{bmatrix} \cos(\theta) & \cos(\theta - 2\pi/3) & \cos(\theta + 2\pi/3) \\ \sin(\theta) & \sin(\theta - 2\pi/3) & \sin(\theta + 2\pi/3) \end{bmatrix} \begin{bmatrix} u_{aM} \\ u_{bM} \\ u_{cM} \end{bmatrix} \quad (2.4)$$

where θ is the angle of the rotating dq system with respect to the stationary abc system. (2.7) can be summarized as follows:

$$\bar{u}_{dqM} = T_{dq} \cdot \bar{u}_M \quad (2.5)$$

By means of the transformation shown in (2.5), (2.3) can be transformed in the dq frame obtaining finally:

$$\bar{u}_{dqM}(t) = L_M \frac{d\bar{i}_{dqM}(t)}{dt} + \Omega \bar{i}_{dqM}(t) + R_M \bar{i}_{dqM}(t) + \bar{v}_{dqM}(t) \quad (2.6)$$

where Ω represents the product of the transformation matrix T_{dq} with the derivative of its inverse:

$$T_{dq} \cdot \frac{d}{dt} (T_{dq}^{-1}) = \Omega \quad (2.7)$$

The equation in (2.6) can be split in two different equations, indicating the components along the axis d and q :

$$\begin{cases} \frac{di_{dM}(t)}{dt} - \omega i_{qM}(t) = \frac{1}{L_M} [-R_M i_{dM}(t) - v_{dM}(t) + u_{dM}(t)] \\ \frac{di_{qM}(t)}{dt} + \omega i_{dM}(t) = \frac{1}{L_M} [-R_M i_{qM}(t) - v_{qM}(t) + u_{qM}(t)] \end{cases} \quad (2.8)$$

where $\omega i_{qM}(t)$ and $\omega i_{dM}(t)$ are the coupling terms between the d and q frames, created by the dq transformation matrix. Eq. (2.8) can be linearized and transformed in the Laplace domain:

$$\begin{cases} U_{dM}(s) = R_M I_{dM}(s) + sL_M I_{dM}(s) - \omega L_M I_{qM}(s) + V_{dM}(s) \\ U_{qM}(s) = R_M I_{qM}(s) + sL_M I_{qM}(s) + \omega L_M I_{dM}(s) + V_{qM}(s) \end{cases} \quad (2.9)$$

The DC and AC side are linked by means the active power transfer. This link is represented by the power equation:

$$v_{dcM}(t) \cdot i_{dcM}(t) = \frac{3}{2} (v_{dM}(t) \cdot i_{dM}(t) + v_{qM}(t) \cdot i_{qM}(t)) \quad (2.10)$$

considering the voltage vector in phase with the d -axis, the $v_{qM} = 0$, that is equivalent to relate the DC power with the d -axis current and voltage in AC side. Rearranging (2.10) to obtain the current:

$$i_{dcM}(t) = \frac{3}{2} \frac{(v_{dM}(t) \cdot i_{dM}(t))}{v_{dcM}(t)} \quad (2.11)$$

this equation expresses the equivalent current in the DC side absorbed in the AC side by the MV converter. Assuming the voltage constant both in DC and AC side, Eq. 2.13 can be linearized obtaining:

$$I_{dcM} + \tilde{i}_{dcM}(t) = \frac{3 V_{dM} \cdot (I_{dM} + \tilde{i}_{dM}(t))}{2 V_{dcM}} \quad (2.12)$$

Simplifying the constant terms and transforming the time-domain terms in the Laplace domain, the DC power transfer function from AC to DC side is obtained:

$$I_{dcM}(s) = \frac{3 V_{dM} \cdot I_{dM}(s)}{2 V_{dcM}} \quad (2.13)$$

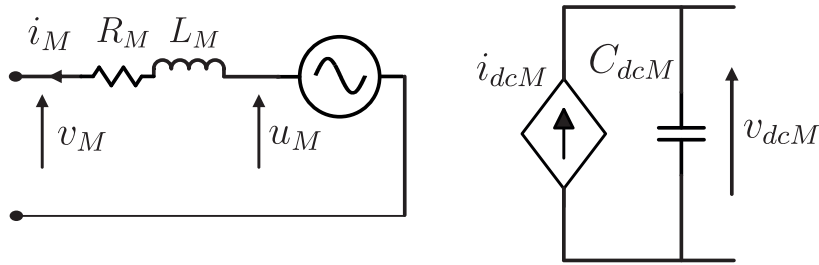


Figure 2.11: Average model of the MV converter.

The equations described above lead to represent the circuit as shown in Figure 2.11. A controlled voltage source regulates the amount of current i_M in the MV controller filter depending on the MV grid voltage v_M . The DC side is modeled as a controlled current source, injecting the current i_{dcM} expressed as (2.13). As shown in the next subsections, this model can be adopted in case of full bridge converters (e.g., if high voltage switching devices are used) or multi-level converters (e.g., NPC, CHB or MMC).

CHB equivalent model

The CHB converter is a multilevel converter with separate DC-link capacitors for each cell, connected with a DC/DC converter (e.g., DAB or SRC) Figure 2.9(c). Differently from the NPC and MMC topologies, having the DC link sharing the whole DC voltage, in the CHB the DC link voltage is divided among the cells connected in series. The total DC link voltage of each CHB phase is the sum of the DC voltage of the cells, and it must be higher than the single-phase voltage peak in the MV grid (8.96 kV for a 11 kV MV grid). For this reason, it has been chosen 10 kV as DC-link voltage. The DC-link capacitor must be sized taking in account the presence of the second order power harmonic oscillation in the DC side. Being a single phase converter, each cell has a constant power component, plus a pulsating power at 100 Hz, that can affect the DC-link lifetime. Each cell is composed of 1200 V IGBT devices (already available in the market and of common use in practise) working at 800 V, thus 13 cells are necessary for covering the total DC-link voltage amplitude. To size the MV DC link capacitor of the i -th cell C_{dcM}^i the following formula is adopted in this work [81]:

$$C_{dcM}^i = \frac{\Delta P_{pk-pk}}{2 \cdot 100\pi V_{dcM}^i \Delta V_{dcM}^i} \quad (2.14)$$

where $\Delta P_{pk-pk} = 160$ kW, equal to the double of the cell nominal power, and $\Delta V_{dcM}^i = 80$ V, corresponding to a peak-to-peak voltage variation of 10% with respect to the nominal voltage magnitude V_{dcM}^i . The resulting capacitance to be implemented in each cell is equal to $C_{dcM}^i = 4$ mF. The aforementioned parameters are listed in Table 2.1

Table 2.1: DAB converter parameters for CHB applications

Parameter	Value	Parameter	Value
f_s	20 kHz	P_{CHB}	1 MW
V_{dcM}	800 V	V_M	11 kV
C_{dcM}^i	4 mF	P_{cell}	80 kW

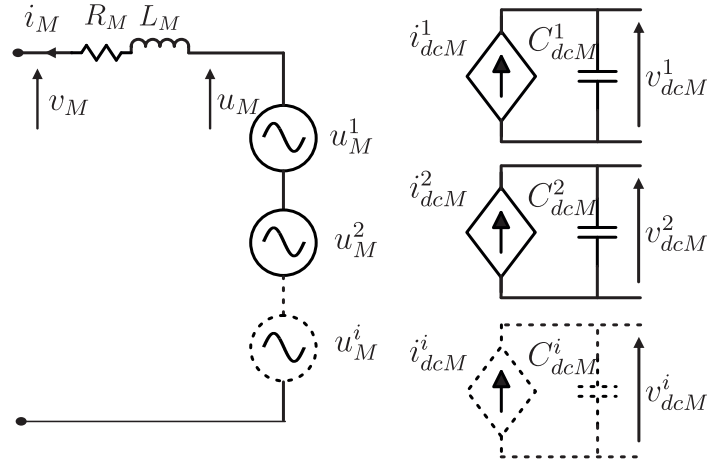


Figure 2.12: Average model of a CHB converter with the DC/DC stage connection.

Following the reasoning above, the CHB has to be modeled as a series of controllable voltage sources v_i , injecting power in the i -th MV DC-link. The power flowing in the DC-link is regulated by means of the controlled current source i_{dcM}^i .

MMC equivalent model

The MMC is a multi-level converter that brings together the advantages of low switching frequencies, the use of low voltage semiconductor devices, and the availability of the MV DC link.

To represent the MMC model, the modeling shown in the previous section must be adapted. The KVL for each phase can be described with (2.1), that remains generally valid. However, the converter's internal dynamics must be taken in account [82]. The converter voltage,

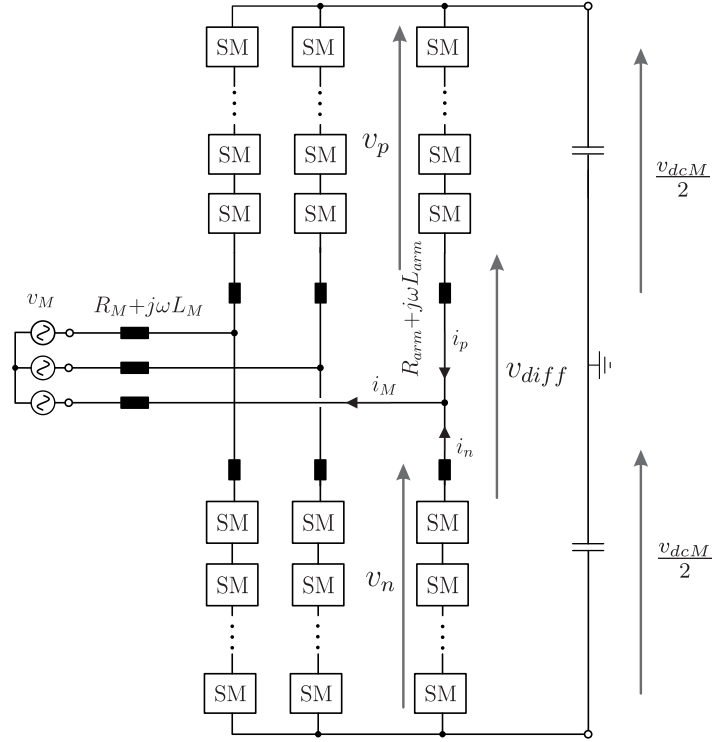


Figure 2.13: Average model of a CHB converter with the DC/DC stage connection.

equal to the half of the difference between the upper leg and lower leg voltages (v_p and v_n respectively), is defined as follows:

$$v_{conv} = \frac{v_n - v_p}{2} \quad (2.15)$$

where v_p and v_n are assumed as the sum of the switching states of all N converter submodules:

$$v_p = \sum_{x=1}^N S_p(x) v_{c,p}(x) \quad (2.16)$$

$$v_n = \sum_{x=1}^N S_n(x) v_{c,n}(x)$$

The arm current has two different contributions: the differential current i_{diff} and the phase current contribution i_M . The first one is the DC component of the converter current, instead the second one is the AC component flowing in the grid. If these two currents contributes equally to the arm current the following relations can be written:

$$i_p = i_{diff} + \frac{i_{ac}}{2} \quad (2.17)$$

$$i_n = i_{diff} - \frac{i_{ac}}{2}$$

Thus, the differential voltage can be written as:

$$v_{diff} = v_{dcM} - (v_n + v_p) = 2L_{arm} \frac{di_{diff}}{dt} + 2R_{arm} i_{diff} \quad (2.18)$$

where L_{arm} and R_{arm} are the arm inductance and resistance respectively. The equations (2.17) and (2.18), together with the (2.1), describe the model of a MMC, including the converter dynamics. It is worth noticing that, being an average model, the internal behavior of the single cells is not included. It is assumed that the capacitor of each converter's submodules are balanced and constant, and the semiconductor devices are represented by ideal switches.

2.3.1 Control of MV converter

The MV converter has fundamentally two tasks: to control the MV DC link voltage and to control the reactive power in the AC side. The first task is performed controlling the current in the AC side in order to keep balance between the current absorbed by the DC/DC converter and the current injected from the AC side. It works in dual way in case of power flow reversal from the LV grid. In ordinary conditions, the ST works with unity power factor, setting the reactive power reference to zero. In case ancillary services are requested from the ST (for instance voltage support in the MV grid), the ST can provide reactive power. The reactive power set-point can be evaluated locally by means of a V/Q droop controller curve, or set remotely from a centralized controller.

As shown in Figure 2.14, the MV controller is divided in two loops. The inner loop is the current controller that receives the dq current references from a power and MV DC link controller, and an external loop that controls the reactive power injection and the voltage in the DC-link capacitor.

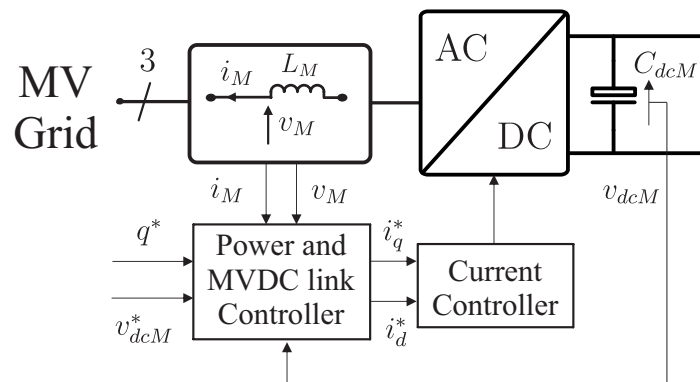


Figure 2.14: Medium Voltage control scheme.

Going more in detail (Figure 2.15), the active power loop is composed of a PI controller that minimize the error of the MV DC link voltage, creating the d current reference i_{dM}^* . Here the reference is compared to the d current read on the filter inductor and sent to a PI controller. The q -axis external loop differs from the d -axis due to the presence of an open-loop function linking the desired voltage amplitude in the MV grid to the q current reference,

in order to support the voltage amplitude control in the MV grid. As matter of simplicity, a droop characteristic $i_{qM}^* = K_{drV} V_{rms}$ is considered in this initial study, where V_{rms} is the AC voltage rms value, and K_{drV} is the droop gain. More advanced controllers are described in the following sections, underlining the impact on the q -axis controller. The current controller in q -axis is similar to the one in the d -axis, and thus further explanations are skipped.

At the output of the current controller the decoupling terms and the voltage feed-forward signals are added. The resulting modulation signals u_{dm} and u_{qm} are transformed in the stationary abc frame by means of the inverse matrix T_{dq}^{-1} and sent to the PWM generator, where the switching signals $S_{1,\dots,6}$ are created. In this case, a general three-phase full bridge converter is considered. Under the control point of view, the topology choice is not relevant, thus this control strategy can be adapted to all the ST-tailored topologies.

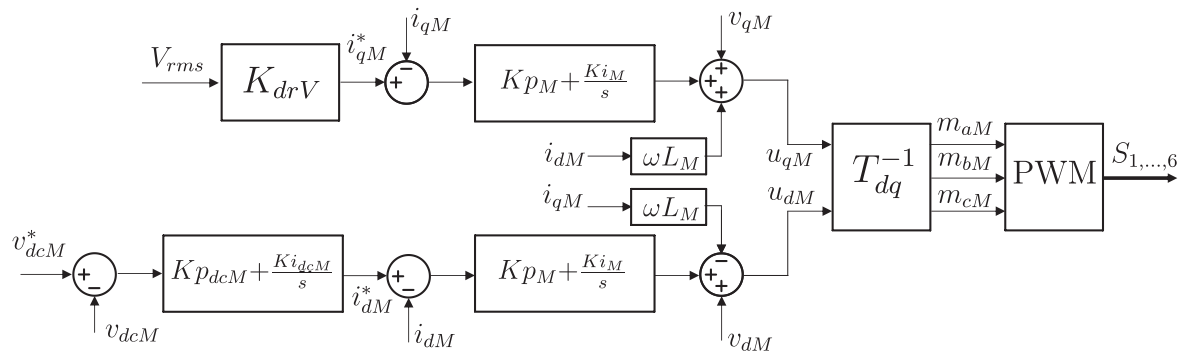


Figure 2.15: Medium Voltage control scheme: outer and inner control loop, with decoupling network and feedforward voltage components.

The tuning of the ST MV converter takes in account the model described in (2.8) and (2.13), and the control shown in Figure 2.15. The equivalent control and plant loop of the MV converter is shown in Laplace transformation system in Figure 2.16.

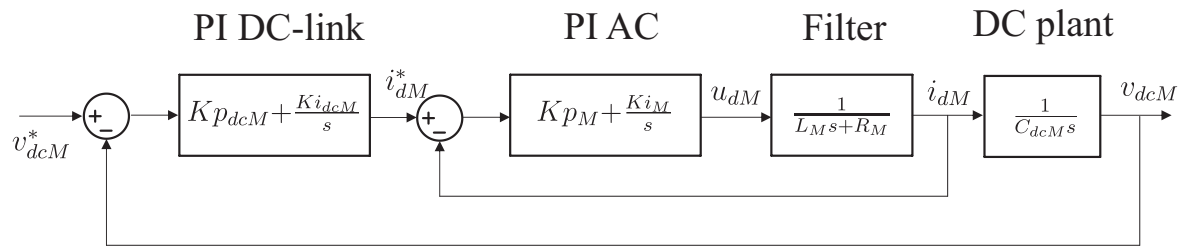


Figure 2.16: MV converter control and plant loop.

From Figure 2.16 two loops can be noted. The inner loop is composed of a current controller (PI) that regulates the current in the filter inductor L_M . This loop has been shown for the d axis, and it is equivalent for the q axis. In the d axis, the outer loop controls the voltage in the MV DC-link capacitor, by means of a PI controller. The DC-link plant dynamic is integral influenced by the capacitor C_{dcL} size. To analyze the DC-link loop dynamic, the inner loop is represented by an equivalent first order transfer function with time constant T_x .

The technique of the technical optimum has been used for evaluating the value of K_{iM} . The

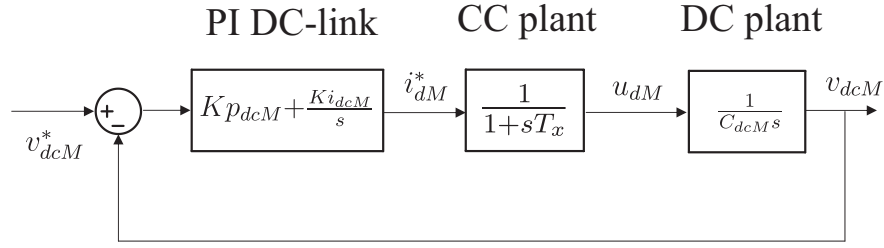


Figure 2.17: MV converter control and plant loop: first order equivalent transfer function of the current controller plant.

time constant $T_{iM}=1/K_{iM}$ is taken as equivalent to the filter plant time constant T_p :

$$\begin{cases} T_{iM} = T_p = \frac{L_M}{R_M} \\ K_{iM} = 1/T_{iM} = 1/T_p \end{cases} \quad (2.19)$$

where R_M is the filter resistor. The value of K_{pM} is obtained with (2.20), defining the current controller loop bandwidth, depending on the time constant T_x .

$$\frac{1}{T_x} = \frac{K_{pM}}{T_{iM}} \frac{1}{R_M} \implies K_{pM} = \frac{T_{iM} R_M}{T_x} \quad (2.20)$$

The obtained parameters of the current loop are listed in Table 2.2 and the current plant closed-loop transfer function is shown in Figure 2.18.

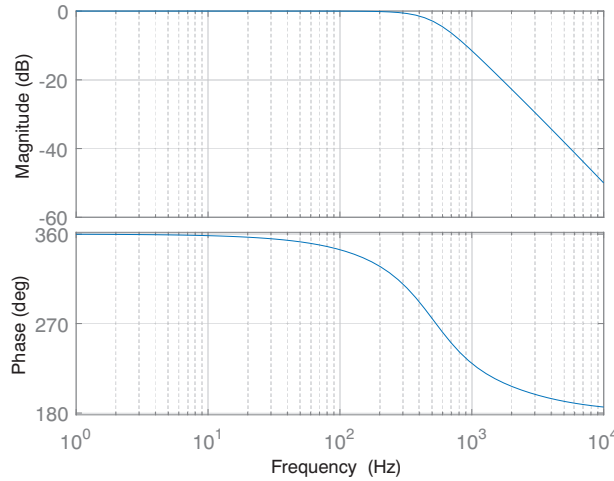


Figure 2.18: Closed-loop bode plot of MV converter current controller.

Once obtained the equivalent current loop transfer function, the dynamic of the DC-link can be studied. The technique of the symmetrical optimum has been chosen to tune the DC-link controller *PI*. As first, the desired phase margin of the outer loop transfer function has to be decided, in order to guarantee sufficient control stability margin. For matter of simplicity, the parameter a has been defined as in (2.21), following what suggested in [81]. This parameter

Table 2.2: ST MV converter parameters

Parameter	Value	Parameter	Value
f_s	10 kHz	K_{pdcM}	0.007
V_{rmsM}	11 kV	K_{idcM}	2.2
C_{dcM}	30 μ F	K_{pM}	30
L_M	16 mF	R_M	100 m Ω
T_x	3,33 ms	K_{iM}	190

is used for the outer loop controller tuning:

$$a = \frac{1 + \sin(\Psi)}{\cos(\Psi)} \quad (2.21)$$

where Ψ represents the desired maximum phase margin of the outer loop transfer function. Knowing the maximum phase margin, the tuning of the DC-link voltage *PI* controller can be obtained by means of (2.22) and (2.23):

$$K_{pdcM} = \frac{C_{dcL}}{2\sqrt{3}aT_x} \quad (2.22)$$

$$K_{idcM} = \frac{1}{T_x a^2} \quad (2.23)$$

Considering a phase margin Ψ equal to 45° , the open loop transfer function of the MV converter controller is shown in Figure 2.19. The obtained gain and phase margin are 26.8 dB and 34.8° , respectively. These values are considered acceptable to ensure a fast controller and stable operations.

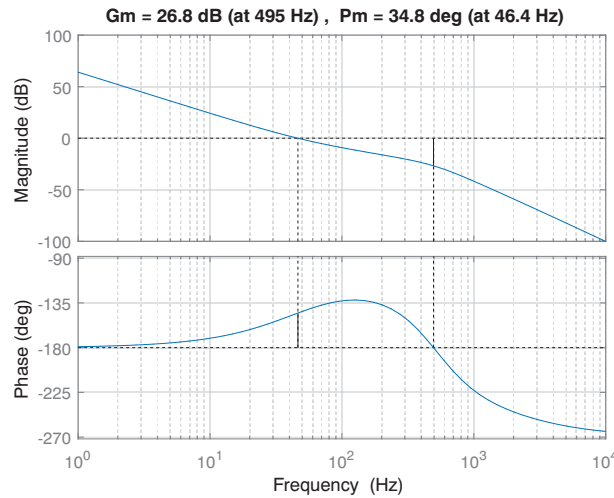


Figure 2.19: Open-loop bode plot of the MV converter transfer function.

It can be noted in (2.22) and (2.23), how the parameters of the outer loop are strictly depen-

dent on the inner loop time constant T_x , thus on the current controller bandwidth, and on the maximum phase margin. Considering constant the current controller bandwidth, the phase margin can be modified to increase the MV converter dynamic. Figure 2.20 shows how the closed-loop transfer function of the MV converter changes if the phase margin varies among 15° , 30° , 45° , and 60° .

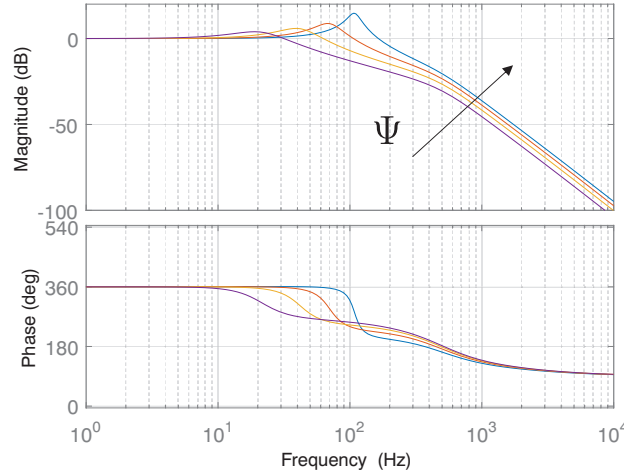


Figure 2.20: MV converter closed-loop transfer function varying the phase margin among 15° (magenta), 30° (yellow), 45° (red), and 60° (blue).

As it can be noticed the converter bandwidth increases due to the transfer function shift on the right side of the bode plot. However, a resonance peak at low frequencies (around 100 Hz) is introduced in the bode plot, that can affect the stability of the converter. The MV converter bandwidth varying the controller phase margin are listed in Table 2.3. The choice of 45° guarantees an acceptable bandwidth and a reduced resonance peak at lower frequencies in the closed-loop transfer function.

Table 2.3: Phase margin influence on MV converter bandwidth

Phase Margin (rad)	Bandwidth (Hz)
$\pi/3$	40
$\pi/4$	75
$\pi/6$	123
$\pi/12$	186

The influence of the phase margin in the converter operations can be observed simulating a step in the LV load power consumption from 200 kW to 300 kW at the second 1 and a reactive power injection of 10 A at the second 1.5. The parameter listed in Table 2.2 have been used in this analysis. As can be seen in Figure 2.21a a higher phase margin slows down the voltage controller, increasing the DC voltage sag during load variations. Similar behavior can be observed in Figure 2.21b, where a phase margin $\Psi=60^\circ$ restores the voltage at the nominal value with very slow dynamic. On the contrary, a low phase margin increases

the disturbance rejection capability of the MV converter. However, the voltage variations have a more oscillating behavior and the stability of the controller can be easily affected during grid parameter variations (e.g., filter's parameter, DC capacitor size). Under these reasons, Figure 2.21 confirms the choice of a phase margin equal to 45° : it guarantees a sufficient controller stability and acceptable dynamic capability during power variations.

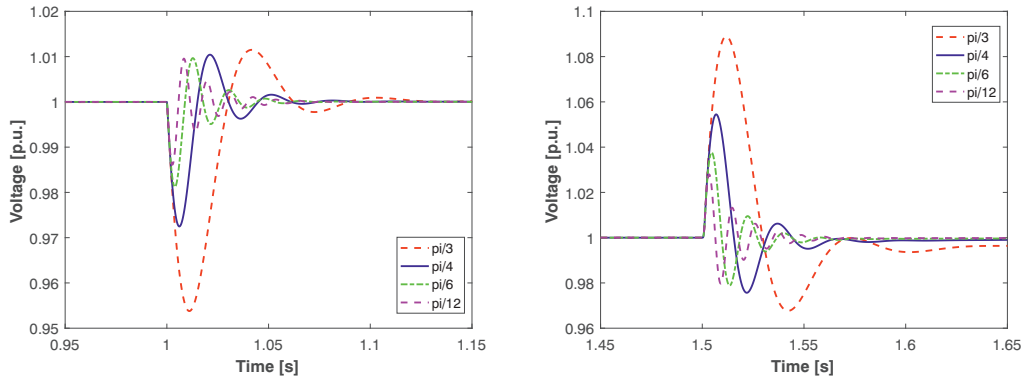


Figure 2.21: MV DC-link voltage during (a) LV active power step from 200 kW to 300 kW, and (b) MV reactive power injection of 10 A.

Harmonic current control

The ST has to absorb sinusoidal and balanced current under any voltage condition. If the voltage is distorted, due to the presence of harmonic loads, the ST has still to control a sinusoidal current with low harmonic content. To achieve this goal, the harmonic controller shown in Figure 2.22 has been implemented [81]. In the ST current controller loop, several harmonic controllers have been implemented, that aim to a specific frequency range. In particular, in Figure 2.22, the 5^{th} - 7^{th} , 11^{th} - 13^{th} , and 17^{th} - 19^{th} current harmonic frequencies are targeted. Fixing the reference equal to zero for these currents, the controller tries to minimize the current error, and thus the harmonic content in the current. The harmonic controller is a nested controller, implemented in the dq -frame. Hence, to control the 5^{th} - 7^{th} harmonics, the controller receives as input the dq currents and it transforms them in the -6^{th} - 6^{th} dq -frames. In similar way, the controllers for the 11^{th} - 13^{th} and 17^{th} - 19^{th} harmonic groups are programmed. The current controller bode diagram is shown in Figure 2.23.

In order to demonstrate the effectiveness of the harmonic controller, a distorted voltage profile is applied in the MV grid. As the previous case, the ST-fed grid requires 200 kW. A 4% 5^{th} and 3% 7^{th} harmonic voltage has been introduced in the voltage profile. The ST, with the harmonic current controller deactivated, absorbs distorted current (Figure 2.24a). After 1 second the harmonic current controller is activated. The harmonic current content is compensated and the resulting current is shown in Figure 2.24b. The current waveform is sinusoidal with low harmonic content, as can be further noted in Table 2.4, where the harmonic content in function of the first harmonic current is calculated. Without control, the ST absorbs 5^{th} and 7^{th} harmonic current higher than 10% of the 50 Hz current. If the harmonic

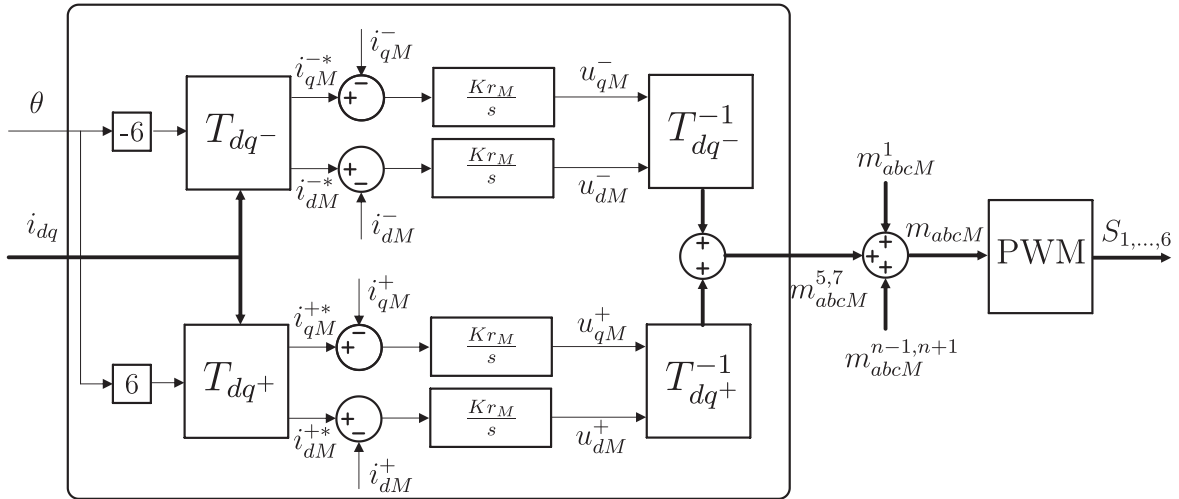


Figure 2.22: MV converter harmonic controller: 5th-7th harmonic compensation case.

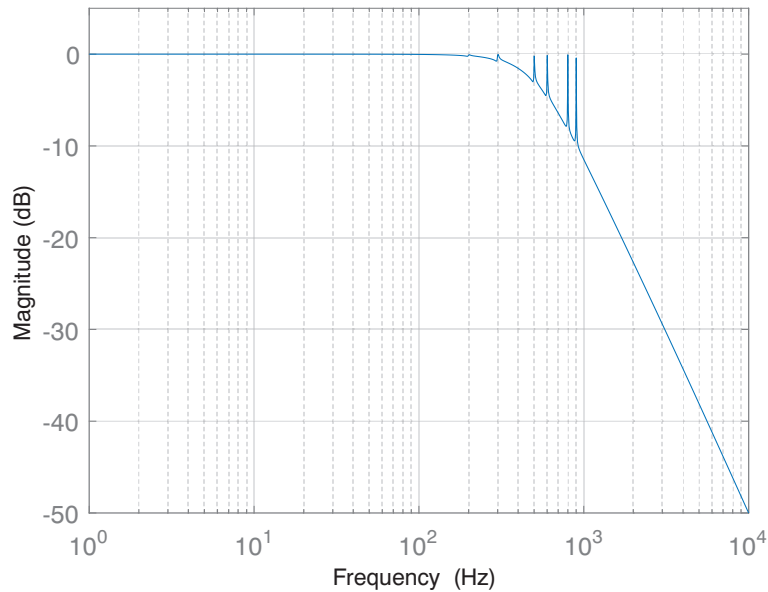


Figure 2.23: Closed-loop bode diagram of the MV converter current controller with the harmonic current controller implemented.

current controller is activated, this quantities drop below 3 %, and the ST is able to draw sinusoidal current from the MV grid.

Table 2.4: Current harmonic content

Harmonic	No control (%)	Harmonic controller (%)
5 th	12,0	2,4
7 th	13,8	1,9

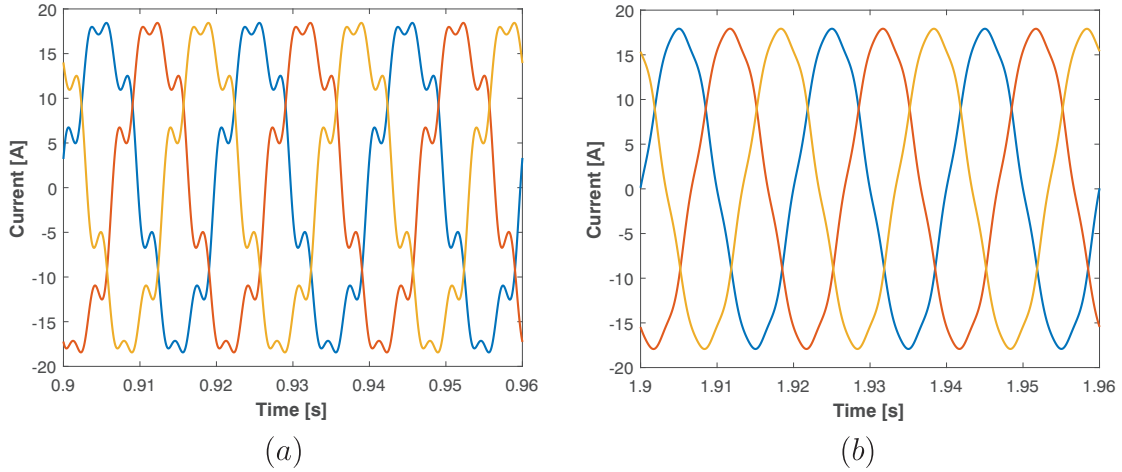


Figure 2.24: ST MV converter currents: (a) basic controller, (b) with harmonic current controller activated.

Power Theory Applications

The ST has the capability to control the power consumption at its MV bus. With the exception of the active power, dependent from the DC link voltage level, the ST is able to absorb any instantaneous power waveform needed. This capability can provide harmonic compensation services to the MV grid. In order to provide harmonic compensation services, the theory developed in [83], has been implemented in the ST MV converter controller, as shown in Figure 2.25. The instantaneous apparent power can be defined in $\alpha\beta$ frame as:

$$s = v \cdot i^* = (v_\alpha + jv_\beta) (i_\alpha - ji_\beta) = \underbrace{(v_\alpha i_\alpha + v_\beta i_\beta)}_p + j \underbrace{(v_\beta i_\alpha - v_\alpha i_\beta)}_q \quad (2.24)$$

the active and reactive power can be sorted in two separate equations

$$\begin{cases} p = v_\alpha \cdot i_\alpha + v_\beta \cdot i_\beta \\ q = v_\beta \cdot i_\alpha - v_\alpha \cdot i_\beta \end{cases} \quad (2.25)$$

and written in matrix form

$$\begin{bmatrix} p \\ q \end{bmatrix} = \begin{bmatrix} v_\alpha & v_\beta \\ v_\beta & -v_\alpha \end{bmatrix} \cdot \begin{bmatrix} i_\alpha \\ i_\beta \end{bmatrix} \quad (2.26)$$

the currents i_α and i_β are the controlled variables in the ST MV converter. In order to find the new current references, the matrix in (2.26) is inverted, writing the current in function of

the voltages and instantaneous powers:

$$\begin{bmatrix} i_\alpha \\ i_\beta \end{bmatrix} = \frac{1}{v_\alpha^2 + v_\beta^2} \begin{bmatrix} v_\alpha & v_\beta \\ v_\beta & -v_\alpha \end{bmatrix} \cdot \begin{bmatrix} p \\ q \end{bmatrix} \quad (2.27)$$

In the ST view, the power theory can be applied to compensate power oscillations in the grid, occurred in case of current harmonic content. Thus from the instantaneous power measurements, the content to be eliminated must be selected. For this reason, the measured power is filtered by means a Low-pass Filter (*LF*), obtaining the average active power, and then subtracted to the power calculated in (2.25). The outcome is the instantaneous active power harmonic content \tilde{p}_M^h , that has to be compensated by the current controller. As in basic ST applications, the DC-link controller regulates the voltage amplitude in the MV DC link regulating the power absorption from MV grid p_{dcM} . The new current references $i_{\alpha M}^*$ and $i_{\beta M}^*$ are created by means of (2.28), that relates the request of active power $p_{dcM} + \tilde{p}_M^h$ and the reactive power $-q$ with the current reference:

$$\begin{bmatrix} i_\alpha^* \\ i_\beta^* \end{bmatrix} = \frac{1}{v_\alpha^2 + v_\beta^2} \begin{bmatrix} v_\alpha & v_\beta \\ v_\beta & -v_\alpha \end{bmatrix} \cdot \begin{bmatrix} \tilde{p}_M^h + p_{dcM} \\ -q \end{bmatrix} \quad (2.28)$$

Finally, the current references are transformed in the synchronous frame *dq* and sent to the current controller, as already shown in Figure 2.15.

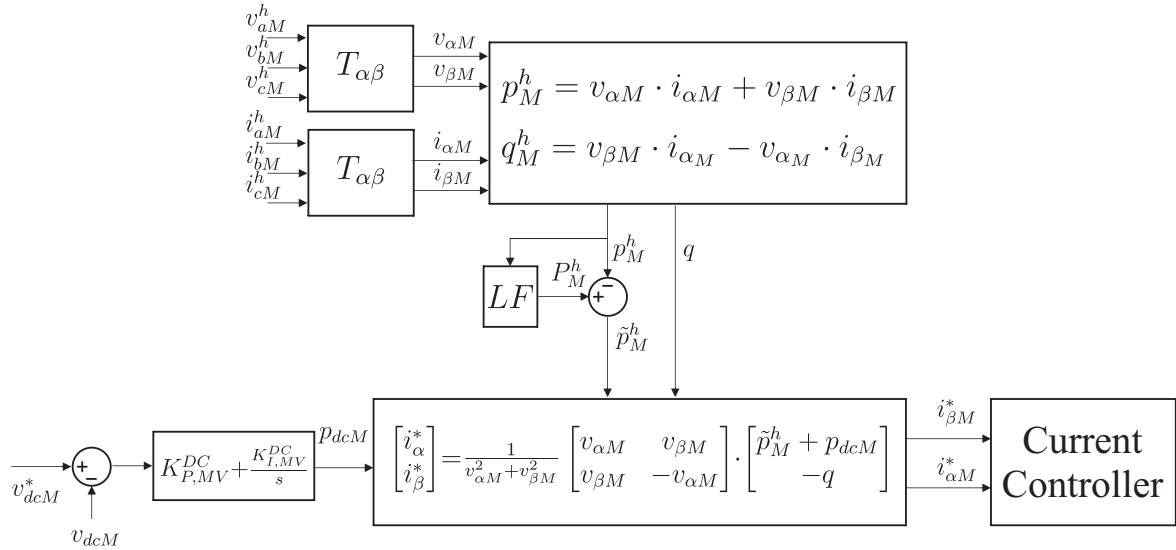


Figure 2.25: Medium Voltage control scheme developed following the power theory suggested in [83].

To demonstrate the advantages of implementing the power theory for ST applications, the two cases depicted for unbalanced and harmonic current demand are considered. The ST is able to compensate the power oscillation caused by unbalanced absorption of current from the MV load, which parameters are listed in Table 2.5.

Table 2.5: Unbalanced load parameter

Phase	Resistance [Ω]	Inductance [mH]
A	1500	15
B	1100	10
C	500	5

As shown in Figure 2.26a the power theory controller is activated after 1 second. The initial grid power oscillation (red line) is affected by the power absorption of the unbalanced load (yellow line), while the ST power requests is constant (blue line). After the controller activation, the ST begins to absorb an oscillating power in order to compensate the load power, operating as an active filter for the MV grid. It results in a lower power oscillation from the grid side, and thus a lower power quality impact for the MV grid. It can be argued that the absorption of oscillating power can affect the DC-link capacitors, due to the presence of 2^{nd} order voltage oscillation. However, it can be noted in Figure 2.26b, how this power oscillation is limited to less than 2% of the nominal voltage, and thus its impact on the DC-link capacitors is negligible.

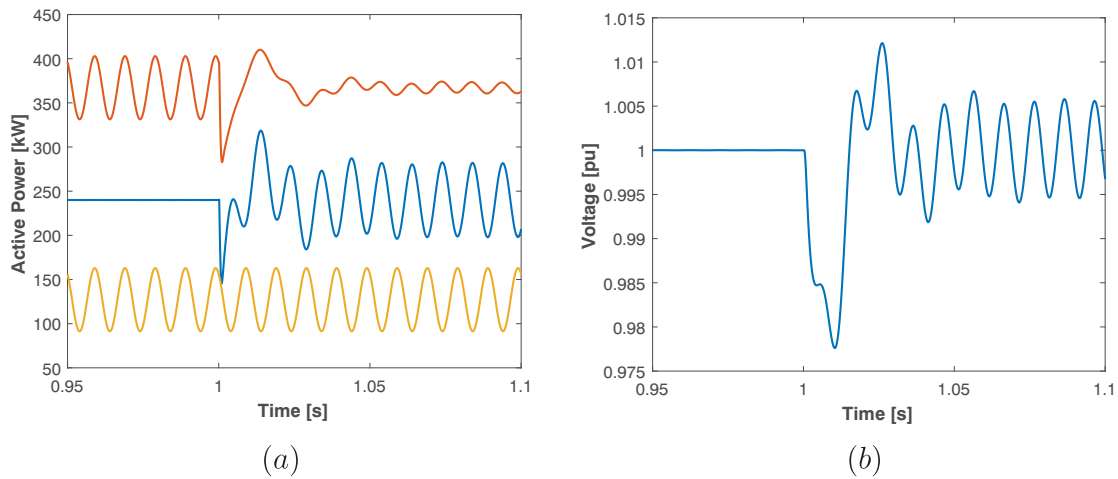


Figure 2.26: Power theory application for unbalanced current absorption: (a) MV grid power (red line), ST power (blue line) and unbalanced load power (yellow line); (b) MV DC-link voltage.

The power theory controller can improve the harmonic content in the grid, providing the harmonic current to a non-linear load. It is considered the case where a three-phase rectified is installed in the MV grid. The rectified load is equal to $R_{harm} = 5000\Omega$. The ST aims to compensate the active power oscillations created by the current harmonic content created by the rectified load. It can be noticed from Figure 2.27a, that the grid power (red line) is affected by the harmonic load power (yellow line), while the ST absorbs constant power (blue line). The ST activates the power theory controller (Figure 2.27b) and begins to absorb harmonic current together with the constant current demand for the loads in the ST-fed grid. The MV grid power harmonic oscillations results decreases, although not eliminated totally,

due to the limited ST current controller bandwidth. In this case, the ST current controller bandwidth has been increased to 500 Hz to increase the compensation controllability.

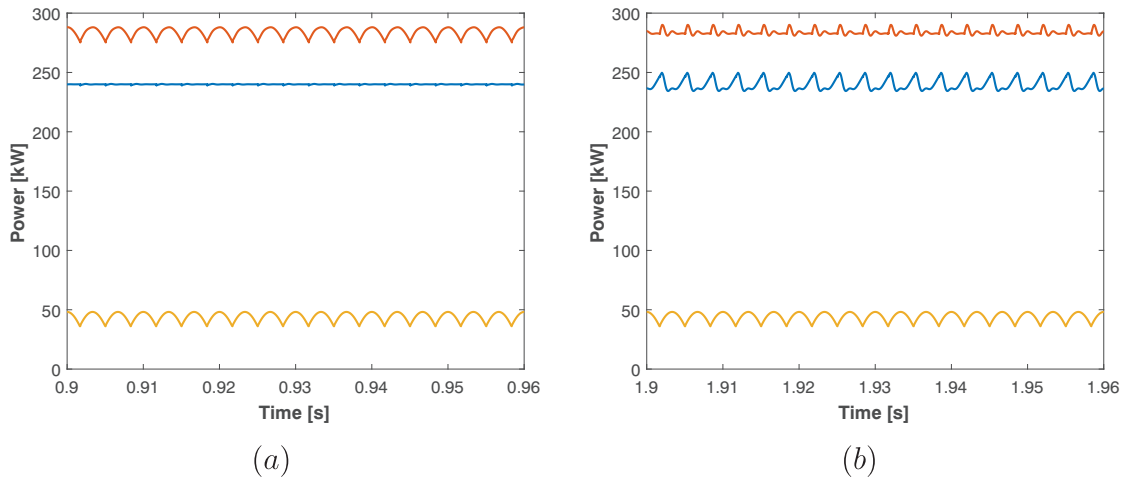


Figure 2.27: Power theory application for harmonic load: MV grid power (red line), ST power (blue line) and unbalanced load power (yellow line), (a) before controller activation, (b) after controller activation.

The power harmonic content shown in Figure 2.27a and Figure 2.27b are listed in Table 2.6

Table 2.6: Power harmonic content

Harmonic	No control (%)	Harmonic compensation (%)
6 th	1,76	0,53
12 th	0,45	0,73
18 th	0,17	0,59

From Table 2.6 it can be noted that the power low harmonic content is compensated, decreasing below 1%. However, due the limited converter bandwidth, the harmonic content of higher frequencies, such as 12th and 18th, increases.

2.4 DC/DC transformation stage

The DC/DC converter has two fundamental tasks: to control the voltage in the LV DC-link capacitor and to guarantee the galvanic isolation between the MV and LV grids. To perform these two tasks, a further AC stage is interposed between the two DC stages and a high frequency transformer is used to step down the voltage. The AC stage is regulated by two converters switching at high frequency, such as from few hundreds Hz for high power applications to few tens of kHz, that allows the voltage transformation in the high frequency transformer. The main advantage in transforming the voltage at high frequency is the reduced size of the transformer. Optimizing the design of the ST, a space reduction can be

obtained. This can represent a key advantage with respect to the traditional transformer in the installation in city's substations, where the space is particularly limited.

Two technologies for the DC/DC converter are addressed in this chapter that can result interesting for ST applications: the Dual Active Bridge and Series Resonant Converter.

2.4.1 Dual Active Bridge

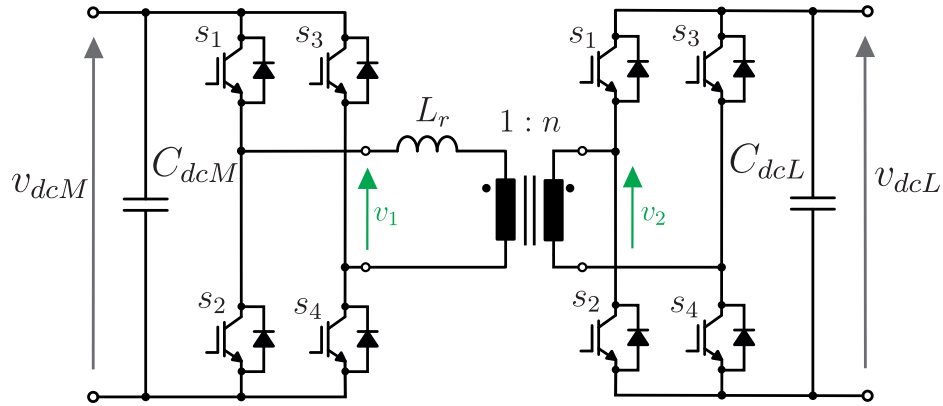


Figure 2.28: Circuitual scheme of a DAB.

The DAB is a DC/DC converter that regulates the power flow between the two DC stages in order to control the LV DC link voltage. The DAB circuit is composed of two converters, in both of primary and secondary side, switching with the same frequency, but with different phase. In Figure 2.29 is explained the working principle of a DAB. The converter at the primary side switches, imposing to the transformer the voltage $v_1 = v_{dcM}$. In that moment, the transformer has at the secondary side the voltage $v_2 = -v_{dcL}$, thus the current i_{dab} increases, passing from a positive to a negative value. When the secondary side converter turns on, imposing the voltage $v_2 = v_{dcL}$, the difference of voltage is zero (taking in account the transformer ratio) and the current remains constant (if a lossless circuit is considered). As soon the primary side converter switches, imposing the negative voltage $v_1 = -v_{dcM}$, the current tends to decrease till reaching a negative value. The current is eventually stabilized as soon as the secondary side converter switches to a negative voltage $v_2 = -v_{dcL}$. Regulating the angle shift φ , it is possible to transfer energy from the primary to the secondary side of the transformer and vice-versa.

Applying the KCL to the LV DC-link, the following relation is obtained:

$$i_{dcL}(t) = i_{cL}(t) + i_{dabL}(t) \quad (2.29)$$

where i_{dabL} is the current supplied by the DAB to the LV DC link, i_{cL} is the current flowing in the LV DC link capacitor, and i_{dcL} is the DC current demand of the ST-fed grid (LV side).

Expressing the current as $i_{cL} = C_{dcL} \frac{dv_{dcL}}{dt}$, leaving only the differential term on the equation

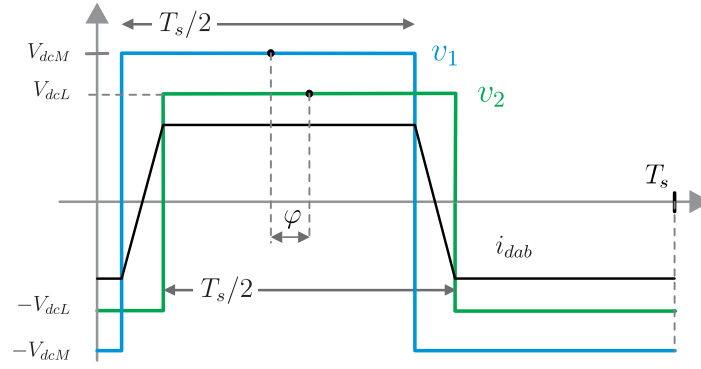


Figure 2.29: Working principle of the DAB.

left side, the DAB dynamic equation can be rearranged as:

$$\frac{dv_{dcL}(t)}{dt} = \frac{i_{dcL}(t)}{C_{dcL}} - \frac{i_{dabL}(t)}{C_{dcL}} \quad (2.30)$$

The power transfer is achieved from the leading bridge to the lagging bridge [84], and it is given by the equation:

$$P_{dabL} = \frac{v_{dcL}V_{dcM}}{2Nf_sL_r}d(1-d) \quad (2.31)$$

where $N < 1$ is the transformer turns ratio, f_s is the switching frequency, L_r is the leakage inductance of the high frequency transformer, and d is the phase shift ratio. The L_r value is decided solely on the maximum power transfer P_{max} for a certain phase shift ratio d . To size correctly the inductance L_r , the maximum power transfer of 1 MW for a phase shift $d = 0.25$ is considered [85]. The DAB parameters values are listed in Table 2.7.

Table 2.7: DAB converter parameters

Parameter	Value	Parameter	Value
f_s	20 kHz	S_{dab}	1 MW
V_{dcM}	20 kV	V_{dcL}	700 V
L_r	700 μ H	R_r	2 Ω
C_{dcM}	30 μ F	C_{dcL}	30 mF
R_d	1 Ω	T_{dab}	350 μ s

The DAB converter can be modeled with two current sources i_{dabL} and i_{dabM} , representing the DAB current injection in the MV and LV DC-link respectively. The power flux between the two DC stages is regulated by means of a PI controller, as shown in the DAB transfer function shown in Figure 2.31. The output of the PI is the new phase shift value d , influencing the power transfer in the high frequency transformer. The reference power is limited between the P_{max} , determined by the ST rating, and P_{min} . The value of P_{min} can be set equal to $-P_{max}$ (allowing bi-directional flow), or equal to zero, if a limitation of reverse power flow

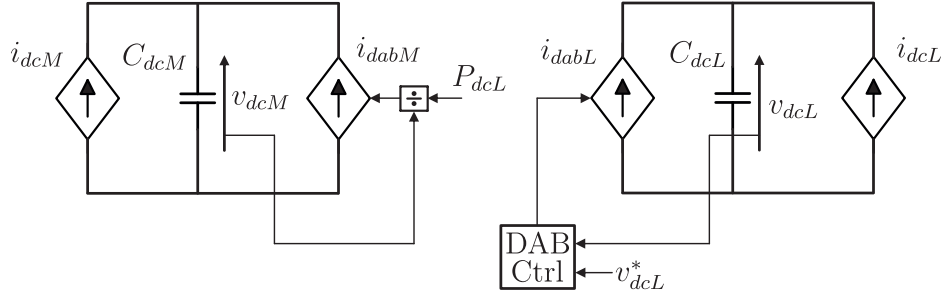


Figure 2.30: Average model DAB converter and controller.

is desired. In this case, the interaction with the local generation and load, for example by means of frequency variation [J9], is necessary. In modeling the DAB with an equivalent model, the converter and the actuator dynamics (PWM signals) can be included in the time constant $T_{dab} = L_r/R_r$, that represents the transformer dynamic and it results to be $350 \mu\text{s}$. Thus, the DAB converter can be represented with the power equation described in (2.31) and with the equivalent first-order transfer function with time constant T_{dab} . The control current of DAB i_{dabL} can be obtained from the transferred power P_{dcL} divided by the DC voltage V_{dcL} (assumed constant). The DC voltage is then obtained multiplying the DAB current for the DC plant transfer function $1/sC_{dcL}$.

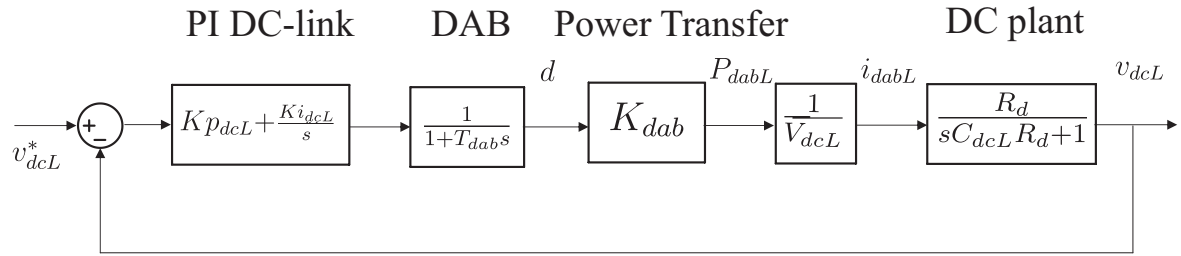


Figure 2.31: Controller and plant loop of a DAB.

The control and plant loop of the DAB is finally shown in Figure 2.31. The tuning of the DAB is performed in order to achieve sufficient control bandwidth without showing undamped phenomena at higher frequencies. A control bandwidth of 1 kHz is chosen in this study. The study of the DAB converter stability is carried out under the following assumptions: the DC voltages in the power transfer equation have been assumed constant; the duty-cycle achievable at the maximum power has been set to $d^* = 0.25$. The parameter values $K_{P_{dcL}} = 1e^{-3}$ and $K_{I_{dcV}} = 0.5$ have been chosen to tune the DAB converter PI controller, and the resulting bode plot of the control scheme in Figure 2.31 is shown in Figure 2.32.

$$K_{dab} = \frac{V_{dcL}V_{dcM}}{2Nf_sL_r d^* (1 - d^*)} \quad (2.32)$$

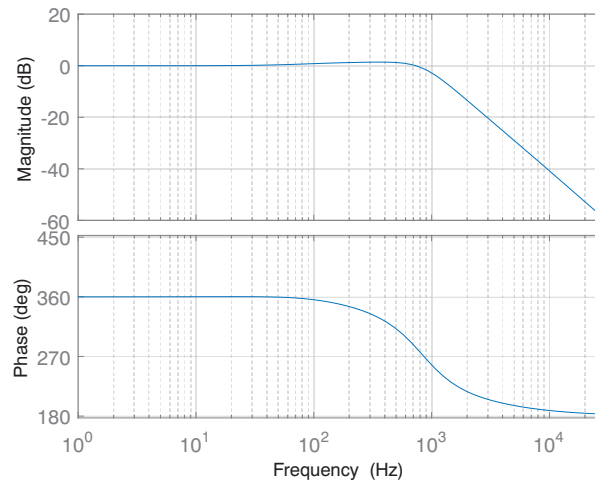


Figure 2.32: Closed-loop bode diagram of the DAB converter at full power condition (1 MW).

2.4.2 Series Resonant Converter

The SRC is a low complexity DC/DC transformer [86]. The SRC operates exploiting the resonance frequency of a LC circuit to transfer power between transformer primary and secondary side [86, 87]. The topology scheme of the SRC is shown in Figure 2.33, where a full-bridge converter is used for explaining the SRC working concept. A resonant tank circuit $L_r C_r$ is employed in the primary side, where L_r and C_r are the resonant tank inductance and capacitance respectively, smoothing the current shape from the square-waveform of the voltage.

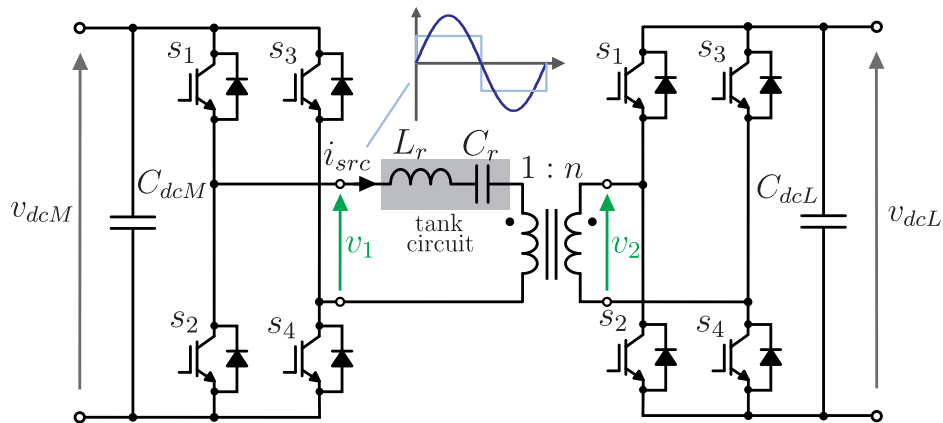


Figure 2.33: Circuitual scheme of a SRC.

The SRC works in discontinuous-conduction-mode (DCM). The switching frequency is slightly below the resonance frequency of the resonant tank, in order to achieve zero-current switching operations, and thus increasing the efficiency. In Figure 2.34, the SRC voltage and current waveforms are plotted at the primary side. As soon as the upper switch s_1 start

to conduct exciting the resonant tank, and the current flows with a frequency equal to the resonant one [86]:

$$i_{src}(t) = \frac{v_1}{Z_0} \sin(\omega_0 t) \quad \text{for } t \leq \frac{T_0}{2} \quad (2.33)$$

where T_0 is the resonance time-step, $Z_0 = \sqrt{L_r/C_r}$ is the resonant impedance, and $f_0 = 1/(2\pi\sqrt{L_r C_r})$ is the resonant frequency of the circuit. Since the second bridge operates as

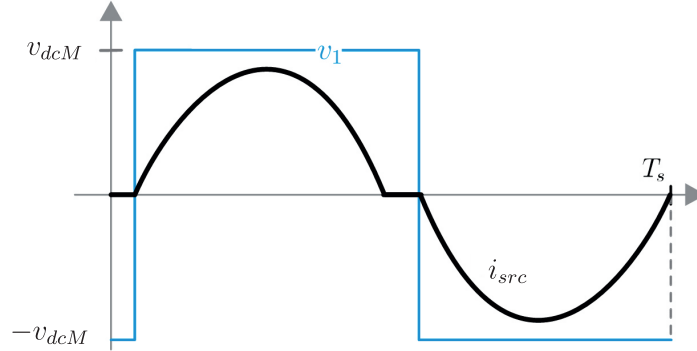


Figure 2.34: Working principle of the SRC.

diode rectifier, the current cannot reverse in the circuit, allowing the zero-current switching mode when the bridge s_2 turns on. Thus, to obtain soft switching conditions, the switching frequency f_s has to be chosen below the resonance frequency. If f_s reaches the resonance frequency f_0 , the maximum power transfer is achieved. However, the soft switching conditions are not anymore respected, increasing the power losses in the converter.

Under these conditions, the SRC behaves like an idealized "DC transformer", where the output voltage is equal to the input voltage, divided by the transformer ratio $v_s = v_p/\eta$. The SRC can be represented with the equivalent circuit shown in Figure 2.35. The SRC MV side is modeled as a current source i_{dcM} , reproducing the power request of the ST-fed grid P_{dcL} . The LV side is modeled as a voltage source V_{dcL}^* , adapting the voltage from the MV DC-link. To simulate the SRC dynamics a RL filter is added to the circuit. The circuit losses are taken into account by means of the dc resistance R_{dc} ; instead L_{dc} is the adapted inductance in order to yield the same stored energy than the inductance L_r . Considering the oscillating current i_L^2 in Figure 2.33 and the current i_{srcL}^2 in the average model in Figure 2.35, the equivalent impedance L_{dc} can be found as [86]:

$$i_{srcL}^2 L_{dc} = i_L^2 L_r \Rightarrow L_{dc} = \frac{i_L^2}{i_{srcL}^2} L_r \quad (2.34)$$

DC/DC stage modeling for CHB applications

In the previous section, the CHB converter topology has been briefly described. It has been noted that each CHB cell has its own DC-link, thus each cell has to be connected in series

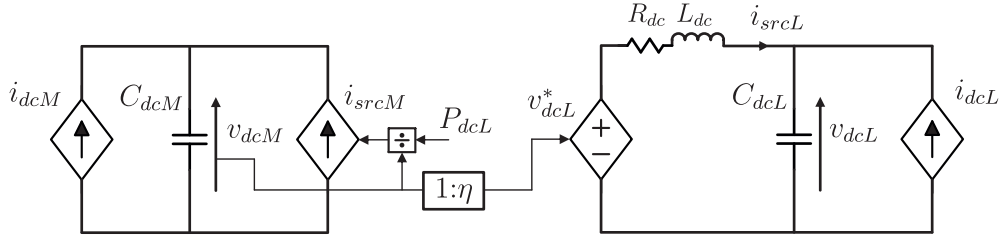


Figure 2.35: Average model of SRC and controller.

with a DC/DC converter in order to transfer power in the LV side. As shown in Figure 2.9b, the CHB cells are in series, thus each cell behaves like a voltage divider of the total DC voltage. The DC/DC converter does not need to work under high voltage ratio, but it can work with a voltage ratio near unity, depending on the amount of cells installed in the MV converter and the devices used. Assuming N cells, the equivalent DC/DC converter scheme for CHB applications is shown in Figure 2.36, where the case of a DAB converter for the DC stages is considered. Each CHB cell has its own DAB converter and the power request of the LV DC-link P_{dcL} is shared among the cells. To model the LV DC-link control, each DAB is represented by means of a current source in parallel with the other DAB converters, that injects the current i_{dabL}^i in the LV DC-link. The sum of all the currents i_{dabL}^i determines the current i_{dabL} flowing in the DC-link.

The DC current of the equivalent DAB converter can be written as:

$$i_{dabL}(t) = \sum_{i=1}^N i_{dabL}^i(t) \quad (2.35)$$

where $\sum_{i=1}^N i_{dabL}^i(t)$ represents the sum of all the current input of the N LV side converters connected to the same DC link. Hence, referring to (2.30) and (2.35), the LV DC link dynamic equation is obtained:

$$\frac{dv_{dcL}(t)}{dt} = \frac{i_{dcL}(t)}{C_{dcL}} - \frac{\sum_{i=1}^N i_{dabL}^i(t)}{C_{dcL}} \quad (2.36)$$

The inner control of each cell is independent from the other cells. However, a central controller, managing the power flow among the cell, can redistribute the power among the cells, varying the set-point of the power transfer P_{dcL}^i of the i -th DAB.

The sizing of the DAB converter has to be varied with respect of the non-modular case shown above. Each converter processes a portion of the total power and each CHB cell works to lower voltage than the total MV DC-link voltage. Supposing that the CHB works with 10 kV DC-link voltage and it is composed of 13 cells, the voltage for each cell is 800 V. This working voltage matches the existing semiconductor devices in the market (nominal voltage 1.2 kV). Each cell has to be sized to share 80 kW at the phase shift ratio of $d^* = 0.25$, thus the leakage inductance to be considered is equal to $L_r = 37.5 \mu\text{H}$. The DAB and CHB values considered in this study are listed in Table 2.8.

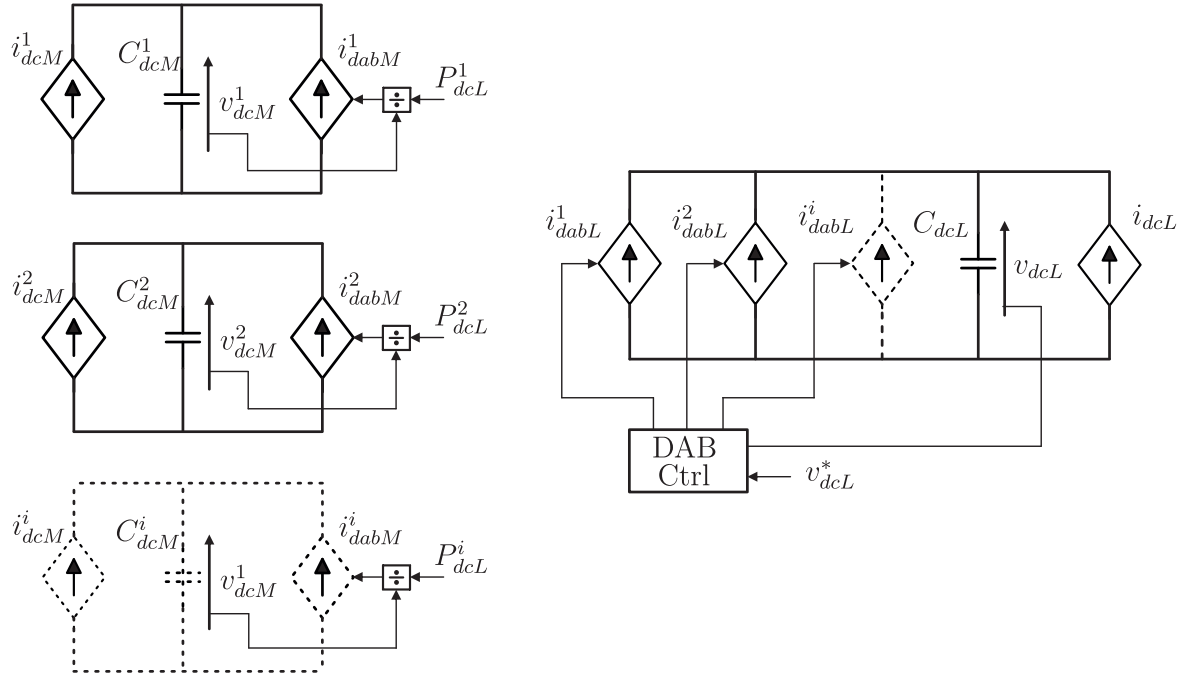


Figure 2.36: Average model of DAB converter applied to CHB configuration.

Table 2.8: DAB converter parameters for CHB applications

Parameter	Value	Parameter	Value
f_s	20 kHz	P_{dab}	80 kW
V_{dcM}	800 V	V_{dcL}	700 V
L_r	37.5 μ H	R_r	2 Ω
C_{dcM}	2 mF	C_{dcM}	30 mF

Comparison on disturbance rejection capability

The two aforementioned topologies are both possible solutions for the ST DC/DC stage. On one side, the SRC converter offers a minimum control complexity [86] and high efficiency [87], on the other side, the DAB offers higher control capability, although with higher control complexity [84]. The capability to reject disturbances coming from the LV and MV stages is a fundamental requirement for the DC/DC converter. As follows, the capability to reject disturbances as load power variations and 2^{nd} harmonic power oscillations is addressed. The DAB, regulating the power flow to maintain the LV DC link voltage constant, offers a power "filtering capability" to the LV DC link. The controller shown in Figure 2.31, allows to minimize the DC voltage error. Thus, in presence of a fast power variation (e.g., load or generator disconnection), the controller is able to control the voltage during the power transient. On the opposite, the SRC behaves as a DC transformer and it is not able to influence the power transfer from the MV to LV DC links, reflecting any power disturbance in LV grid in both MV and LV DC link.

To explain better this concept, a power step example is made as follows. It is assumed that

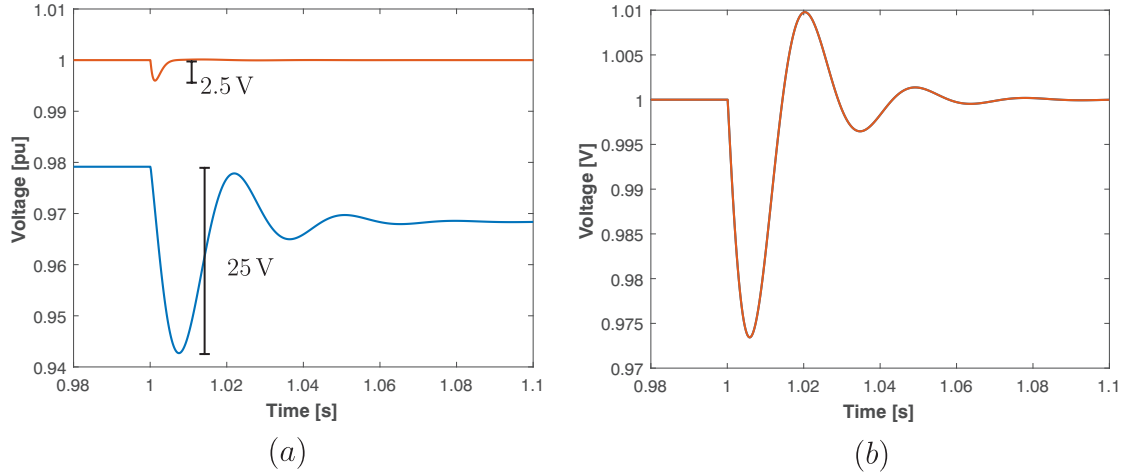


Figure 2.37: Rejection of disturbances: power consumption step from 200 kW to 300 kW.

the ST-fed grid is absorbing 200 kW active power, with unity power factor. A load power step increase of 100 kW is applied at 1 second. The response of DAB (red line) and SRC (blue line) are plotted in Figure 2.37. In Figure 2.37a, it can be noted as the DAB, although the higher control complexity, is able to damp the voltage oscillation in less than half cycle (about 7 ms) and the voltage deep reached during the power variation is limited to 0.35 % (2.5 V absolute value). The SRC behaves in different way. From the initial steady state, it can be noted how the DC-link voltage does not reach 1 pu, but it is reduced to 0.98 pu. This voltage drop is caused by the presence of the resistance R_{dc} and the inductance L_{dc} of the high frequency transformer. During the power step, the voltage dip reaches almost 4 % (25 V absolute value) and the voltage transient is damped after 3 cycles (60 ms). The reason behind this degrade of performance with respect to the DAB case, can be found in the control of SRC. The MV DC-link is subjected to the same voltage oscillation (Figure 2.37b), both in the DAB and SRC case. The difference is that the DAB controls directly the voltage on the LV DC-link, instead the SRC behaves as an ideal transformer, thus it transforms directly the voltage from MV to LV DC-link, without any possibility to control it. Hence, the voltage variation of 2.5 % obtained in MV side (Figure 2.37b), results to be a voltage variation with similar dynamic of 3.5 % in the LV side (Figure 2.37a).

Similar considerations can be done regarding the issue of the 2nd harmonic power oscillations, caused by an unbalanced load in the ST-fed grid. To the basic load of 200 kW, a 100 kW $pk-pk$ power oscillation has been added to simulate the unbalanced load conditions. The DAB (red line in Figure 2.38a) is able to restrain the voltage oscillation in less than 1 % (4 V) of the voltage nominal value, while the SRC follows the MV DC-link voltage oscillation, equal to 1.5 % (10 V) of the nominal value. Although it does not represent an issue for the power oscillation considered in this case, the SRC shows a degrade of performances with respect to the DAB case.

Concluding, the DAB offers higher disturbance rejection capability than in the SRC case, although with higher control complexity. With respect to the SRC, during transients, it is able to reduce the voltage excursion caused by power variations, and in steady-state it is able

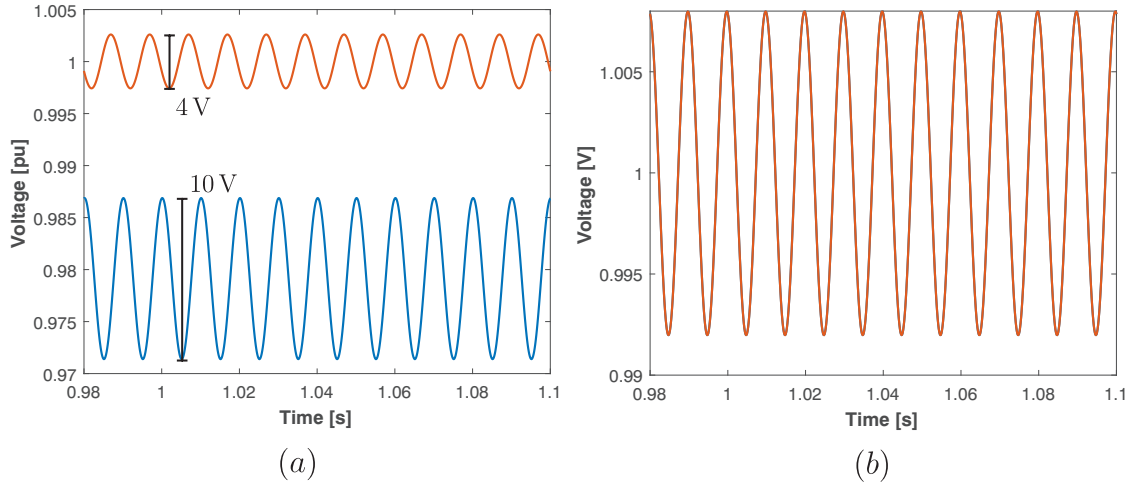


Figure 2.38: Rejection of disturbances: 2^{nd} harmonic power oscillations deriving from 100 kW_{pk-pk} : (a) LV DC link voltage v_{dcL} , and (b) MV DC link voltage v_{dcM} .

to reduce the 2^{nd} harmonic voltage oscillation coming from load unbalance conditions in the ST-fed grid.

2.5 LV converter

The LV grid is characterized by the presence of single-phase loads and the need for loads of local earthing. These needs lead the DSOs in the world to adapt mostly 4-wire TT systems. The earthing is performed locally, both at transformer and load level and a fourth-wire (neutral conductor) is present. The necessity for a 4^{th} wire derives from the need to install single-phase loads, connected between one phase and the neutral, and the local earthing due to safety concerns (e.g., use of differential protection). For these reasons, the ST topology must have the access to the fourth-wire connection, in order to create the neutral conductor path. This connection is available in the middle-point of the LV DC-link. However, connecting simply the neutral conductor to the middle-point of the DC-link leads to an uneven energy distribution between the upper and lower leg of the DC-link capacitors. Thus the LV DC-link oscillations have to be controlled by the ST LV converter. Analyzing the literature [J10][88][89], the three solutions shown in Figure 2.39 are considered suitable for ST LV converter, that are NPC converter, T-type converter, and four-leg converter.

The aforementioned topologies can be represented with the equivalent circuit model shown in Figure 2.40. Three controlled voltage sources control the voltage on the LV LC filter capacitor C_L . The capacitors are star-connected to the neutral conductor and to the DC-link middle point. The DC-link middle point is in turn grounded by means of the ground impedance \dot{Z}_g .

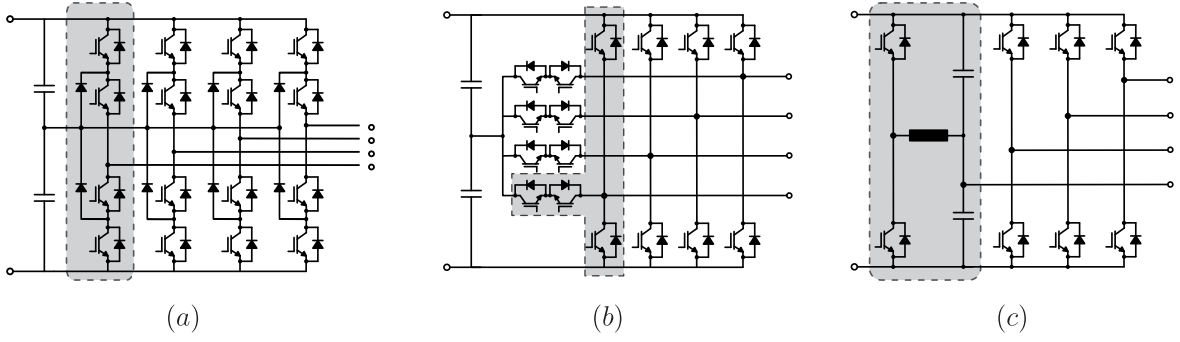


Figure 2.39: ST LV converter topologies: (a) Neutral Point Clamped (NPC) converter, (b) T-type converter, (c) four-leg converter.

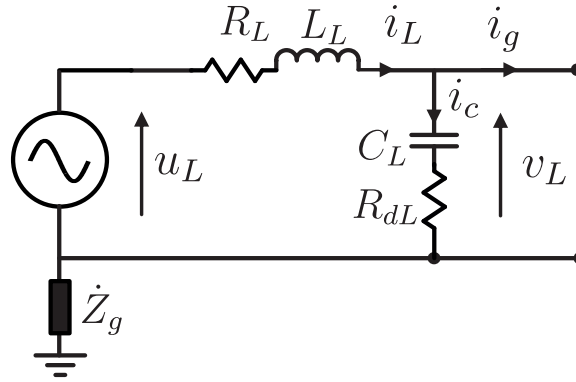


Figure 2.40: Average model of the ST LV converter, general topology case.

The KVL of the LV side converter circuit can be written in vectorial form:

$$\begin{cases} \bar{v}_L(t) = \bar{u}_L(t) - R_L \bar{i}_L(t) - L_L \frac{d\bar{i}_L(t)}{dt} \\ \bar{i}_c(t) = C_L \frac{d\bar{v}_L(t)}{dt} \end{cases} \quad (2.37)$$

Rearranging the equations leaving only the differential term on the left side

$$\begin{cases} \frac{d\bar{i}_L(t)}{dt} = \frac{1}{L_L} (\bar{u}_L(t) - \bar{v}_L(t) - R_L \bar{i}_L(t)) \\ \frac{d\bar{v}_L(t)}{dt} = \frac{1}{C_L} (\bar{i}_L(t) - \bar{i}_g(t)) \end{cases} \quad (2.38)$$

Assuming that

$$\bar{u}_L(t) = \bar{p}(t) \cdot v_{dcL}(t) \quad (2.39)$$

the model of the LV converter is obtained:

$$\begin{cases} \frac{d\bar{i}_L(t)}{dt} = \frac{1}{L_L} (\bar{p} \cdot v_{dcL}(t) - \bar{v}_L(t) - R_L \bar{i}_L(t)) \\ \frac{d\bar{v}_L(t)}{dt} = \frac{1}{C_L} (\bar{i}_L(t) - \bar{i}_g(t)) \end{cases} \quad (2.40)$$

Transforming (2.40) in Laplace domain, the LV converter side equations become:

$$\begin{cases} U_L(s) = R_L I_L(s) + sL_L I_L(s) + V_L(s) \\ I_L(s) = sC_L V_L + I_g(s) \end{cases} \quad (2.41)$$

2.5.1 Control of the LV converter

The LV converter is controlled to provide a sinusoidal voltage waveform at constant amplitude and frequency under any load condition. The voltage reference can be fixed or it can vary depending on the services requested in the ST LV side: an outer grid controller can vary the voltage magnitude, frequency and phase to provide services to the ST itself (OVC) or to the grid (RPFL controller, OLLI, or RTFR).

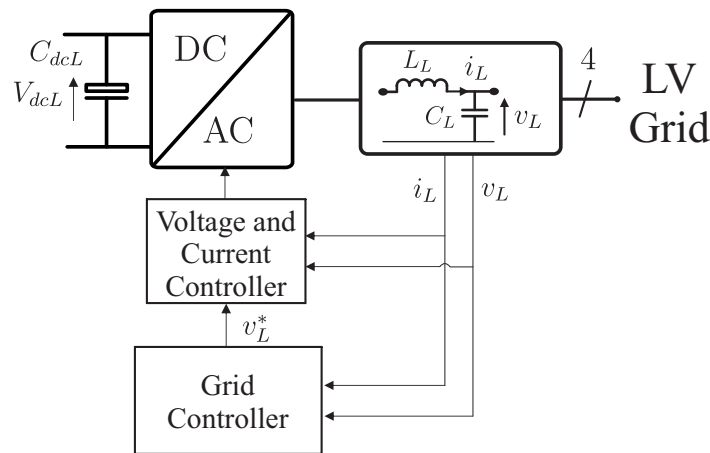


Figure 2.41: Low Voltage control scheme.

On the contrary of the MV converter, with a controller integrated with a dq -frame, an abc -frame controller is implemented in the LV converter. The reason lies in the possibility to provide unbalanced voltage operations (e.g., for compensating unbalanced voltage drops along each phase) or harmonic compensation. The use of an abc -frame makes the unbalance control simpler, due to the possibility to act on each single-phase directly, and without the implementation of negative frame controllers, like in the dq -frame case. The same goes for the voltage harmonic compensation, where the use of an abc frame makes the implementation simpler, integrating resonant controllers at the interested frequencies, instead of implementing a dq -frame for each harmonic controlled.

The ST LV inner controller is composed of two loops. The external loop controls the voltage on the LC filter capacitor, where the voltage error is minimized by means of a $P+R$ controller, tuned at 50 Hz. The $P+R$ output is the current reference to be compared with the current measurement on the filter inductor. A P controller is used to minimize the current error. Finally, the voltage reference is added to create the abc modulation signals. On the opposite of the MV converter case, the reference voltage is chosen as feed-forward signal. The voltage waveform is directly controlled by the ST, and thus the error between the measured voltage and the reference voltage is minimum.

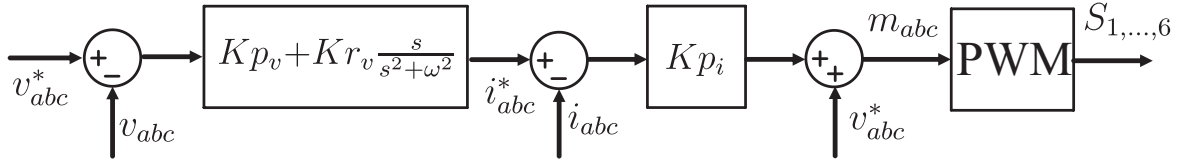


Figure 2.42: ST LV converter controller scheme.

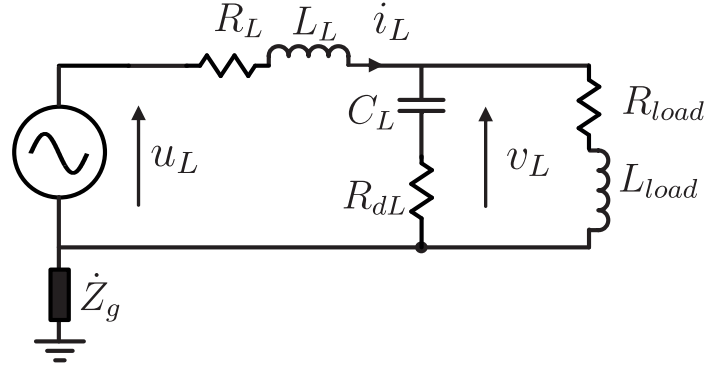


Figure 2.43: Circuitual scheme of the ST LV converter, plant and LV grid equivalent load.

The ST LV converter has to remain stable in a wide range of load conditions, from no-load to the nominal load power consumption, and under different power factors. To evaluate the stability of the ST LV converter, the circuit shown in Figure 2.43 is considered, where the ST is connected to an equivalent load characterized by the resistance R_{load} and inductance L_{load} . Analyzing the circuit, it can be noticed how the equivalent load is connected in parallel with the filter capacitor C_L and its damping resistance R_d . The load has been considered balanced, for matter of simplicity in the analysis. The parallel transfer function of load and filter capacitor is defined as:

$$G_{Par}(s) = \frac{(R_{load} + L_{load}s)(R_d + 1/(C_Ls))}{R_{load} + L_{load}s + R_d + 1/(C_Ls)} \quad (2.42)$$

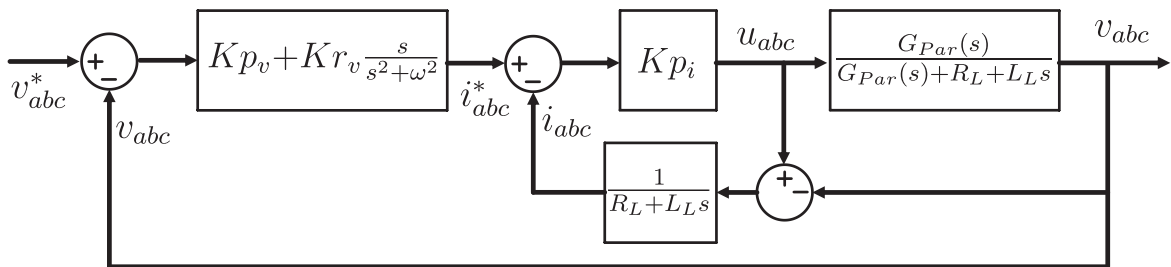


Figure 2.44: Controller and plant scheme of the ST LV converter.

The parallel between the filter capacitor and the load impedance can influence the stability of the converter. As can be seen from Figure 2.43, the system works as a voltage divider between the converter output voltage u_{abc} and the capacitor voltage v_{abc} , thus the load impedance influences the plant transfer function. This effect is marked particularly in Figure 2.44, where the transfer functions of the ST LV converter and plant are described. The transfer function $G_{Par}(s)$, influenced by the load impedance, varies the equivalent transfer

function $v_{abc}^*(s)/v_{abc}(s)$. An analytic tuning, as already seen for the MV converter, is not suggested in this case due to the parameters dependency on the load connected. However, the controller parameters can be tuned to keep the system stable under any possible load condition.

For this reason, the system stability has been evaluated varying the load from the no-load condition to the full load (here 1 MW, power factor $\cos(\phi) = 0.9$). The LV converter data are shown in Table 2.9, where f_0 is the LC filter resonance frequency. To choose the filter components, the capacitor C_L has been firstly fixed to 0.02 pu, and then the inductor L_L is evaluated from the resonance formula:

$$L_L = \frac{1}{(2\pi f_0)^2 * C_L} \quad (2.43)$$

Table 2.9: ST LV converter parameters.

Parameter	Value	Parameter	Value
v_L	230 V_{rms}	S_{base}	1 MVA
f_{sw}	10 kHz	f_0	4 kHz
C_L	0.02 pu	L_L	0.01 pu
R_L	0.5 Ω	R_{dL}	2 Ω
K_{pv}	0.05	K_{rv}	2000
K_{pi}	0.25		

The root locus of the system is shown in Figure 2.45a. The system is always stable independently from the load power consumption and the lowest stability margin is given by the no-load condition. Considering the closed-loop transfer function bode plot (Figure 2.45b), the converter behaves with a flat response in the frequency spectrum from few Hertz to 800 Hz, representing the converter bandwidth. The impact of the load variation in the bode plot is negligible in the interested frequency range.

The loads reactive power request may impact on the system stability, thus the same analysis performed for the active power, must be repeated considering variable reactive power. In Figure 2.46, the load reactive power has been increased acting on the load equivalent impedance inductor. The active power is fixed to 500 kW and the power factor has been varied among 0.95, 0.9, and 0.8. Only inductive reactive power request has been considered, under the hypothesis of reactive power consumption of loads. The system results stable under any reactive power demand level. Increasing the reactive power request, the system tends to move the poles towards the left side of the diagram.

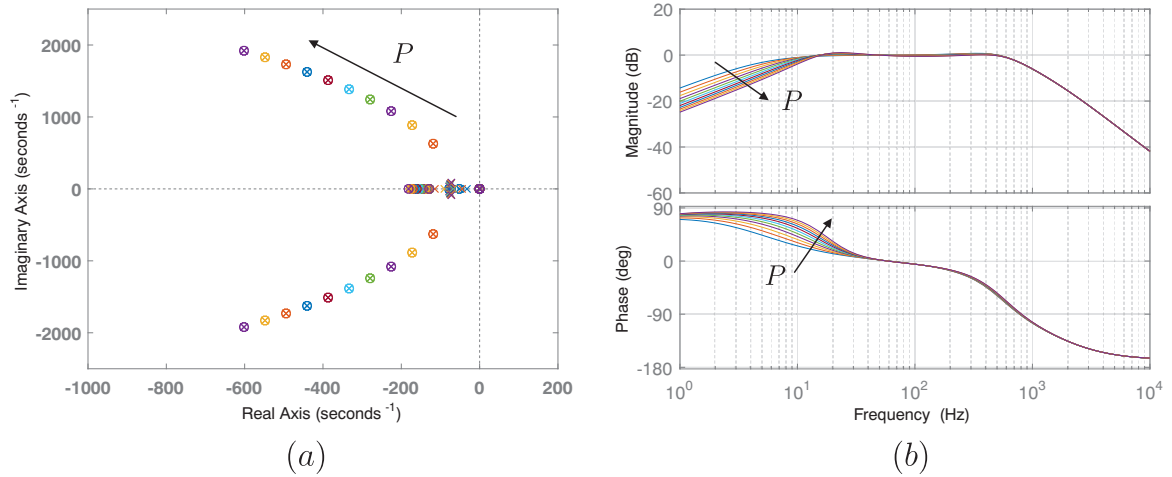


Figure 2.45: Stability analysis of the ST-fed grid varying the active power absorption: (a) root locus, (b) closed-loop bode plot.

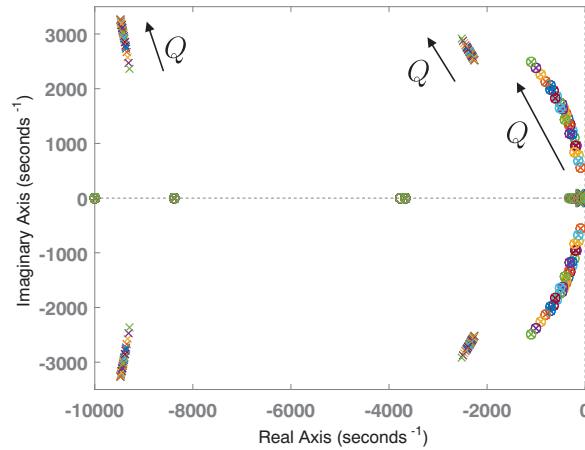


Figure 2.46: Root locus of the ST-fed grid transfer function varying the inductive reactive power absorption.

Disturbance rejection capability

The ST has to offer high disturbance rejection capability in order to guarantee a sinusoidal voltage waveform independent from the load current. To study the disturbance rejection capability, the superposition principle can be adopted. A disturbance signal i_0 , as shown in Figure 2.47, has been added to the scheme shown in Figure 2.44, in order to include the load current disturbance effects in the ST voltage waveform.

The transfer function $H(s)$, relating the current signal i_0 to the voltage waveform v_{abc} , is obtained considering the superimposed scheme shown in Figure 2.48, where the voltage reference v_{abc}^* is neglected. The resulting circuit is composed of the filter elements and the load in parallel with the current source i_0 . Thus $H(s)$ can be written as:

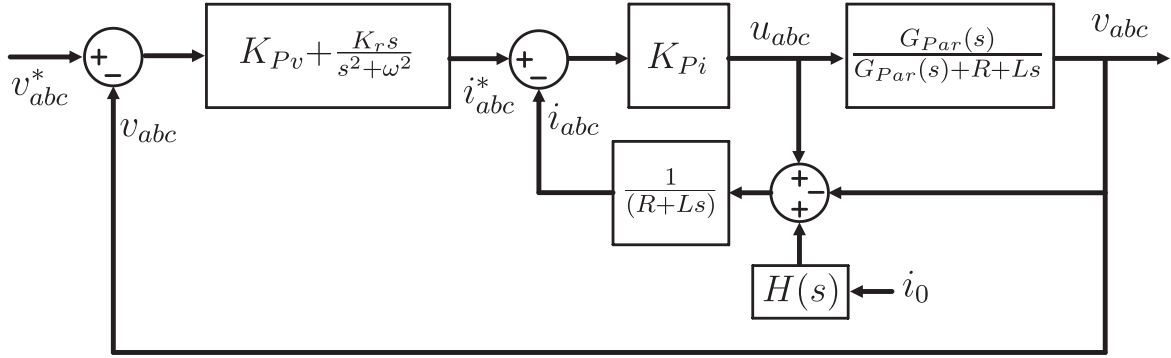


Figure 2.47: Controller and plant scheme of the ST LV converter considering a current disturbance in the load current.

$$\begin{aligned}
 H(s) &= 1 / (Y_L(s) + Y_{CL}(s) + Y_{load}(s)) = \\
 &= 1 / \left(\frac{1}{R + Ls} + \frac{1}{1/C_Ls + R_d} + \frac{1}{R_{load} + L_{load}s} \right)
 \end{aligned} \tag{2.44}$$

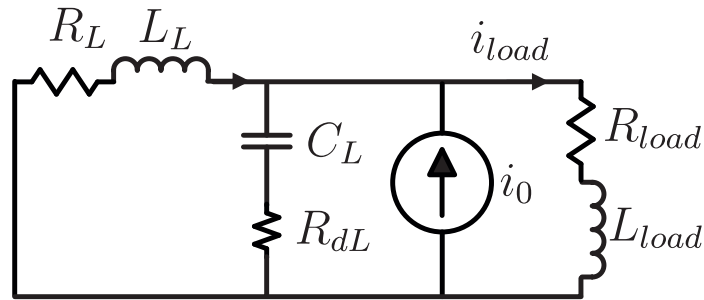


Figure 2.48: Superposed circuit scheme for the load disturbance rejection analysis.

The ST parameters must be chosen in order to damp the current disturbances under any load condition. To verify this, the current controller gain K_{Pi} is firstly varied from the initial guessing of $K_{Pi}=0.25$ to the final value of $K_{Pi}=1.5$ ($K_{Pi}=1.25$ is the first unstable condition). The influence of the controller, on the capability to reject disturbances, can be seen from Figure 2.49a, where the controller has limited influence at low frequency, but it contributes to decrease the damping at high frequencies. Supposing to have a damping higher than 10 dB (0.3 pu), starting from $K_{Pi}=0.5$, all the values give less damping than the one requested. Thus the initial guessing of $K_{Pi}=0.25$ gives a good damping capability of current disturbances. The ST disturbance rejection capability is finally evaluated varying the load from no-load condition up to 1 MVA load, under a power factor $\cos(\varphi) = 0.95$. This is for ensuring the rejection capability in the whole operative range of the ST. As shown in Figure 2.49b, the ST is able to damp any load current disturbance in the whole frequency spectrum with more than 10 dB of gain in the worst condition (no-load, blue line).

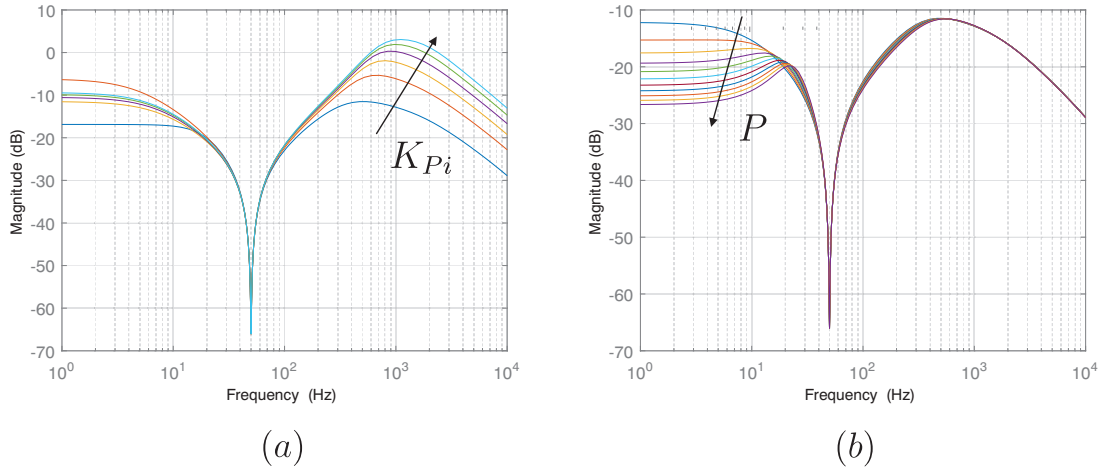


Figure 2.49: Closed-loop bode plot of the ST-fed disturbance rejection capability varying: (a) the current controller gain K_{Pi} , and (b) the load active power absorption.

Harmonic compensation

The ST has to provide sinusoidal voltage waveforms, independently from the load current demand. However, applying the control shown in Figure 2.42, in case of current high harmonic content, the voltage is affected by distortion, due to the voltage drop on the filter impedance. To solve this issue, the solution proposed in Figure 2.50 can be applied. In the voltage control loop, resonant controllers, tuned on odd multiples of the fundamental frequency, are added in order to minimize the harmonic errors in the voltage. The transfer function for a resonant controller at the n -th frequency can be written as:

$$R_n(s) = \frac{K_r s}{s^2 + (n \cdot \omega)^2} \tag{2.45}$$

where K_r is the resonant controller gain, and ω is the fundamental frequency.

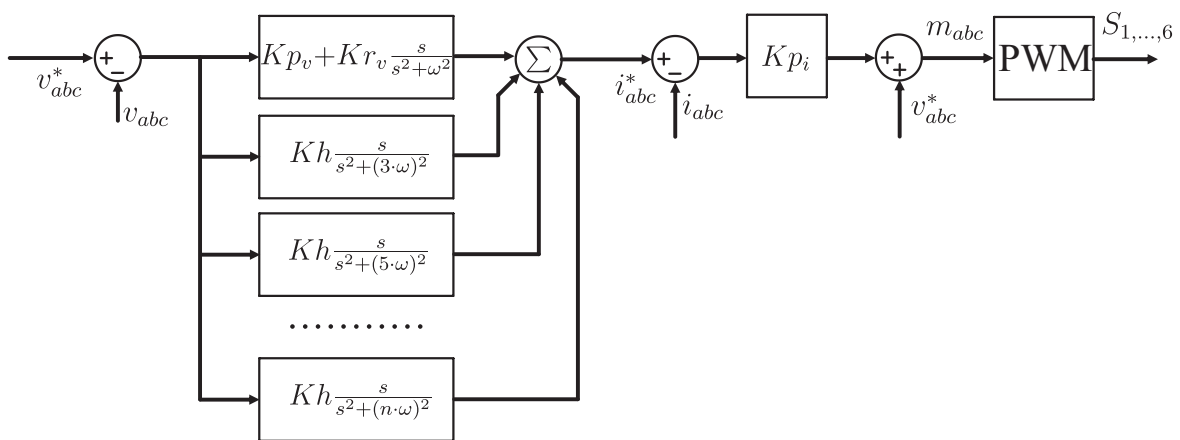


Figure 2.50: ST LV converter harmonic controller scheme.

The closed-loop transfer function of the ST LV side controller becomes now as shown in Figure 2.51. The harmonic resonant controllers creates spikes in the frequency spectrum for

each controlled harmonic, offering high rejection capability.

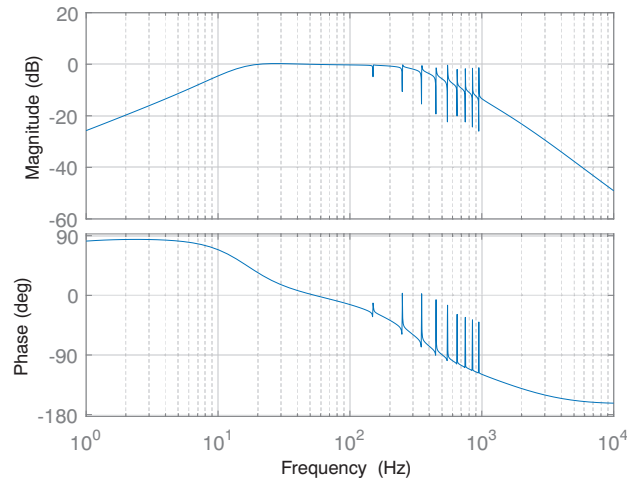


Figure 2.51: Closed-loop bode plot of the ST LV converter harmonic controller.

To verify the effectiveness of the harmonic controller a diode-rectified load has been connected in the circuit, to introduce current harmonic content in the grid. The rectifier load resistance R_{harm} is taken equal to $2\ \Omega$. Figure 2.52 shows the difference in the voltage waveform without harmonic compensation (Figure 2.52a) and after the activation of the harmonic controller (Figure 2.52b). The ST, activating the harmonic controller, compensates the low order harmonics, improving the quality of the voltage sinusoid. This effect becomes clearer performing the DFT of the voltage signal, before and after the harmonic controller activation, as shown in Table 2.10. The harmonic content decreases sensibly in the low order harmonics (5^{th} and 7^{th}) and improves till the 13^{th} harmonic. Being the converter bandwidth equal to 800 Hz, the impact on high order harmonics is limited (17^{th} and 19^{th}). However, if this harmonic content represent an issue to the ST-fed grid management, the ST LV converter bandwidth has to be increased.

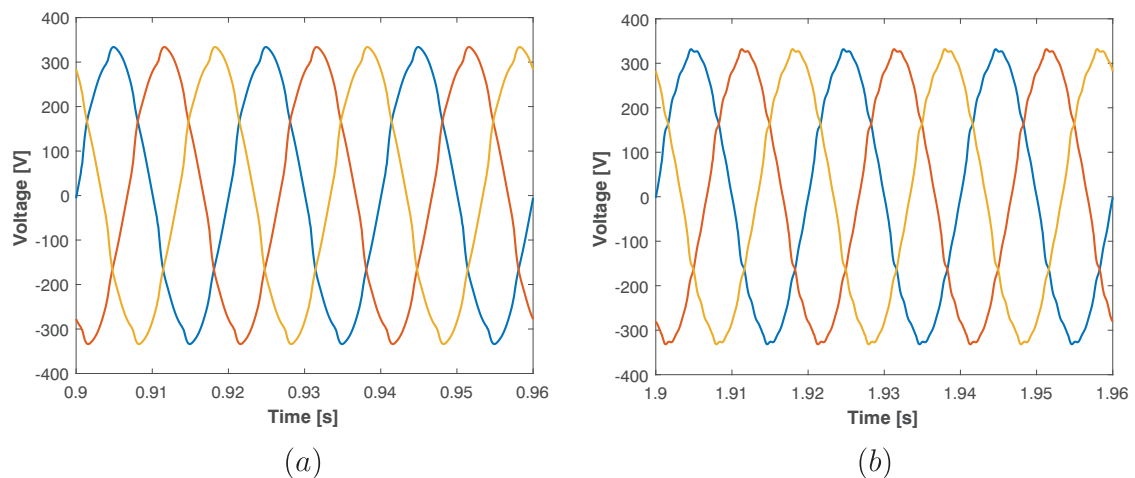


Figure 2.52: ST LV converter harmonic controller: (a) no harmonic control, (b) harmonic controller activated.

Table 2.10: LV grid voltage harmonic content

Harmonic	No control (%)	Harmonic controller (%)
5 th	3,2	1,7
7 th	1,7	0,9
11 th	1,3	0,8
13 th	0,8	0,6
17 th	0,5	0,8
19 th	0,3	0,8

2.6 Conclusions

This chapter introduces the Smart Transformer concept, describing the new control capability for providing services to distribution grids. The ST does not aim simply to adapt the voltage from MV to LV grid, but to offer ancillary services to both grids. The modeling procedures of each ST stage have been explained, taking into account the model variations deriving from different topologies (e.g., MMC for the MV converter, or DAB and SRC for the DC/DC stage). The controllers of each ST stage have been addressed, giving particular attention to the system level controllers. For the MV converter, the harmonic and unbalances compensation controllers have been explained to increase the power quality in the MV distribution grid. In the DC/DC converter, the capability to reject disturbances (e.g., fast power variations) is compared in two different DC/DC topologies (DAB and SRC). It shows how higher control complexity (DAB case) increases the disturbance rejection capability with respect to simpler and more robust topology, such as SRC. In the LV side, the ST has the task to control the three-phase voltage waveform. It must be kept sinusoidal and balanced under any load condition (e.g., harmonics), and the ST must offer a high disturbance rejection capability. The ST hardware has been sized and its controller tuned in order to keep a stable behavior under all possible load conditions, and to offer current disturbance damping in the whole frequency spectrum. An external controller can modify the voltage reference values to offer additional services, like ST overload control, reverse power flow limitation control, on-line load identification and transmission grid real time frequency support. These services are not treated in this chapter, but Chapters 4, 5, and 6 are dedicated to them.

3 Experimental validation of ST services: laboratory test descriptions

The ST is a complex system composed of many components and controllers. In chapter 2, its controllers and features have been depicted by means of simulations. However, the analysis of the ST features taking in account each single component can be challenging in terms of accuracy and computational capability and it may not lead always to realistic results. The critical points can be summarized as [90]:

- difficulty in representing critical dynamics, leading to an oversimplification of the system and its constraints.
- need for creation of physical-based models, that, although accurate, require extensive simulation time, creating substantial delays in the apparatus and controller development.

Thus, for validation purposes, an experimental validation is preferred in case of the ST. If from one side the validation is performed in a more realistic environment, on the other it increases the complexity of the test. Indeed, working in lab reproducing certain conditions (e.g., a ST-fed grid) may represent a difficult task, requiring space and availability of many devices (e.g., loads and DERs). To overcome this limitation and to choose the proper environment to test the ST hardware or any of its controllers, in this chapter, three possible testing solutions for ST are presented. Depending on the application and the feature to be validated, one of the proposed solution can be adopted:

- a "hardware solution", with a microgrid setup composed by two commercial converters and a passive load. The main advantage of this solution is the realistic test condition in which the ST controllers and features are validated, including all the components dynamics, although in a simplified environment. For example, if a harmonic damping control (like the one explored at the end of chapter 5) shall be tested, the microgrid setup allows to analyze the whole harmonic spectrum without any filtering derived from intermediate interfaces (e.g., analog-digital cards);
- a "external controller" solution, the Control Hardware In Loop, where the whole ST-fed grid (ST included) is implemented in a RTDS and the ST is controlled by means of external hardware (e.g., dSPACE). This solution is particularly suitable in case of algorithm testing, where the interest lies in the algorithm performance more than in the hardware. The CHIL is employed to validate the On-Line Load sensitivity Identification method presented in chapter 4 and 5;
- a "hybrid" solution, the Power Hardware In Loop, that merges the lab experiments and simulation advantages in one system. The ST hardware is interfaced with a grid simulated in RTDS and the two systems are interfaced by means of a power amplifier. This solution aims to merge the advantages of the microgrid setup and the CHIL evaluation [91, 90]:

- possibility to investigate the interaction between the hardware under test and an extensive grid environment;
- the experiments can be performed in a controlled environment, reducing the risk to validate them in field tests;
- high flexibility to vary and adapt the system and conditions of the tests;
- possibility to test scaled-down prototypes.

As follows in this chapter, these three evaluation setup solutions are described more in details.

3.1 Microgrid setup

A microgrid setup has been built in the laboratory at the Chair of Power Electronics using a system composed of two Danfoss *FC-302* Voltage Source Converter and a passive load as shown in Figure 3.1. The goal of this microgrid setup is to reproduce in small scale the behavior of the ST-fed grid. The main components in this microgrid are:

- the ST-emulating converter, that acts as grid-forming converter in the grid, with the tasks to control the voltage waveform and to provide ancillary services as described in the next chapters. Being the current demand decided by the ST-fed grid loads, the ST-converter must have stable performances from no-load to full load power demand;
- a resistor, emulating the aggregate passive load of the grid. To this category can be grouped all the loads behaving as constant impedance loads or loads sensitive to voltage variations, such as electric heaters and refrigerators [92];
- the DER-converter, that is controlled to emulate the behavior of any power-controlled device in the grid. It can represent:
 - a constant power load, if the power set-point is negative (e.g., power electronics-based appliances);
 - a DG power plant, if the power set-point is positive (e.g., photovoltaic or small wind power plant);
 - an aggregate of load plus DG with controlled DERs, if the power set-point is free to vary from positive to negative and viceversa (e.g., systems supported by batteries).

More generally, it represents the concept of "Prosumers" that are small consumers able to play an active role in the electricity generation and the provision of grid services [93]. The prosumer has installed generation that compensates for its own load and it can be able to control the power injection in the grid, if equipped with controllable resources, such as batteries.

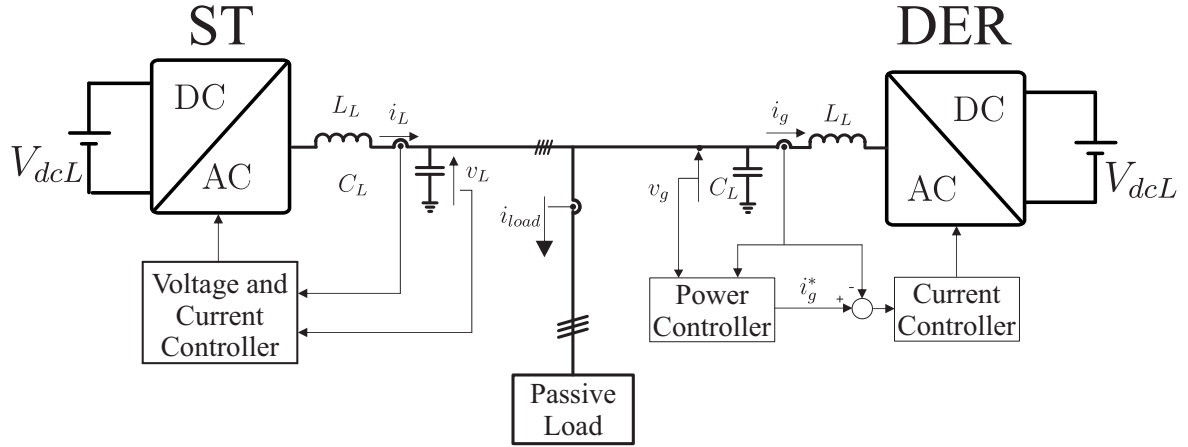


Figure 3.1: Microgrid setup develop at the chair of Power Electronics.

The two converters are connected in AC, with the AC microgrid, and in the DC side, by means of a common DC-link. The energy is supplied by means of a DC power source, connected to the DC-link, that controls the DC voltage V_{dcL} . This permits the power circulation in the setup, avoiding to send back power to the grid (not possible due to the DC power supply current and voltage uni-directionality). In this case, the DC power supply must provide the losses of the two converter, plus the power consumed by the AC passive load.

The ST-converter controller is implemented as described in the previous chapter, however the parameter values have been changed due to the scaled-down ST-converter prototype installed in lab. In Table 3.1 are listed the variables quantities, as well as the passive elements size.

Table 3.1: Experimental setup parameters.

Parameter	Value	Parameter	Value
$V_{dcL}(ST)$	700 V	$V_{dcL}(DG)$	700 V
S	4 kVA	L_L	5.03 mH
C_L	1.5 μ F	v_L	230 V_{rms}
f_s	10 kHz	R_{dL}	2 Ω
Kp_v	0.1	Kr_v	200
Kp_i	0.75		

As mentioned above, the ST converter has to be tuned to control the voltage waveform. The values of the voltage and current controllers are listed in Table 3.1 and the open-loop transfer function v_L/v_L^* bode plot is shown in Figure 3.1, in case of a resistive load equal to 26.5 Ω , equivalent to 2 kW load in nominal conditions. It can be noted that the LC resonance peak is located at 1.8 kHz, and the presence of damping resistors R_{dL} helps to reduce the peak below the 0 dB threshold.

The DER-converter controller is implemented in dq frame. PI regulators are used for the current control, tuned to maximize the controller's bandwidth without resonance phenomena.

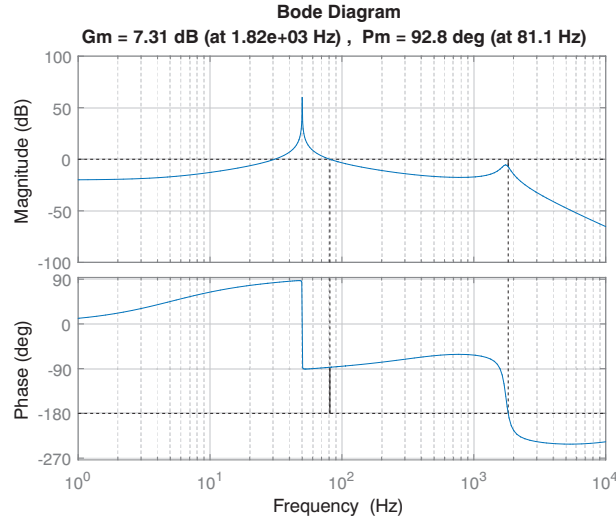


Figure 3.2: Open-loop bode plot of the ST converter transfer function in the microgrid setup. LV load power consumption equal to 2 kW.

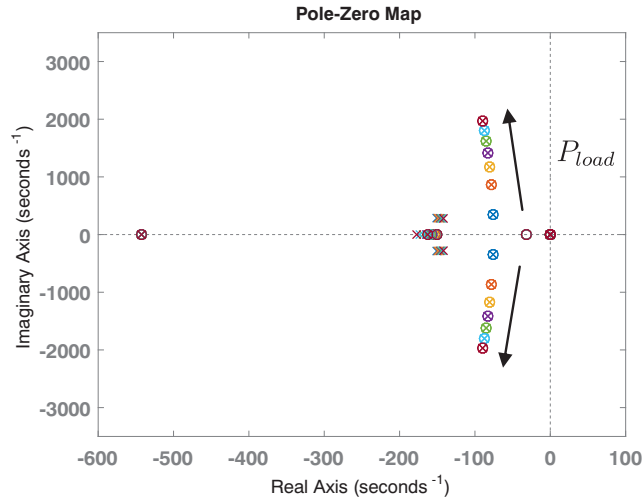


Figure 3.3: Rootlocus of the ST converter transfer function varying the active power request from the LV load.

A power loop can be added externally to the current loop to control the power instead of the current injection, as shown in red in Figure 3.4. In this case, a feed-forward power calculation has been adopted, meaning that the current references are obtained dividing the powers with the voltage measurements. The equations linking the active and reactive power to currents are described as follows:

$$i_{dL}^* = \frac{2 p_L^* \cdot v_{dL} - q_L^* \cdot v_{qL}}{3 (v_{dL}^2 + v_{qL}^2)} \quad (3.1)$$

$$i_{qL}^* = \frac{2}{3} \frac{p_L^* \cdot v_{qL} + q_L^* \cdot v_{pL}}{v_{dL}^2 + v_{qL}^2} \quad (3.2)$$

Additionally, closed-loop power controllers can be adopted to increase the power controllability or to let the DER offer additional services to the grid (e.g., harmonics compensation). Although this solutions are outside the scope of this microgrid setup, aimed to represent the general case of inverter-connected DER, in chapter 5 a frequency adaptive voltage controller is presented (FORC, section 5.5), able to offer advanced control capabilities in presence of variable frequency grid with current harmonic content.

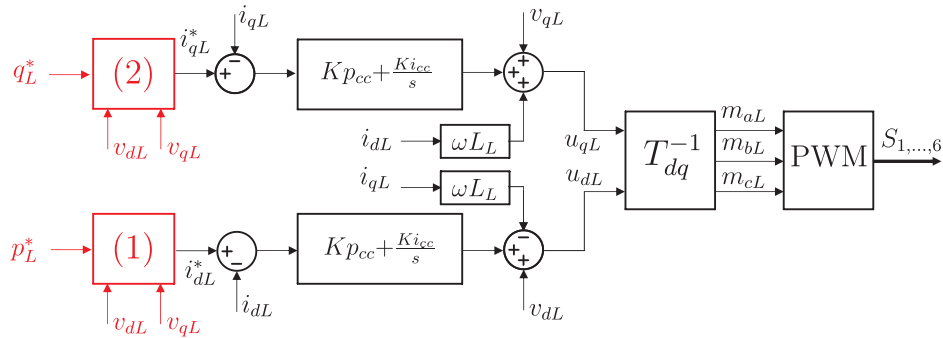


Figure 3.4: DER converter controller scheme.

Considering the implementation of the only current controller without power references, the bode diagram of the DER-converter controller plus plant is shown in Figure 3.5. The controller’s parameters have been chosen equal to $Kp_{cc} = 10$ and $Ki_{cc} = 10$. The choice of these values gives a good tradeoff between controller bandwidth (about 650 Hz) and gain and phase margin values.

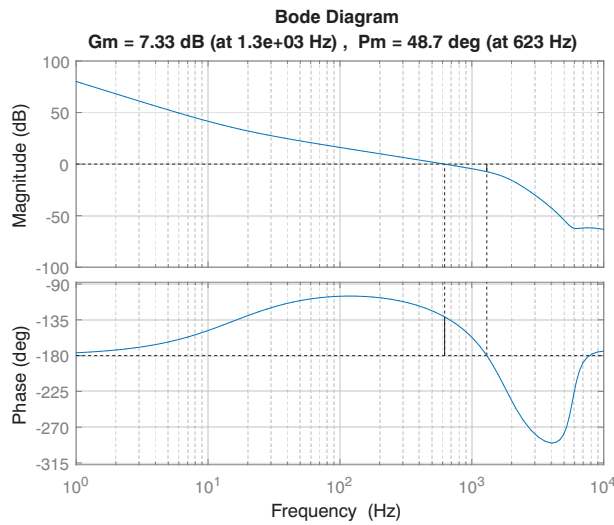


Figure 3.5: Bode plot of the DER converter controller and plant.

3.2 Control Hardware In Loop evaluation

The simulation approach allows to simulate large grids and to test control strategies with high accuracy. However it gives no indication about the real time performances of the these strategies, and although the microgrid setup described above represents a good solution to prove control concept and methodologies in hardware, it is limited in space and number of components that can be installed. The CHIL evaluation allows instead to test a certain algorithm or control strategy in real time without the need of physical hardware. In the CHIL, both grid and Hardware under Test (HuT) are simulated in RTDS and the HuT is controlled using the control strategies under investigation implemented in the external hardware [94]. The testing conditions are flexible to be modified (e.g., different voltage and current levels or rated powers), and combining with the possibility to implement a large grid in RTDS, the impact of HuT controller actions on the emulated grid can be easily evaluated. Complex control strategies can be realized in hardware or on different control platform interfaced with the RTDS, such as dSPACE. As shown in [95], a microgrid supervisor controller has been realized in a separate unit and it communicate with the RTDS by means of analog and digital signals.

An interesting variation of CHIL approach is to interface of the Real Time System (in our case RTDS) with another software, working in a different domain (e.g., phasorial, frequency, etc.) [96]. This possibility enables to run part of the system in real time with different time steps, without being limited by the real time system computational capability. As described in [97], a voltage/var optimization is realized, where the measurements are read from the RTDS system, and transferred to another software platform (i.e., Matlab) by means of communication standards (i.e., IEC61850). Then it is possible to perform an optimization in Matlab environment, suitable for solving complex and large optimization problems, without being constrained by real time limitations. Eventually, to apply the corrective control action, the new set-points are sent back to the system running in real time.

The CHIL evaluation setup installed in lab has been implemented to simulate both the ST and the LV grid in RTDS and using the dSPACE 1104 system as ST controller (Figure 3.6). The RTDS systems has the possibility to simulate two parts of the grid with two different time-steps: a large time-step (typically $50 \mu\text{s}$), used for grid components such as lines, machines, and loads; and a small time-step (below $2 \mu\text{s}$), used for simulating the switching behavior of power electronics converters. The latest possibility has been exploited to simulate the ST LV side for power system studies. The RTDS grid is implemented in the large time-steps domain, where loads and DER equivalent models are simulated. The ST is instead implemented in a small-time steps subsystem, with a switching elements model. In our application, the ST has been implemented using a NPC converter due to the need of the fourth wire connection availability. In the case of the NPC, the neutral conductor connection comes from the DC link middle point.

The CHIL evaluation consists on sampling the voltage and current in the PCC of the ST with the ST-fed grid, and sending the signals to the ST controller implemented in dSPACE.

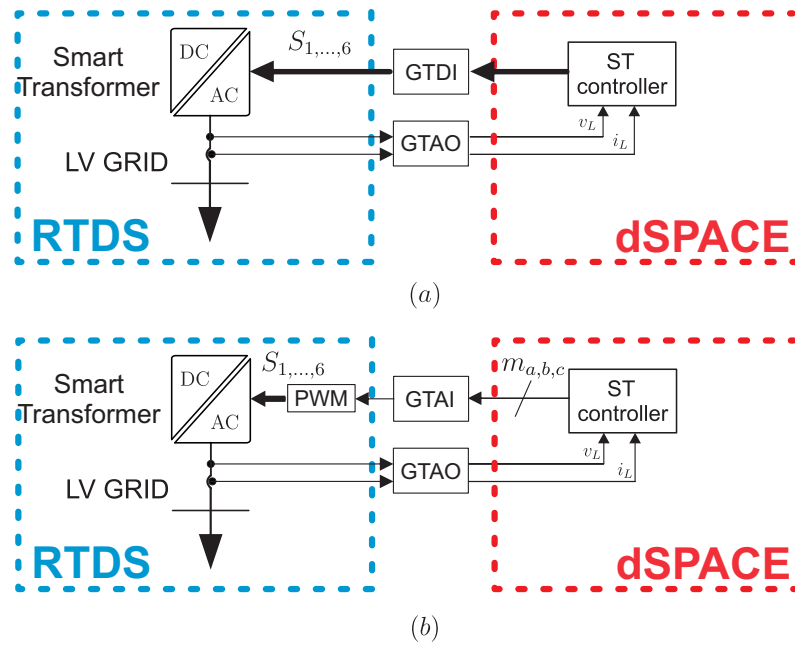


Figure 3.6: Control Hardware In Loop: (a) PWM signals as interface between dSPACE and RTDS; (b) modulation signals as interface between dSPACE and RTDS.

These signals are analog, and they are sent from RTDS to dSPACE by means of a Gigabit Transceiver Analog Output (GTAO) card present in the backspace of the RTDS.

Two different approaches have been considered to interface the connection from dSPACE system to the RTDS. In the first approach digital signals are the input for the Gigabit Transceiver Digital Input (GTDI) card of RTDS (Figure 3.6a), while in the second case analog signals are sent from the dSPACE to the RTDS through the Gigabit Transceiver Analog Input (GTAI) (Figure 3.6b). In both cases the controller is implemented in a discrete time frame in Simulink/Matlab. While in the first case the behavior of the converter can be estimated, integrating also the dead-time in the PWM, the loop accuracy in case of high switching frequencies decreases considerably. The not correct synchronization between the RTDS small time-steps subsystem, where the converter is simulated, and the dSPACE PWM signals leads to a superposed oscillation to the controlled variable (e.g., current or voltage). Indeed, the RTDS small time-steps subsystem tries to minimize the time step during the simulation, calculating beforehand the time needed for solving the system equations. This does not allow to choose a desired time-step in the small time-steps subsystem where the RTDS may select asynchronous time-step values (e.g., $1.73 \mu\text{s}$) with respect to the dSPACE system (working with $100 \mu\text{s}$ time-step). This creates an asynchronous sampling of the dead-time of each PWM signal and thus a low frequency oscillation (e.g. 0.1-1 Hz) of the controlled variable. This effect is strongly damped when the switching frequencies are lower (e.g., from few hundreds Hertz to few kHz), due to the higher ratio between the switching time-step and the simulation time-step.

In the second case, the RTDS creates the PWM switching signals directly in RSCAD, thus the PWM signals are synchronized with the system time-step, and the low frequency oscillations are not anymore present. However, this approach limits the possibility to implement complex

PWM controllers, due to implementation complexity in the RSCAD environment. The dead-time of the PWM signal cannot be freely chosen or modified, due to the dependency on the RTDS time step. It can be either absent (ideal switching case) or chosen as single time step delay. Depending the dead-time from the rated current and voltage of the device, in case of low-power applications, the dead time can be overestimated, while for high-power applications may result too tight.

3.3 Power Hardware In Loop evaluation

In order to show the ST features in realistic conditions, the implementation in a test distribution grid is needed. However the simple simulation of ST in software environment may lead to not realistic results due to the models adopted, meanwhile the ST hardware test in a research lab with large LV grids results to be unpractical due to the grid size and complexity. At this regard the PHIL simulation by means of the RTDS system offers new opportunities for hardware testing [91, 90, 98, 99]. With respect to the classical CHIL evaluation, used for testing controllers and relays, the PHIL simulation allows to analyze the impact on the grid of the hardware under test using a scaled model connected to the RTDS by means of an interface converter. This feature increases the testing possibilities and allows to perform hardware tests without affecting the real grid (e.g., faults, overvoltages, high harmonic content, etc.).

Despite the many advantages that the PHIL has, its implementation is complex and the stability and accuracy of the loop must be studied in order to replicate accurately the behavior of the simulated grid in the hardware setup. The accuracy of the PHIL evaluation is related to the capacity of the interface converter controller (e.g., a linear power amplifier) to follow the reference signals sent by RTDS, keeping the system stable without any undesired behavior (e.g., instability caused by loop delays). The stability and accuracy of the loop depend on the chosen interface algorithm between software and hardware and on the interface converter [91, 90, 100]. The interface algorithm must be tailored to the application of the PHIL and incorrect tuning may lead to hardware behavior, which is not consistent with the RTDS simulation.

3.3.1 Current-type PHIL evaluation setup

The PHIL adopted in the Chair of Power Electronics is realized by means of a current-type loop. The ST controls the voltage v_L on the filter capacitor. The measurement system measures the voltage and send the measurement signals v_L to the RTDS software, RSCAD. Here the voltage is applied directly in the simulated grid by means of an ideal controlled voltage source. The current demanded by the grid i_g^* is sampled in RTDS and sent to a current controller, that controls the current injection i_g of the linear power amplifier in order to reproduce accurately the grid current in RTDS i_g , closing the loop. Between the simulated grid and the ST hardware, a current scale factor can be chosen to represent in software systems bigger than the HuT size. In this case a scale factor of 50 has been introduced in

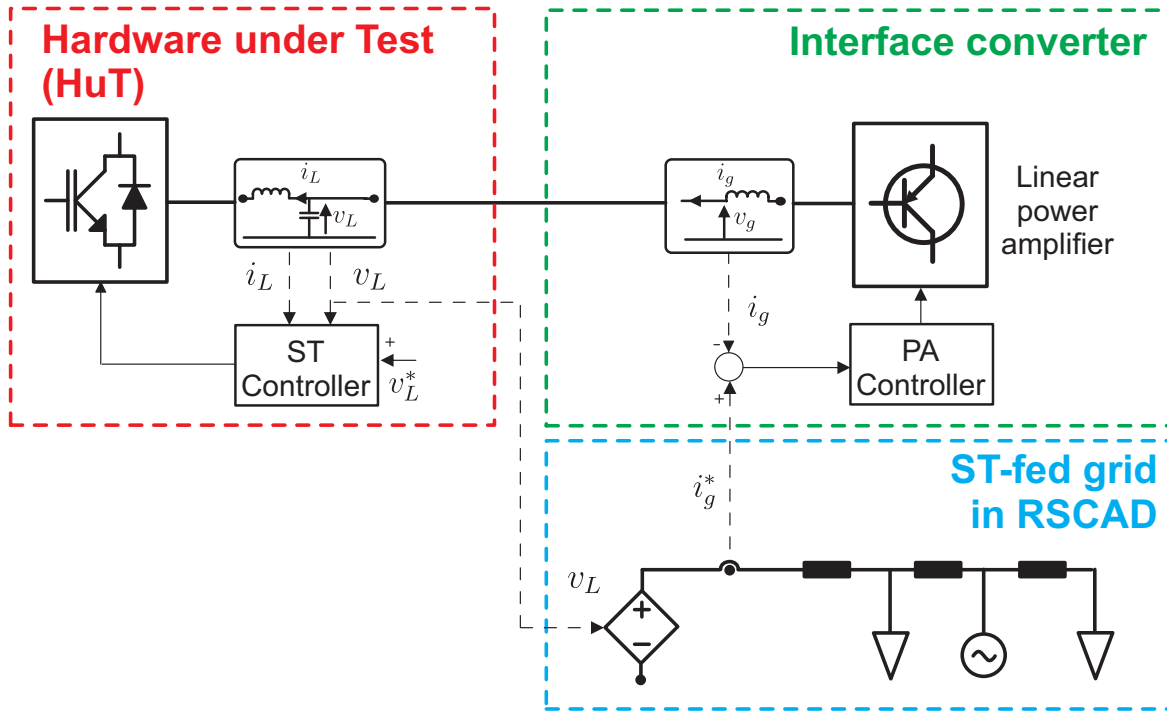


Figure 3.7: PHIL: Hardware system (red frame), simulated system (green frame).

the current to cope with the limited power capability of the hardware in lab. It means that 1 A current change in the hardware side corresponds to 50 A current change in RSCAD. Any change in the current absorption in RSCAD, due to a different load demand, influences the ST controller, and, vice-versa, any change in the ST voltage amplitude or frequency, impacts on the grid power consumption.

Stability and accuracy evaluation of the current-type PHIL system

The PHIL stability and accuracy are important for achieving the distribution grids conditions in lab. They are interlaced: the stability is a necessary condition for the PHIL evaluation, and it is needed for the evaluation accuracy and the equipment safety [90]. The accuracy of the PHIL can be defined as the capacity of the PHIL to reproduce in hardware a certain variable simulated in RSCAD with a certain dynamic. In the particular case of the current-type PHIL, it refers to the capacity of the power amplifier current controller to reproduce in hardware the current flowing in RSCAD.

However, the PHIL is composed of several interconnected elements, such as RTDS, power amplifier and HuT (i.e., the ST), working with their own controllers and dynamics. Hence, their interaction can affect the stability and accuracy of the loop in reproducing in the hardware side what simulated in RTDS. The purpose of this section is to analyze mathematically the stability and the accuracy of the loop in Figure 3.7, and to perform a proper tuning of the power amplifier controller in order to get a tradeoff between accuracy and system stability.

The system shown in Figure 3.7 can be represented mathematically as in Figure 3.8. The ST and the RTDS are interfaced due to the voltage measurement v_L , that is reproduced in

RSCAD as voltage source. Following, the RTDS provides the current reference i_L^* to the current controller implemented in RTDS, which controls the current on the inductor L_{PA} . This current i_g corresponds to the same output current of the ST filter on the grid side.

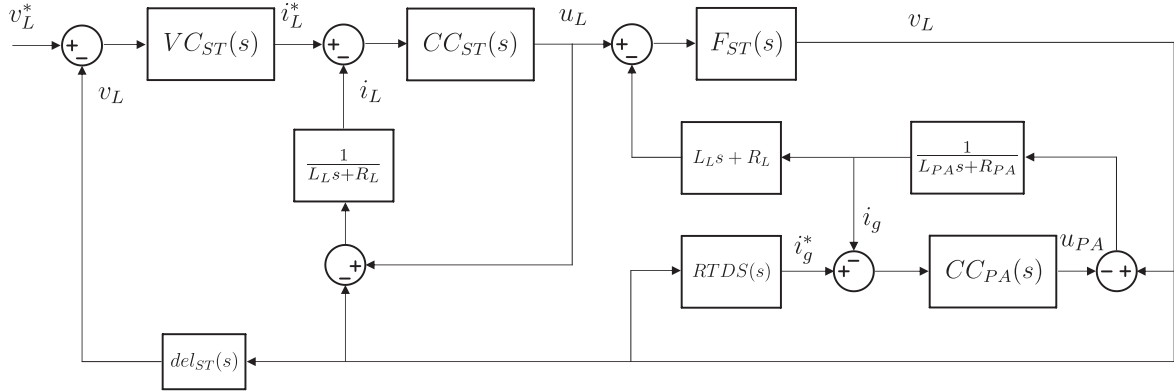


Figure 3.8: Equivalent transfer function scheme of the PHIL setup depicted in Figure 3.7

The transfer function written in the blocks in Figure 3.8, are defined as follows:

$$\begin{aligned}
 F_{ST}(s) &= \frac{\frac{1}{sC_L} + R_{dL}}{\frac{1}{sC_L} + R_{dL} + L_L s + R_L} \\
 RTDS(s) &= \frac{1}{L_{load}s + R_{load}} \cdot del_{RTDS}(s) \\
 CC_{ST}(s) &= K_{pi} \cdot del_{ST}(s) \\
 VC_{ST}(s) &= K_{pv} + K_{rv} \frac{s}{s^2 + w^2} \\
 CC_{PA}(s) &= K_{pPA} + \frac{K_{iPA}}{s} + K_{rPA} \frac{s}{s^2 + w^2} \cdot del_{RTDS}^2(s) \\
 del_{ST}(s) &= \frac{-T_c s + 1}{T_c s + 1} \\
 del_{RTDS}(s) &= \frac{-T_c/2s + 1}{T_c/2s + 1}
 \end{aligned} \tag{3.3}$$

where F_{ST} represents the ST LC filter transfer function, except for the contribution of the grid current $(L_L s + R_L)i_g$; $RTDS(s)$ is the equivalent grid implemented in RSCAD, composed of a passive LR load; CC_{ST} and VC_{ST} are respectively the ST current and voltage loop transfer function, tuned as described in the microgrid setup section; CC_{PA} is the current controller of the power amplifier transfer function; and $del_{ST}(s)$ and $del_{RTDS}(s)$ are the delay transfer function of the ST and the RTDS, represented as Padé first order approximation of a time step $T_c=100 \mu s$. This approximation is an acceptable tradeoff between accuracy and complexity in representing the delay. Moreover, the number of poles and zeros introduced in the transfer function are kept at the minimum. The Padé approximation equations of a single time step

delay are described in (3.4), where the approximations up to the third order are listed. As can be noted in Figure 3.9, where a delay of the single time step $50 \mu\text{s}$ is considered (i.e., $del_{RTDS}(s)$), increasing the order of the Padé approximation does not give substantial benefits in the dynamics on the opposition of higher complexity and introduction of more poles pairs in the transfer function.

$$\begin{aligned} Pade^1(s) &= \frac{2 - sT_c}{2 + sT_c} \\ Pade^2(s) &= \frac{12 - 6sT_c + (sT_c)^2}{12 + 6sT_c + (sT_c)^2} \\ Pade^3(s) &= \frac{120 - 60sT_c + 12(sT_c)^2 - (sT_c)^3}{120 + 60sT_c + 12(sT_c)^2 + (sT_c)^3} \end{aligned} \quad (3.4)$$

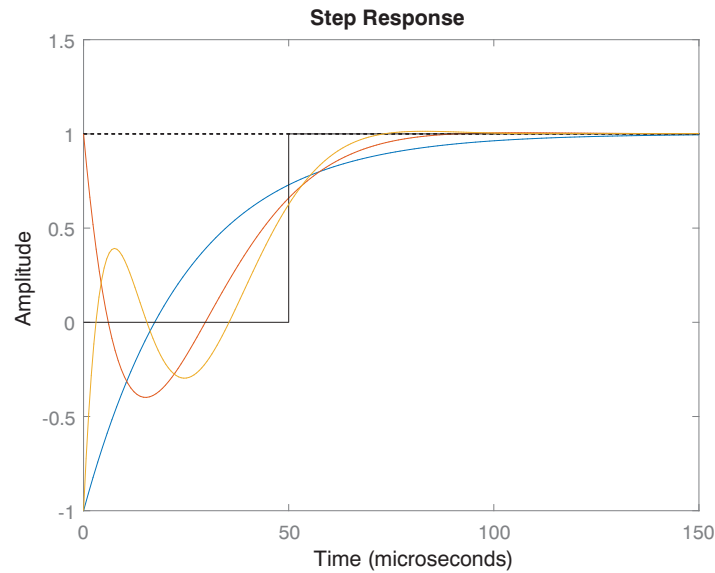


Figure 3.9: Padé delay approximation for a delay $50 \mu\text{s}$: reference (black line), first order (blue line), second order (red line), and third order (yellow line).

Although the dynamics among the different Padé orders looks similar, the stability of the system can differ depending on the phase behavior along the frequency spectrum. In Figure 3.10, the phase plot of the first three orders of the Padé approximation and the ideal delay e^{-sT_c} (black line) have been plotted. As can be noticed, for phenomena up to 3 – 4 kHz, there is no substantial difference in the phase behavior among the ideal delay and its Padé approximation. However, if phenomena behaviors are expected at higher frequencies (e.g., above 5 kHz), the model has to be represented with a Padé order higher than the first one. As demonstrated later in this section (Figure 3.17), in the analysis of our PHIL setup, the order of Padé approximation has negligible influence on the stability and dynamic of the system.

In order to solve this complex block diagram, following it is offered its step-to-step solution.

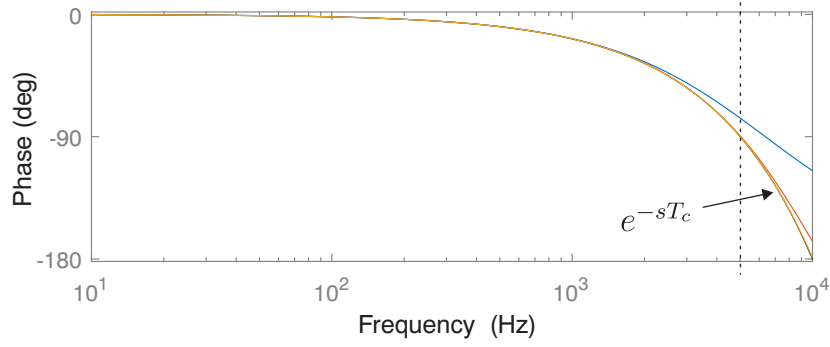


Figure 3.10: Phase plot of Padé delay approximation for a delay $50 \mu\text{s}$: reference (black line), first order (blue line), second order (red line), and third order (yellow line).

The equivalent transfer function $PA_{eq1}(s)$ is created, including the ST filter transfer function and power amplifier LR filter. The ST current control loop is solved and called $CC_{eq}(s)$.

$$PA_{eq1}(s) = F_{ST}(s) (L_L s + R_L) \frac{1}{L_{PAS} + R_{PA}} \quad (3.5)$$

$$CC_{eq}(s) = \frac{CC_{ST}(s)}{1 + CC_{ST}(s) (1/L_L s + R_R)}$$

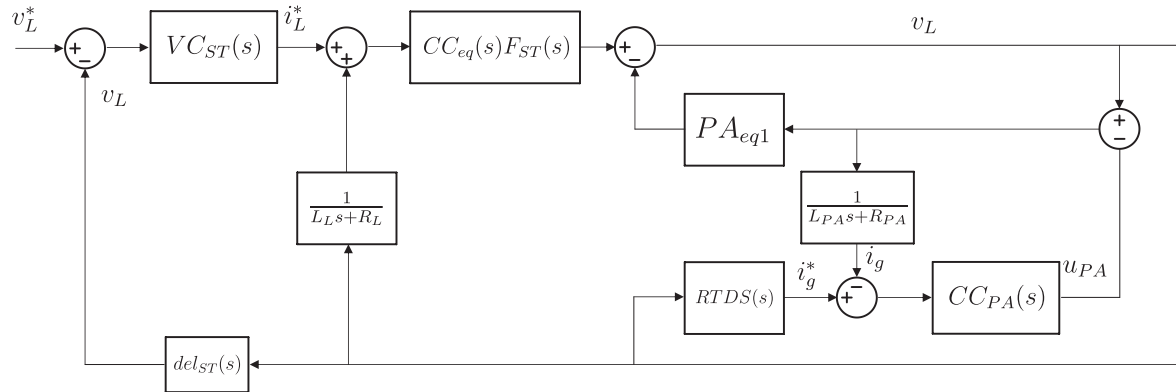


Figure 3.11: Equivalent transfer function scheme of the PHIL setup depicted in Figure 3.7, Step 2.

The power amplifier controller and its plant are grouped within the transfer function $PA_{eq2}(s)$, and the transfer function B is created to simplify the loop. Eventually, the RTDS transfer function and the power amplifier current controller are grouped in the equivalent transfer function D .

$$PA_{eq2}(s) = \frac{1}{L_L s + R_R} CC_{PA}(s)$$

$$B(s) = \frac{1}{1 + PA_{eq2}} \quad (3.6)$$

$$D(s) = RTDS(s) CC_{PA}(s)$$

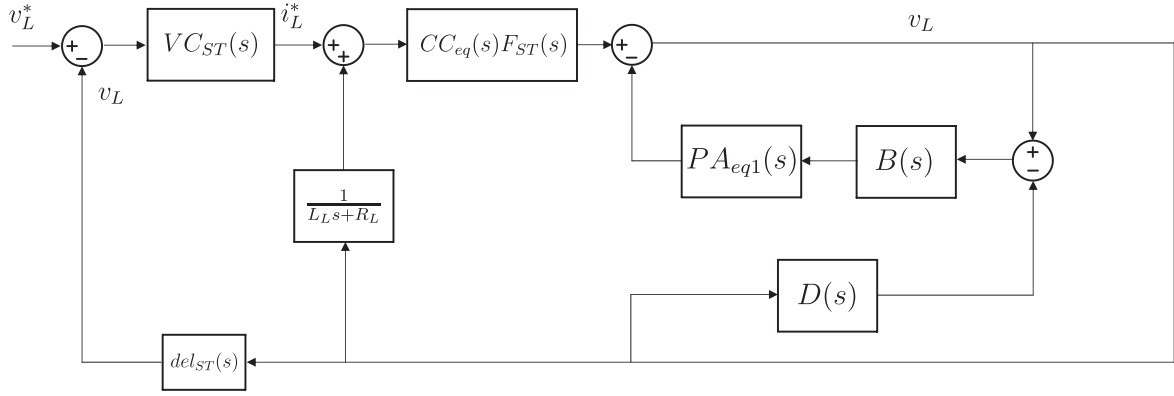


Figure 3.12: Equivalent transfer function scheme of the PHIL setup depicted in Figure 3.7, Step 3.

Grouping the transfer functions in the same branches $C(s)$ and $E(s)$, the inner loop on the right of Figure 3.12 becomes like in Figure 3.13:

$$C(s) = PA_{eq1}(s)B(s) \quad (3.7)$$

$$E(s) = CC_{eq}(s)F_{ST}(s)$$

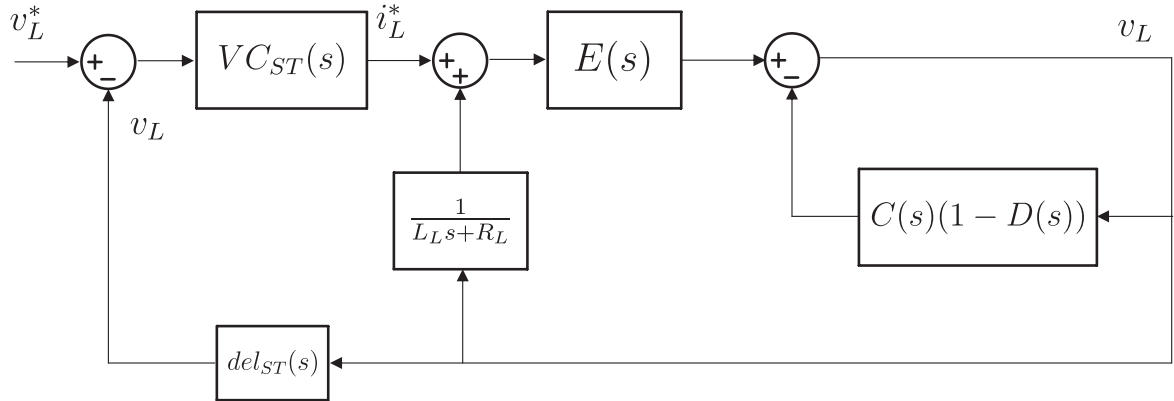


Figure 3.13: Equivalent transfer function scheme of the PHIL setup depicted in Figure 3.7, Step 4.

and calling $H(s)$ the equivalent transfer function of the closed-loop on the right of Figure 3.13, the equivalent loop in Figure 3.14 is obtained.

$$H(s) = E(s) \frac{1}{1 + C(s)(1 - D(s))} \quad (3.8)$$

Solving the inner loop as shown in (3.9), the transfer function v_{LV}/v_{LV}^* is obtained as in (3.10):

$$K(s) = \frac{H(s)}{1 - H(s) \frac{1}{L_L s + R_L}} \quad (3.9)$$

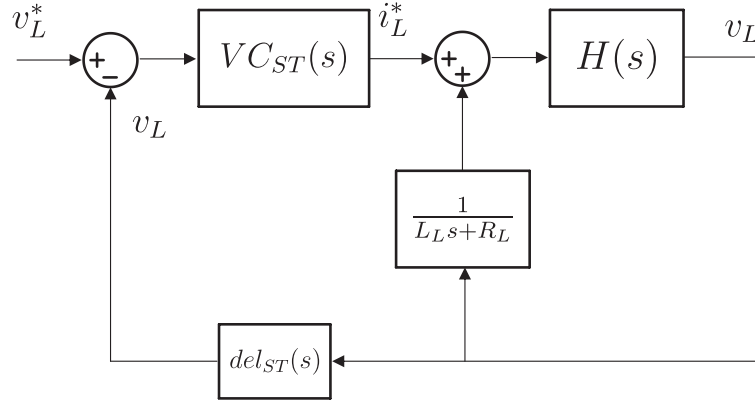


Figure 3.14: Equivalent transfer function scheme of the PHIL setup depicted in Figure 3.7, Step 5.

$$\frac{v_L}{v_L^*} = \frac{VC_{ST}(s)K(s)}{1 + VC_{ST}(s)K(s)del_{ST}(s)} \quad (3.10)$$

The HuT used in the PHIL evaluation is the ST converter described in the microgrid section, and its parameters are listed in Table 5.6. The power amplifier parameters and ST-fed grid data simulated in RSCAD are listed in Table 3.2. A current ratio i_{ratio} between the software and the hardware side is set to 50 initially in order to simulate large grids (hundreds of kW) with a small lab setup (4 kW).

Table 3.2: PHIL power amplifier parameters

Parameter	Value	Parameter	Value
T_c	50 μ s	T_{ST}	100 μ s
L_{PA}	2.4 mH	R_{PA}	0.1 Ω
R_{load}	1 Ω	L_{load}	1 mH
i_{ratio}	50 pu		

As mentioned above, the accurate reproduction of the simulated grid phenomena requires a current controller bandwidth able to reproduce accurately in hardware the current dynamics present in RSCAD. The power amplifier controller bandwidth can be increased, incrementing the value of the proportional controller K_{pPA} . In Figure 3.15, the gain K_{pPA} has been varied from 1 to 19 with steps of 3, in order to show three effects created by the different controller bandwidth: the resonant peak present with low proportional gain (about 700 Hz) decreases, till disappearing with a gain higher than 7; a new resonance peak is present for higher gains at higher frequencies (1100 Hz), but of minor magnitude; and the power amplifier current controller bandwidth increases from 700 Hz in case of low gains, up to 3 kHz with gain $K_{pPA}=19$.

However, high power amplifier bandwidth may lead the system to instability. As shown in

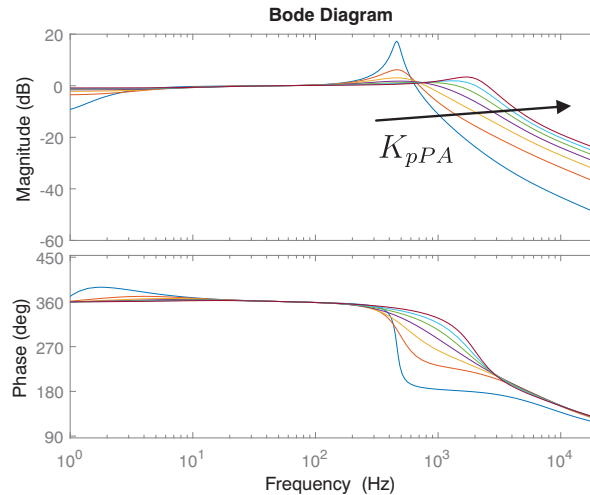


Figure 3.15: Power amplifier current controller and plant closed-loop bode plot.

Figure 3.16a, where the transfer function v_L/v_L^* is plotted, increasing K_{pPA} values, the stability of the system is affected. For a gain higher than 16, the system is not stable, and slightly lower gains (e.g. 13) may lead to high oscillatory behavior in the system. Another point to be noted, is the behavior over the frequency spectrum of the loop transfer function (Figure 3.16b). Increasing the power amplifier controller gain, the response of the system tends to flatten over the frequency spectrum, and the resonance peak at high frequency (around 4 kHz) increases till the point it is not damped anymore (0 dB condition). As aforementioned, the

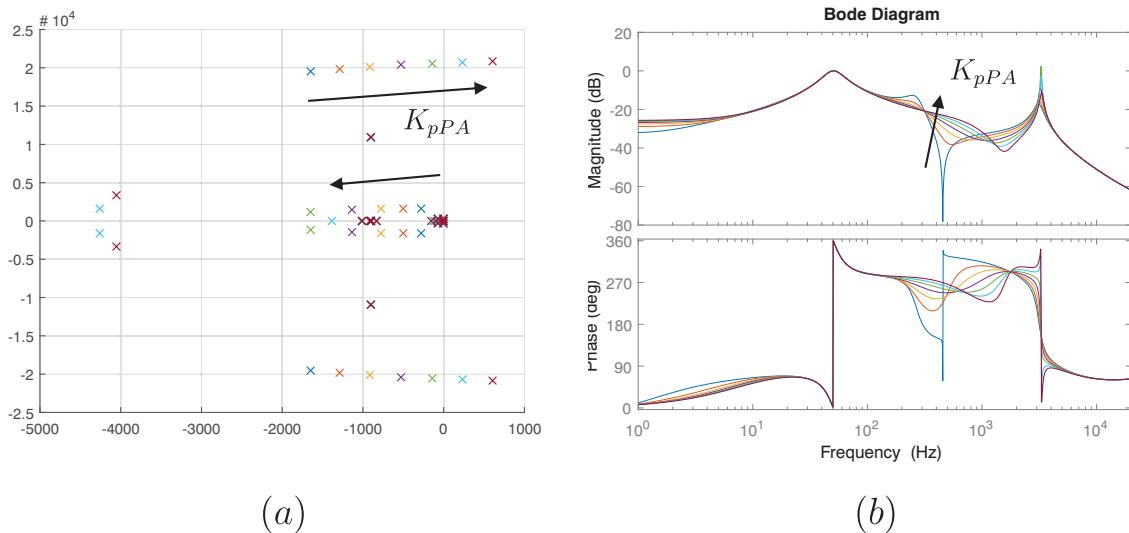


Figure 3.16: Loop stability analysis: (a) Root locus, and (b) closed-loop bode plot of the transfer function v_L/v_L^* .

tuning of the power amplifier controller must be done following a tradeoff between stability of the system and accuracy in reproducing the software phenomena in hardware side. For the ST testing, it is need a power amplifier current controller bandwidth high enough to represent the current dynamics at the fundamental frequency. Thus the current controller tuning must have flat response in amplitude and limited phase shift in the desired range. For these

reason, the tuning parameters listed in Table 3.3 have been chosen.

Table 3.3: Power amplifier current controller parameters

Parameter	K_{pPA}	K_{iPA}	K_{rPA}
Value	10	6	20000

As introduced above, the way to represent the ideal delay with a Padé approximation can play some role in the system stability, mostly at higher frequencies. In Figure 3.17 the poles of the v_L/v_L^* transfer function have been plotted with the parameters chosen in Table 3.3, considering the approximation of the delay with the first three Padé orders (circled in the picture). It can be noted that the influence of the order in representing the delay in the PHIL setup case is negligible and thus the delay can be represented by a simple first-order Padé approximation.

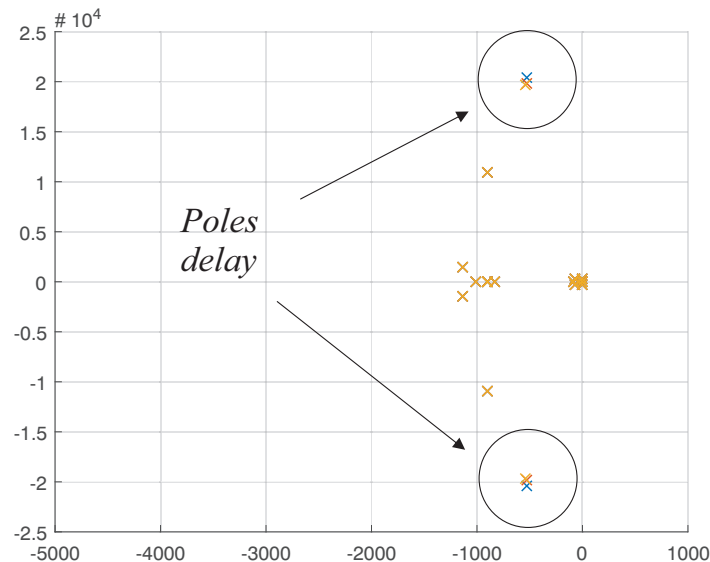


Figure 3.17: Impact of Padé delay approximation in the root locus of the transfer function v_L/v_L^* : first order (blue points), second order (red points), and third order (yellow points).

The PHIL allows to test reduced size hardware's prototype, emulating the effect of the full size hardware in the RSCAD grid by means of scaling factors between the software/hardware current, voltage and power. In the literature, it is always recurring the importance of these scaling factors between the simulated and hardware systems [91, 90, 98, 99]. However, all the previous references concentrate the focus on the voltage-type PHIL applications, and thus on the voltage/current scalability of the HuT. In the ST case, the voltage remains constant, unless a low voltage (e.g., $120 V_{rms}$) experiments must be carried out. Instead the current varies considerably, due to the limited power of the hardware's prototypes. Considering the ST converter present in our lab, the current i_g^* going out from the RTDS and into the power amplifier current controller is scaled down from a factor $i_{ratio}=5$ to $i_{ratio}=100$. It can be noted

in Figure 3.18, the stability of the system decreases with the increasing of the current ratio between software and hardware. This effect has been noticed also in the voltage-type PHIL loops [98]. In the case described, a ratio of 100 keeps still the system stable.

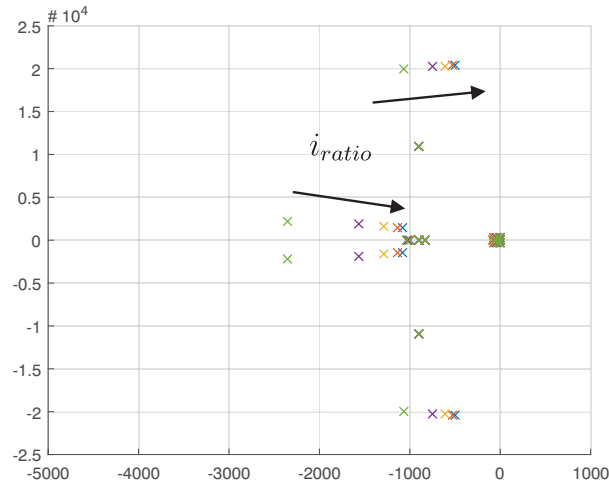


Figure 3.18: Root locus of the PHIL loop considering different current ratio between software and hardware sides.

Disturbance rejection capability

An important aspect to take into account when designing the PHIL evaluation is the rejection of disturbances in the loop. In this section, it has been considered a current disturbance d_1 in the $RTDS(s)$ transfer function. This disturbance represents any perturbation created by the load in the grid implemented in RSCAD. The disturbance is summed up to the measured load current i_{load}^* , that, multiplied by the inverse of the software/hardware current ratio i_{ratio} , gives the current reference for the power amplifier controller i_g^* .

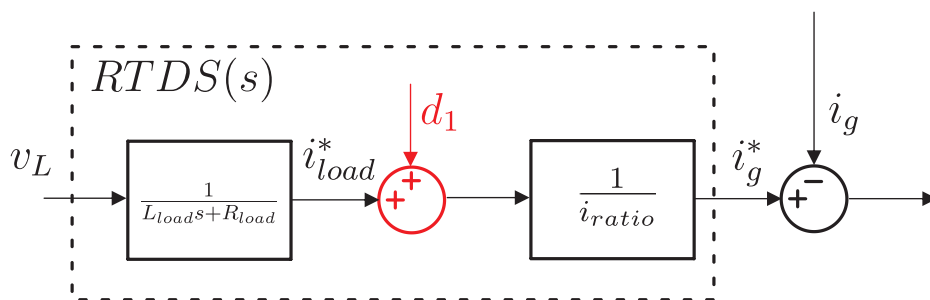


Figure 3.19: Disturbance signal implemented in the $RTDS(s)$ transfer function block shown in Figure 3.8.

To study the disturbance rejection capability of the loop, the superposition of effects has been applied. The input voltage v_L^* is nullified and the disturbance signal is added as shown in red in Figure 3.20.

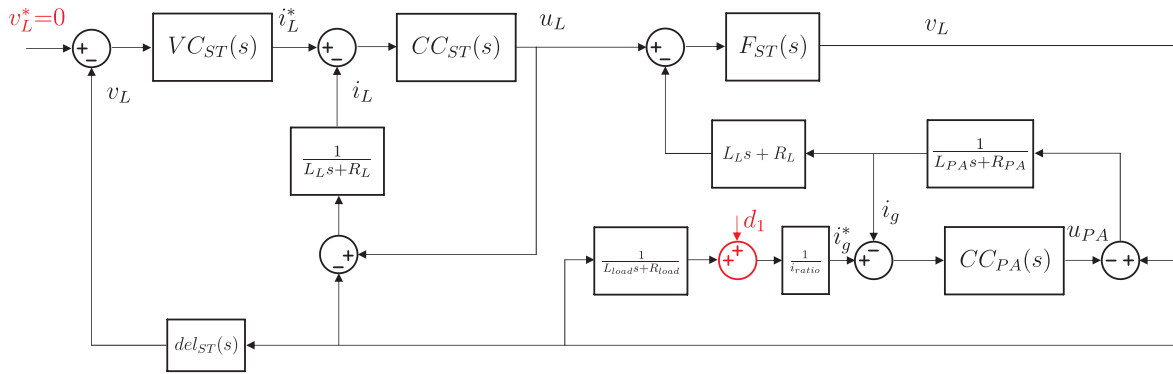


Figure 3.20: Disturbance signal implemented in the PHIL loop shown in Figure 3.8.

As first step the left part of the scheme is simplified as depicted in Figure 3.21. The new transfer function $G_{ST}(s)$ is equal to:

$$G_{ST}(s) = \left(\frac{1}{L_L s + R_L} - VC_{ST}(s) \right) CC_{eq}(s) F_{ST}(s) \quad (3.11)$$

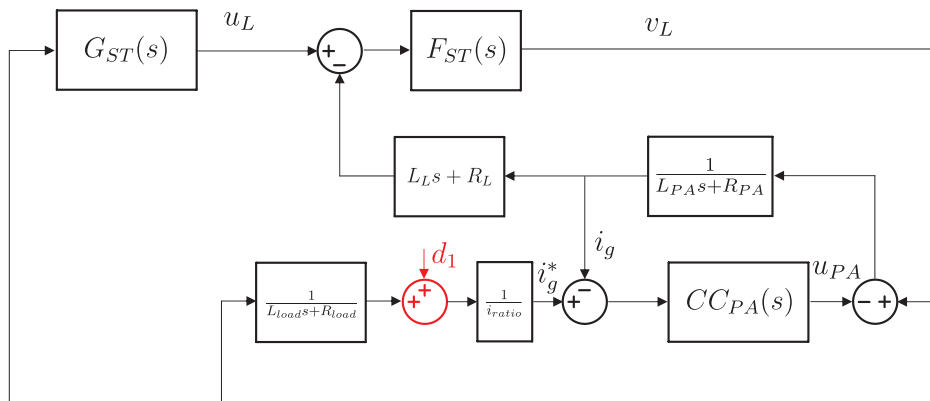


Figure 3.21: Disturbance signal implemented in the PHIL loop shown in Figure 3.8, step 2.

Then, the same procedure followed for the loop stability analysis has been performed, till obtaining the loop shown in Figure 3.22.

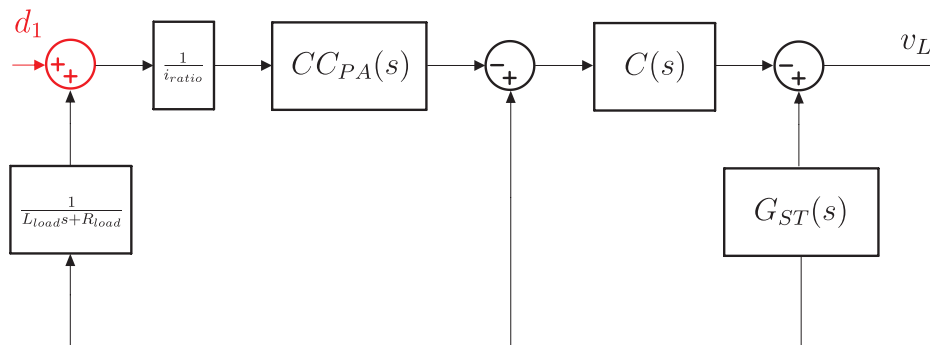


Figure 3.22: Disturbance signal implemented in the PHIL loop shown in Figure 3.8, step 3.

Eventually, the disturbance signal transfer function d_1/v_L can be derived:

$$Q(s) = \frac{1}{G_{ST} - 1}$$

$$S(s) = \frac{Q(s)C(s)}{1 - (Q(s)C(s))} \quad (3.12)$$

$$\frac{d_1}{v_L} = \frac{-CC_{PA}(s) \frac{1}{i_{ratio}} S(s)}{1 + \frac{1}{L_{load}s + R_{load}} CC_{PA}(s) \frac{1}{i_{ratio}} S(s) del_{RTDS}^2}$$

Two parameters have been varied to analyze the disturbance rejection capability of the loop: the power amplifier current controller gain K_{pPA} , and the software/hardware current ratio i_{ratio} . The goal is to see the impact of the disturbance on the ST voltage v_L . The power amplifier gain is varied again from 1 to 19. As seen in Figure 3.23, increasing the proportional gain K_{pPA} , the disturbance rejection capability of the loop decreases, particularly for high frequencies. At values higher than $K_{pPA}=7$ (yellow line in Figure 3.23), some disturbances at RTDS level may be not damped, and higher gains may cause disturbance magnification.

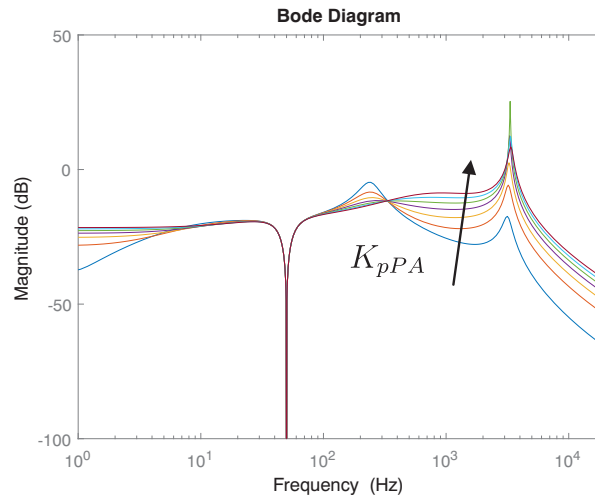


Figure 3.23: Closed-loop bode plot of the transfer function d_1/v_L varying the power amplifier current controller gain K_{pPA} .

Varying the software/hardware current ratio, it can be noticed that higher the ratio is, more the system is able to reject the disturbance. As can be noted in Figure 3.24, an increasing of the current ratio leads to damp the disturbance. On the other side, a low ratio magnifies the disturbance effect on the ST voltage v_L . To demonstrate further the concept, a simulation has been carried out in Figure 3.25 with two different current ratio: (a) $i_{ratio}=5$, and (b) $i_{ratio}=50$. The chosen disturbance signal d_1 has an amplitude of 10 A and a frequency of 950 Hz. It results clear from Figure 3.25 that the disturbance is damped in case of high current ratio (red line), and instead it is magnified in case of low current ratio (blue line). The explanation lies on the PHIL transfer function. Decreasing the current ratio i_{ratio} , the disturbance gain contribution to the current i_g^* increases, thus any disturbance will be magnified with low

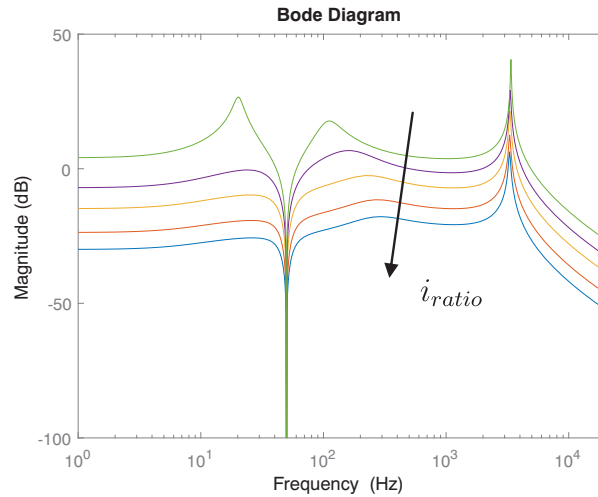


Figure 3.24: Bode plot of the transfer function d_1/v_L varying the software/hardware current ratio i_{ratio} .

current ratio.

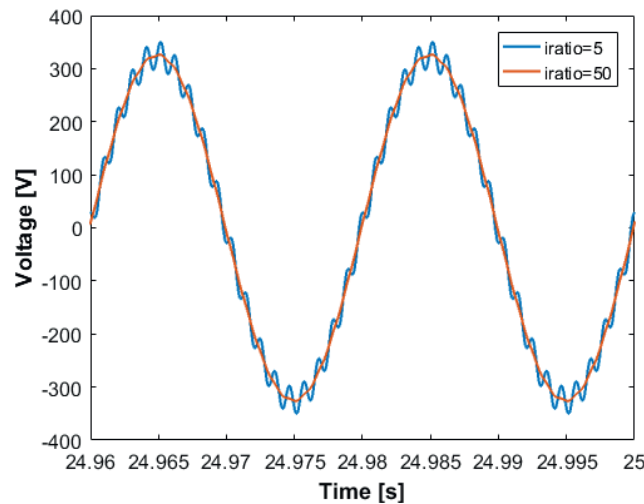


Figure 3.25: Disturbance rejection capability varying the software/hardware current ratio: (a) $i_{ratio}=5$ (blue line), and (b) $i_{ratio}=50$ (red line).

Current-type PHIL applicative example

To fully understand the operations of the current-type PHIL, a ST-fed grid has been implemented in RSCAD and interfaced with the ST-converter described in the microgrid section by means of the linear power amplifier [C2]. The goal is to show with simple examples the interaction between the ST and the simulated grid, that is the ST-fed grid shown in Figure 3.26. In this section, it is shown that the current controller of the power amplifier has been chosen of a bandwidth high enough to reproduce in hardware the power systems dynamics that occur in the simulated grid.

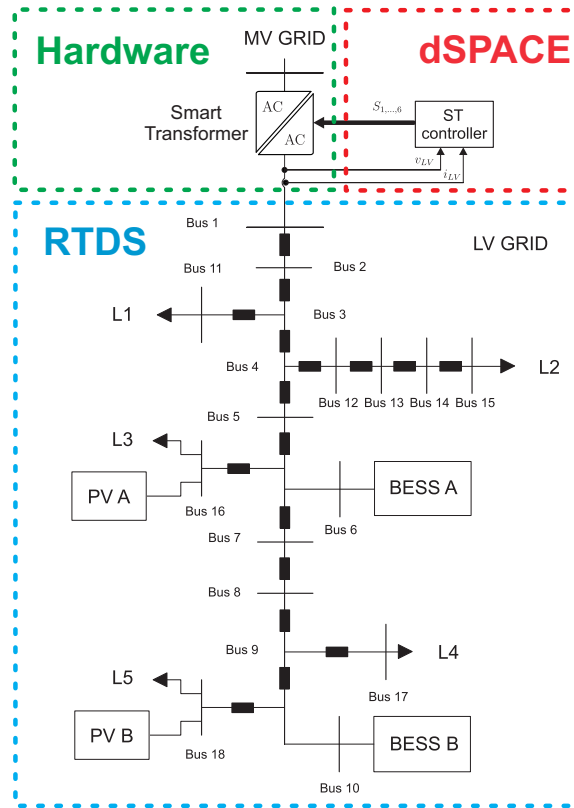


Figure 3.26: modified CIGRE European LV distribution network benchmark implemented in RSCAD.

The grid considered is composed of passive loads, modeled as constant impedance loads. To achieve this modelling in RSCAD two components have been used: the "Coefficient Exponential" and the "Dynamic Load" blocks. The nominal powers of the load are given as input P_0 and Q_0 , in the "Coefficient Exponential" block implemented in RSCAD, that regulates the power output P_{set} and Q_{set} in order to respect the exponential model equations, equal to:

$$P_{set} = P_0 \left(\frac{V}{V_0} \right)^{K_p} \quad (3.13)$$

$$Q_{set} = Q_0 \left(\frac{V}{V_0} \right)^{K_q}$$

where K_p and K_q are set equal to 2 to simulate a constant impedance load. Then the "Dynamic Load" model in RSCAD operates as power-controlled load, just following the power set-point given from the "Coefficient Exponential" model. The loads data for the ST-fed grid are given in Table 6.2.

The DER integrated in the grid in Figure 3.26, that are 2 photovoltaic power plants, and 2 BESSs, have been modeled with the same controller shown for the microgrid setup DER in Figure 3.4. The control has been performed in the dq frame: a PLL gives the angle reference to the dq transformation block, in order to transform current and voltage from the static

Table 3.4: Load Data

Load	Bus	Active Power (kW)	$\cos\phi$
L_1	11	12.4	0.95
L_2	15	38.4	0.95
L_3	16	38.4	0.95
L_4	17	5.4	0.95
L_5	18	17.6	0.95

abc frame to the rotating dq frame. A power controller, as described for the DER-converter in the microgrid setup is implemented. This controller gives the current references to the current controller, which outputs are the control voltages. In the grid side, the DER have been implemented with an average model, composed of a voltage source and a L filter. Thus, there is no need for the creation of PWM signals, but the output of the current controller is directly applied to the voltage source connected with the grid. In this case, a inductive filter equal to $L_{DER}=5$ mH is put in series to the DER equivalent model. The DERs nominal power and position in the grid are listed in Table 6.3.

Table 3.5: DERs Data

DER	Bus	Apparent Power (kVA)	$\cos\phi$
BESS A	6	75	1.00
BESS B	10	25	1.00
PV A	16	4	1.00
PV B	18	3	1.00

The examples to show the interaction between ST and RSCAD-based ST-fed grid are the following: *a)* BESS power variation; and *b)* ST voltage amplitude control. In the first example the impact of a software change (e.g., a power step) on the hardware is shown; instead in the second case the effect of a hardware parameter variation (e.g., reduction of voltage amplitude) is depicted.

BESS power variation

In this section the case of power variation of BESS A from 10 to 50 kW, leaving invariant the reactive power (Figure 3.27b), has been analyzed. The ST active power decreases to compensate the power unbalance in the LV grid, decrementing the provided power from 100 to 55 kW. This variation can be seen also in the hardware side (Figure 3.28). The ST current varies passing from $4 A_{peak}$ to $2.5 A_{peak}$ (Figure 3.28b), while the ST voltage remains constant during the transient and in steady state (Figure 3.28a). The ST active power changes from 2 kW to 1.1 kW, reflecting the power change seen in the software side, scaled down of a factor 50.

The same current profile shown in (Figure 3.28b) can be visualized as RTDS plot in Figure 3.29. The current waveform in red represents the current measured in the RTDS simu-

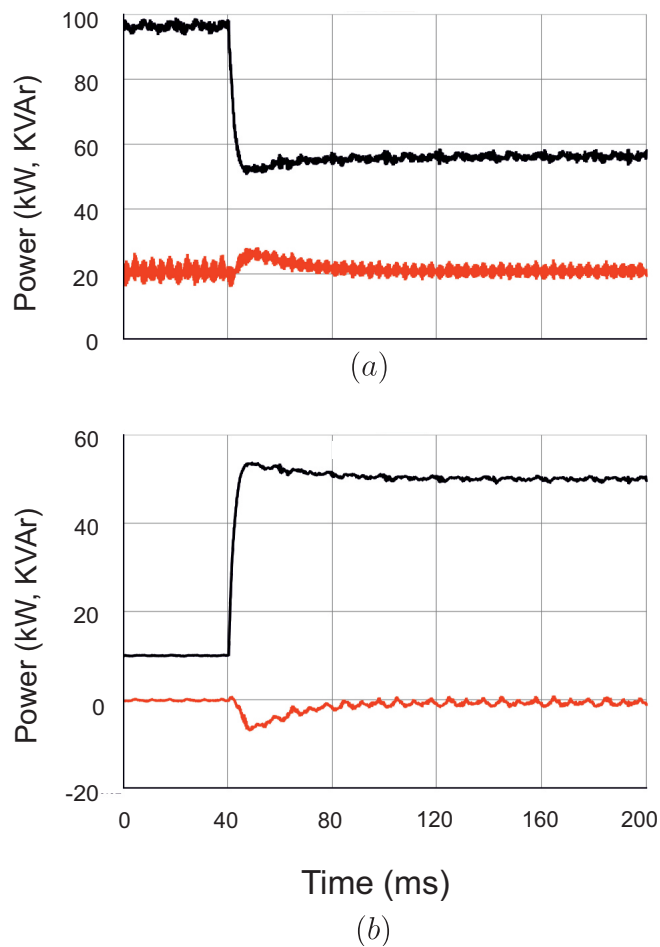


Figure 3.27: RTDS side: (a) ST active (black line) and reactive (red line) power; (b) BESS A active (black line) and reactive (red line) power

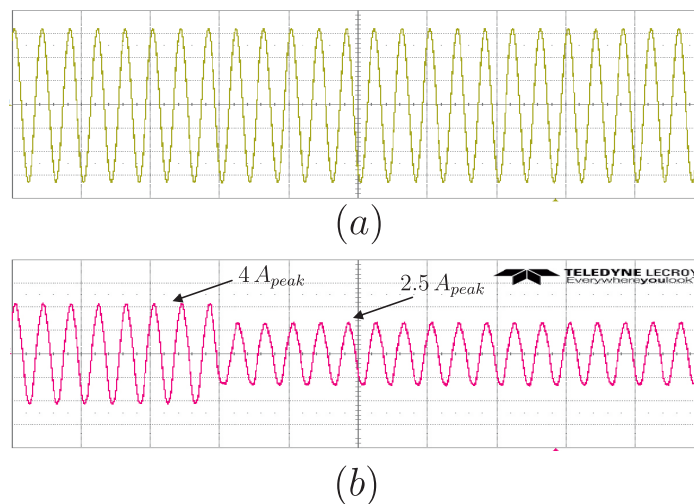


Figure 3.28: Hardware side: (a) ST voltage, and (b) ST current during the power transient

lated grid (scaled down of a factor 50). The black curve is the measured current in the hardware side. As can be noticed, the current controller of the interface can control in hardware the current measured in the RTDS simulation, both in steady-state and during transients.

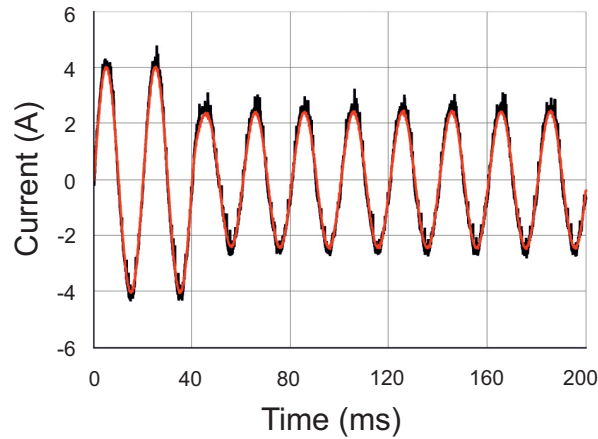


Figure 3.29: ST current: measured current in RTDS (red line, scaled down) and measured current in hardware side (black current).

During the transient the PHIL follows correctly the current change that occurs in the hardware side, as depicted in Figure 3.30. The RTDS current controller is able to reproduce the current behavior also in case of step power variation, like in the battery case. In Figure 3.30, only a small amplitude variation can be seen during the transient (around 1% of relative error). However this small attenuation is compensated after half cycle, restoring in the hardware side the reference current value. This results go in accordance with what seen in the theory. Tuning the parameter as depicted in section 4.1, the PHIL is able to follow the current reference given by the grid in RSCAD and no phase shift is present at 50 Hz. It means that the current controller of the power amplifier has been tuned with a bandwidth high enough to cope with power systems phenomena, that is the main goal of this work.

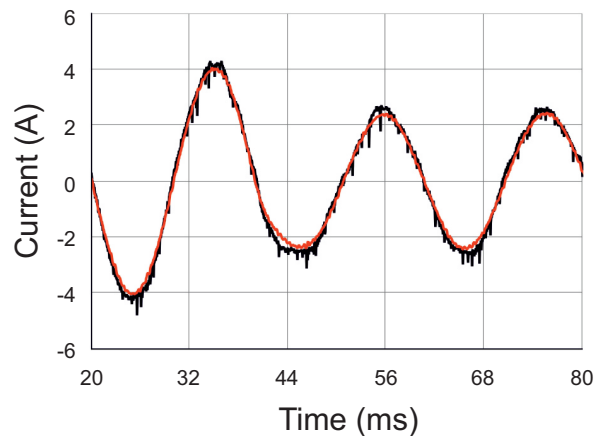


Figure 3.30: ST current, zoomed: measured current in RTDS (red line, scaled down) and measured current in hardware side (black current).

One of the main advantages to perform a PHIL evaluation is the possibility to analyze which impact certain actions have on the grid. In Figure 3.31 the rms voltage profiles have been plotted during the BESS power variation. As can be noted, the voltage profile changes in the grid, due to the battery power re-despatching. The voltage tends to increase in the grid, not uniformly, but depending on the position of the BESS. The buses in green and violet in Figure 3.31, corresponding to Bus 15 and 11 respectively, result to be less influenced by the

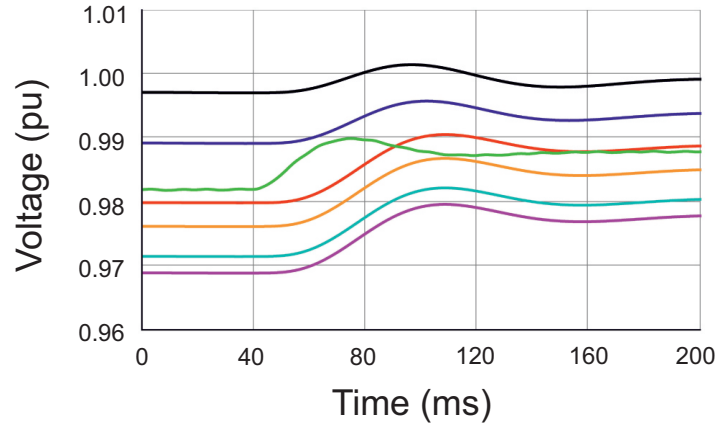


Figure 3.31: Voltage profiles in different grid buses.

battery power step, with respect of all the other buses. This is due to the position of these two buses nearer to the ST than the other buses in the grid. On the other side, the battery power step does not impact on the ST (black line), that keeps the voltage near 1 pu. Thus, the PHIL allows to determine the interaction of certain control actions in the grid with the ST, and to see if they can affect negatively, for example, the ST voltage control.

ST voltage amplitude variation

As second example, the impact of a hardware change on the RTDS simulated grid side is considered. In particular, the ST applies a voltage amplitude variation to the ST-fed grid. This kind of control action has its application in services like the ST overload control [J6] (chapter 5). In this case a voltage decrease from $325 V_{peak}$ to $300 V_{peak}$ has been applied, corresponding to about 8% voltage variation. The impact on the grid can be seen in Figure 3.32. The voltage decreases in not uniform way in the grid, and in several of them (the furthest away from the MV/LV substation) the voltage drop is severe (below 0. pu). On the hardware side, the voltage variation can be seen in Figure 3.33a. The voltage decreases of the requested amount and the ST injected power decreases from 2 kW to 1.75 kW. This specific application is re-proposed in chapter 6, where the ST converter is used for controlling the ST-fed grid to offer services to the transmission grid, such as frequency support.

3.4 Conclusions

The Smart Transformer is a system composed of several components and controllers, that, in a simulation environment, may be difficult to represent with all the dynamics, from electromagnetics to electro-mechanical ones. In this chapter, three possible experimental testing approaches are proposed to overcome the limitations of the pure simulation evaluation: pure hardware evaluation, with a two converter and one load microgrid setup; Control Hardware In Loop evaluation by means of RTDS and an external controller, such as dSPACE; and Power Hardware In Loop, that interfaces a simulated grid in RTDS with external hardware (Smart Transformer), by means of a linear power amplifier.

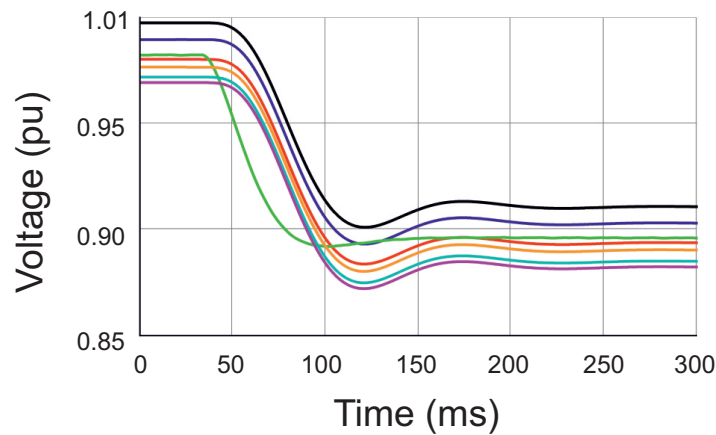


Figure 3.32: Voltage profiles in different grid buses.

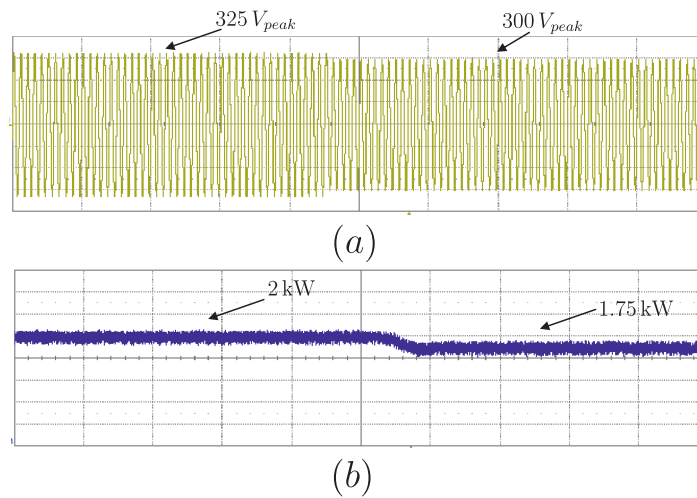


Figure 3.33: Hardware side: (a) ST voltage, (b) ST power during the power transient

Depending on the applications, one solution can be chosen over the others:

- If considering all the ST dynamics has higher priority than representing a large grid, the microgrid setup allows to analyze the ST performances taking in account the real hardware behavior. As example, this solution is employed to test the ST reverse power flow limitation control in this thesis (chapter 5). The microgrid setup has given the possibility to verify the accuracy of the mathematical analysis performed in the theory part, taking in account the non-ideality of components, like the DC link capacitor capacitance tolerance ($\pm 20\%$ of the nominal capacity).
- In case the goal is to verify the effectiveness of the proposed controller in large grids, the CHIL gives the validate the control performances without the need of external hardware. The ST-fed grid is entirely simulated in RTDS (ST included) and only the proposed ST controller is implemented in an external hardware (e.g., dSPACE). Referring as before to the reverse power flow controller, the CHIL validates in chapter 5 its performances and stability, including the effects of the interaction with different components in the ST-fed grid, like P/f droop controllers implemented in more than one DER.

- Eventually, if the evaluation aims to underline the effects of real hardware operations in large grids, the PHIL has the advantages of both microgrid setup and CHIL evaluation. It can interface the ST hardware with the ST-fed grid simulated in RTDS, by means of a current-controlled linear power amplifier. This kind of evaluation has been applied in chapter 6, where the real time frequency support service to transmission grid is described. The PHIL evaluation focuses to verify the dynamic response of the ST voltage controller under variable frequency signal coming from the transmission grid. Although this evaluation has the advantage to test real hardware in realistic grid conditions, its implementation is more complex and stability and accuracy issues can arise. The accuracy, defined as the capacity of the PHIL to reproduce in hardware the current flowing in the RSCAD grid with a certain dynamic, is strongly interlaced with the stability. In the PHIL evaluation setup realized in lab, the current controller bandwidth of the power amplified can be increased up to 700 Hz without affecting the system stability. This bandwidth allows to reproduce accurately slow transients, such as power systems dynamics (e.g., load/generators power changes or ST interaction with loads and generators), or lower harmonic phenomena. For faster transients or higher harmonic analysis, the setup plant must be re-thought in order to increase the current controller bandwidth without affecting the stability.

4 On-line load sensitivity evaluation

In recent years the penetration of DG, mostly based on renewable energy sources (RES), has increased the variability in the power grid [3]. The DG variability can impact adversely the control actions on the grid. For instance, voltage control for stability purposes [101][28], or voltage and frequency regulation [102][103], without a proper understanding of the aggregate load active and reactive power response to voltage and frequency variations, may lead to an incorrect estimate of grid stability [104]. As introduced in [105], this is the case of the demand side management, where shifting a certain category of load (e.g., induction machines and constant impedance loads) in the time affects temporarily the stability, decreasing the system damping during the load shift. Another example is the regulation of load power consumption by controlling the voltage magnitude. It is a relatively low-cost mean for enhancing system stability, that avoids to resort to other, more stringent corrective actions, such as firm load shedding, in case of emergency conditions [101], or for energy-saving purposes. Particular attention in the last years has been given to the Conservation Voltage Reduction (CVR) method, where energy saving can be achieved decreasing the voltage in the grid by means of transformer tap-changer's operations [106][57]. The saved energy in the year can reach more than 2 % in average [106], saving money and decreasing the environmental impact of the energy production (e.g., reduced coal plants energy production). However, this control action may affect the connected customers. It has been evaluated in [107][108] that the impact can be greatly limited if the voltage is constrained in the range of [0.94-1.00] pu, with the number of customers non-compliant with the minimum voltage limit below 1 %. Outside of this range, the affected customer ratio can reach up to 10 %, that is not acceptable in terms of quality of service.

Similarly, in microgrids, or in ST-fed grids, voltage control can be used as a means to modify the power consumption of the local loads, in order to achieve smooth operations [C6][J6], provided again that the load sensitivity is known, at least approximately. On the other hand, load dependency on voltage can vary considerably from bus to bus due to the different nature of each connected load, and even in the same distribution feeder, due to seasonable and time of day variations, different workday or weekend load patterns, etc.

In all the above cases the load sensitivities to voltage variation are assumed known *a priori* and are not evaluated in real time and this can lead to incorrect maneuvers during grid management [109]. To overcome this serious limitation, in this chapter is proposed a method to evaluate the load voltage and frequency sensitivity in real time, thus providing accurate information to system controllers. The method proposed is based on applying an intentional small perturbation in voltage magnitude and frequency and subsequently measuring the load power variation. Since only a small variation is necessary (i.e. about 2 %) the experiment can be repeated as often as deemed necessary, e.g. every hour or every 10 minutes. The OLLI algorithm is implemented receiving the grid voltage and currents measurements and applying in output the desired voltage waveform to the converter voltage and current controller, as shown in Figure 4.1. A three-phase identification is performed, i.e. the load on each phase is

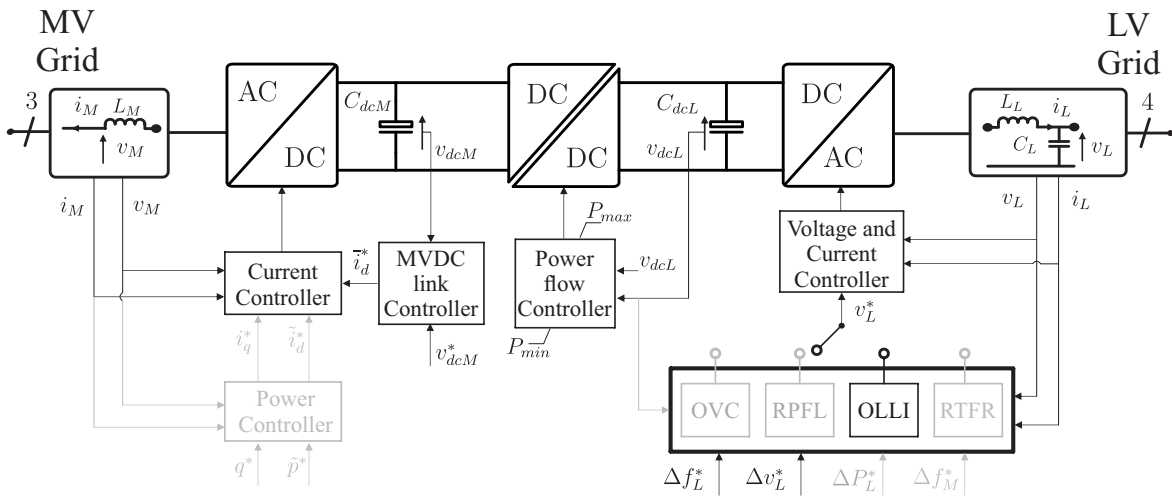


Figure 4.1: Smart transformer basic control and On Line Load Sensitivity Identification controller.

identified separately, so that the differences between phases, which is necessary in LV networks for a correct identification. It should be noted that the measurement method is general and does not depend on the load model simulated. The OLLI algorithm developed can be applied using any intelligent device able to influence the voltage and frequency in the grid, for instance a voltage controlled power electronics converter.

4.1 Representation of voltage and frequency dependency of loads

The load dependence on voltage and frequency has been object of study in the literature for many years [110][111][112]. An interesting survey is performed in [109], where the utilities around the world answered on their load modeled for steady-state and dynamic power system studies. Three interesting outcomes have been found:

1. there is no a common practice worldwide on the load models for dynamic power system studies;
2. only half of utilities measures the load sensitivity parameters;
3. less than 50 % of utilities has updated their parameters in the last 10 years.

The survey concludes that, for steady-state analysis (e.g., power flow), constant power models or constant current for active power and constant impedance for reactive power have been used by the majority of the utilities. A possible reason in the survey authors opinion, can be found in [110], where in absence of correct information about the load composition, constant current for active power and constant impedance for reactive power are suggested. However, looking at Figure 4.2, where the solutions adopted for simulating the load dynamic response to active (Figure 4.2a) and reactive (Figure 4.2b) powers are depicted, no standard industry common practice has been adopted. It can be deduced that the majority of the utility uses standard load models, like exponential and ZIP models, and only few utilities include detailed and customized information for loads (e.g., induction motor simplified models).

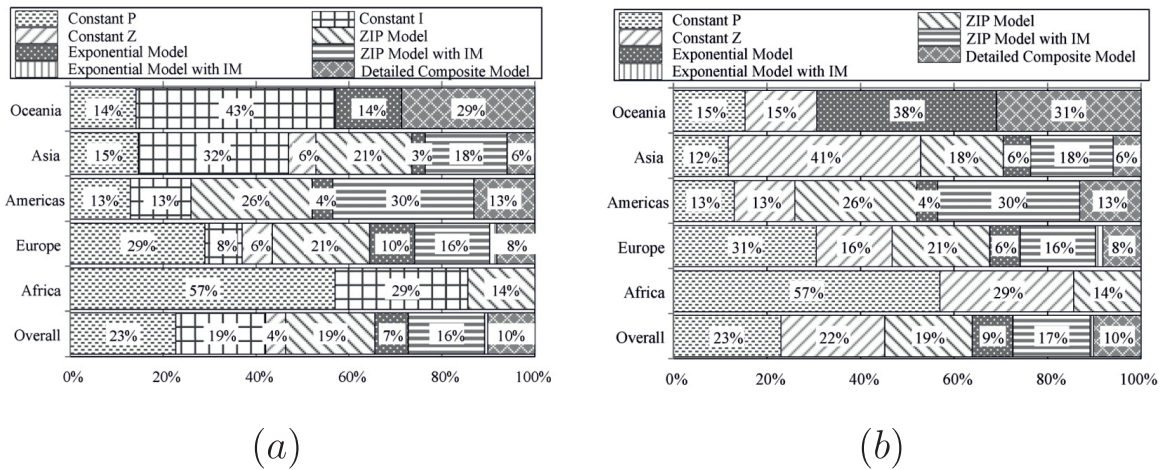


Figure 4.2: Dynamic power system load models used by utilities for *a)* active power, *b)* reactive power [109].

An interesting point is to find out the reason for choosing a certain load model. As shown in Figure 4.3 only 50 % of the utilities use measurement-based methods for computing the sensitivity parameters of the load adopted. It may be noted how almost 40 % of the utilities follow literature recommendations or sampled customized surveys. More important is to notice how frequently the load models are updated. Currently, less than 50 % of the utilities have updated the load models in the last 10 years. The reason may be found in the difficulty on evaluating these parameters on the field. However, this lack of updates may lead to misjudgments of grid behavior due to the increasing integration of renewables in the grid. As underlined later in this chapter, the power injected from the renewables influences the sensitivity parameters of the net load seen from the substation. This may lead to invalid any analysis because the use of old sensitivity parameters (e.g., the one adopted for more than 10 years).

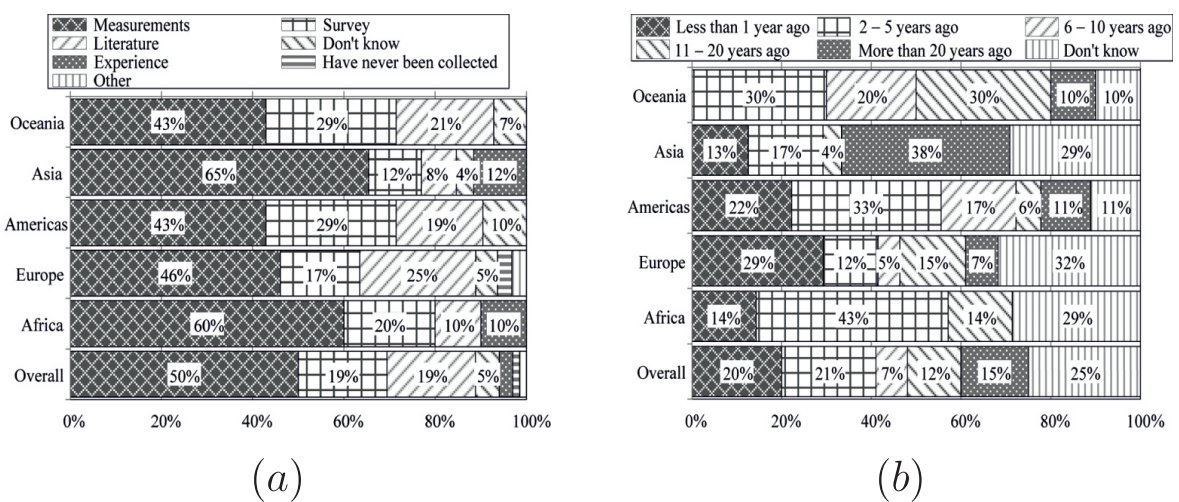


Figure 4.3: *a)* Sources for load modeling used by the utilities, *b)* Last update of the load models for power systems with IM studies by the utilities [109].

Commonly practice in load modeling

To represent correctly the load active and reactive power dependency on voltage and frequency, the literature suggests to adopt models in which the power consumption depends on the measured voltage. Two large categories of models are commonly used: exponential model and ZIP model (constant impedance, constant current, constant power) categories. These models have been employed for representing the dynamic and steady-state behavior of loads in simulation software, and seldom, to apply corrective control actions in the grid. More complex models can be always proposed, taking in account the load dynamics (such as induction machines), or the power restoring capability of the loads [113]. However, these models add more complexity in the analysis and are not suitable for real time approaches. As following a brief explanation of these two models is given, together with the advantages and disadvantages on using a certain model for simulation studies.

- Exponential model

The exponential model is a general model for describing the load active and reactive power dependency on voltage variation with a reduced number of parameter [104]. The expression of this load can be found in the formula (4.1)

$$\begin{aligned} P &= P_0 (V/V_0)^{K_p} \\ Q &= Q_0 (V/V_0)^{K_q} \end{aligned} \quad (4.1)$$

where V is for the rms voltage, V_0 is the reference voltage, K_p , K_q , are the exponential load voltage sensitivity coefficients, and P_0 and Q_0 are the nominal load powers referred to V_0 . The advantage of this modeling approach lies on the simplicity of the model itself, with only two parameters to be identified. On the other side, being described with just two parameters, it can be less accurate when larger power variations are measured.

- ZIP model The ZIP model is an aggregate model that express different responses of load power variation on voltage changes. It can be described with the formula (4.2)

$$\begin{aligned} P/P_0 &= P_1 (V/V_0)^2 + P_2 (V/V_0) + P_3 \\ Q/Q_0 &= Q_1 (V/V_0)^2 + Q_2 (V/V_0) + Q_3 \end{aligned} \quad (4.2)$$

where P/P_0 , Q/Q_0 , and V/V_0 are the normalized active and reactive power consumptions and voltage respectively; P_1 , P_2 , P_3 , Q_1 , Q_2 , Q_3 are the *per-unit* constant impedance, constant current, constant power share of nominal load active and reactive power, assuming that $P_1 + P_2 + P_3 = 1$ and $Q_1 + Q_2 + Q_3 = 1$.

This model can well represent the load voltage sensitivity. However several issues arise when the power dependency to voltage is higher than in the case of constant impedance load [111]. It is the case of the transformer reactive power dependency on

voltage that can reach sensitivity values up to 4 to 7 pu/ pu . By means of ZIP model, it is difficult to model this higher order voltage dependency, and higher order equations must be considered.

Frequency influence on active and reactive load power

The frequency can impact on the load power consumption. However, its load power sensitivity study in literature is quite limited, due the difficulty to obtain accurate evaluation. In methodologies used for load modeling, fields events can be used for obtaining enough data to obtain the active and reactive power response to frequency variation. The problem lies on the number of these events (e.g., frequency oscillations), greatly inferior in numbers than voltage events. Lab validation can be used for achieving these data, although it is difficult to validate in the field due to the elevate variety of appliances installed in the grid. For this reason, no extensive studies have been performed in literature. Currently, a linearized frequency dependency model has been employed in industry and academia as described in [114]:

$$\begin{aligned} P &= P_0(K_{fp}((f - f_0)/f_0)) \\ Q &= Q_0(K_{fq}((f - f_0)/f_0)) \end{aligned} \quad (4.3)$$

where f and f_0 are the measured and nominal frequency respectively, and K_{fp} and K_{fq} are the frequency dependency of active and reactive power respectively.

4.2 Load Sensitivity to voltage and frequency

The load sensitivity to voltage and frequency expresses the variation in power consumption during a voltage amplitude and frequency change in the grid. The load power consumption depends on 4 parameters: voltage amplitude and frequency, time, and initial operating point. The load power consumption can be mathematically generalized as follows:

$$\begin{aligned} P &= P(V, f, t, P_0) \\ Q &= Q(V, f, t, Q_0) \end{aligned} \quad (4.4)$$

where V and f are the *per-unit* values of voltage amplitude and frequency, respectively; t represents the power dependency on the time, due to the capability of certain loads to restore the nominal power consumption after a certain time; P_0 and Q_0 are the amount of the power consumer by the load at a give voltage V_0 , referred as load demand. P_0 and Q_0 clearly depends on the amount and type of connected equipment. For matter of simplicity, the dependency on the time t has been neglected in these studies. Due to the bigger time constants involved in the load power restoring after a certain event, the restoring capability of the loads can be

neglected when small time frames are considered. Let us define the normalized sensitivity for voltage and frequency as:

$$\begin{aligned}\chi &= \frac{dP/P_0}{dV/V_0} & \gamma &= \frac{dP/P_0}{df/f_0} \\ \delta &= \frac{dQ/Q_0}{dV/V_0} & \varepsilon &= \frac{dQ/Q_0}{df/f_0}\end{aligned}\quad (4.5)$$

where the parameters χ , β , δ , and ε indicate the relationship linking the active and reactive power variations to the voltage and frequency variations, respectively. Although these sensitivities depend only on the nature of the load, their mathematical representation depends on the load model adopted.

Exponential model

In this section, the load sensitivity to voltage and frequency, computed analytically for the exponential load model, have been described.

$$\begin{aligned}P &= P_0 (V/V_0)^{K_p} (1 + K_{fp}((f - f_0)/f_0)) \\ Q &= Q_0 (V/V_0)^{K_q} (1 + K_{fq}((f - f_0)/f_0))\end{aligned}\quad (4.6)$$

To compute the sensitivity of the powers with respect to voltage in the point V_0 , the grid frequency is left unchanged to the nominal value f_0 . Then the load power sensitivity to voltage is obtained as:

$$\begin{aligned}\frac{dP}{dV} &= K_p P_0 \left(\frac{V}{V_0}\right)^{K_p-1} \frac{1}{V_0} \\ \frac{dQ}{dV} &= K_q Q_0 \left(\frac{V}{V_0}\right)^{K_q-1} \frac{1}{V_0}\end{aligned}\quad (4.7)$$

Rearranging the equations, evaluating the sensitivity in the point $V=V_0$, we obtain:

$$\begin{aligned}\frac{dP/P_0}{dV/V_0} &= K_p \\ \frac{dQ/Q_0}{dV/V_0} &= K_q\end{aligned}\quad (4.8)$$

In case of exponential load (4.6) the sensitivity is equal to the exponent K_p , while V_0 can be chosen arbitrarily as any voltage V_1 . For the corresponding power P_1 it is easily shown that:

$$\begin{aligned}\frac{P_1}{V_1^{K_p}} &= \frac{P_0}{V_0^{K_p}} \\ \frac{Q_1}{V_1^{K_q}} &= \frac{Q_0}{V_0^{K_q}}\end{aligned}\quad (4.9)$$

Thus the active and reactive power sensitivities to voltage variation can be calculated independently from the i -th operating point:

$$\begin{aligned}\frac{dP/P_i}{dV/V_i} &= K_p \\ \frac{dQ/Q_i}{dV/V_i} &= K_q\end{aligned}\quad (4.10)$$

The sensitivities with respect to frequency are defined in a similar way. Considering the case where the voltage is at the nominal value (i.e., $V = V_0$), so that (4.6) becomes:

$$\begin{aligned}P &= P_0 (1 + K_{fp}((f - f_0))) \\ Q &= Q_0 (1 + K_{fq}((f - f_0)))\end{aligned}\quad (4.11)$$

With respect to the voltage sensitivities case, now the relation between power and frequency is assumed linear. The frequency sensitivity of load power is computed as:

$$\begin{aligned}\frac{dP/P_0}{df} &= K_{fp} \\ \frac{dQ/Q_0}{df} &= K_{fq}\end{aligned}\quad (4.12)$$

Due to linearity, (4.12) can be assumed independent from the operating point P_0 . Thus, the generalized active and reactive power sensitivities to frequency variations can be expressed as:

$$\begin{aligned}\frac{dP/P_i}{df} &= K_{fp} \\ \frac{dQ/Q_i}{df} &= K_{fq}\end{aligned}\quad (4.13)$$

Analyzing (4.10) and (4.13), it can be noticed that the active and reactive power sensitivities to voltage and frequency variation corresponds directly to the exponential model parameters K_p , K_q , K_{fp} , and K_{fq} of the exponential model, and they are independent from the initialization point.

ZIP model

The ZIP model is largely used for load modeling in the industry and academia. Similarly to the exponential model case, the load active and reactive powers sensitivity on voltage can be obtained also in the ZIP model case. Assuming the (4.2), the derivative over the voltage is performed as follows:

$$\begin{aligned}\frac{dP}{dV} \frac{1}{P_0} &= P_1 (V/V_0) + P_2 \\ \frac{dQ}{dV} \frac{1}{Q_0} &= Q_1 (V/V_0) + Q_2\end{aligned}\quad (4.14)$$

If the derivative is evaluated at the operating point $V = V_0$, (4.14) becomes:

$$\begin{aligned}\frac{dP/P_0}{dV} &= P_1 + P_2 \\ \frac{dQ/Q_0}{dV} &= Q_1 + Q_2\end{aligned}\quad (4.15)$$

Remembering that $P_1 + P_2 + P_3 = 1$ and $Q_1 + Q_2 + Q_3 = 1$, the active and reactive power sensitivities to voltage variation depend on 6 parameters, of which only 4 independent. However, the load power share composition cannot be determined *a-priori*, and it depends on the loads connected to the grid. Thus, to solve (4.15), at least one power for each equation must be assumed dependent on the other one in order to solve the system.

Moreover, as shown in [109], each ZIP model can be always transformed to an exponential model by means of linearization. The main advantage is in the number of parameters to be considered (1 instead of 2 for each power equation), and thus in the simplicity to represent the load behavior without losing in accuracy.

4.2.1 Load sensitivity evaluation methodologies

Modeling the load dependency to voltage and frequency variations presents several challenges. Even when the behavior of the single load is well known in the lab, or in simulation, the aggregate load sensitivity to voltage is difficult to be evaluated. Two approaches have been adopted for modeling the aggregate load characteristic: the measurement-based method, and the component-based method [104], [114]- [115]. In the first approach the measurements are taken from the field and the parameters of the loads are estimated by fitting methods [116]. The second approach implies experimental tests of load components and then aggregating them in composite loads [117]. The first approach is largely employed by utilities due to the availability of field measurements [109]. However, the aforementioned methods require a long data history and are computationally demanding. This represents a limitation for on-line control actions due to the high variability of DG, and load composition. On the contrary, the latter one is less exploited, due to the lack of information on the load composition in the grid.

Measured-based approach

Measured-based approach are based on collecting field data from certain grid events and on processing them by means of fittings methods. The steps to perform this methodology are

described in Figure 4.4 [112]:

1. Collect the system data from disturbances of power/voltage changes (timestamp, time-domain voltages and current for each phase).
2. Post-process the data in order to select suited events fitting for the load model parameters estimation.
3. Use a DFT-base signal process algorithm to convert the time-domain signals (voltage and current) in positive-sequence voltage, active power and reactive power signals.
4. Select a proper load structure, such as ZIP model, exponential model, composite model (mix of the previous two models with the additions of differential equations for describing time-dependent parameters).
5. Validation of the derived load model using commercial available software packages, comparing the measured results with the simulated ones.

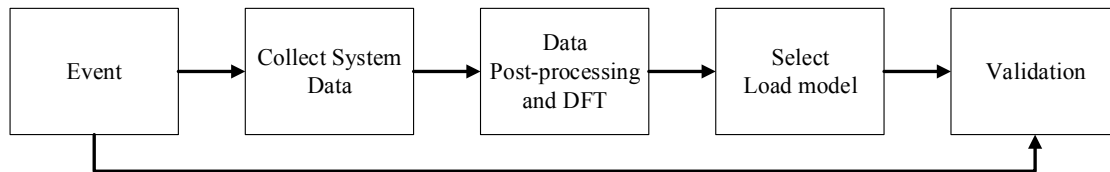


Figure 4.4: Measured-based load modeling approach.

This methodology have been largely employed in academia and industry practice. The advantages of this methods are clear:

- Large availability of data due to the application of this method worldwide. Each operator can provide its own data set to contribute to the common knowledge of load response to voltage or frequency events.
- Existing equipment available on the market for sampling the needed data. Digital Fault Recorder (DFR) or Phase Measurement Units (PMU) are cheap and reliable for recording events.

However, the drawbacks of this method represent the real bottleneck for applying this methodology to grids with highly variable topology and load composition:

- The event should be preferably a three-phase disturbance, and only small unbalances may be accepted (up to 10 %).
- The event must not be an interruption, due to the difficulty of optimization algorithm to handle discontinuities.
- It is not able to identify phenomena like motor stalling or tripping.

- It needs for long data histories of events. Although few cycles are needed for identify an event, several samples of this event must be gathered for obtaining accurate behavior of loads. Several seconds of sampling are suggested for improving the algorithm accuracy.
- Load classes percentages and load component information in the grid are needed. This represent a time-consuming activity due to the variety of events in the grid (e.g., different fault tipologies).
- Some events used for sampling (e.g., voltage sags) can create load disconnection, bringing discontinuities in the load modeling approach.

Component-based approach

The component-based approach is based on the analysis of the load response to voltage and frequency variation in lab, and then on its aggregation in equivalent load in the modeled grid.

The procedure adopted for identifying the load active and reactive power sensitivity to voltage and frequency variation can be summarized as follows [112] (Figure 4.5):

1. Knowledge from lab experiment of the active and reactive power sensitivity to voltage and frequency variation for each load taken in consideration from the analysis. Equivalent mathematical models can be used as well.
2. The load is divided mainly in three classes, residential, commercial, and industrial, and then in sub-classes indicating specific load characteristic (e.g., heating system based on gas or electrical).
3. Set specific condition of the load (e.g., high/low load condition, summer/winter time, geographic collocation).
4. Define a model for each class and sub-class. The aggregation of the devices can be done as equivalent load model.
5. Choice of load sensitivity parameter. Depending on the model adopted for the load representation (e.g., ZIP, exponential, composite), specific parameters must be chosen.
6. Model verification by means of measurements.

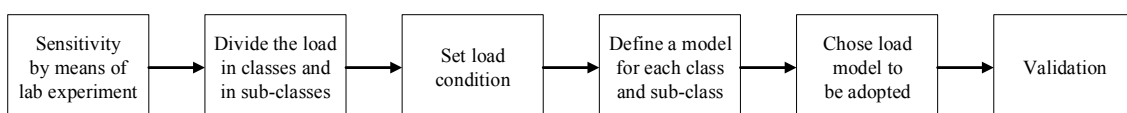


Figure 4.5: Component-based load modeling approach.

Although this methodology increases the accuracy of the single loads representation in power system studies, it has several drawbacks that limit its application in practice:

- The number of load to be considered is large and not practical to accomplish an accurate survey.
- The analysis does not take in account the different age, manufacturer and device's unique characteristics.
- The composition of the load changes continuously in the grid. The distributed generation in the grid impacts also on the sensitivity parameters.

4.3 On-Line Load sensitivity Identification algorithm

The aforementioned methodologies are suitable for modeling loads for steady-state or dynamic studies, however, they lack of capability to provide information on load in real time. During real time controls, the status of the grid is vital for a proper corrective action. These methods, being based on long sampling times (at least several minutes) cannot follow the quick changes in the grid due to the high variability of load consumption / renewables production variations (in the order of tens of seconds).

The on-line load sensitivity identification, is a real time evaluation of the load active and reactive power sensitivity to voltage and frequency variation, obtained by means of a controlled voltage or frequency disturbance in the ST-fed grid. It allows, on the contrary of the previous methodologies, to follow the grid changes and to update in real time the load sensitivity coefficients. Thus it results particular suitable for corrective actions applications, being able to evaluate continuously (e.g., every 5 minutes) the load status. It must be underlined that the identification method is independent on the load model and is based on measurements. The identification does not aim to model the grid equivalent load, but to evaluate in real time the load response to voltage and frequency variations.

The ST varies the voltage in order to obtain a controlled voltage disturbance in the grid. In this study, a trapezoidal profile has been adopted as controlled voltage variation, as shown in Figure 4.6. The ST imposes the voltage variation and measures the change in the grid power consumption, in order to perform mathematically the calculation of the load dependence on voltage. The trapezoidal shape used in this study varies the voltage amplitude of 0.02 pu for 2 seconds, with a voltage decreasing ramp is equal to 0.04 pu/s. The choice of the disturbance characteristics comes from the compromise to limit the impact on the power quality in the grid (deep or long-lasting voltage variations), and to create a voltage variation that cannot be confused with the one caused by the stochastic load switching noise.

The normalized sensitivities $(dP/P_0)/(dV/V_0)$ and $(dQ/Q_0)/(dV/V_0)$ can be discretized in a certain instant t_k , obtaining:

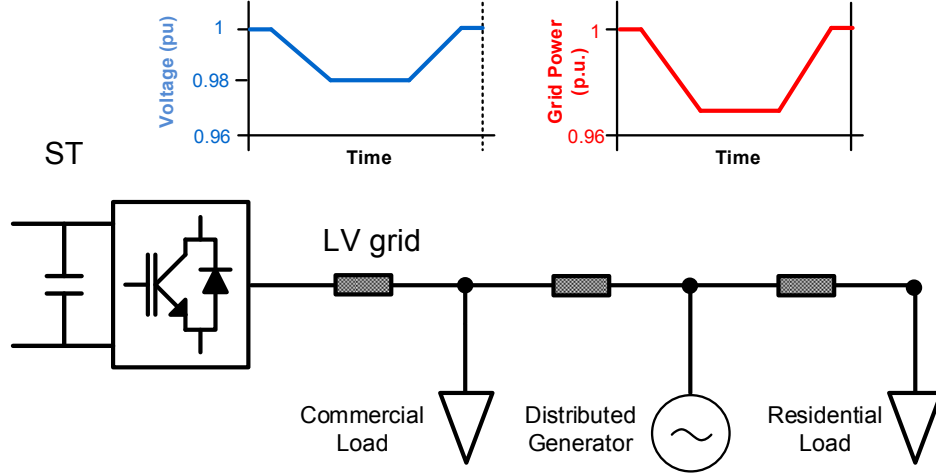


Figure 4.6: On-line load sensitivity to voltage evaluation

$$\frac{\frac{P(t_k) - P(t_{k-1})}{P_i}}{\frac{V(t_k) - V(t_{k-1})}{V_i}} = K_p \quad (4.16)$$

$$\frac{\frac{Q(t_k) - Q(t_{k-1})}{Q_i}}{\frac{V(t_k) - V(t_{k-1})}{V_i}} = K_q$$

The voltage and power values of the time step t_{k-1} can be taken as base values instead of V_i , P_i , and the equations for evaluating the load exponents becomes:

$$\frac{\frac{P(t_k) - P(t_{k-1})}{P(t_{k-1})}}{\frac{V(t_k) - V(t_{k-1})}{V(t_{k-1})}} = K_p \quad (4.17)$$

$$\frac{\frac{Q(t_k) - Q(t_{k-1})}{Q(t_{k-1})}}{\frac{V(t_k) - V(t_{k-1})}{V(t_{k-1})}} = K_q$$

Applying this method, the voltage sensitivity coefficients can be calculated as algebraical equations at any time.

Similarly to the voltage case, the frequency sensitivities can be computed algebraically. A frequency variation is imposed in the ST-fed in order to vary the power consumption in the grid, as shown in Figure 4.7.

Discretizing equations (4.13) at the time t_k , the frequency sensitivity of the active power can

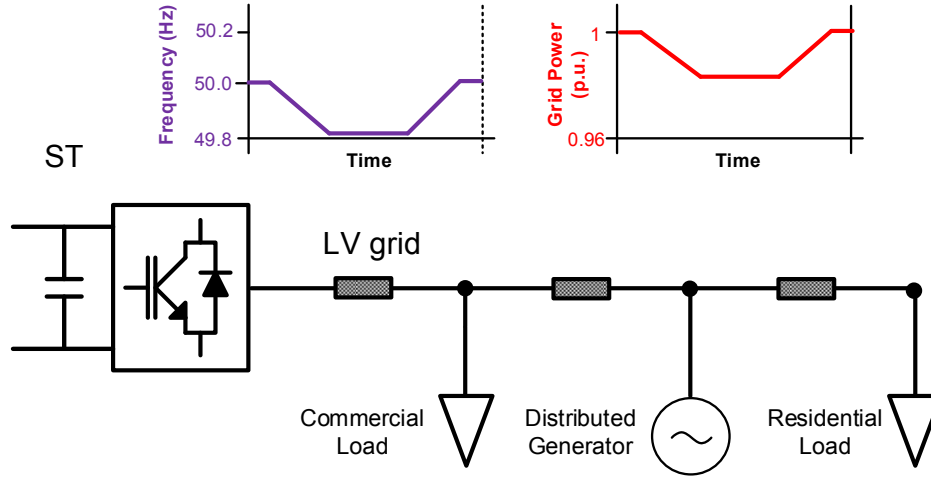


Figure 4.7: On-line load sensitivity to frequency evaluation

be algebraically calculated as follows:

$$\frac{\frac{P(t_k) - P(t_{k-1})}{P(t_{k-1})}}{\frac{f(t_k) - f(t_{k-1})}{f_0}} = K_{fp} \quad (4.18)$$

$$\frac{\frac{Q(t_k) - Q(t_{k-1})}{Q(t_{k-1})}}{\frac{f(t_k) - f(t_{k-1})}{f_0}} = K_{fq}$$

To better explain the load sensitivity evaluation the implementation method is explained in the case of the voltage in Figure 4.8. The On-Line Load sensitivity Identification controller (Figure 4.1) applies a trapezoidal voltage disturbance as described in [J5] for a certain time window (in this case equal to 2 seconds). The OLLI algorithm waits for a time delay t_d (in this case equal to 100 ms), in order to avoid to measure fast transients caused by the initial voltage variation, and it begins to calculate the voltage sensitivity. For the calculation time window t_c , corresponding to the negative and positive voltage slopes, the OLLI algorithm evaluates the K_p and K_q , obtained from the active and reactive powers P , Q , and the *RMS* voltage V measurement. Using the measured values at time t_k and the previous time instant t_{k-1} , the sensitivities at time t_k are computed as in (6.2). For each time step, these values are summed up to the ones obtained in the previous time steps and divided for the total number of the time steps in the calculation time window ($2t_c = 800$ ms in this case). As can be noted in Figure 4.8, the K_p and K_q sensitivity values grow in the time window t_c , while remaining constant in the time windows t_d and t_s . Applying this averaging method, there is no need to store data in memory and the last time step's K_p and K_q values are the active and reactive power sensitivity to voltage of the LV grid. Between the two voltage slopes, the voltage is kept constant for a time window t_s (in this case for 1 second) to avoid abrupt change in the voltage passing from the negative to the positive voltage slope. It is worth to notice that the choice of the waveform, as well as the time windows t_d , t_c and t_s can vary, adapting to the

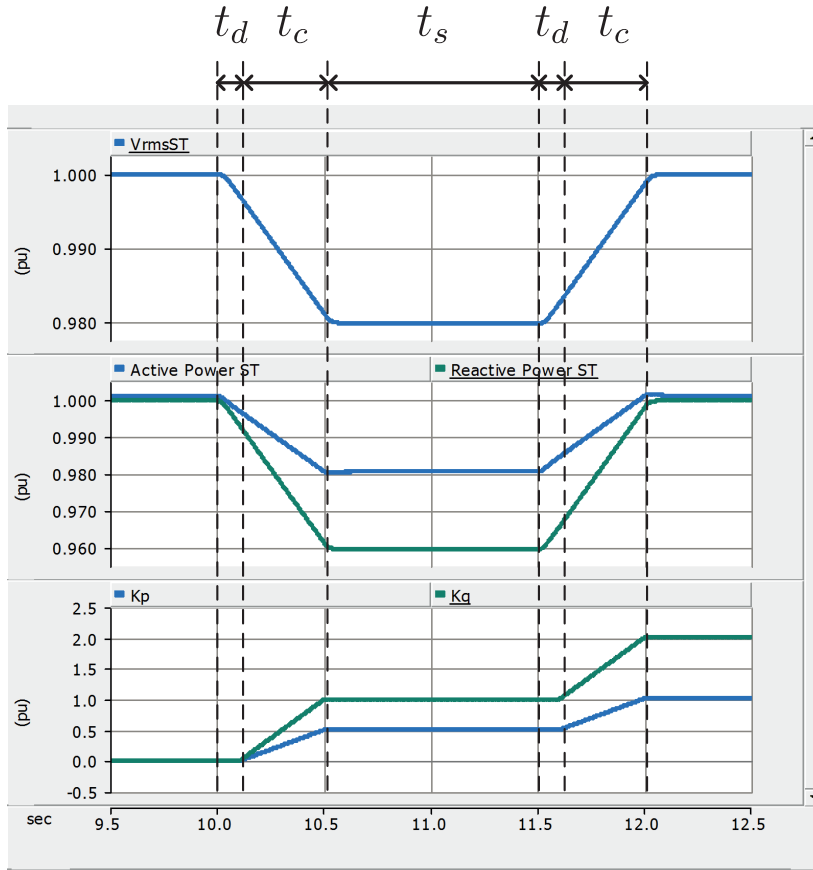


Figure 4.8: Load voltage sensitivity evaluation: time-domain development of the OLLI algorithm.

need of the grid. However, this analysis is omitted in this work, due to the need of real field measurements to tune these parameters. The load sensitivity to frequency can be evaluated using the same procedure, and thus it is not repeated in this work.

4.3.1 Effect of DG power injection in voltage sensitivity values

When a significant DG penetration is present, a marked effect on the sensitivity of the net feeder load is expected. This section is focused on the active power sensitivities, assuming that the DG is operating at unity power factor so that $Q_G = 0$.

Assuming a feeder with connected load P_L and distributed generation $P_g < P_L$ (i.e. the feeder is still providing power) the net load seen by the feeder is:

$$P_0 = P_L - P_g > 0 \quad (4.19)$$

if the load P_L has a normalized voltage sensitivity $K_{p,L}$:

$$K_{p,L} = \frac{\Delta P_L / P_L}{\Delta V / V_0} \quad (4.20)$$

and the active power of the DG is insensitive to voltage (considering negligible its contribution to the losses), i.e. $K_{p,G} = 0$, the net feeder load changes for a voltage disturbance ΔV as follows:

$$\Delta P = \Delta P_L = K_{p,L} (\Delta V/V_0) P_L \quad (4.21)$$

Using (6.2), (4.20) and (4.21) the apparent feeder load sensitivity is given by:

$$K_p = \frac{\Delta P/P_0}{\Delta V/V_0} = K_{p,L} \frac{P_L}{P_L - P_g} \quad (4.22)$$

The net load sensitivity is used in order to estimate the effectiveness of voltage reduction in controlling feeder load (as will be discussed in the next section) and it depends on the (unknown a priori) DG penetration. Clearly (4.22) is meaningless when the DG penetration is close to 100%. It is worth noticing how in grid with great demand variability due to DG fast output power variation, the classical approach for load identification based on long history data or statistical analysis can provide inaccurate info about the grid behavior during voltage changes. Indeed, an analysis performed in a certain time of the day cannot be valid after few hours, due to the stochastic power profile of DG (e.g., photovoltaic, wind turbines).

4.4 Simulation results

The effectiveness of the method has been proved simulating in PSCAD/EMTDCTM the LV grid ($V_{rms} = 230$ V) shown in Figure 4.9, for 20 s with a time-step of $50 \mu s$. A ST has been chosen as MV/LV interface due to the direct voltage and frequency control in LV grid. The single-phase aggregate loads representing the grid are unbalanced and with different active and reactive power dependency from the voltage and frequency values as shown in Table 4.1. In the simulation the voltage coefficients (exponents) are calculated starting from the

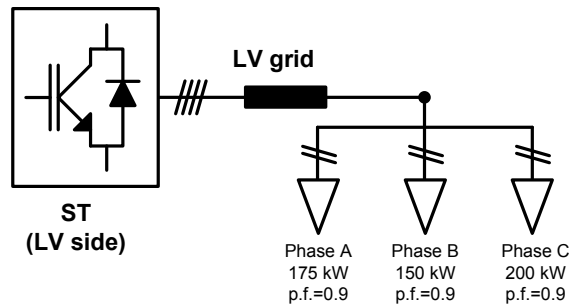


Figure 4.9: Grid simulated in PSCAD/EMTDCTM

10^{th} second, applying a perturbation of -0.01 p.u. simultaneously in all three phases lasting for 1 second, while the frequency coefficients at the 15^{th} second, applying a variation of -0.1 Hz for 3 seconds, as shown in Figure 4.10. Gaussian noises with standard deviation equal to 5 V and 5 A have been added respectively to the voltage and current measurements to simulate measurement noise. During the voltage and frequency ramp variations (0.2 s for the voltage and 0.5 s for the frequency), the coefficients are evaluated each time step

Table 4.1: Comparison between theoretical and calculated values

Phase		K_p	K_q	K_{fp}	K_{fq}
A	Theoretical	0.70	1.20	2.50	1.20
	Calculated	0.78	1.09	2.65	1.44
B	Theoretical	1.40	1.40	5.00	4.00
	Calculated	1.53	1.47	4.63	4.04
C	Theoretical	2.00	3.20	0.00	-2.50
	Calculated	1.95	3.14	0.19	-2.34

and stored in memory. At the end of the time window the final coefficients are computed averaging the stored values, as shown in Table 4.1. As can be noticed, the load is correctly identified with negligible errors, caused by the load time constants, and the noise impact is minimized. Errors can be minimized by increasing the entity of the controlled variable perturbation, but this will have a stronger impact on grid power quality.

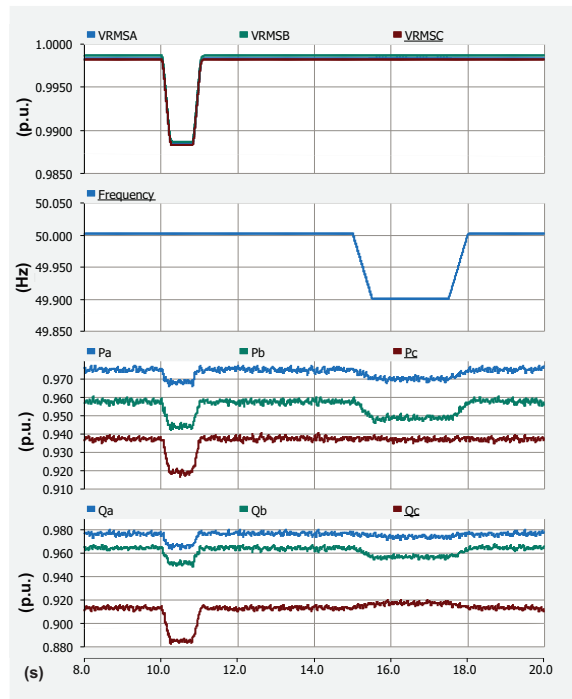


Figure 4.10: (a) single-phase ST rms voltages, (b) grid frequency, (c) single-phase consumed active powers, (d) single-phase consumed reactive powers

4.5 CHIL validation of On-Line Load sensitivity Identification

The experimental verification of ST Load Identification and associated services has been performed with the CHIL method by means of a RTDS system. The ST-fed grid, shown in

Figure 4.11, is implemented in RSCAD, the RTDS software, in order to evaluate the possibility of a real-time implementation with commercial hardware. The ST control scheme described in Figure 4.1 is implemented in dSPACE. The ST topology considered is an IGBT-based NPC converter, due to the availability of the neutral conductor connection in the DC link. The IGBT switches have the rating current of 145 A and maximum voltage equal to 1200 V, and they are implemented as equivalent model in RTDS for real time applications, as described in [118]. The switching frequency of the single IGBT is 5 kHz and Phase Disposition PWM (PD-PWM) technique has been implemented in RTDS in order to balance the DC link capacitors voltage. The modulation signals are sent by dSPACE to RTDS, where the PD-PWM controller creates the new switching signals for the ST LV-side converter. The switching dead-time considered is one time step delay of the small time-step model of RTDS, in this case $1.73 \mu s$. The grid load consist of a balanced constant impedance loads, indicated with Z_L , an induction machine I_{m1} , and unbalanced constant power loads, as described in Figure 4.11 and listed in Table 4.3. In order to add variability to the net load power consumption, a variable active power injection has been considered for the photovoltaic power plants, as shown in Figure 4.12.

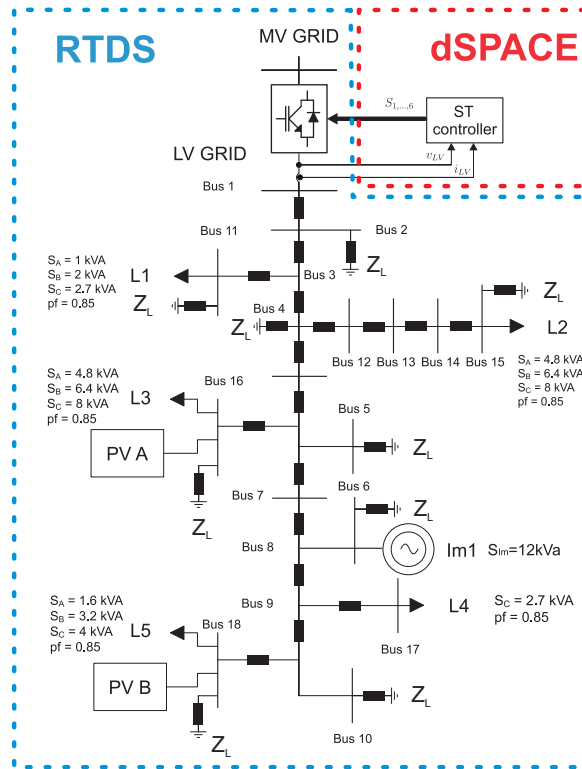


Figure 4.11: ST-fed grid implemented in RSCAD and CHIL description

Table 4.2: Smart Transformer data

ST parameter	Value	Grid Parameter	Value
S_{ST}	100 kVA	V_{rms}	230
C_L	$100 \mu F$	V_{dcL}	800 V
L_L	0.5 mH		

Table 4.3: ST-fed grid data

Load	Variable	Phase A	Phase B	Phase C
L_1	Apparent Power (kVA)	1	2.0	2.7
	Power Factor (pu)	0.85	0.85	0.85
L_2	Apparent Power (kVA)	4.8	6.4	8.0
	Power Factor (pu)	0.85	0.85	0.85
L_3	Apparent Power (kVA)	4.8	6.4	8.0
	Power Factor (pu)	0.85	0.85	0.85
L_4	Apparent Power (kVA)	0	0	2.7
	Power Factor (pu)	1.0	1.0	0.85
L_5	Apparent Power (kVA)	1.6	3.2	4
	Power Factor (pu)	0.85	0.85	0.85
Z_L	Apparent Power (kVA)	0.66	0.66	0.66
	Power Factor (pu)	0.9	0.9	0.9
I_{m1}	Apparent Power (kVA)	4.0	4.0	4.0
	Power Factor (pu)	0.8	0.8	0.8

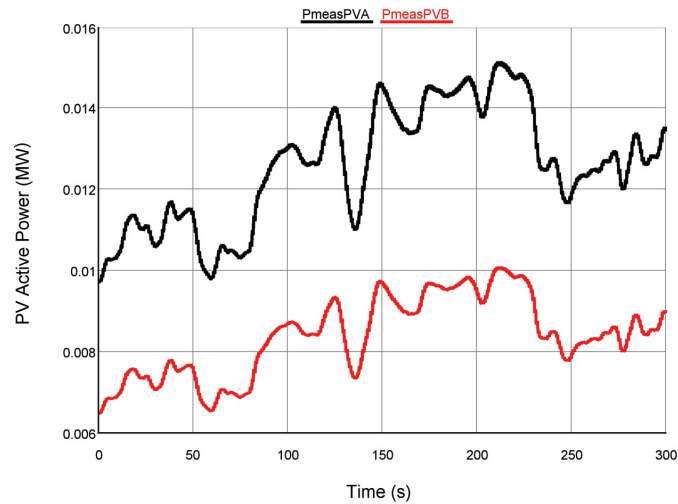


Figure 4.12: PV active power injection: PV A (black line), PV B (red line).

Three test cases have been analyzed: in Test Case A, the grid works in steady state and the Photovoltaic plant A is producing 20 kW with unity power factor. Photovoltaic plant B is shut down. A voltage variation of -0.05 p.u. is applied to measure the real power consumption and compare it with the estimated one calculated with the On-Line Load Identification method. In Test Case B, the conditions are the same as in Test Case A, but with a voltage variation of -0.10 p.u.. In this condition the non-linearity of the load response in case of low voltage conditions is taken in account. In Test Case C, the same conditions of Test Case B are applied with the PV A power production set to 0 and purely passive grid. The test cases are summarized in Table 4.4.

Table 4.4: Accuracy evaluation Test Cases

Test Case	Voltage Variation (p.u.)	PV A power (kW)
A	-0.05	20
B	-0.10	20
C	-0.10	0

In all the three test cases On-Line Load Identification is performed and subsequently the voltage variation is applied (e.g., Figure 4.13, Test Case B). The results for the active and reactive power exponential coefficients are shown in Table 4.5. As expected the active power coefficients tend to decrease in the absence of PV generation. This confirms what demonstrated in theory in Section 3. The reactive power coefficients remain unchanged due to the unity power factor operation of PV A. The accuracy of the On-Line Load Identification can

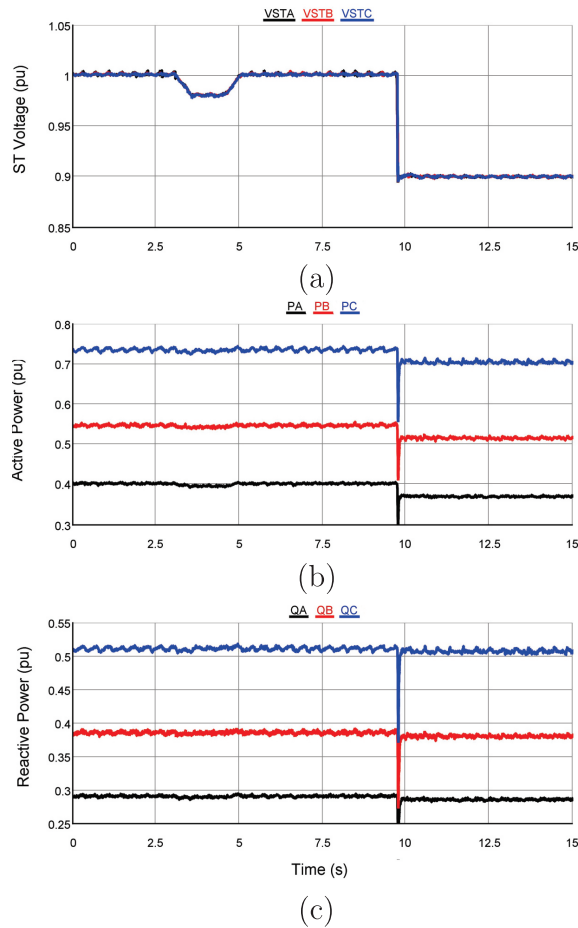


Figure 4.13: On-Line Load Identification accuracy evaluation, Test Case B: (a) ST voltages, (b) ST active powers, (c) ST reactive powers.

be evaluated by means of the comparison between the measured powers after the voltage step and the estimated ones, obtained from the calculated active and reactive power coefficients. The relative errors of the two active and reactive powers are listed in Table 4.6. It can be noted how the relative errors never exceed the 2% in the worst case, and when the voltage change is reduced (i.e., -0.05 p.u.) the relative errors decrease below the 1%. This is explained by the fact that the evaluation of the sensitivities are performed in a point

(0.98 p.u.) nearer to the Test Case A voltage variation point (0.95 p.u.) than the Test Case B and C voltage variation points (0.90 p.u.).

Table 4.5: Coefficients values.

Phase	Parameter	Test Case A	Test Case B	Test Case C
A	K_p	0.77	0.93	0.62
	K_q	0.35	0.34	0.29
B	K_p	0.61	0.70	0.42
	K_q	0.21	0.25	0.21
C	K_p	0.50	0.53	0.31
	K_q	0.07	0.17	0.15

Table 4.6: Relative errors between the expected power and the measured one after the voltage variation (%).

Phase	Power	Test Case A	Test Case B	Test Case C
A	P_A	0.3	1.2	1.6
	Q_A	0.8	1.8	1.7
B	P_B	0.9	0.8	1.0
	Q_B	0.6	1.3	1.4
C	P_C	0.5	1.3	0.2
	Q_C	0.2	1.8	1.0

Impact of DER on active power sensitivity

The impact of generation on the voltage dependence of grid load is further demonstrated in Figure 4.14, where the measured net load voltage sensitivities in the three phases for varying DG (PV) generation are shown. Figure 4.15 shows the effect (measured active power reduction) of a voltage variation of -0.05 pu applied from 100 s up to 200 s. If the active power sensitivities are not accurately evaluated, the expected load reduction following a voltage variation can be wrongly assessed. The blue line shows the actual load reduction using the photovoltaic power profiles shown in Figure 4.12. The black line shows the expected load reduction using the sensitivities found in Test Case C (i.e. neglecting the effect of the DG in net load sensitivity). The red line is the estimated load reduction by the On-Line Load Identification as applied in this paper. It takes into account the DG influence, using the last computed sensitivity before the load reduction, as shown in Figure 4.14. The sensitivity evaluation has been performed in this case every 20 s excluding the time of voltage reduction.

As can be noticed, if the effect of DG is ignored an underestimation of load reduction is expected during the voltage dip (average 2.12 % reduction), which is in line with what was found in Test Case C. On the other hand, when the DG is taken into account in the net load, the expected load variation (average 2.65 %) has a better match to the average of the real load variation (2.83 %) during the voltage step. The difference with respect to the actual

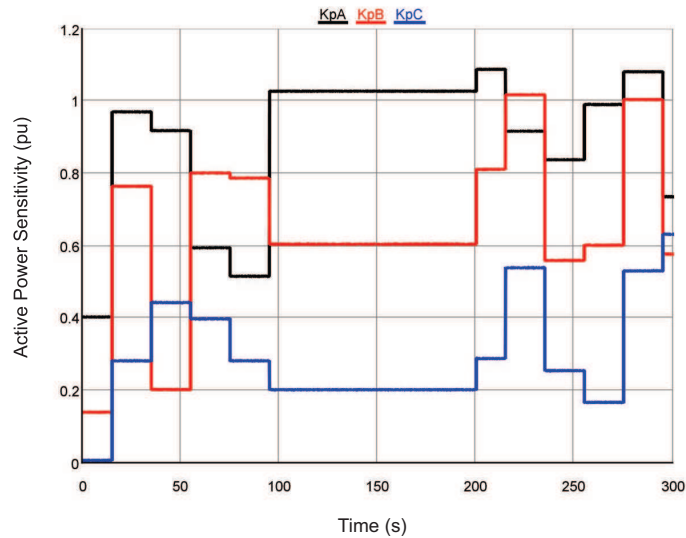


Figure 4.14: Voltage dependence of net active power: sensitivity coefficients in phase A (black line), phase B (red line), and phase C (blue line).

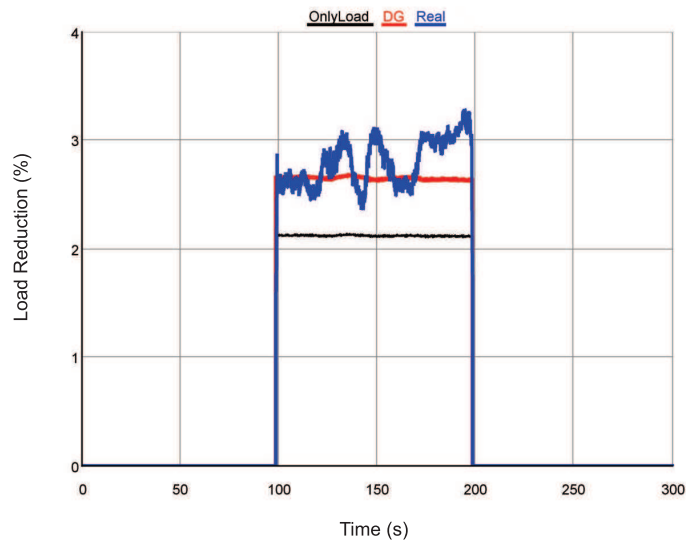


Figure 4.15: Impact of DG on the voltage dependence of active power: *a*) load reduction estimation taking into account only passive load (black line); *b*) load reduction estimation using the On-Line Load sensitivity Identification (red line); *c*) actual load reduction with varying PV injection (blue line).

load reduction is due to the fact that the voltage sensitivities are calculated before the load reduction and they do not change during the transient. The actual active load reduction curve is influenced instead from the variable PV plants power production.

The results obtained in Figure 4.15 confirm the main advantage that the On-Line Load sensitivity Identification has with respect to the approaches based on statistical evaluations or interpolation of long history data. The generators power output tends to change continuously, modifying the net load sensitivity to voltage. Thus, an algorithm able to track these changes and to recognize on-line the real behavior of the aggregate load can improve the effectiveness of control actions in the grid.

4.6 Experimental validation of DER impact on sensitivity evaluation

This section is dedicated to the experimental validation of the DER impact on voltage sensitivity. It has been performed using the microgrid setup described in Chapter 3. The validation is carried out comparing the power measured after a certain voltage variation and the estimated power obtained from the voltage sensitivity coefficients calculated with the on-line load sensitivity identification.

A first test has been carried out considering a passive grid, with the connection of a three-phase resistance of $57,5\ \Omega$ to the ST. The on-line load sensitivity identification has been performed once, resulting in a active power load dependency from voltage variations equal to 1.68 pu. Then, the voltage has been varied within a range [0.9-1.1 pu] and the active power measured, as shown in Figure 4.16 (red line). By means of the calculated load voltage sensitivity, the expected power variation is estimated and plotted in Figure 4.16 (dotted blue line). The relative errors between the measured and the estimated power are displayed on the right axis (blue diamond signs). It can be noted that the power evaluation error in case of voltage variation is limited to 3 % in the considered voltage range, and it increases with the amplitude of the variation. The reason can be found in the linearization done in the on-line load sensitivity identification algorithm, that becomes less accurate moving from the linearized point (i.e., 1 pu).

In order to demonstrate the impact of the DER, the DER-converter in the microgrid setup injects 1 kW active power, under unity power factor. At nominal voltage, the net load consumption (resistance minus DER active power) is equal to 1.6 kW. The on-line load sensitivity identification has been performed again, and the new k_p is obtained equal to 2.68 pu. The voltage has been varied between the range [0.9-1.1 pu] and the measured and calculated power have been plotted in Figure 4.17a, with the red and dashed blue lines respectively. The error of the power evaluation has been plotted as well in Figure 4.17 (blue diamond signs). As it can be noticed, the error is limited to 5 % at the range extremities (0.9 pu), but it remains within 3 % in the range [0.94-1.1 pu]. The higher error is caused by the linearization issue described above, and the fact that the DER tends to sustain the voltage with active power injection. Larger voltage variations are needed for improving the algorithm accuracy in case of low voltage analysis.

If the sensitivity evaluation has not been performed timely and the DER injection varied, the power estimation after a voltage variation may have really large error. If the sensitivity value found in Figure 4.16 is applied, the power variation expected due to a voltage change (dotted magenta line in Figure 4.17b) does not follow the measured power after the voltage change. The achieved error is considerably higher than in the previous case (Figure 4.17b, magenta crosses), and it can reach values up to 17 %.

The results in Figure 4.17b show how a not timely sensitivity evaluation can affect the control action. As demonstrated in the previous section by means of CHIL, control algorithms may under- or over-estimate the impact of a control action on the grid, due to the not update

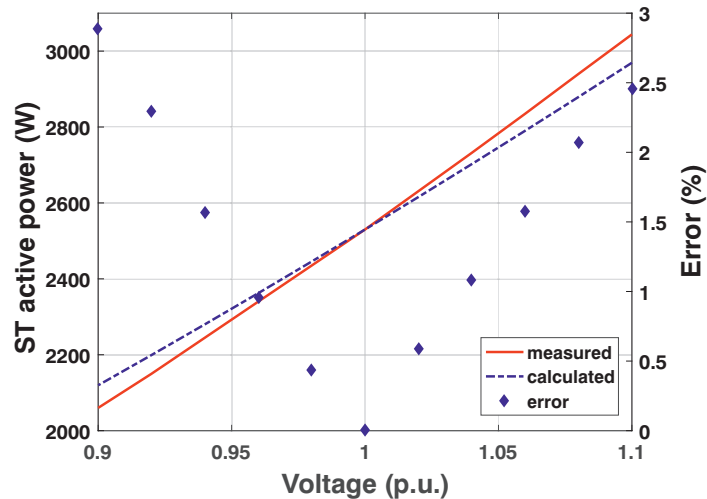


Figure 4.16: Impact of DER on the load active power sensitivity to voltage variation for passive grids: measured power (red line), calculated power (dashed blue line), and relative errors (blue diamond signs).

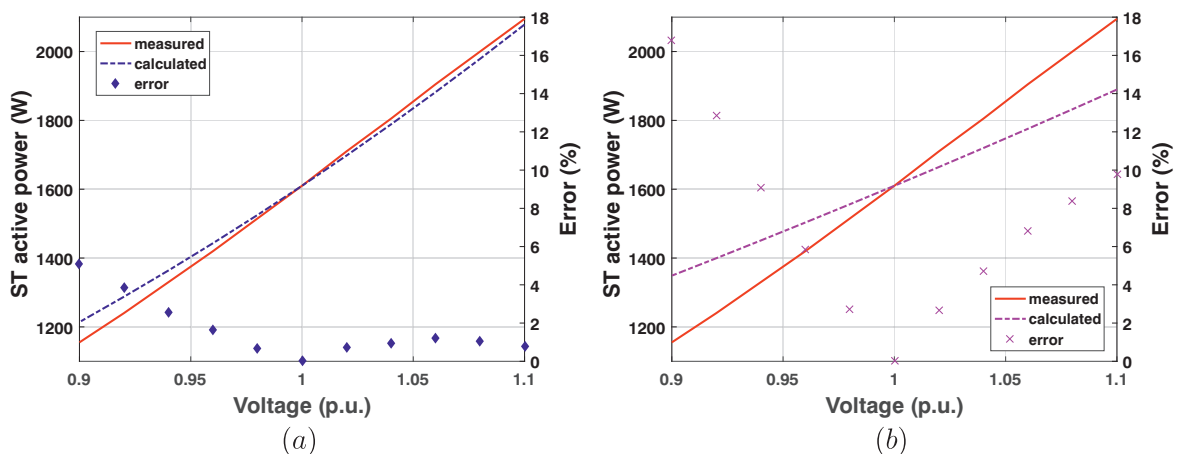


Figure 4.17: Impact of DER on the load active power sensitivity to voltage variation: *a*) applying OLLI algorithm, *b*) applying the passive grid sensitivity.

sensitivity value. This represents the main advantage of the on-line load sensitivity identification with respect to classical approaches: it can be repeated as deemed necessary (e.g., every 5-15 minutes) and follow in real time the power variability of the renewables; on the opposite, the classical approaches need long data histories and complex algorithm evaluation and they are hardly performed in real time.

Influence of Q/V droop controllers on sensitivity evaluation

Resources like photovoltaic power plants or BESS have the possibility to support the voltage regulation in the LV grid by means of reactive power injection. For this purpose, the use of droop controllers is widely adopted in LV grid. However these droop controllers have an impact on the sensitivity evaluation. The reactive power sustains the voltage in the grid, re-

ducing the load sensitivity to voltage variations. To quantify this impact the DER-converter controller in the microgrid setup has been modified, adding a droop control curve. In Figure 4.18, the droop controller gain has been varied and the K_p value computed each time. If the droop value has been set equal to 1, it means that the DER provides 10 % of its ampacity in reactive power during a voltage variation of 10 %. Two different test cases have been considered: (a) same test case of the previous section (resistor of 57,5 Ω and DER injecting 1 kW); (b) DER-converter working with negative power of -0.5 kW (e.g., BESS case).

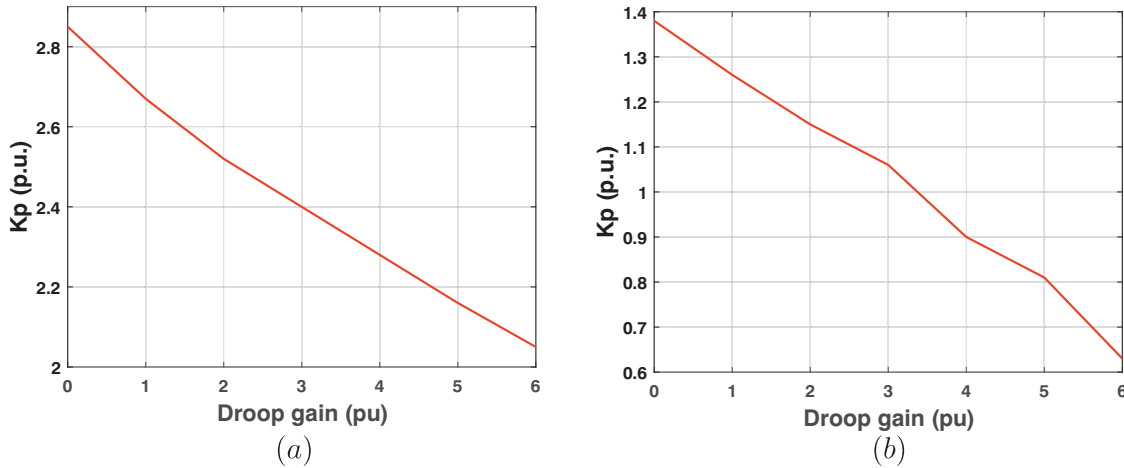


Figure 4.18: Influence of Q/V droop controllers on sensitivity evaluation: (a) DER power injection (+1 kW); (b) DER power injection (-0.5 kW).

The results shown as in both cases the reactive power injection from the DER-converter reduces the K_p value linearly with the controller's droop gain. In case (a) it reduces the sensitivity exponential parameter from 2.8 pu in absence of droop control, to 2.05 pu in case of droop control equal to 6. In the second case, the active power sensitivity exponent is halved from the case of null droop controller gain ($K_p=1.4$ pu), to the case of droop equal to 6 pu ($K_p=0.65$ pu).

Also in the case of droop controller reactive power injection, the OLLI algorithm is able to evaluate correctly the active power load sensitivity to voltage (Figure 4.19). The error remains always below 2 % (blue diamond signs in Figure 4.19) in the whole measurement range, with good estimation of the power curve.

Thus, as already recommended in [108], in case of application of ST load control in ST-fed grids, as it will be seen in the next chapter, the local resources must be coordinated with the ST. The DER supporting the voltage by means of reactive power injection can reduce the ST load shaping capability in the ST-fed grid.

4.6.1 Load sensitivity accuracy in case of ST low power conditions

Being a perturbation-based method, the on-line load sensitivity identification can be affected by measurement noise or stochastic load switch, in case of the power flowing in the ST is near zero. The ST power variation during the sampling window depends, in absolute value, on

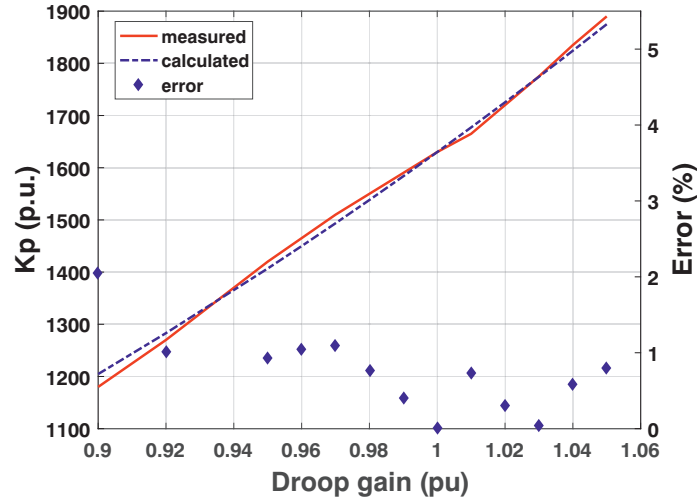


Figure 4.19: Influence of droop controllers on sensitivity evaluation: measured ST power (red curve), and estimated ST power during voltage change (dashed purple curve) on left axis; and relative error (purple diamond signs) on right axis.

the power flowing in the ST. Thus lower is the ST power during the sensitivity identification, higher is the influence of noise on the measurement. This section describes the behavior of the on-line load sensitivity identification during low power conditions of ST. The active and reactive power of the DER-converter has been varied in order to modify the power flowing in the ST. For each power variation, the sensitivities have been re-evaluated and the absolute error between the measured sensitivities and the ones evaluated from the formula (4.22) has been plotted in Figure 4.20. In Figure 4.20a, the ST is injecting active power in the grid, instead, in Figure 4.20b, the power is reversed in the ST DC link. As can be noted, the error tends to increase when the ST power is small in magnitude (i.e., less than 700 W) and misleading results can come from applying control action based on these values. If, on one side, the estimation error tends to increase under the ST low power condition, on the other side, the impact of a wrong control action is limited, due to the low controlled power by the ST. In this case, to compensate the lack of voltage control on the ST-fed grid, further control actions can be taken into account, such as the frequency control of the ST-fed LV grid [J6].

Similar to the active power case, also the load reactive power sensitivities are affected from low power conditions of ST (Figure 4.21). If the reactive power consumption/injection is less than 500 VAR, the K_q error can be high enough to mislead eventual control actions.

4.7 Conclusions

The evaluation of the load power sensitivity to voltage and frequency has been long discussed in the literature. The methodologies applied for the sensitivity evaluation are either measurement-based or component-based. In the first one, the voltage and power measurements are taken during major events in the grid (e.g., faults) or in long time window, and the sensitivity are evaluated by means of fitting methods. In the second case, the sensitivities

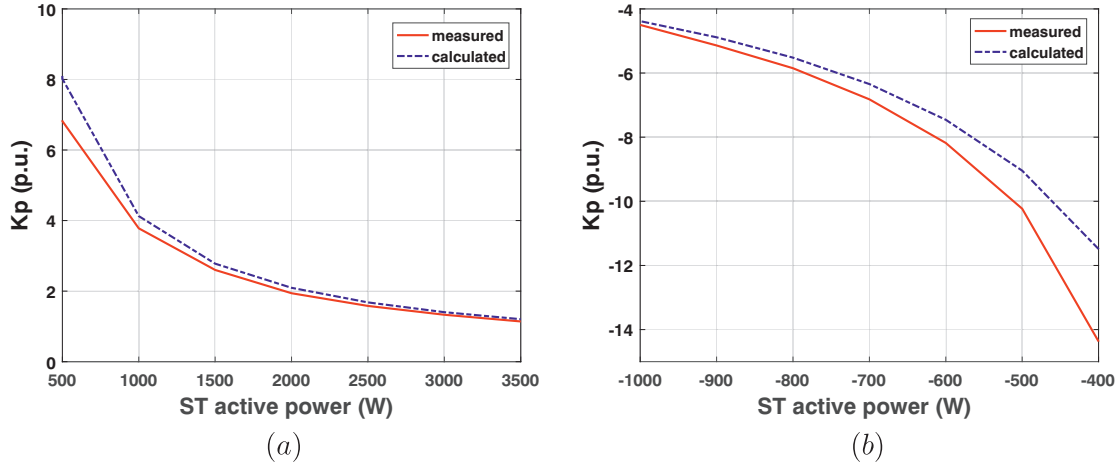


Figure 4.20: Accuracy evaluation of load active power sensitivity to voltage variation in case of ST low power conditions: *a)* positive active power; *b)* negative active power.

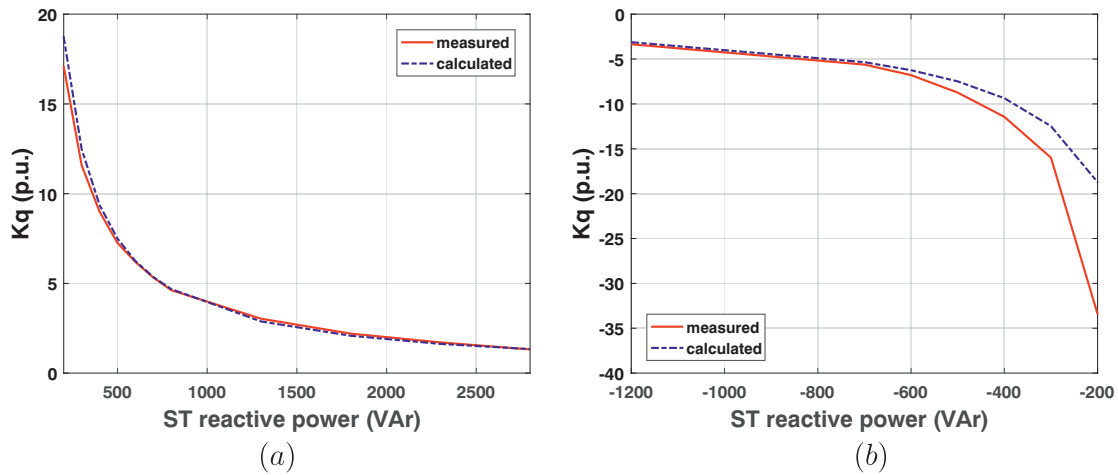


Figure 4.21: Accuracy evaluation of load active power sensitivity to voltage variation in case of ST low power conditions: *a)* inductive reactive power; *b)* capacitive reactive power.

of each load are evaluated in lab, and then an aggregate load model of the grid is assumed. These methods, although largely employed in the current practice, suffer of several drawbacks: they need long data histories measurements, major events in the grid, or assumption on the grid composition. This may represent a problem in the current grid, where the power variability is increased substantially, due to the introduction of renewables and new loads (e.g., electric vehicles). These methodologies cannot provide accurate evaluation of load sensitivities, due to their variability in the time. In this chapter, a On-Line Load sensitivity Identification algorithm is proposed, where the ST is able to influence the voltage and the frequency in the grid and evaluate the load sensitivities. Applying a controlled voltage and frequency variation in the grid, and measuring the power during this variation, the load sensitivity can be calculated algebraically. The OLLI algorithm is able to take in account the contribution of the local resources as well. In particular, it has been shown in this chapter how the active and reactive power injection from the local resources can affect the net load

sensitivity to voltage. In case of active power injection, the voltage sensitivity increases, and the net load power results to be more sensitive to voltage variation. This feature is particularly important in grid with high power variability, where the load sensitivity varies in the time. At this regard, the OLLI algorithm shows clear advantages with respect to the current approaches, that are not able to follow the grid high power variability. On the opposite, supporting the voltage with reactive power injection decreases the net load voltage sensitivity. For this reason, it is suggested a coordination in the service provision between ST and the local resources. As explained in the next chapters, the ST is able to influence the power consumption in the ST-fed grid, thus an uncoordinated interaction with the local resources can lead to reduce the ST power shaping capability.

5 Voltage/frequency control of a ST-fed grid: distribution grid services

The idea to control the load consumption has been widely addressed in literature and applied in the industry practice. It has been considered a valid alternative to classical approaches for balancing the load demand and power generation. The advantages in controlling the load consumption are several [119]:

- Lower variability in the power contribution of a large number of small loads with respect to a small number of large generators.
- Immediate response to operator request, due to the absence of inertia.
- Distributed control available, due to the distributed presence of the load in the grid.
- Reduction of pollutant emission while sustaining the generators during the power ramp up.
- Higher power balancing capability, and thus possibility to integrate more intermittent resources (e.g., renewables).

This flexibility in shaping the load consumption can be employed to control the variability in the grid, and in particular to offer ancillary services difficult to achieve with the current resources without higher expenses (e.g., generators ramp up and down). In [119], the following services have been considered:

- Economic dispatch and unit commitment: the total load consumption is shaped to avoid high peak during the day, and moving the energy consumption in the "off-peak" hours.
- Frequency restoration mechanisms: the load can regulate the frequency, adapting the power consumption on the frequency deviation value. It can be an effective measure against the power imbalances in the grid.
- Contingency reserves: due to the fast response, the loads can be employed to enhance the stability during disturbances (e.g., large generator disconnection). Selective load shedding (e.g., on low priority loads) can help the system to remain stable also during large perturbations.

As emphasize in [119], one of the main issues in the load control is the choice of the input signal. Its selection is not simple to achieve, because the relationship between input signal and power consumed must be known. The input signal can be directly the active and reactive power consumption, however it can only be realized by means of advanced device-level monitoring. Alternatively, functional quantity, such as temperature, lighting intensity, or batteries State Of Charge (SOC), can be used as well. The use of this signal implies the presence of a communication infrastructure, able to receive inputs from the control center, and to send back the device status.

The methodology proposed in [119] considers a direct control of the loads, by means of input signals. However in literature and utilities practice, it has been demonstrated how controlling a certain grid variable, such as frequency and voltage amplitude, the load consumption can be shaped. A method called Conservation Voltage Reduction [106][57] has been applied since 70s in North America proving that decreasing the voltage in the grid (5 %) by means of LTC leads in saving energy during the year (2-3 %). This concept, although reduces the energy consumption over a long time window, it has not been applied to curtail the power demand in the short term. In [120, 108], the project "Customer Load Active System Services - CLASS" shows the possibility to enhance the flexibility of the grid by means of voltage regulation. The idea is to decrease the load demand, if deemed necessary, without interfacing with the customers, but acting directly on the LTC voltage set-points. In this way, a power reserve, to be deployed anytime, can be achieved without the use of energy storage systems. However, how underline in [120], this reserve depends on the load sensitivity on voltage and it varies daily, weekly and seasonally. The typology of loads used in certain hours can be more sensitive to voltage variations (e.g., during the evening due to the lighting systems) or less sensitive (e.g., during the central part of the day, due to the employment of electronics-based devices).

To overcome this limitation, in this chapter a voltage/frequency control of ST-fed grid is proposed. The Smart Transformer, being a three-stage power-electronics based transformer, decouples the AC power flow between the MV and LV grids, offering new control capabilities in the LV grid side: the ST LV-side converter controls the grid voltage waveform independently from the MV grid, and thus the waveforms characteristics (amplitude, phase, frequency) can be varied to provide new services to the distribution grid, as seen in this chapter, and to the transmission grid, as shown in chapter 6. The idea is to interact with the local loads and resources (e.g., generators or DERs) in order to shape their power consumption in the grid by means of voltage and frequency variation. For example, if the load is insensitive to voltage, the ST can act with the frequency for varying the generators power and thus the net load consumption. Or vice-versa, if there is not sufficient generation capability, the net load demand can be varied decreasing the load consumption using the voltage amplitude control. In particular, the control of voltage and frequency in a ST-fed grid has been applied to solve specific problems, such as power flow reversal in MV grid in case of high DG production/low load consumption, and the ST current overload. The provision of these services can be further enhanced if the on-line load sensitivity evaluation algorithm explained in the previous chapter is applied. Knowing beforehand the load sensitivity to voltage and frequency, the control action, such as voltage or frequency variations, can be more effective. Finally in this chapter, the issue of guaranteeing an optimal voltage control during frequency changes has been addressed. The current used controllers are optimized for working at specific frequency (e.g., 50 Hz). Thus here is proposed a voltage Fractional-Order Repetitive Control (FORC), able to work under variable frequency.

5.1 Reverse power flow control in distribution grids

This section addresses the ST feature of the Reverse Power Flow Limitation controller to handle the power flow reversal from LV to MV grids. The basic idea lies on the interaction between ST and the DG in order to limit the power produced in case of low load demand, exploiting regulations allowing a power-frequency derating curve implemented in the DG [121]. This derating characteristic has been originally thought to help the transmission system during frequency large deviations. If the frequency increases due to an imbalance between generation and consumption, or due to a perturbation (e.g., faults, line disconnections, etc.), the DG must reduce its power output. The ST, activating the RPFL controller, acts on the voltage waveform adapting the ST-fed grid frequency (Figure 5.1) in order to control the DG power output in case of reverse power flow conditions, limiting the power reversal in the line.

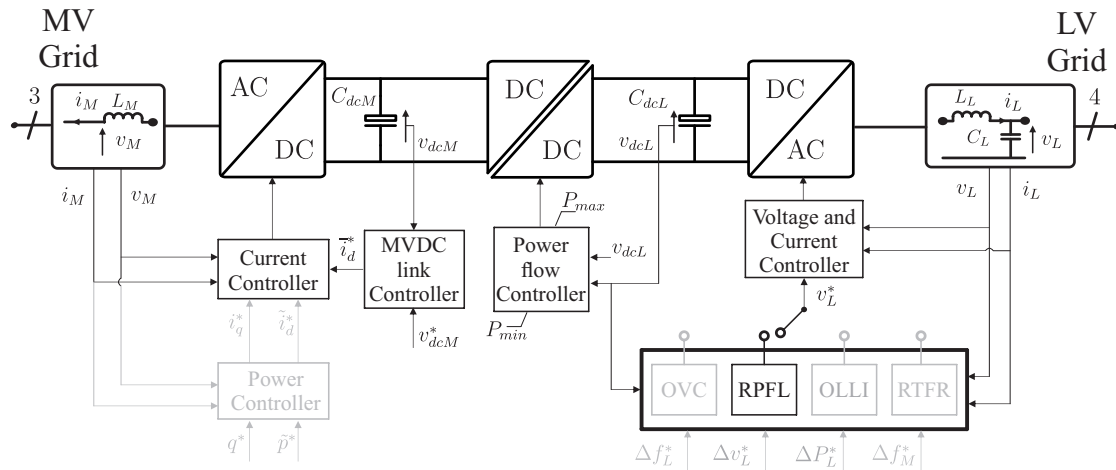


Figure 5.1: Smart Transformer control scheme and proposed Reverse Power Flow Limitation (RPFL) controller.

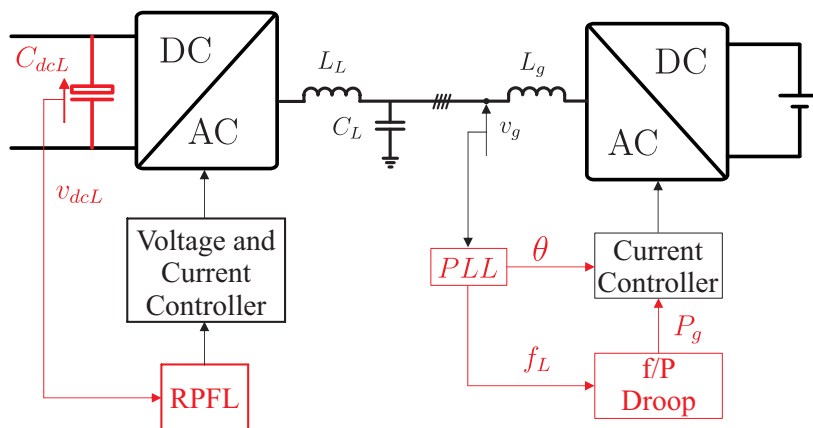


Figure 5.2: Smart Transformer control scheme and proposed controller to avoid the reverse power flow in MV grid (red dotted square).

The application of this approach involves several actors (Figure 5.2, red-marked), that are the PLL bandwidth of the DG inverters and the ST DC-link capacitor. The ST frequency

set-point depends on the LV DC link voltage and varies during DC link voltage fluctuations. During the power flow reversal, the DC/DC converter, here assumed as controllable (e.g., DAB), limits the minimum phase shift in the DC controller to zero. The energy coming from the LV grid cannot be transmitted to the MV side, and the DC link voltage increases. To avoid high DC voltage, the RPFL controller modifies the waveform frequency in accordance with the linear characteristic depicted in Figure 5.3a, to interact with the local generation. In the considered case, the controller increases linearly the frequency from 50 Hz to 51.5 Hz when the DC link voltage goes above 930 V till reaching the maximum allowable voltage of 1100 V. These values are referred to topologies like NPC converters with $600 V_{peak}$ semiconductor devices or two-level converter with $1700 V_{peak}$ semiconductor devices.

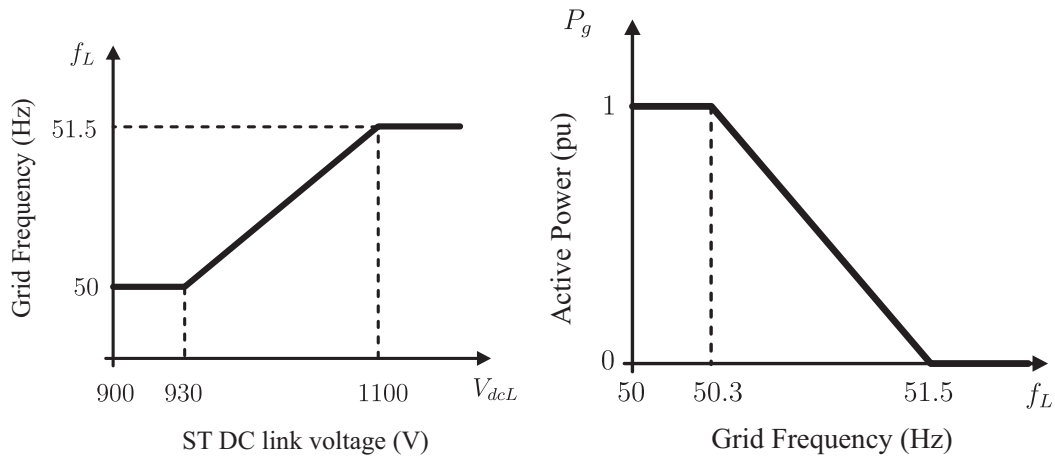


Figure 5.3: (a) ST DC link voltage and grid frequency characteristic curves adopted, (b) derating curve of a grid-connected inverter as a function of the grid frequency.

Following the frequency change, the local generators decrease the power injection in the grid. Recent regulations specify a linear derating characteristic of the power supplied by the converters to the grid as the grid frequency increases. Considering the Italian CEI 0-21 [121], at the maximum operating frequency of 51.5 Hz, the grid-connected equipment must inject no active power into the grid (Figure 5.3b).

The equilibrium is reached when the energy produced by the DG matches the energy consumed by the loads: the DC link voltage is kept to a constant value higher than the nominal one and the reverse power flow is avoided. Only when the DG production naturally reduces (e.g., lower irradiance in the PV plants) or the load consumption increases, the DC link voltage decreases and the reverse power flow controller restores the nominal frequency. However, as it will be demonstrate in the next sections, the PLL of DG plays a role in the stability of the RPFL controller. If the PLL bandwidth is near to the DC-link capacitor dynamic, the RPFL controller can resonate with the PLL angle (and consequently frequency) detection, creating large oscillations in the DG power injection.

Phase Locked Loop (PLL) basic concept

As introduced in the previous section, ST RPFL controller and the DG inverter interacts by means of frequency variation signals. Hence, the DG PLL, called to detect this frequency variation, plays a fundamental role in the controller operations. However, it is demonstrated later in this chapter, that a slow PLL impacts on the system stability. To study this phenomenon, the PLL concept and its mathematical model are introduced in this section. The PLL is a feedback system that tracks the phase of an input signal with zero steady state error [122]. To track the phase angle of a certain signal, the PLL is composed of 3 parts: the phase detector (PD); the Low-pass Filter (LF); and the voltage-controlled oscillator (VCO). The basic PLL scheme is given in Figure 5.4.

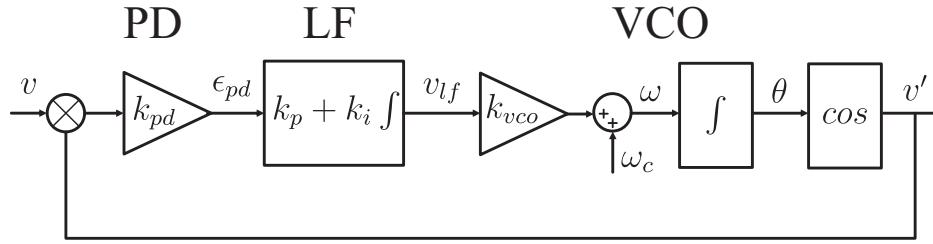


Figure 5.4: PLL basic scheme

Considering the input signal of PLL equal to:

$$v = V \sin(\theta) = V \sin(\omega t + \phi) \quad (5.1)$$

and the signal generated by VCO given by

$$v' = \cos(\theta') = V \cos(\omega' t + \phi') \quad (5.2)$$

the phase error from the multiplier PD is equal to:

$$\begin{aligned} \epsilon_{pd} &= V k_{pd} \sin(\omega t + \phi) \cos(\omega' t + \phi') \\ &= \frac{V k_{pd}}{2} \left[\sin((\omega - \omega')t + (\phi - \phi')) + \sin((\omega + \omega')t + (\phi + \phi')) \right] \end{aligned} \quad (5.3)$$

As first, the high order terms can be neglected, obtaining:

$$\epsilon_{pd} = \frac{V k_{pd}}{2} \sin((\omega - \omega')t + (\phi - \phi')) \quad (5.4)$$

Assuming that the VCO is well tuned, so $\omega \approx \omega'$ and $\phi \approx \phi'$, (5.4) can be linearized:

$$\epsilon_{pd} = \frac{V k_{pd}}{2} (\phi - \phi') \quad (5.5)$$

The averaged frequency of VCO is calculated as:

$$\bar{\omega}' = \omega_c + \Delta\bar{\omega}' \quad (5.6)$$

where ω_c is the angular frequency center of the VCO and it is supplied to the PLL by means of a feed-forward signal.

Thus the small signal variations in the VCO frequency are given by

$$\tilde{\omega}' = k_{vco}\tilde{v}_{lf} \quad (5.7)$$

Eventually, the phase angle variations can be determined integrating the (5.7) as:

$$\tilde{\theta}' = \int \tilde{\omega}' dt = \int k_{vco}\tilde{v}_{lf} dt \quad (5.8)$$

The model described above can be translated in the frequency domain by means of Laplace equations. Considering $k_{pd} = k_{vco} = 1$, the phase detector, the loop filter, and the controlled oscillator can be modeled as follows:

$$E_{pd}(s) = \frac{V}{2} (\Theta(s) - \bar{\Theta}(s)) \quad (5.9)$$

$$V_{lf}(s) = k_p(1 + K_i s) \varepsilon_{pd}(s) \quad (5.10)$$

$$\Theta'(s) = \frac{1}{s} V_{lf}(s) \quad (5.11)$$

By means of (5.9), (5.10), and (5.11), the open loop transfer function of the PLL is obtained

$$G_{PLL,ol}(s) = G_{PD}(s) \cdot G_{LF}(s) \cdot G_{VCO}(s) = \frac{k_p(1 + K_i s)}{s} = \frac{sk_p + k_i}{s^2} \quad (5.12)$$

it suggests that the system is a type 2 system, able to track a ramp signal without steady-state error. Finally the closed-loop transfer function for a basic PLL can be written as:

$$G_{PLL}(s) = \frac{\Theta'(s)}{\Theta(s)} = \frac{LF(s)}{s + LF(s)} = \frac{sk_p + k_i}{s^2 + sk_p + k_i} \quad (5.13)$$

RPFL controller stability analysis

To investigate the stability of the RPFL controller in the ST-fed grid, the system in Fig. 5.5 has been adopted. The ST LV side is supposed connected with n converter-based DG plants. Each converter is equipped with the basic PLL explained in the previous section, that creates the angle reference for a dq -frame current controller to control the DG power injection in the grid. Fig. 5.6 represents the mathematical model of the system described in Fig. 5.5, to study the stability of the RPFL control.

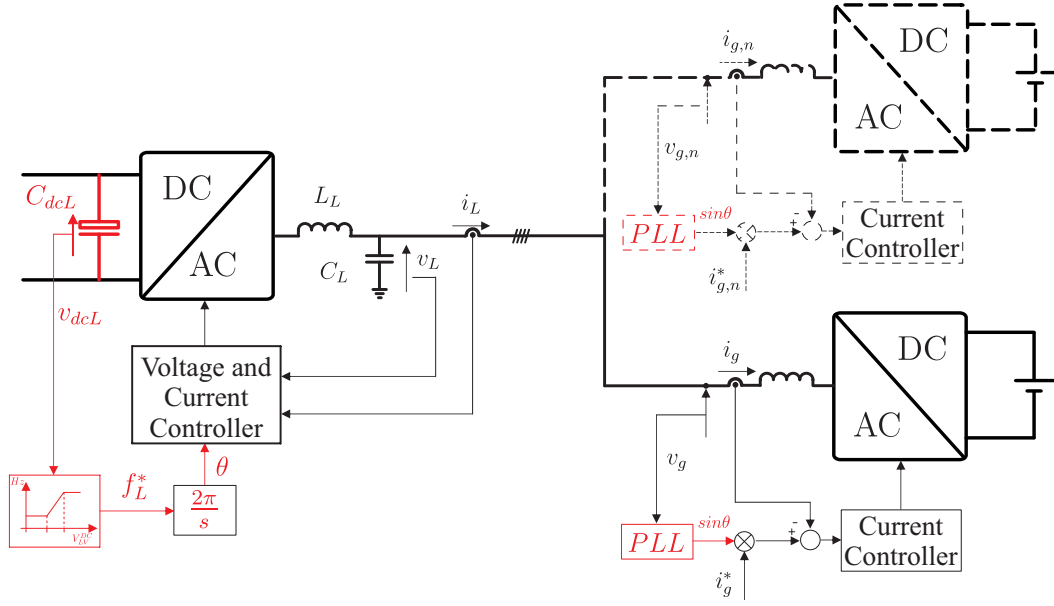


Figure 5.5: Grid adopted for the stability analysis, with the ST interfacing n grid connected generators.

The stability analysis has been carried out considering a small signal analysis (assuming the load constant) of the interaction between ST DC-link voltage and DG current injection. The relationship between the DC current i_{dcL} and the three-phase AC current i_L can be expressed as:

$$i_{dcL}(t) = \frac{3}{2} \frac{v_L(t)i_L(t)}{v_{dcL}(t)} \quad (5.14)$$

Eq. (5.14) is further averaged over the sinusoidal period and the ST-fed grid voltage average value V_{LV} is considered constant. Following, Eq. (5.14) is linearized around the working points I_L and V_{dcL} , representing the average values of the instantaneous values i_L and v_{dcL} over a period, and the obtained second order terms are neglected. Finally, it can be transformed in the Laplace domain as:

$$I_{dcL}(s) = \frac{3}{2} \left(\frac{V_L}{V_{dcL}} \right) I_L(s) \quad (5.15)$$

The DC link voltage depends directly on the current flowing in the DC-link and on the capacitor C_{dcL} size.

$$V_{dcL}(s) = \frac{1}{sC_{dcL}} I_{dcL}(s) \quad (5.16)$$

The frequency/DC-link voltage droop characteristic shown in Figure 5.3 can be represented with a droop coefficient K_f :

$$f_L(s) = K_f V_{dcL}(s) \quad (5.17)$$

As explained in the previous section, the PLL transfer function can be formulated as:

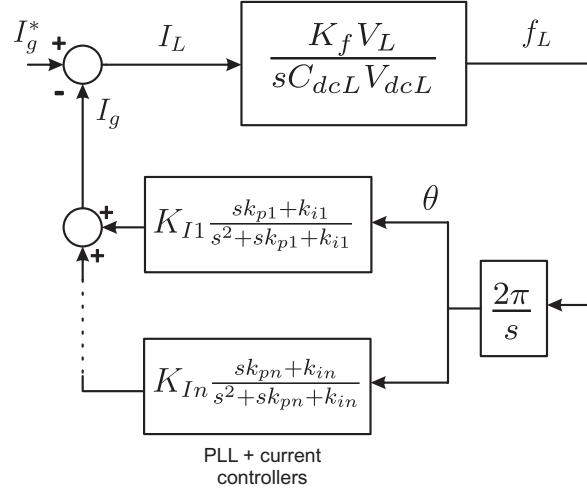


Figure 5.6: Block diagram for the stability analysis.

$$G_{PLL}(s) = \frac{sk_{pn} + k_{in}}{s^2 + sk_{pn} + k_{in}} \frac{2\pi}{s} f_L(s) \quad (5.18)$$

where the constants k_{pn} and k_{in} represent the parameters of the n -th PI regulator of the DG inverter n -th PLL. In fact, for this simplified analysis, it is assumed that the PLL is an ideal feedback system with the grid angle at its output. The integral of the frequency f represents the grid angle θ , that is then processed by the grid connected inverters. This corresponds to the case of a synchronous reference frame PLL in a three-phase system and no voltage imbalance. In real system, Second-Order General Integrator (SOGI) [81] and notch filters can be adopted to limit the effect of the grid non-idealities, while for single-phase systems the delay introduced by the quadrature system generation should be considered. Finally, the equation linking the PLL transfer function with the power/frequency droop curve of the DG, as shown in Figure 5.3b, is given as following:

$$I_{g,h}(s) = K_{I,h} G_{PLL}(s) \quad (5.19)$$

where $K_{I,h}$ is the droop coefficient related to the power of the h -th inverter. Re-arranging all the previous equations, the characteristic equation can be found in (5.20)

$$1 + \frac{2\pi}{s} \frac{K_f V_L}{s C_{dcL} V_{dcL}(s)} \sum_{h=1}^n K_{I,h} \frac{sk_{p,h} + k_{i,h}}{s^2 + sk_{p,h} + k_{i,h}} = 0 \quad (5.20)$$

Influence of PLL tuning on the RPFL controller stability To tune the PLL controller, a target bandwidth (f_{BW}) for the frequency tracking and a settling time for the tracking error, that depends on the target phase margin (Ψ), must be decided. Considering the PLL open-loop transfer function:

$$G_{PLL,ol}(s) = \frac{sk_p + k_i}{s^2} \quad (5.21)$$

The phase of the transfer function in (5.21) is determined by

$$\arctan\left(\frac{k_p f_{BW}}{k_i}\right) - \pi = \varphi_{cf} \quad (5.22)$$

where φ_{cf} is the crossover frequency of the PLL transfer function. Thus the phase Ψ can be expressed as:

$$\tan(\Psi) = \frac{k_p f_{BW}}{k_i} \quad (5.23)$$

The PLL transfer function amplitude at the crossover frequency is given by the formula:

$$\left| \frac{k_p j f_{BW} + k_i}{f_{BW}^2} \right| = 1 \quad (5.24)$$

that, solving the absolute value in (5.24) and substituting (5.23), it becomes:

$$k_p^2 f_{BW}^2 + k_p^2 \frac{f_{BW}^2}{\tan^2(\Psi)} = f_{BW}^4 \quad (5.25)$$

(5.23) and (5.25) can be re-order for the h -th PLL, obtaining the tuning parameter of the PLL PI controller for a given bandwidth f_{BW} and phase margin Ψ :

$$k_{ph} = \frac{f_{BW}}{\sqrt{1 + 1/\tan^2(\Psi)}} \quad (5.26)$$

$$k_{ih} = k_{ph} \frac{f_{BW}}{\tan(\Psi)}$$

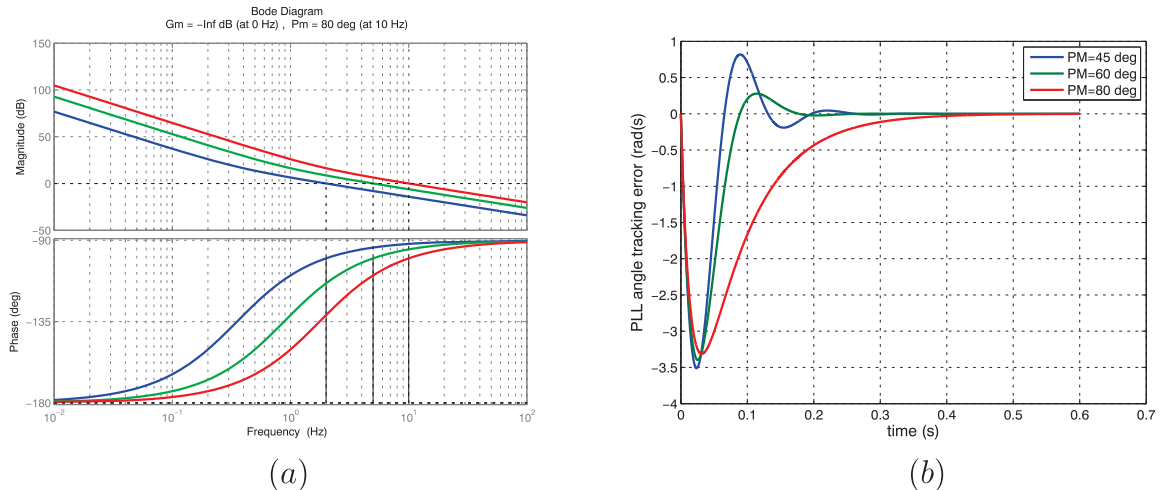


Figure 5.7: (a) Bode diagrams of the PLL, considering a tuning with PM = 80 deg., (b) PLL Tracking error in response to a ramp signal considering different phase margin.

Figure 5.7a shows the open-loop transfer function of the PLL when a phase margin of 80 deg is chosen and different bandwidths. Instead, Figure 5.7b shows the PLL tracking error when different phase margins are chosen. Reducing the phase margin shortens the settling time,

while the frequency tracking is not heavily affected. Since a wide bandwidth and a reduced phase margin imply a higher sensitivity to grid disturbances [123], a conservative tuning is chosen, with $PM=80$ deg, and the effect of the PLL bandwidth on the comprehensive system will be considered.

Control Hardware In Loop evaluation

The RPFL controller can be tested in a real LV grid by means of CHIL, described in Chapter 3. The dSPACE output chosen for this test is a digital signal containing the firing pulses to be applied to the ST switching elements simulated in RTDS.

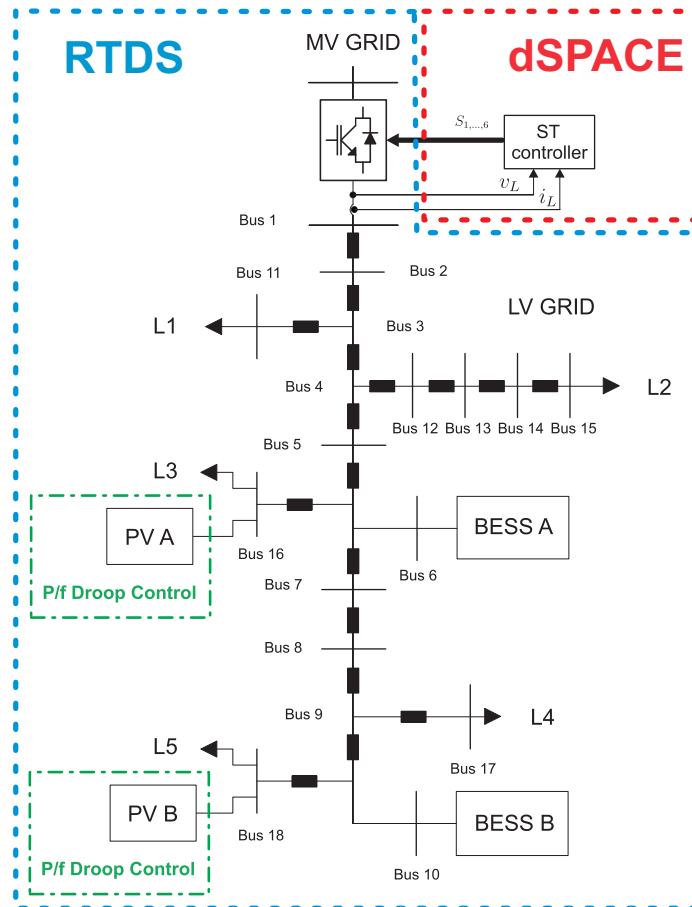


Figure 5.8: CHIL: modified CIGRE European LV distribution network benchmark implemented in RTDS (large-dotted cyan square), ST controller implemented in dSPACE (dotted red square), photovoltaic power plants with frequency droop controller (point-dotted green square).

The grid analyzed is the CIGRE European LV distribution network benchmark [112] (Figure 5.8). The following assumptions have been made due to the limited computation capability of the RTDS system without losing in generality in the proposed methodology: 1) the loads are assumed balanced and modeled as constant impedance; 2) the two BESS active and reactive power set points are set to 0; 3) the wind turbine has been removed. The load and ST data are listed in Table 5.1.

Table 5.1: Load and ST Data

Load	Bus	Apparent Power (kVA)	$\cos\phi$	ST Parameter	Value
L1	11	11.4	0.85	f_{sw}	2 kHz
L2	15	39.4	0.85	V_{dcL}	900 V
L3	16	39.4	0.85	C_{dcL}	10 mF
L4	17	5.4	0.85	L_L	1.7 mH
L5	18	17.6	0.85	C_L	100 μ F

The stability analysis has been performed following the system characteristic equation (5.20) and the ST data listed in Table 5.1. The root locus is then plotted considering a bandwidth varying for 1 Hz to 20 Hz and a single converter-based DG (Figure 5.9). This approach does not imply a loss of generality, since the slowest converter determines the stability behavior of the system.

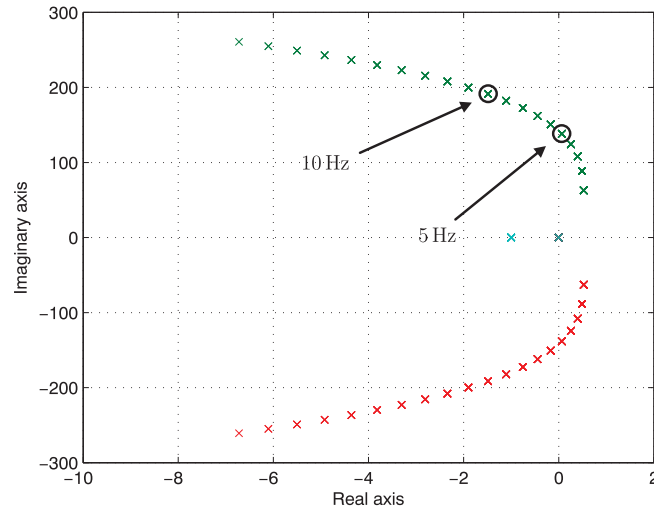


Figure 5.9: Root locus with variable PLL bandwidth.

As can be seen, a narrow bandwidth of the PLL (small gain) leads to instability conditions. A bandwidth of 5 Hz makes the control system unstable, instead a PLL with a 10 Hz bandwidth performs the control action in stable conditions. Nevertheless, as the grid synchronization is a key feature for grid-connected inverters, it is reasonable to expect that the bandwidth of the PLL be sufficiently broad to make the entire system stable.

Considering the stability analysis outcomes, two test cases have been considered: Test Case A with the PLL bandwidth equal to 10 Hz; and Test Case B with the PLL bandwidth reduced to 5 Hz. The stability analysis of these two cases are marked in Figure 5.9. The analysis has been performed in a time window of 300 s where a variable PV power profile has been given to the photovoltaic power plant PV A and PV B (black lines in Figure 5.10(c₁) and (d₁)). In the case of a power production of the PV plants that exceeds the power absorbed by the loads, the DC link voltage increases due to the saturation of the DC/DC converter.

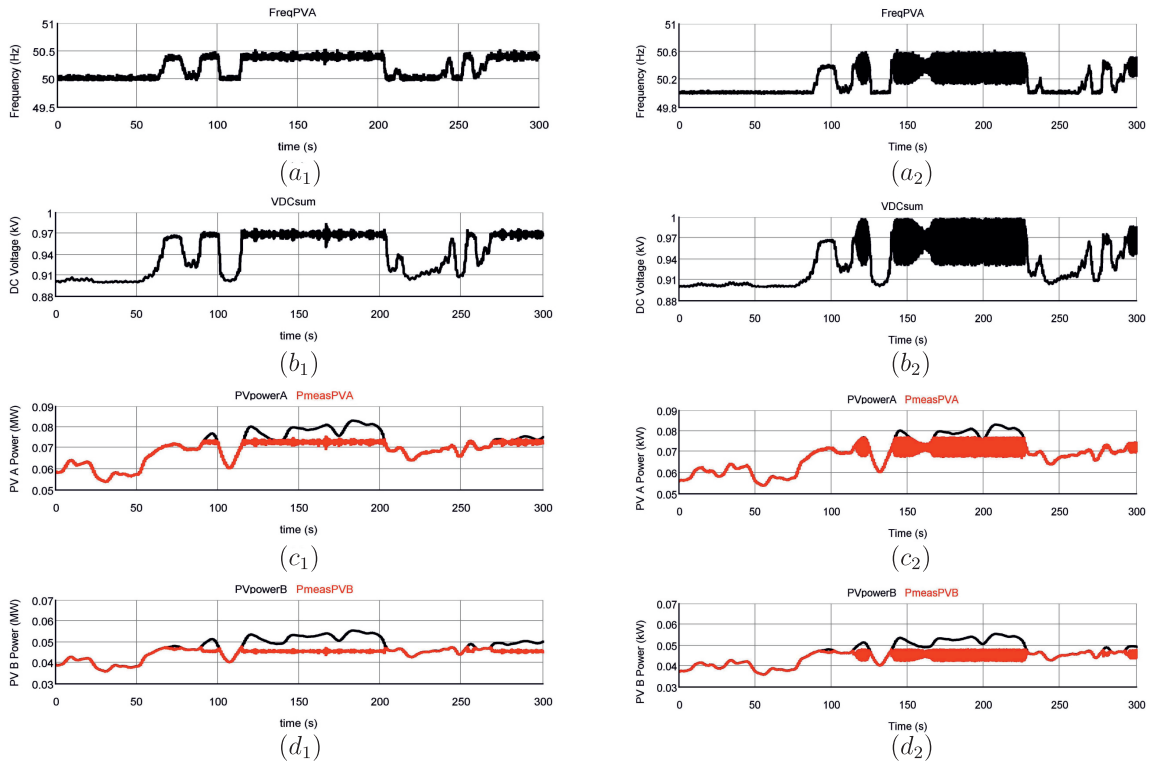


Figure 5.10: Test Case A (marked with sub-caption 1) and Test Case B (marked with sub-caption 2): (a) PLL-frequency of PV A, (b) ST DC voltage, (c) Theoretical PV A active power (black line), measured PV A active power (red line), (d) Theoretical PV B active power (black line), measured PV B active power (red line).

In the Test Case A, as soon as the voltage goes above the threshold of 930 V, the frequency controller is activated increasing linearly the frequency, as shown in Figure 5.10(a_1) and (b_1). The PLL of the PVs calculates the new frequency, and if it results above 50.3 Hz, the PV curtails the power output, as can be noticed in Figure 5.10(c_1) and (d_1) (red lines). As soon as the PVs reduce the power injection, the DC link voltage decreases and the frequency returns to the nominal value. In this case, the PV can inject in the grid the full available power. It is worth noticing in Figure 5.10 that the stability of the PLL is guaranteed also in case of frequency change from the nominal value.

In Test Case B, where the PLL bandwidth is reduced to 5 Hz, the PLL presents an oscillating behavior, affecting the whole grid, as shown in Figure 5.10 a_2 and Figure 5.10 b_2 . An oscillatory PV power production leads to an oscillating behavior of the DC link voltage in the ST. This forces the frequency controller to follow the DC voltage oscillation and change continuously the grid frequency. The whole system has an unstable behavior, affecting heavily the quality of the service. This is caused by the slow dynamics of the PLL, not able to follow the frequency change operated by the ST.

Experimental evaluation by means of microgrid setup

The stability analysis, described in the previous section and evaluated with CHIL, has been validated in lab with the microgrid setup described in Chapter 3. The converter parameters adopted in this work are listed in Table 5.6. The controller of the inverter emulating the ST LV side has been realized following the scheme in Figure 5.5.

Table 5.2: Experimental setup parameters

Parameter	Value	Parameter	Value
V_{dcL}	650 V	V_{dcg}	650 V
C_{dcL}	3.3 mF	L_L	5.03 mH
C_L	10 μ F	v_L	220 V_{rms}
f_s	10 kHz	i_g	6.5 A

The DC side of the ST is supplied by an DC power supply and the DC link unidirectional saturation has been realized by means of a series diode, effective to block the reverse power flow in the DC stage. The other VSC, representing the grid connected converter, is supplied with a DC source with a series resistance that emulates the photovoltaic panels. The PV converter is controlled with a classical current control loop, regulating the current injection on the grid. The PLL has been tuned as described in (5.26) with different bandwidths in order to verify the stability analysis. Three bandwidth cases have been chosen: a) $PLL_{bw} = 10$ Hz, b) $PLL_{bw} = 5$ Hz, c) $PLL_{bw} = 3$ Hz. The experimental setup parameters are listed in Table 5.6 and the controllers of both inverters are implemented in a dSPACE 1103.

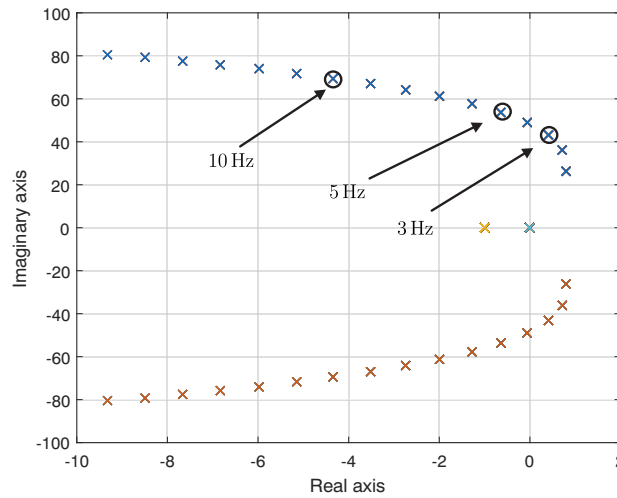


Figure 5.11: Root locus with variable PLL bandwidths of the experimental setup

The stability analysis of the experimental setup has been performed and the root locus is shown in Figure 5.11. The analysis shows how the system is stable under the cases $PLL_{bw} = 10$ Hz and $PLL_{bw} = 5$ Hz, but not for the case $PLL_{bw} = 3$ Hz. However a degradation of performance is expected for the case $PLL_{bw} = 5$ Hz with respect to the case $PLL_{bw} = 10$ Hz.

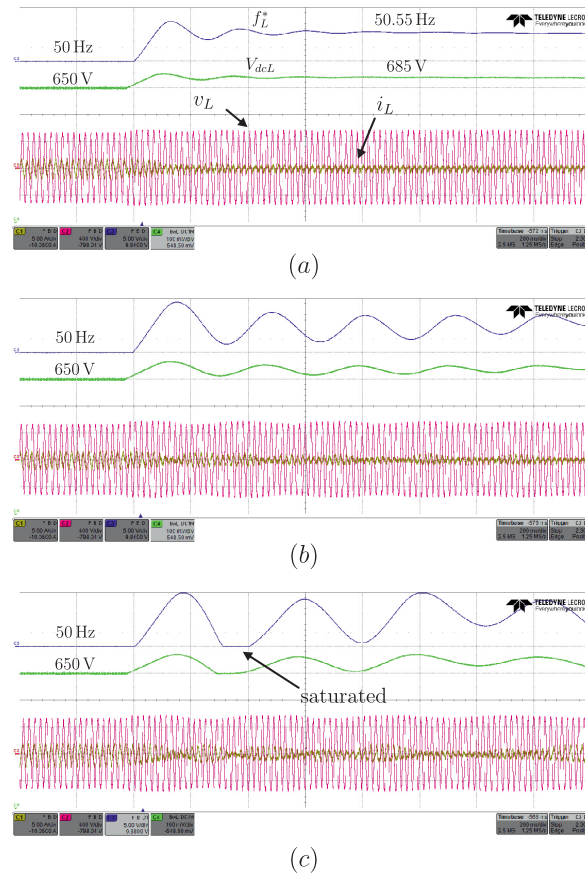


Figure 5.12: Experimental results under different PLL-bandwidths: a) $PLL_{bw} = 10$ Hz, b) $PLL_{bw} = 5$ Hz, c) $PLL_{bw} = 3$ Hz.

The experiments have been carried out performing a step variation of the resistor from 28Ω to 45Ω , while the current controlled converter is injecting 6.5 A. As the power flow reverses, the DC Link voltage increases. In Figure 5.12 the results for the three chosen PLL bandwidths have been plotted. In Figure 5.12a the system shows a stable behavior. The frequency and DC link voltage are stabilized respectively at 50.55 Hz and 685 V after 500 ms and the DG converter reduces the current output from 6.5 A to 4.9 A. If the PLL bandwidth is decreased to 5 Hz (Figure 5.12b) the system results be still stable, however with increased oscillations and longer settling time (more than 1.5 s). In case of further reduction of bandwidth, i.e. 3 Hz (Figure 5.12c), the system becomes strongly oscillating till the trip of frequency protection after few seconds. The experiment results plotted in Figure 5.12 confirms what described in the stability analysis and shown in Figure 5.11. Thus the DG PLL bandwidth must be high enough for guaranteeing stable operations of the RPFL controller.

Discussion on the capacitor sizing of the ST

As already depicted, in the PLL bandwidth lies the stability of the RPFL controller. However, the limited bandwidth of the DG converters can be compensated acting on the ST DC capacitor, as depicted in Eq.5.20. In Figure 5.13 a PLL bandwidth of 10 Hz has been considered and the stability analyzed varying the capacity of DC link. Two capacitor sizes are

considered in this analysis: the one employed in the CHIL evaluation (10 mF); and the capacitor size that limits the voltage oscillation to 5 % during a 25 % power oscillation in the DC link (2 mF). The choice of the latter lies on the fact that the ST must have a minimum size for the DC capacitor able to handle the 2nd harmonic oscillation deriving from unbalances in the LV loads.

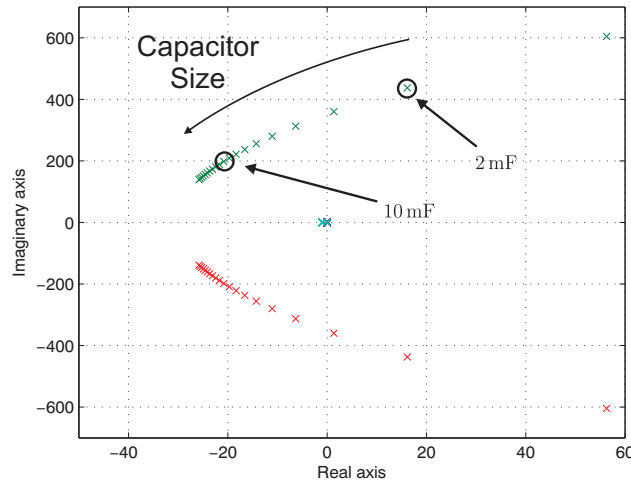


Figure 5.13: Stability analysis varying the ST DC link capacitor with PLL bandwidth fixed to 10 Hz

As can be noted, with the same bandwidth that kept stable the system in the Test Case A, where the DC capacitance was 10 mF, a capacitor of 2 mF can destabilize the control. In order to verify it, the Reverse Power Flow Limitation control has been performed by means of CHIL in the Test Case C, where the ST DC capacitor is equal to 2 mF. The results are plotted in Figure 5.14. The controller becomes unstable as soon as the DC voltage triggers the controller. With respect of the Test Case B (Figure 5.10)b, where the system had a limited oscillation, the DC link voltage oscillates with an amplitude of 100 V and the frequency is continuously changing from 50 Hz to 50.7 Hz during the control and keeps oscillating also in nominal conditions.

Discussion on lost revenue

The proposed reverse power flow limitation controller reduces the power output from the DG in order to avoid the power flow reverse in MV grid. However, with this method the revenue of the DG owner is reduced as well. In order to evaluate the impact on the DG owner, an economical analysis is carried out. As highlighted in a report from Energex Limited [124], the reverse power flow events can occur in up to 13 % of the LV/MV substations during the daylight hours, with approximately 20 % of active users in the grid. This condition can be taken as a test case for active grids with high penetration of renewables. In Figure 5.15, the analysis of the annual curtailed energy from the reverse power flow controller has been performed. It has been assumed that the reverse power flow impacts negatively on the MV

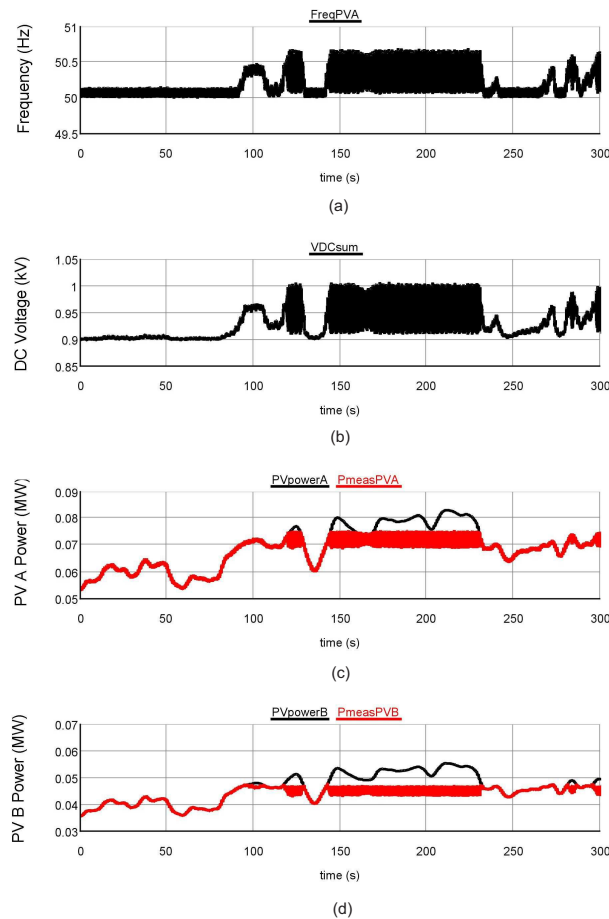


Figure 5.14: Test Case C: (a) PLL-frequency of PV A, (b) ST DC voltage, (c) Theoretical PV A active power (black line), measured PV A active power (red line), (d) Theoretical PV B active power (black line), measured PV B active power (red line).

grid voltage in a reduced number of cases (here considered up to 30 %) and the maximum power that can be curtailed from the DG is 25 %. As can be seen, the annual curtailed energy results be less than 1 %, that is an acceptable tradeoff, considering the risk of overvoltage trips and local black-outs.

Referring to the case described in the CHIL evaluation, an economical evaluation of the lost revenue under Feed-In-Tariff (FIT) strategies developed in different countries has been performed in Table 5.3. Two cases have been considered applying the 2015 FITs in effect in European countries: in the first case, the hypothesis of 10 % of voltage violation in MV grid and with 10 % of reduced power from the PV has been considered; in the second case, the same calculations have been performed under the more conservative hypothesis of 25 % of voltage violation in MV grid and 25 % of reduced power from PVs. Assuming that the PVs work 1100 hours at nominal power, the total revenue is within the range of [9424.8 € (France) ÷ 27104 € (Switzerland)]. As can be noted, the lost revenue for both PV A and PV B is not elevated, considering that the total size of both PV plants is 140 kW. Further revenue mechanisms can be studied for compensating the DG owners for the lost revenue.

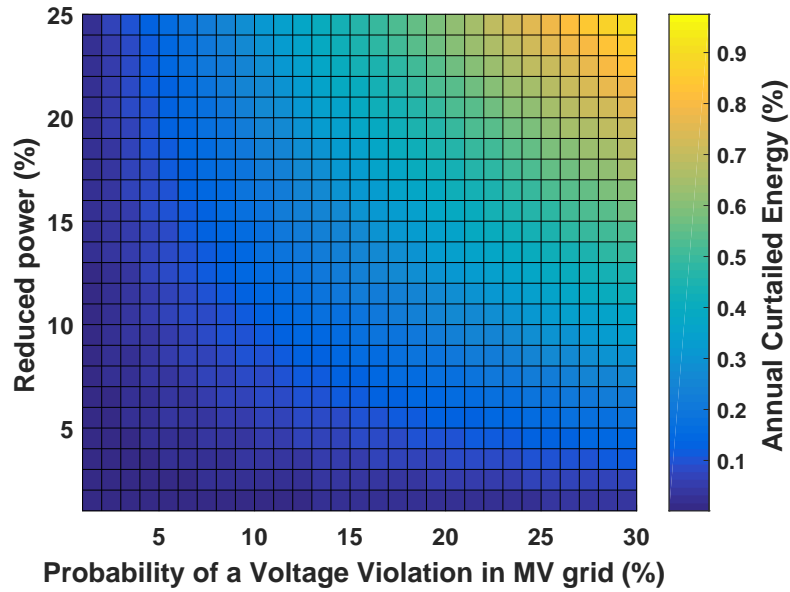


Figure 5.15: Annual curtailed energy depending on voltage violation probability in MV grid and DG amount of reduced power.

Although this method implies a certain energy loss during the year depending on the grid conditions, its impact is limited, when compared to the remote disconnection planned in [54]. In the reverse power flow controller, the plant is still producing, but at limited power. In case of remote disconnection, the plant is shut down till the reconnection command coming from the DSO control center. This implies longer waiting time between the disconnection and reconnection to the grid, and thus higher energy losses for the interested power plants.

Table 5.3: Lost revenue

Country	<i>FIT</i> (€/kWh)	Lost revenue 10% (€)	Lost revenue 25% (€)
France	0.0612	12.25	76.57
Germany	0.1071	21.44	134.01
Greece	0.1150	23.02	143.89
Switzerland	0.1760	35.24	220.22
Spain	0.1217	24.36	152.28

5.2 ST overload limitation control

The ST, differently from the conventional transformer, has a limited overload capability. Its overload capability is limited and depending on the semiconductors temperature [125]. Several factors, such as the overload time and the external temperature, can influence the devices temperature. A current higher than the nominal one reduces the ST lifetime, and in extreme cases leads to semiconductor devices fault. In this section a ST overload control has been

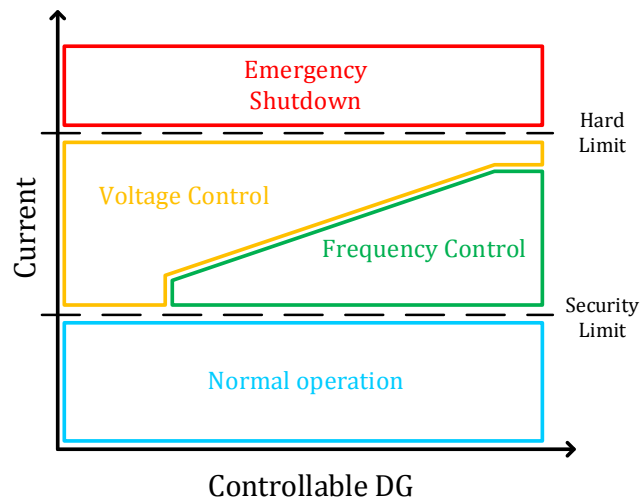


Figure 5.16: ST Overload Control concept: control action performed depending on the amount of controllable DER integrated in the grid

proposed, based on the interaction with the local loads and generators in LV grid by means of voltage and frequency signals (Figure 5.16). Under normal operations, with a current below the security limit, the ST keeps the voltage and frequency at the nominal value. Approaching the overload condition, the ST decreases the frequency in order to increase the local generators power output, if they are equipped with droop controllers. In case of not sufficient power handling capability of these resources, the ST resorts to the voltage controller. Decreasing the voltage, the load reduces the power absorption, avoiding the overload condition. If the voltage controller is not able to manage the overload, due to the low sensitivity of load power to voltage variation (e.g., constant power loads), and the current increases above the hard limit, the ST is forced to an emergency shut down or to a load shedding in the LV grid. Similar methods have been applied for energy saving purposes, like the CVR method [106][57]. Unlike the proposed overload controller, the CVR is applied in steady state and not during transients, and the current value is not controlled during the voltage variation.

Smart Transformer overload controller

The ST LV side controls the LV grid voltage waveform. It provides symmetrical voltage waveforms with constant amplitude and frequency independently from the load power request. The current amplitude and shape, instead, is decided solely by the load. The voltage

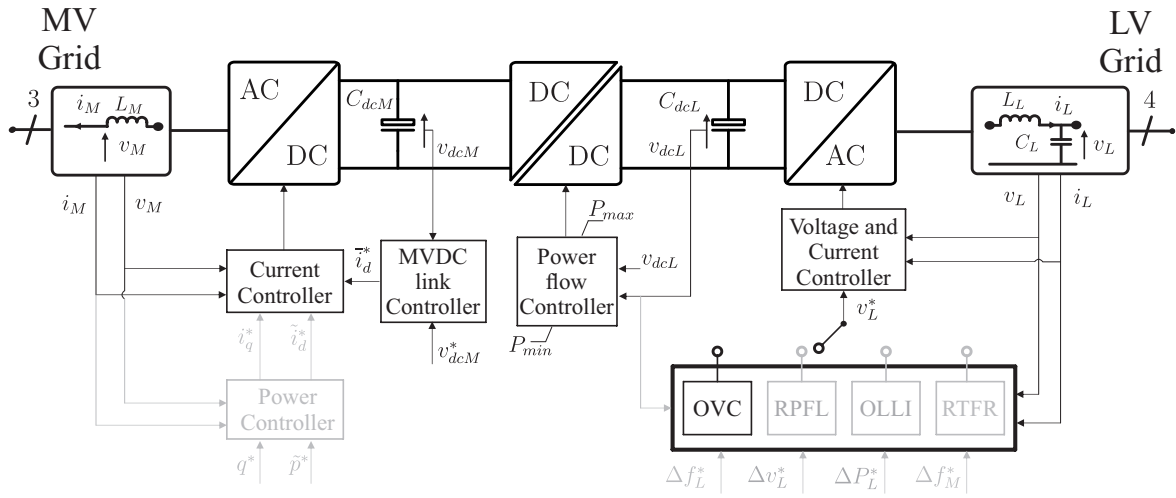


Figure 5.17: Smart Transformer control scheme and proposed controller to avoid overload condition.

waveform reference, however, can be modified for providing additional services to the LV grid. In this case the voltage amplitude is given by the OVC (Figure 5.17), so that the ST overload condition is timely managed.

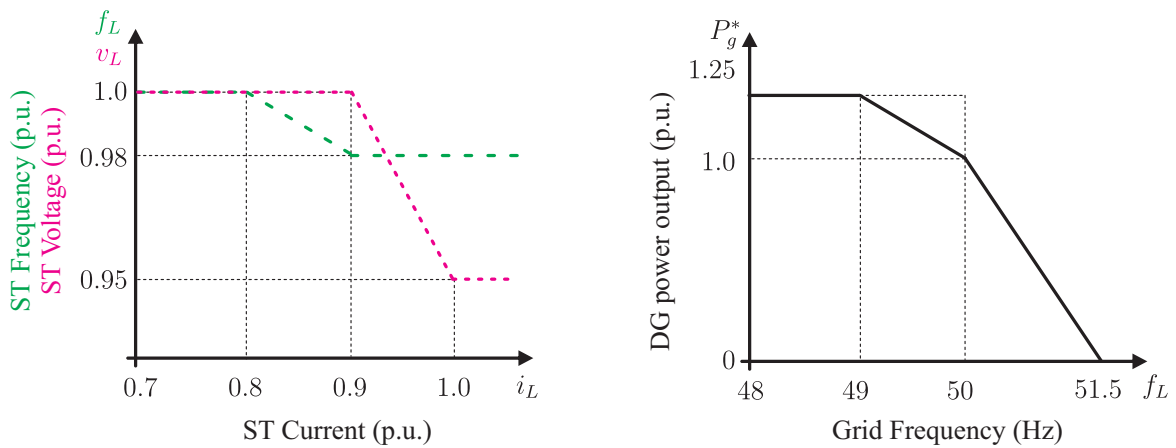


Figure 5.18: ST overload controller and DER voltage/frequency droop controller

The ST measures the current rms value and sets two current thresholds for the frequency and voltage controller respectively. As shown in Figure 5.18, the frequency controller is activated as soon as the rms current exceeds the 80 % of the maximum current limit, set as the current at ST nominal power and voltage. If the controllable resources size is not sufficient or the controller hits the minimum frequency limit (e.g. 49 Hz), the current rises till the 90 % of the maximum limit and activates the voltage controller. Here, the ST decreases the voltage amplitude to keep the current within the allowable range. In case the current reaches the current maximum limit, despite the overload controller action, the system resorts to load shedding in the LV grid. In the case of emergency, the ST is forced to shut down in order to avoid hardware damages or feeder blackouts. As soon as the ST current decreases, the voltage controller at first, followed by the frequency controller, are deactivated. In the voltage controller, a rate limiter has been implemented in order to avoid disruptive interactions

with the frequency controller during the voltage recovery. If the voltage controller is too fast in recovering the grid voltage, the frequency controller may oscillate, destabilizing the system.

In the controllable DER resources, the frequency droop controller curve is implemented as shown in Figure 5.18. The interface converter decreases its power output until shut down in the case of high frequency (51.5 Hz) [121] and increases its power injection up to 125% in the case of frequency decrease (49 Hz). The DER considered may be generators or renewables equipped with battery energy storage systems (i.e., for the upwards regulation). Implementing such droop controllers, the DER converters can interact with the ST under frequency variation signals. The frequency threshold values chosen for this work respects what asked in the Italian standard [121]. The DER converter must remain connected to the grid within the frequency range (47.5-51.5) Hz. In case of over-frequency, the DER must reduce the power output from nominal power (50.3 Hz) to zero power (51.5 Hz).

Table 5.4: Load and ST Data

Load	Bus	Nominal Power (kW)	$\cos\varphi$	ST Parameter	Value
L1	11	20.0	0.90	S_{ST}	120 kVA
L2	15	10.0	0.90	V_{dcL}	800 V
L3	16	10.0	0.90	C_{dcL}	2.0 mF
L4	17	25.0	0.90	L_L	8.0 mH
L5	18	15.0	0.90	C_L	50.0 μ F

To depict the OVC operations, simulations are carried out in a modified CIGRE European LV distribution network benchmark [112] (Figure 5.19) implemented in PSCAD / EMTDCTM. The assumptions made in this work are as follows: (1) the loads are balanced three-phase; (2) the distributed resources, such as BESSs and PVs are working at unity power factor; (3) the loads are assumed as constant impedance by means of an exponential load model. The load and ST data are listed in Table 5.4. The battery energy systems and the photovoltaic power plants are controlled by means of an external power loop that gives the reference current to a current loop. The nominal data of the batteries and PV are listed in in Table 5.5. The energy resource models are tuned following the standard procedures for renewable converters described in [81].

Table 5.5: BESS and PV data.

Resource	Nominal Power (kVA)
BESS A	35
BESS B	25
PV A	4
PV B	3

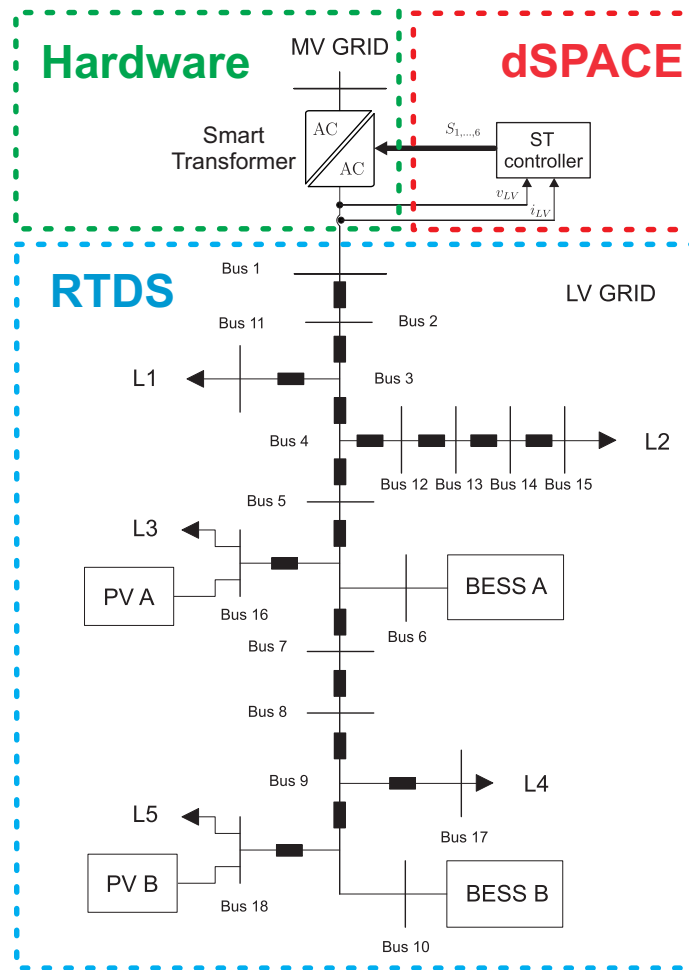


Figure 5.19: Grid simulated in PSCAD/EMTDC™

The maximum current allowable in the ST is 174 A, corresponding to the current flowing in the ST working at nominal power (120 kVA) under nominal voltage ($230 V_{rms}$). The sum of the load and BESS profiles are shown in Figure 5.20. Without losing in generality on the methodology, an unique load profile for the loads has been considered. The voltage controller ramp limiter has been set in this simulation to 0.5 V/s.

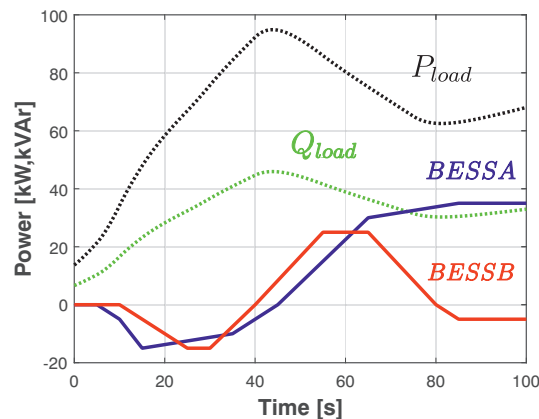


Figure 5.20: BESS A active power (blue line), BESS B active power (red line), sum of load active power (dotted black line), sum of load reactive power (dotted green line).

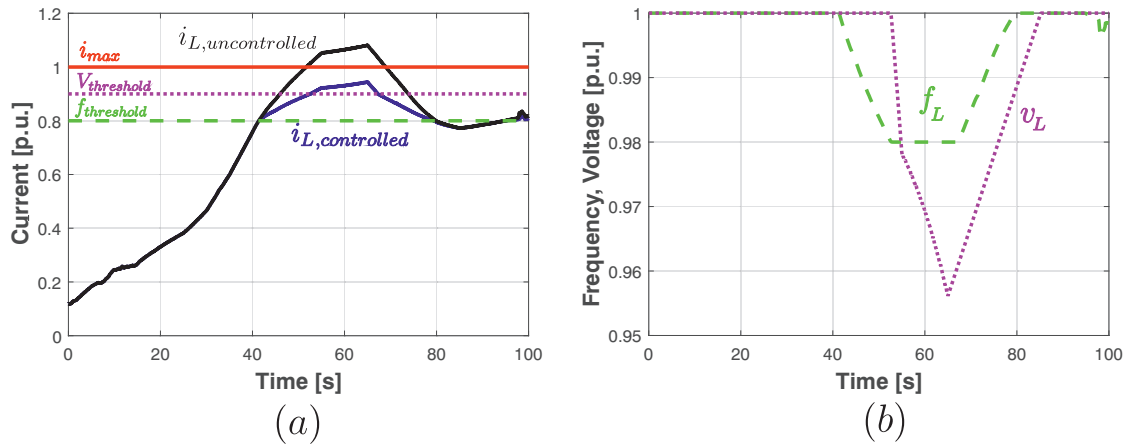


Figure 5.21: Overload controller simulations: (a) ST current without controller (black line), ST current with the proposed overload controller (blue line), frequency controller threshold (dashed green line), voltage controller threshold (dotted magenta line), current maximum limit (red line); (b) grid frequency (dashed green line), ST bus voltage (dotted magenta line).

The frequency controller is activated when the current goes above the 80 % threshold and the voltage controller follows at 90 % of the nominal current. In Figure 5.21a the current profile in absence of overload control is plotted (black line). As can be noted, without control, the current exceeds the current maximum limit for more than 20 seconds in the considered time window. This may lead to damages to power semiconductor and reduction of the ST expected lifetime.

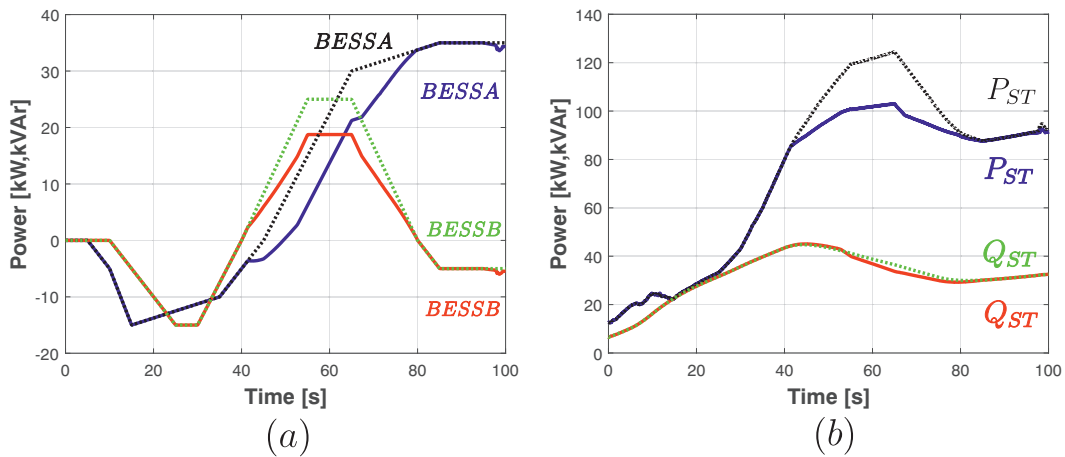


Figure 5.22: (a) Active power without controller BESS A (dotted green line), with overload controller (red line), active power without controller BESS B (dotted black line), with overload controller (blue line); (b) ST: Active power without controller (dotted black line), with overload controller (blue line), reactive power without controller (dotted green line), with overload controller (red line).

Applying the ST overload controller, the current is kept below the maximum limit. As plotted in Figure 5.21, as soon as the current exceeds the frequency threshold, the ST decreases the output frequency till reaching the minimum value of 0.98 p.u. (49 Hz). The current slope is decreased with respect to the no-control case, but due to the limited amount of controllable

resources, the current still exceeds the voltage threshold. Here, the voltage amplitude is decreased in order to reduce the loads power consumption. It can be noted in Figure 5.21, how the current is controlled below the current maximum limit and the voltage is decreased till 0.955 p.u., while the frequency is kept constant to 49 Hz. When the overload condition is solved and the load power request is decreased, the ST restores the voltage to the nominal voltage, and controls the current profile with the frequency controller. Until the overload is not completely solved, the ST maintains the frequency controller activated.

The batteries power profiles are shown in Figure 5.22a. The batteries increase the power output when the frequency is modified due to the droop controller action (solid lines) with respect to the base case (dotted lines). The effectiveness of the combined action of frequency and voltage controllers can be observed in the ST power profiles in Figure 5.22b. Without control, the active power alone exceeds the ST size (dotted black line). Applying the ST overload control, both active and reactive power are reduced (continuous lines).

Experimental validation by means of microgrid setup

The overload controller simulated in the previous section has been verified experimentally with the microgrid setup depicted in Chapter 3. The experimental setup is composed of two three-phase VSC and a variable resistor used to create the overload conditions. The controller of the inverter emulating the ST has been implemented as described in Figure 5.17. The experimental setup parameters are listed in Table 5.6 and the controllers of both inverters are implemented in a dSPACE 1103. In the DER side converter the droop controller described in Figure 5.18 has been implemented.

Table 5.6: Experimental setup parameters

Parameter	Value	Parameter	Value
v_{dcL}	650 V	v_{dcg}	650 V
C_{dcL}	3.3 mF	L_L	5.03 mH
C_L	10 μ F	v_L	220 V_{rms}
f_{sw}	10 kHz	i_{max}	6 A

The maximum current has been set to 6 A_{rms} , and the frequency and voltage controller threshold have been set to 80% and 90%, respectively. The voltage controller ramp limiter has been set equal to 0.2 V/s. The variable resistor has been operated from 28 Ω to 21 Ω for about 20 s. In Figure 5.23 the operations of the overload controller have been plotted. As soon as the ST current exceeds the 4.8 A threshold, the frequency controller is activated, and it decreases the frequency from 50 Hz to 49 Hz. When the current increases above 5.4 A the voltage is decreased, limiting the ST overload to 5.6 A, with a further margin for load increase. The voltage drops from 220 V to 215.5 V during the steady state condition. As soon as the variable resistance increases, the ST current decreases, and the voltage and frequency are slowly restored to the nominal value.

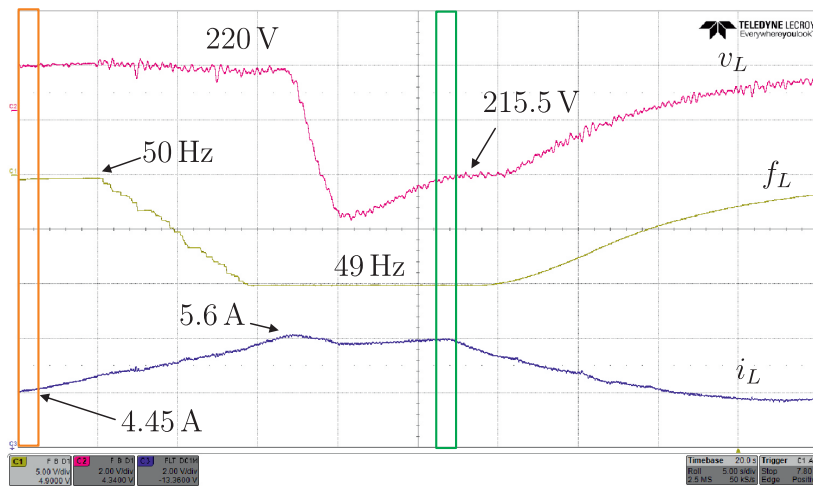


Figure 5.23: Experimental results: ST rms voltage v_{LV} (magenta line), grid frequency f_{LV} (yellow line), and ST rms current i_{LV} (blue line).

A better understanding of the overload controller operations can be obtained looking at Figures 5.24 and 5.25. These figures represent the steady-state waveforms before the overload condition and during the controller operation, marked respectively with the orange and green boxes in Figure 5.23. In Figure 5.24, the ST controls the voltage waveform v_{LV} at the nominal amplitude and frequency, being the ST current i_{LV} lower than the frequency controller threshold. The DER current i_{gc} amounts to $4 A_{peak}$ and the load absorbing about $i_{load} = 11 A_{peak}$. As soon as the load increases, the overload controller acts on the voltage amplitude and frequency values. The steady-state behavior during the controller operations (Figure 5.23, green box) is shown in Figure 5.25. The ST decreases the voltage v_{LV} amplitude and frequency, and the DER is able to recognize the frequency change and increase the current output up to $5 A_{peak}$. The load current consumption is maintained at $14.4 A_{peak}$ by the voltage controller, instead to increase to $14.8 A_{peak}$. Both frequency and voltage controllers are able to avoid the ST overload.

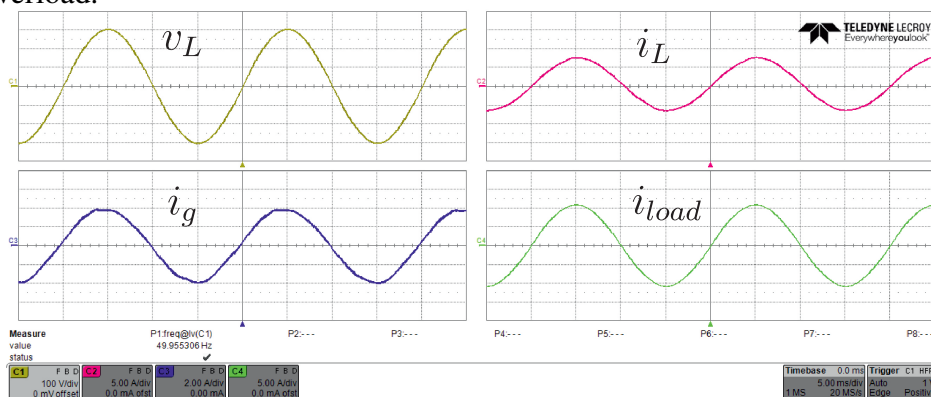


Figure 5.24: Steady-state before the overload (Figure 5.23, orange box): ST voltage (yellow line, 100 V/div), ST current (magenta line, 5 A/div), DER current (blue line, 2 A/div), load current (green line, 5 A/div).

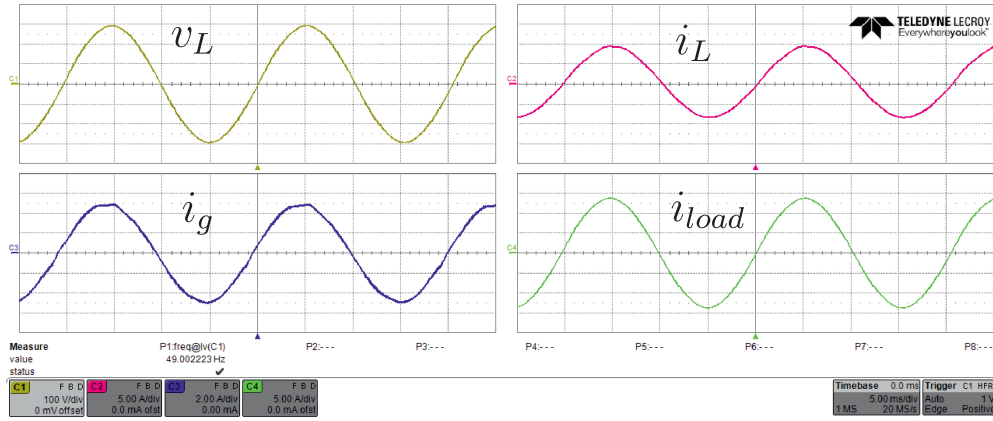


Figure 5.25: Steady-state during the overload controller operations (Figure 5.23, green box): ST voltage (yellow line, 100 V/div), ST current (magenta line, 5 A/div), DER current (blue line, 2 A/div), load current (green line, 5 A/div).

5.3 Sensitivity-based ST Overload Control

The on-line load sensitivity evaluation method, described in the previous chapter, is applied in this chapter to the ST OVC. The correct identification of voltage load sensitivity allows the evaluation of the appropriate voltage variation to alleviate the overload of the ST. Indeed, not knowing the load sensitivity to voltage, the overload condition can be worsened: if the load is a constant impedance type, a voltage decrease leads to a current decrease [C6]; on the contrary, with constant power load the voltage decrease increases the current, worsening the ST overload.

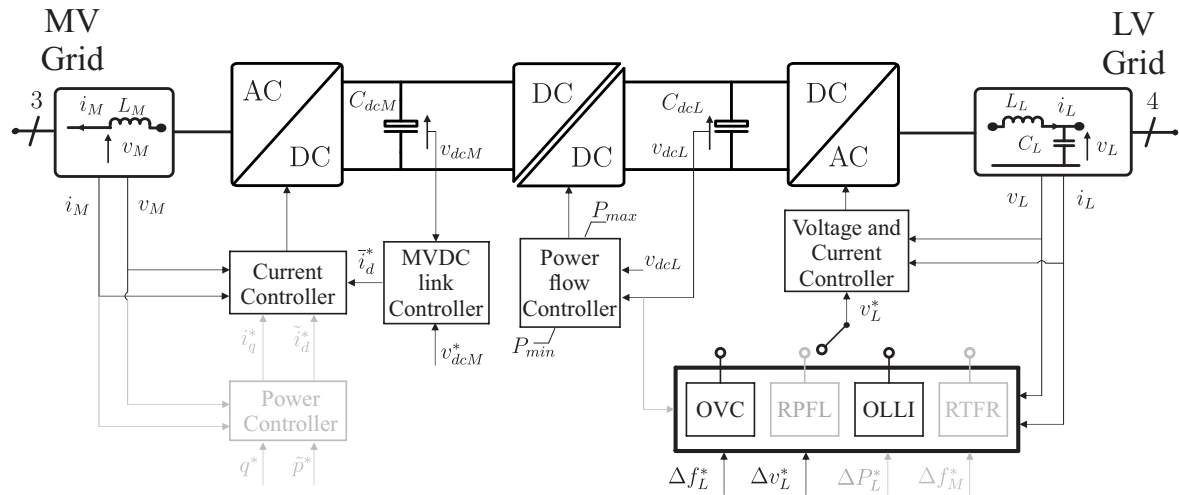


Figure 5.26: Smart Transformer control scheme with OLLI algorithm and OVC activated.

The on-line load control based on OLLI algorithm described in chapter 4 can increase the accuracy of the OVC control action. As marked in Figure 5.26, the OLLI algorithm works in parallel with the OVC in order to provide the load current sensitivity to voltage variation, and thus deciding if the voltage must be increased or decreased to reduce the current flow. The combined algorithm is represented with more details in Figure 5.27. Computing the load sensitivities, the overload conditions are alleviated in real time by adapting the voltage

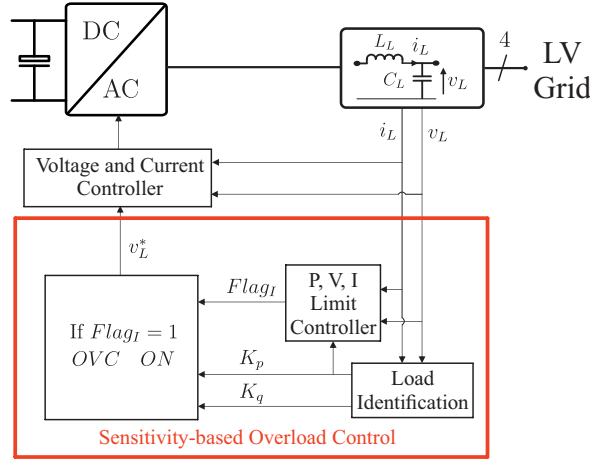


Figure 5.27: Sensitivity-based OVC: the limit controller triggers the OVC, depending on the external signal coming to ST and the ST internal status (e.g., temperature or current).

in the grid appropriately. If the ST security current limit is exceeded in one phase, the limit controller triggers the Voltage-Based OVC. The OLLI algorithm evaluates the active and reactive power sensitivities and decides to increase or decrease the voltage. Since the behavior of load active power can be different from that of reactive power, in this section the sensitivity of current with respect to voltage is evaluated for each phase taking into account both sensitivities. It is worth mentioning that the current sensitivity can also be determined by direct measurement. However, it is demonstrated in this section that the active and reactive power sensitivities are sufficient to reconstruct the sensitivity of the current.

In order to apply a balanced control action, the voltage variation to be applied to control ST overload must be the same in all phases. Consider the current and apparent power equations for one of the phases:

$$I = S/V \quad (5.27)$$

$$S^2 = P^2 + Q^2$$

which are linearized by taking first order partial derivatives and assuming small variations around the operating point $V_0, S_0 (P_0, Q_0)$:

$$\Delta I = \Delta S/V_0 - (S_0/V_0^2)\Delta V \quad (5.28)$$

$$2S_0\Delta S = 2P_0\Delta P + 2Q_0\Delta Q \quad (5.29)$$

Considering the measured normalized sensitivities of P and Q with V :

$$\frac{\frac{P(t_k) - P(t_{k-1})}{P(t_{k-1})}}{\frac{V(t_k) - V(t_{k-1})}{V(t_{k-1})}} = K_p$$

$$\frac{\frac{Q(t_k) - Q(t_{k-1})}{Q(t_{k-1})}}{\frac{V(t_k) - V(t_{k-1})}{V(t_{k-1})}} = K_q \quad (5.30)$$

and substituting in (5.29) and (5.28), the current variation following a voltage variation is obtained:

$$\Delta I = [(P_0/S_0)^2 K_p + (Q_0/S_0)^2 K_q - 1] (S_0/V_0^2) \Delta V \quad (5.31)$$

the normalized current sensitivity to voltage is defined with the formula:

$$\Delta I/I_0 = K_i \Delta V/V_0 \quad (5.32)$$

where the equivalent normalized sensitivity coefficient of current K_i can be calculated from (5.31) as:

$$K_i = (\cos\varphi_0)^2 K_p + (\sin\varphi_0)^2 K_q - 1 \quad (5.33)$$

Once the normalized current sensitivity of the apparent power is known, the voltage variation to be applied can be calculated using:

$$\begin{aligned} & \text{if } I > I_{sec} \\ & \frac{V}{V_0} = 1 + \left(\frac{I_{sec} - I}{I_{sec}} \right) / K_i \end{aligned} \quad (5.34)$$

where I_{sec} is the security current limit, at which the sensitivity-based OVC is triggered. Note that each time the above condition holds for one phase, the new V is applied to all three phases simultaneously. If the corrective voltage action calculated in one phase leads to overload another phase, a single-phase voltage control must be applied, following the voltage sensitivity of that specific overloaded phase. However, this should be used as last resort, due to the application of intentionally unbalanced voltage and the following decrease of power quality in the grid. In this application the I_{sec} has been set equal to 95 % of the ST maximum current. If K_i is positive, corresponding to a load condition in the constant impedance direction, the ST decreases the voltage to deal with the overload. If K_i is negative, the case of constant power loads, the ST increases the voltage. For conditions where $K_i = 0$, meaning a constant current load, other control strategies should be applied, i.e. frequency-based OVC with controllable resources [J6][C6], as already shown in Section 5.2.

In order to demonstrate the Voltage-Based OVC concept the power curves described in Figure 4.12 are applied to the PV plants. The grid described in Chapter 4 and shown in Figure 4.11 has been adopted for this study. At $t = 100$ s the PV A is suddenly disconnected from the grid for 100 seconds (Figure 5.28a), causing a current increase in the ST. If no control action is taken, the current of Phase C goes above the maximum current limit of the ST (Figure 5.28b, black line), equal to $145 A_{rms}$ (Figure 5.28b, red line), corresponding to $205 A_{peak}$ in sinusoidal conditions. If the Voltage-Based OVC is applied in this case together with the OLLI, the voltage in all three phases is increased (Figure 5.28c), decreasing the current below the maximum limit. It is worth noting that without a proper identification of the load sensitivity a voltage variation may worsen the overload condition of the ST, instead of alleviating it. In case of insufficient control range (upper or lower voltage limit), the need for energy storage elements (i.e., batteries, diesel generators) becomes essential for solving the ST overload.

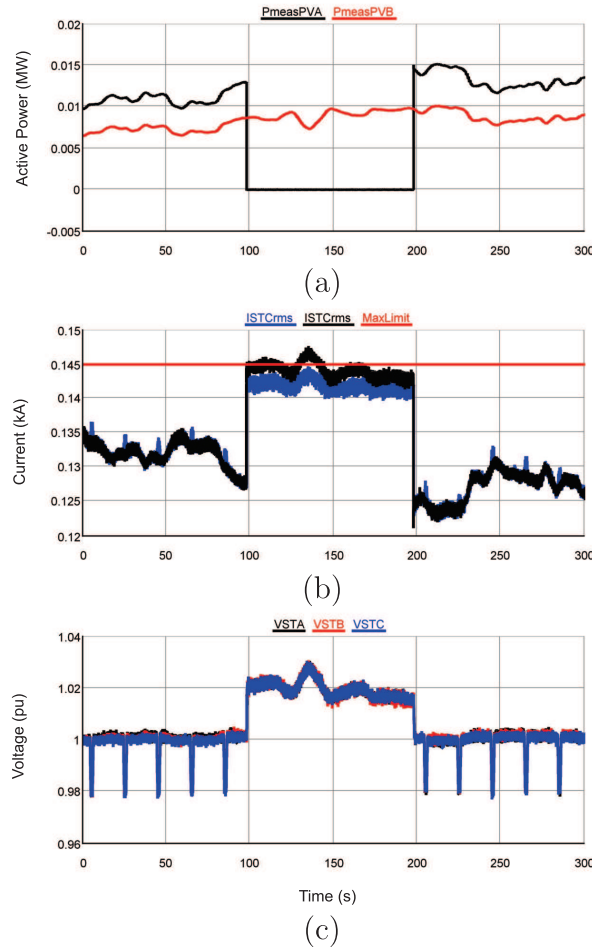


Figure 5.28: ST OVC: (a) PV power profiles, (b) Maximum current (red line), ST current without any applied control (black line), and ST current with sensitivity-based OVC (blue line), (c) ST voltages

5.4 Control of variable-frequency ST-fed grid

As seen in this chapter, a ST-fed distribution grid offers the advanced control capability to vary on-line the grid frequency to interact with the local generation. One of the main challenges of frequency control is to regulate ST voltage waveform under variable frequency. The design of the controller of a power converter in traditional distribution grid/microgrid usually assumes signals with specific fundamental frequency (e.g. 50/60 Hz signal) and offers good voltage/current control performance as well as harmonic elimination under nominal frequency condition [126].

In case of grid with variable frequencies, for example in a ST-fed distribution grid, some of the conventional control strategies as well as design criteria may lead to performance degradation. There are several conventional frequency-adaptive control strategies including: hysteresis control [127], deadbeat control [128], proportional integral (PI) control and proportional resonant (PR) control with frequency adaptivity [129], which could independently maintain their performance of grid frequency to some extent. Nevertheless, these methods have drawbacks: the hysteresis control can suffer from high switching stress or inaccurate

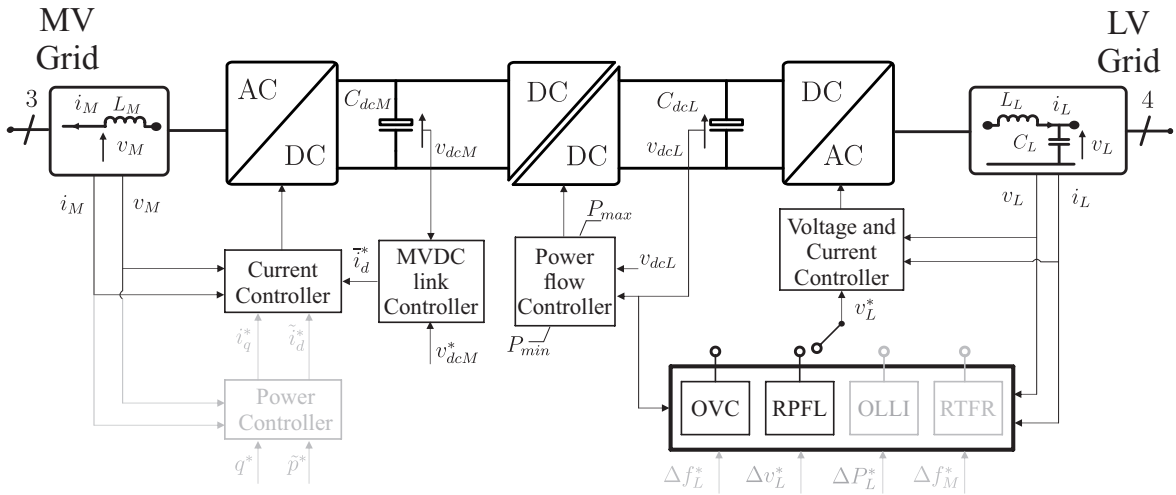


Figure 5.29: Smart Transformer control scheme adopted for FORC applications.

harmonic elimination due to its nonlinear nature; the deadbeat control is sensitive to the accuracy of system parameters; both PI and PR with frequency adaptivity can well handle the fundamental frequency signals but may not perform optimally in case of high harmonic content. Multiple resonant controllers with frequency adaptivity can indeed achieve good tracking ability at selective harmonic frequencies, however it is computational heavy and complex to tune. Based on the Internal Model Principle (IMP), repetitive control offers a simple way to achieve zero steady-state error tracking of any periodic signal with a known period due to the introduction of high gains at interested harmonic frequencies [130], but the Conventional Repetitive Control (CRC) with fixed sampling rate is sensitive to the frequency variation from the harmonic control point of view. In this context, a simple and compact structure frequency adaptive Fractional-Order Repetitive Control (FORC) scheme has been proposed [131][J7], derived from the IMP and able to provide high control performance with arbitrary frequency. Several case studies on FORC-controlled systems have been proposed in literature for different applications, such as programmable AC power supply [131], grid-connected power converter [132], and active noise cancellation [133]. Equipped with the FORC, the ST-fed distribution grid is able to modify online the generator production and load consumption by changing LV grid frequency, while maintaining good voltage/current waveforms under variable frequency condition [J4].

Fractionary Order Repetitive Control (FORC)

The IMP-based control schemes, for instance, CRC, have been well developed for power converters because of their zero steady-state error tracking ability [134]. Including the internal model of a generic periodic signal, the CRC can accurately track or suppress any periodic input or disturbance. A typical closed-loop digital control system with a plug-in CRC for a power converter is shown in Fig. 5.30, where $R(z^{-1})$ is the reference input, $Y(z^{-1})$ is the system output, $E(z^{-1})$ is the control error, $D(z^{-1})$ represents the disturbance; $G_c(z^{-1})$ is the transfer function of the original feedback controller, $G_d(z^{-1})$ is the $1.5T_s$ (sampling time) delay of the computation and PWM, and $G_f(z^{-1})$ is the transfer function of the output filter.

A CRC can be plugged into the feed-forward channel and its transfer function is given by [130]

$$G_{rc}(z^{-1}) = \frac{U_r(z^{-1})}{E(z^{-1})} = k_r \frac{z^{-N} Q(z^{-1}) G_{lf}(z^{-1})}{1 - z^{-N} Q(z^{-1})}. \quad (5.35)$$

where k_r is the gain of CRC, $G_{lf}(z^{-1})$ is the phase leading element which stabilizes the overall system, $Q(z^{-1}) = a_1 z + a_0 + a_1 z^{-1}$ with $2a_1 + a_0 = 1$ is the low-pass filter which improves the system robustness, $N = f_s/f \in \mathbb{N}$ with f_s and f being the sampling frequency and the fundamental frequency, is the so-called CRC order. It is worth noting that the poles of CRC are exactly located at $2m\pi f$, with $m \in \mathbb{N}$. Therefore, the magnitudes of CRC at frequencies of $2m\pi f$ approach infinite if $Q(z^{-1}) = 1$, which allows the CRC to provide zero steady-state tracking error of DC, fundamental component and all harmonic components below the Nyquist frequency.

Nevertheless, in a frequency-adaptive ST-fed distribution grid, the frequency of LV side can be modified within a certain range. With a fixed sampling rate, the RC order N would often be a fractional value during frequency changes. A fractional order indicates that a Fractional Delay (FD) appears and it cannot be directly implemented in a digital controller. To address this issue, one solution is to use variable sampling rate while it will significantly increase the real-time implementation complexity. On the other hand, the FORC scheme with a fixed sampling rate has been proposed. The fractional order N can be splitted into a integer order N_i and a small fractional order F , where $N = N_i + F$. The main idea of FORC is to approximate the potential FD z^{-F} by using the FD design methods [135]. Among these methods, the Lagrange interpolation-based FD design only needs a small number of sums and multiplications and at the same time can provide high approximation accuracy [136]. The FD can be well approximated by a Lagrange interpolation polynomial Finite-Impulse-Response (FIR) filter as follows:

$$z^{-F} \approx \sum_n^{k=0} A_k z^{-k}. \quad (5.36)$$

where $k \in \mathbb{N}$, the Lagrange coefficients A_k of (5.36) are given by

$$A_k = \prod_{\substack{i=0 \\ i \neq k}}^n \frac{F-i}{k-i}. \quad (5.37)$$

Substituting (5.36) into (5.35), the frequency-adaptive FORC will be obtained as

$$G_{forc}(z^{-1}) = \frac{z^{-N_i} \sum_{k=0}^n A_k z^{-k} Q(z^{-1})}{1 - z^{-N_i} \sum_{k=0}^n A_k z^{-k} Q(z^{-1})} G_{lf}(z^{-1}). \quad (5.38)$$

The detailed FORC block diagram of (5.38) is presented in Fig. 5.31. It is shown that two time scales have been utilized in the control system: 1) the changing rate of delay orders (N_i and F) is highly dependent on the dynamic response of frequency detector; 2) the update

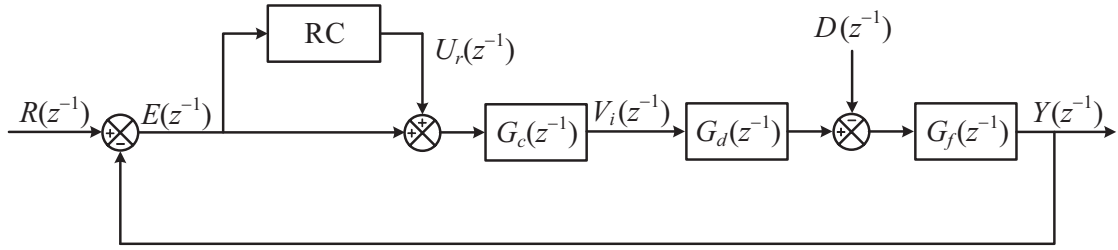


Figure 5.30: Block diagrams of a plug-in RC system: overall system.

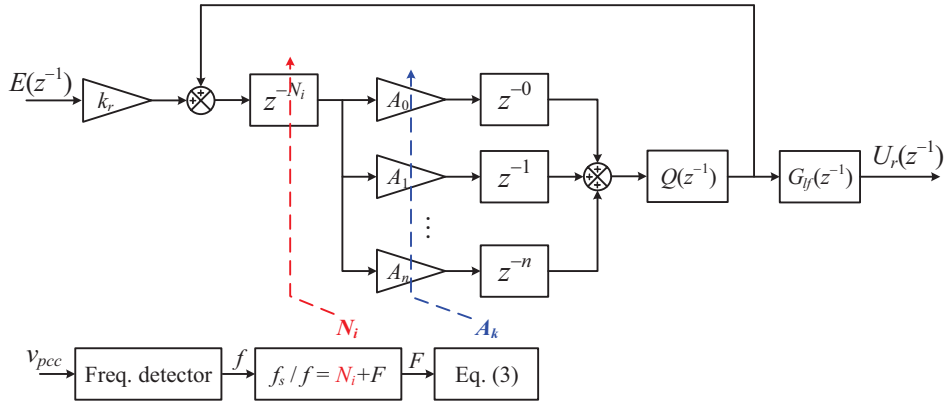


Figure 5.31: Block diagrams of a plug-in RC system: frequency-adaptive FORC.

rate of A_k depends on the sampling frequency. In a distribution grid application, the changing rates of both the N_i and F are much slower than the sampling rate. In each sampling interval, the detected frequency as well as N_i and F can be regarded as constant values.

As can be seen in Fig. 5.33, frequency-adaptive control strategy has been implemented in the ST LV converter.

The PI-plus-FORC control strategy has been utilized for both control systems to ensure frequency adaptability. It is known that the PI controller under $\alpha\beta$ frame is independent from frequency variation. Using proper gains, the PI-controlled system can offer high stability margin and good transient response. The plug-in FORC controller improves steady-state performance and guarantees zero steady-state error under variable frequency condition.

The PI-plus-FORC control has been applied to the outer voltage loop to meet error-tracking requirements with specific bandwidth. The selection of control bandwidth BW_{ST} refers to $BW_{ST} < f_s/10$, where f_s is the sampling frequency. The phase margin is selected between 45° and 60° according to the usual design rules. The gains of the PI controller for ST voltage control can be determined based on the above-mentioned rules. The open-loop Bode diagrams are presented in Fig. 5.32 using the system parameters listed in Table 5.7. The blue plot represents the open-loop frequency response of the control system without FORC. By using the control parameters of Table 5.7, the bandwidth is 267 Hz and the phase margin is 47° . The frequency response of the control with plugged-in FORC is shown by the red plot, where large magnitudes and zero phase shifts at interested frequencies have been introduced.

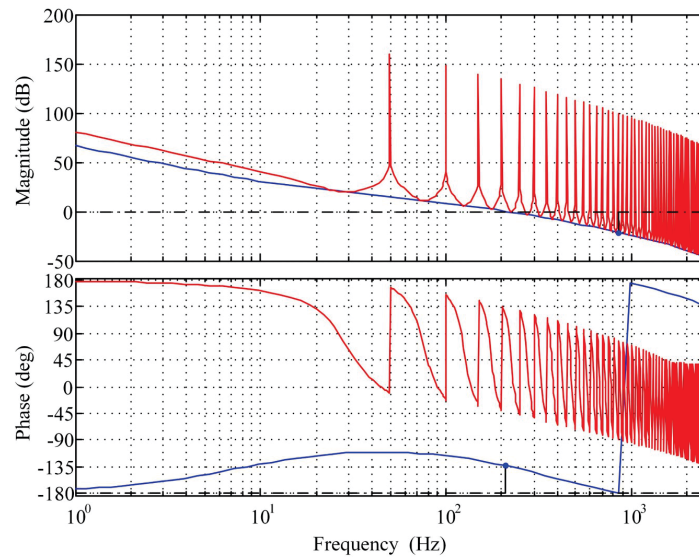


Figure 5.32: Bode diagrams of frequency-adaptive voltage control systems: ST LV side voltage control.

FORC Validation: simulation results

For validation purpose, the proposed frequency-adaptive control strategy has been simulated in a ST-fed distribution grid of Fig. 5.33 in MATLAB/Simulink with PLECS toolbox. The frequency-adaptive controller has been implemented in both the ST LV voltage and the DER current control to achieve high performance under variable frequency condition.

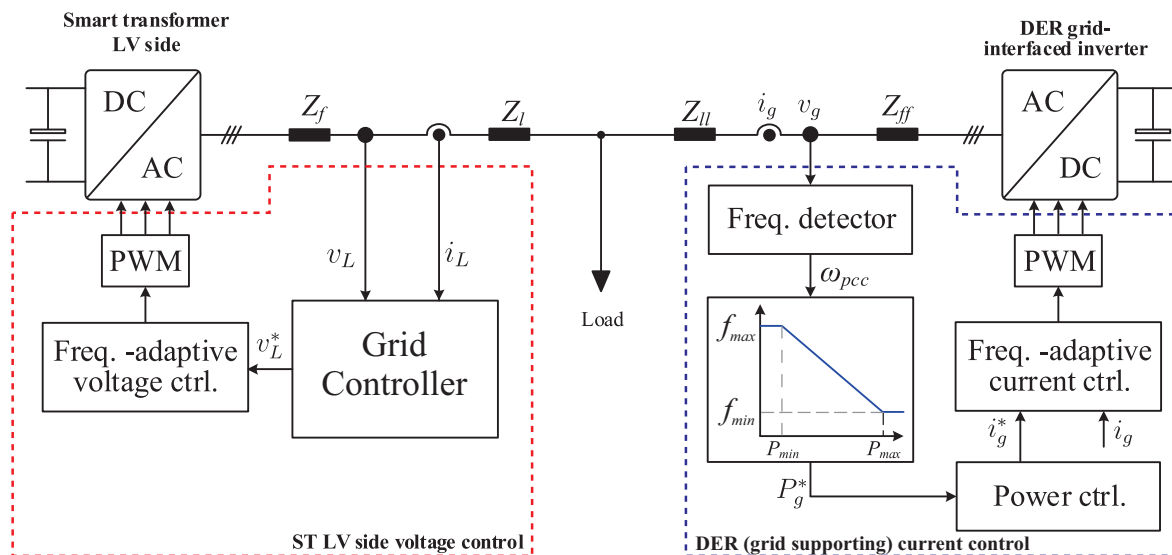


Figure 5.33: Schematic diagram of a frequency-adaptive ST-fed distribution grid.

The two aforementioned case studies are investigated in this section: the frequency-based OVC and the RPFL controller scenarios. In this section, only the frequency controller has been activated, leaving the voltage amplitude at the nominal value. The system parameters listed in Table 5.7 and Table 5.8 have been utilized for the simulations. In both case studies, the frequency range of the ST-fed distribution grid is defined as [49-51] Hz.

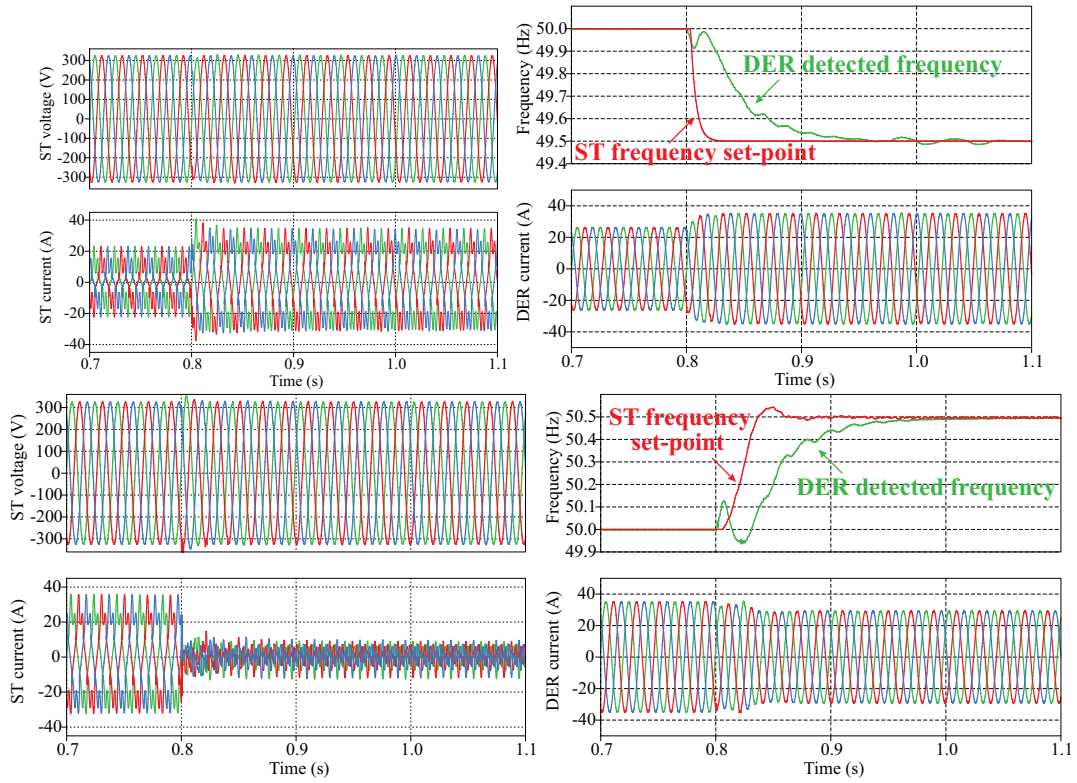


Figure 5.34: Performance evaluation of frequency-adaptive ST-fed grid under two scenarios (overloading, reverse power flow): (a) ST voltage (top) and current (bottom) under overloading scenario, (b) DER detected frequency (top green), ST frequency set-point (top red) and DER output current (bottom) under overloading scenario, (c) ST voltage (top) and current (bottom) under reverse power flow scenario, and (d) DER detected frequency (top green), ST frequency set-point (top red) and DER output current (bottom) under reverse power flow scenario.

Table 5.7: System Parameters of ST LV Converter

Symbol	Quantity	Value
v_L	LV grid voltage	230 V (RMS)
L_L	inductance of LC filter	2.4 mH
C_L	capacitance of LC filter	8 μ F
T_s	sampling frequency	10 kHz
K_{pv}	proportional gain of PI	5e-3
K_{iv}	integral gain of PI	0.25
K_{pi}	gain of inner loop	10
K_{forc}	gain of FORC controller	0.1

In the overload control scenario, the security limit of ST LV current is 25 A_{RMS} . The DER is assumed to operate at unity Power Factor (PF) with 17 kW nominal power. Initially, the overall system operates at 50 Hz. The power rating of the DER is 12.8 kW, and a 15.9 kVA (PF= 0.9) linear load and a 6.1 kVA nonlinear load are connected to the grid. At $t = 0.8$ s, the load increases from 22 kVA to 32.6 kVA. As soon as the current of ST LV side exceeds

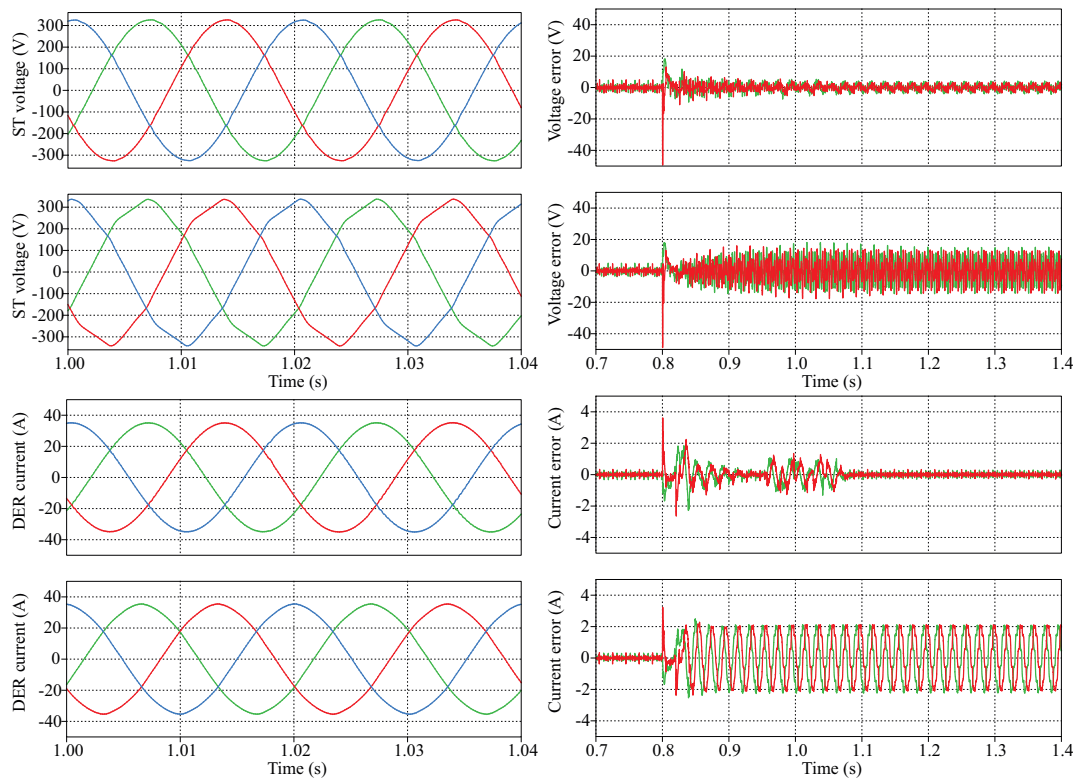


Figure 5.35: Performance comparisons of two different control strategies (FORC, CRC) under overloading scenario: (a) zoomed ST voltages at 49.5 Hz by using FORC (top) and CRC (bottom), (b) voltage control errors by using FORC (top) and using CRC (bottom), (c) zoomed DER currents at 49.5 Hz by using FORC (top) and CRC (bottom), and (d) current control errors by using FORC (top) and using CRC (bottom).

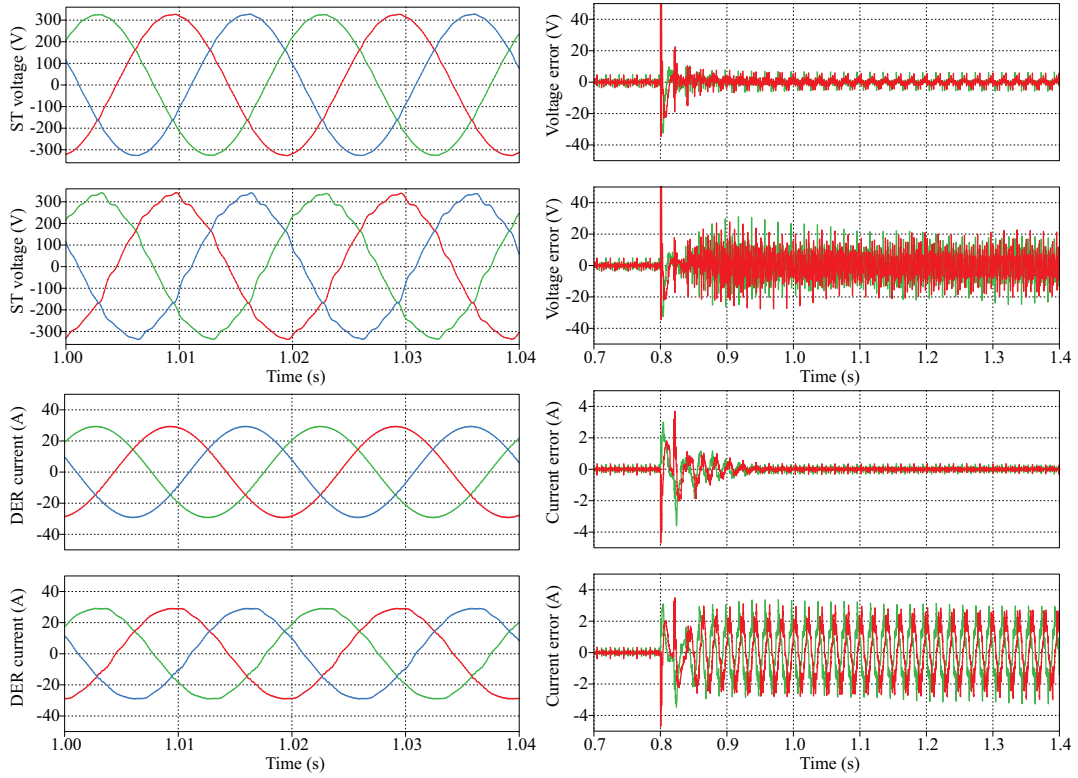


Figure 5.36: Performance comparisons of two different control strategies (FORC, CRC) under reverse power flow scenario: (a) zoomed ST voltages at 50.5 Hz by using FORC (top) and CRC (bottom), (b) voltage control errors by using FORC (top) and using CRC (bottom), (c) zoomed DER currents at 50.5 Hz by using FORC (top) and CRC (bottom), and (d) current control errors by using FORC (top) and using CRC (bottom).

Table 5.8: System Parameters of DER Grid Inverter

Symbol	Quantity	Value
i_g^*	DER nominal current	7.5 A (RMS)
L_{ff}	inverter-side inductance of <i>LCL</i> filter	2.4 mH
C_{ff}	capacitance of <i>LCL</i> filter	1 μ F
R_{ff}	damping resistance of <i>LCL</i> filter	2 Ω
L_{gf}	grid-side inductance of <i>LCL</i> filter	0.5 mH
T_c	sampling frequency	10 kHz
K_{pcc}	proportional gain of PI	2.5
K_{icc}	integral gain of PI	300
K_{icc}	gain of inner loop	10
$K_{forc,cc}$	gain of FORC controller	0.1

the security limit, the ST frequency-based overload control is activated, as shown in Fig. 5.34. The frequency decreases in order to activate the DER droop controllers, and the ST current decreases till below the security limit, reaching its new equilibrium point. The volt-

age amplitude remains constant and it regains the nominal value in less than one cycle after the application of the frequency change. Following the frequency change, the DER proportionally increases its power generation according to the given P - f droop curve. A new power equilibrium is established and the frequency holds the line of 49.5 Hz.

In the reverse power flow scenario, the overall load consumption is 32.6 kVA and the DER operates initially at the nominal power. At $t = 0.8$ s, the load demand decreases from 32.6 kVA to 16.7 kVA. As a result, a power flow reversal occurs (Fig. 5.34), and the ST frequency-based reverse power flow controller is activated. The ST LV side frequency increases until the power flow direction is changed and a new equilibrium is reached. The voltage amplitude remains constant and it regains the nominal value in less than one cycle after the frequency change. The DER behavior during the frequency control is shown in Fig. 5.34. The frequency detected by the SOGI-PLL can well follow the ST frequency change. Following the frequency change, the DER proportionally decreases its power generation according to the given P - f droop curve. A new power equilibrium is established and the frequency holds the line of 50.5 Hz.

The effectiveness of the proposed frequency-adaptive control strategy is verified in both scenarios as follows. Comparisons of ST voltage control and DER current control by using CRC and FORC schemes during the frequency control are presented in Fig. 5.35 and Fig. 5.36. In the overloading scenario (Fig. 5.35), it is seen that both the ST LV side voltage and the DER output current are well controlled by using FORC-based frequency-adaptive control, providing satisfactory performance even during the frequency control, while the CRC-controlled systems present considerable control errors when frequency deviates from the nominal value, leading to worse voltage and current waveforms. Similarly, in the reverse power flow scenario (Fig. 5.36), the FORC-based frequency-adaptive control offers better accuracy compared to the CRC-based control in terms of waveform and control error. Generally speaking, the FORC-based control is adaptive to the frequency variation, whereas the CRC-based control is not.

FORC Validation: experimental results

In the following section, the effectiveness of the frequency-adaptive control in a ST-fed grid has been experimentally validated by means of the microgrid setup described in Section 3. A 3.75 kW linear load and 1.12 kVA nonlinear load have been connected into the grid. The system parameters listed in Table 5.7 and Table 5.8 are used for the control systems and the output filters of both inverters.

Firstly, the distribution grid initially works under nominal condition (50 Hz), with the above-mentioned linear load. Then, the nonlinear load connects to the ST-fed grid, leading to a higher loading. The frequency control is activated when the ST current exceeds its security limit. In order to alleviate the overloading issue, the frequency gradually decreases from 50 Hz to 49.6 Hz so that the DER production increases and the load consumption decreases. A new power balance is eventually reached at 49.6 Hz. The ST LV side voltage waveform

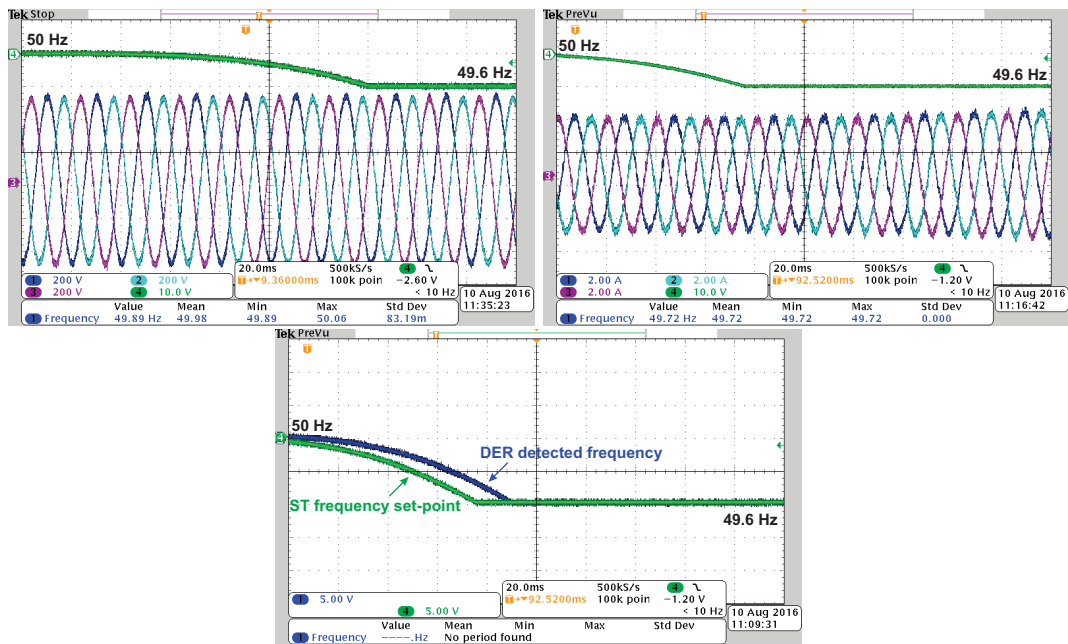


Figure 5.37: Voltage and current waveforms of a ST-fed distribution grid during overloading condition (time: 20 ms/div, voltage: 200 V/div, current: 2 A/div): (a) ST LV side frequency (top green) and ST LV side voltage (bottom), (b) DER detected frequency (top green) and DER output current (bottom), and (c) ST frequency set-point (green) and DER detected frequency (blue).

and its frequency set-point during frequency control are shown in Fig. 5.37a. The DER output current and the detected frequency during frequency control are shown in Fig. 5.37b. It is shown that the voltage amplitude stays constant and the power quality is ensured during both the steady-state and the transient stage. The current amplitude linearly increases according to the droop curve of the DER. To guarantee accurate frequency detection, the SOGI-PLL has been adopted in the DER for grid synchronization. The comparison between the ST frequency set-point and the detected frequency via SOGI-PLL is shown in Fig. 5.37c. It is seen that the frequency detected by the PLL can timely follow the ST frequency with less than 10 ms delay, offering good performance during frequency control stage.

Following, the zoomed voltage and current waveforms in a ST-fed grid during frequency control stage by using different control strategies are compared. In Fig. 5.38 and Fig. 5.39, the CRC scheme has been employed for both the ST voltage control and the DER current control. It is seen that both the ST LV side voltage and DER output current are distorted during frequency control (e.g. 49.7 Hz). When the proposed FORC-based voltage and current control are used, the ST LV side voltage and DER output current are shown in Fig. 5.38 and Fig. 5.39, with less harmonic distortion. More details of the performance comparison have been listed in Table 5.9. The case study shows that CRC is sensitive to grid frequency variation in terms of THD and amplitude, whereas FORC is not. By using the proposed frequency-adaptive control, the ST-fed distribution grid can provide satisfactory performance in terms of control accuracy and power quality.

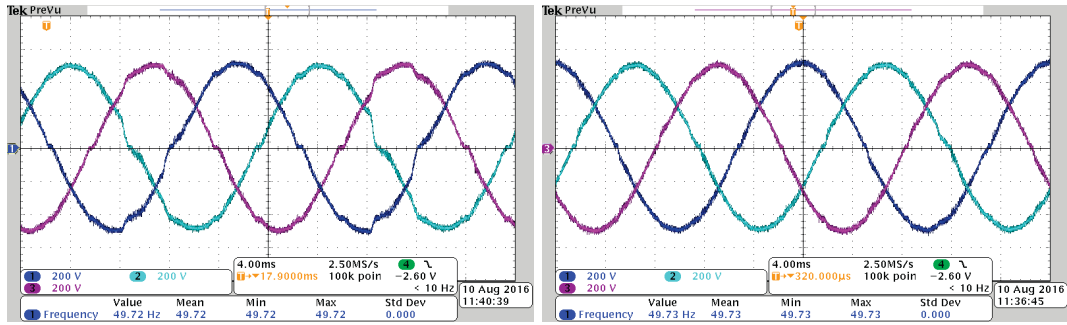


Figure 5.38: Comparison of ST LV side voltages with different control strategies during overloading condition ((time: 20 ms/div, voltage: 200 V/div): (a) CRC-controlled ST LV side voltage and (b) FORC-controlled ST LV side voltage.

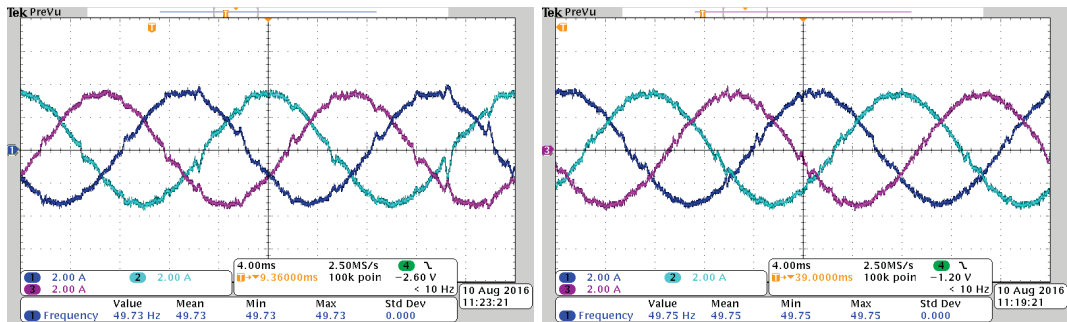


Figure 5.39: Comparison of DER currents with different control strategies during overloading condition ((time: 20 ms/div, current: 2 A/div): (a) CRC-controlled DER current and (b) FORC-controlled DER current.

Table 5.9: Performance Comparison of CRC- and FORC-Controlled Systems

Control	Frequency	Voltage	Current	THD_V	THD_I
CRC	50 Hz	0.987 p.u.	0.987 p.u.	2.90%	3.76%
	49.8 Hz	0.967 p.u.	0.938 p.u.	6.54%	6.97%
	49.6 Hz	0.959 p.u.	0.917 p.u.	7.21%	8.36%
FORC	49.8 Hz	0.981 p.u.	0.975 p.u.	3.12%	4.21%
	49.6 Hz	0.979 p.u.	0.958 p.u.	3.35%	4.69%

5.5 Conclusions

The Smart Transformer has the capability to influence the power consumption in the ST-fed grid by means of voltage and frequency variations. On the opposite of the current practice, the ST is able to combine the voltage and frequency control to interact with the local loads and generators, in order to influence the net load demand. In this chapter 2 services are presented: the reverse power flow limitation controller and the ST overload controller. The first one contributed to the management of the MV grid, limiting the power flow reversal from LV to MV grid. The RPFL controller, increasing the frequency in the grid, interacts

with the local generators to reduce their power production, and thus solving the reverse power flow. In the second case, the issue of ST limited overload capability is dealt with. With a combined voltage/frequency control, the ST can manage conditions that without control would have led to overload. The frequency controller is activated as first, trying to increase the power production of the local resources. In case of limited power availability, the voltage controller operates, acting directly on the load sensitivity to voltage. Thus reducing the voltage, also the load demand is automatically reduced. The OVC can be further improved implementing the OLLI algorithm shown in the chapter 4: the ST is able to recognize if the load behaves like a constant power, constant current or constant impedance load, and thus applies the correct voltage variation to solve the overload condition. If a constant power load is recognized, the ST increases the voltage in order to decrease the current. A decrease in the voltage, instead, leads only to an increase of the current in the ST, and thus a worsening of the overload conditions. Eventually, a fractional order repetitive controller has been presented to deal with the issue of the optimal voltage control under variable frequency. The actual controllers can deal with the voltage control also in presence of harmonic content. However, their optimal performances are guaranteed only in case of nominal frequency application. The FORC guarantees instead an optimal voltage control and harmonic compensation, also in case of different voltage frequencies (e.g. 49.6 Hz), that can be met during the OVC or RPFL controller application.

6 Voltage control of ST-fed grid: transmission grid services

The ST feature to control the LV load described in chapter 5, focuses particularly on services provided to the distribution grids, like the reverse power flow control or the ST overload control. It has been seen that the ST can modify the loads and generators active power consumption by means of voltage and frequency variations, calling the LV grid resources (loads and generation) to participate to the distribution grid control. Moreover, with the application of the on-line load sensitivity identification algorithm, the load control accuracy improves, allowing the net load power consumption controllability within a certain power range (e.g., $\pm 10\%$). In this chapter, this control capability is extended to provide ancillary services for the transmission grid. The ST is seen from the transmission grid as an active load able to influence its power consumption instantaneously, and thus able to provide support to the HV grid.

The ENTSO-E has gathered in a survey the services that the loads can provide at transmission level [55]. In countries like France, Spain, Belgium and Poland, the load participates actively to the balancing services, and the case of aggregated small size consumers (active in France, Belgium and Poland) fits particularly to the ST-fed grid one. The ST can work as interface between the request of services from the TSO and the loads willing to participate to services market. The importance of the collaboration between TSOs and DSOs (and their customers) has been acknowledged by the Agency for the Cooperation of Energy Regulators (ACER) in [137], where a stricter collaboration between DSOs and TSOs is desired. The loads give the permission to the ST to vary the grid parameters (e.g., voltage amplitude and frequency) from the nominal values in order to vary accurately the LV grid active power consumption. Thus the ST-fed grid works as despatchable resource and it enables the participation to the ancillary services market like any energy resource present in the grid, such as generators and storage plants.

Real Time Frequency regulation

Following a disturbance in the grid (faults, lines disconnection, etc.), the frequency deviates from the nominal value. If the system is stable, the frequency restores close to the nominal value after a short transient. However, in case of disturbances in weak systems (e.g., lack of power reserve or connection lines), the frequency may collapse. The increasing integration of DG, due to the converter-based connection, reduces the stiffness and the inertia of the grid, increasing the frequency excursion, affecting the grid stability in the most severe cases [138][139]. A particular case is related to the high penetration of wind power plants, that increases the frequency deviation and the frequency rate of change during perturbation due to the lower grid inertia. As noted in [140], the rate of change of the frequency results to be independent from the wind generators technology adopted, showing only small differences among the different solutions. Only exception is the induction generator-based machines, where, being directly connected to the grid, the rotors follow the frequency variation [141].

Control actions for supporting the frequency are based on firm under-frequency load shedding [142] and energy reserves, for instance BESSs [143]. Of particular interest is the application in wind turbines, due to the massive integration in the grid [144]. A potential solution is the implementation of frequency controller in the wind plants. In [141], a combined inertia control and frequency droop characteristic has been proposed to support the frequency during grid perturbation and to damp the effect of wind fluctuations in weak grids. In the grid of the future, the consumers will be involved more in the energy market and in participating in ancillary services. The implementation of frequency-dependent controllers in electrical appliances such as refrigerators has been proposed in [49]. It has been proved that reducing the power consumption during demand step-changes helps the generators to cover the power imbalance during transients.

The ST, by means of the Load Identification and Control, can offer a Real Time Frequency regulation, where the frequency deviation signal determines the quantity of load reduction to be performed. Applying the on-line load identification and control, the ST can vary instantaneously the LV load within a certain limit (for instance, $\pm 10\%$) in order to support the transmission system in the frequency regulation.

Generator ramp rate support

In order to regulate the frequency under high power production variability from renewables, the controllable resources (e.g., conventional generators, hydro) must follow the renewables production increasing or decreasing rapidly the power output. At higher penetration of renewables, the required ramp ranges increases, as well as the operating costs for the generators [145]. A possible solution to this issue is to include the generators ramp limitation in a multi-interval problem as proposed in [146]. Including the forecasted renewables energy production in more time intervals (e.g., 5 minutes each one), the multi-interval problem solution imposes a pre-ramping of generators, maximizing the economic use of the generators ramp capability. An alternative is the installation of battery energy storage systems with a ramp rate control in photovoltaic power plants [45]. In case of fast power variation of the plant, the battery supplies the power needed to respect the maximum allowable ramp rate.

Applying the on-line load identification and control, the ST can follow the renewable production, adjusting the load consumption within a certain limit (e.g., $\pm 5\%$) in order to alleviate the generator's power tracking. It is shown in this chapter that the ST can vary the load consumption to smooth the generators operation during perturbations in the grid (e.g., generators / big loads disconnections).

6.1 On-Line Load sensitivity Identification and Control

The OLLI algorithm presented in chapter 4 and the sensitivity-based OVC presented in chapter 5 showed that the ST is able to regulate the LV grid active power consumption acting on

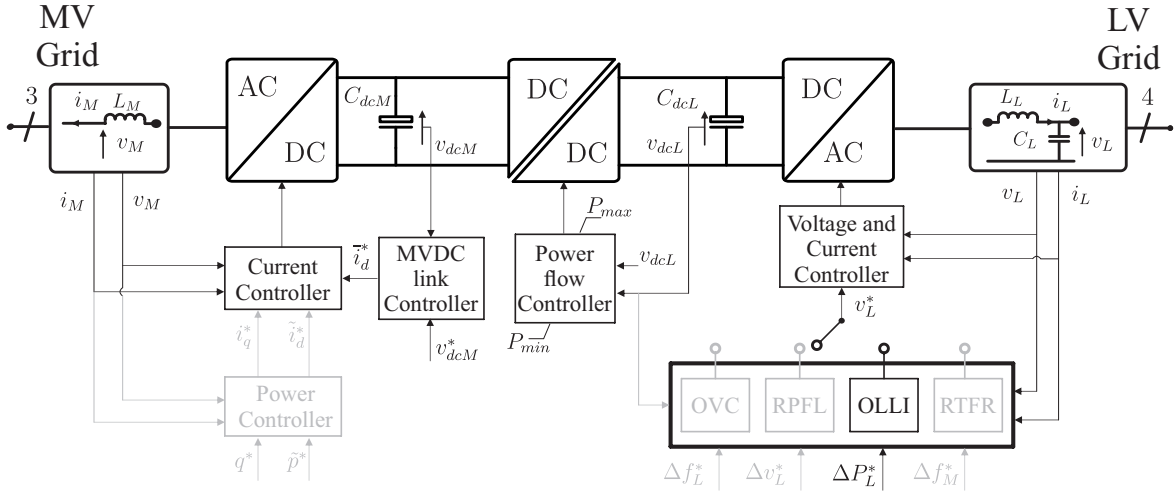


Figure 6.1: Smart Transformer control scheme and On-Line Load sensitivity Identification and Control (e.g., Soft Load Reduction) implementation.

the voltage amplitude. Here an analog concept is presented, based not anymore on a signal internal to ST (e.g., current or temperature), but coming from a higher level controller. In particular, this chapter refers to the TSO control room, where the bulk power system is managed. If the TSO sends a request to modify the power consumption (both upwards and downwards), the ST adapts the voltage amplitude set-point in order to get the requested power variation. To control the power variation, the ST has to evaluate the load active power sensitivity to voltage K_p in real time. Applying the on-line load sensitivity identification algorithm and measuring the active power flow, the ST gets all the needed information for controlling properly the active power in the grid. In this section the load control method is described, referring particularly on the active power sensitivity to voltage.

In an unbalanced three-phase system, such as the LV grid, it is possible that each phase has a different load sensitivity. Thus the proposed algorithm evaluates separately the sensitivities K_p of each phase, using a simultaneous balanced three-phase load disturbance. Assuming a required percentage of requested load variation $-0.1 < \lambda < 0.1$ ($\pm 10\%$ of the total load), the desired load change is:

$$\Delta P = \Delta P_A + \Delta P_B + \Delta P_C = -\lambda(P_A + P_B + P_C) \quad (6.1)$$

where P_A , P_B , P_C are the initial consumed active powers in each phase and ΔP_A , ΔP_B , ΔP_C , ΔP the corresponding phase and total load variations.

Considering the normalized load power sensitivity:

$$\frac{\frac{P(t_k) - P(t_{k-1})}{P(t_{k-1})}}{\frac{V(t_k) - V(t_{k-1})}{V(t_{k-1})}} = K_p \quad (6.2)$$

and applying it to all three phases:

$$\begin{aligned}\Delta P_A &= \frac{P_A}{V_A} K_{pA} (V - V_A) \\ \Delta P_B &= \frac{P_B}{V_B} K_{pB} (V - V_B) \\ \Delta P_C &= \frac{P_C}{V_C} K_{pC} (V - V_C)\end{aligned}\quad (6.3)$$

the voltage to be applied for achieving a specified power variation ΔP is:

$$V = \frac{\Delta P + (P_A K_{pA} + P_B K_{pB} + P_C K_{pC})}{\frac{P_A}{V_A} K_{pA} + \frac{P_B}{V_B} K_{pB} + \frac{P_C}{V_C} K_{pC}} \quad (6.4)$$

The ST is able to impose three phase voltages with equal amplitude independently from the load, so that (6.4) can be simplified assuming $V_A = V_B = V_C = V_0$. The voltage variation to be applied in p.u. is now defined with the formula:

$$\frac{V}{V_0} = 1 + \frac{\Delta P}{P_A K_{pA} + P_B K_{pB} + P_C K_{pC}} \quad (6.5)$$

If the ST receives the request to modify the grid consumed active power and the voltage to be applied does not exceed neither the minimum nor the maximum voltage limit, the On-Line Load sensitivity Identification and Control algorithm applies the new voltage set-point as described in (6.5). As follows, the On-Line Load sensitivity Identification and Control is applied for complying with the TSO request to curtail the power consumption for a certain amount of time due to unexpected severe events in the grid (e.g., faults). This application, called "Soft Load Reduction", can be a valid alternative to firm load shedding, due to the flexibility to reduce the power consumption without disconnecting the loads.

Soft Load Reduction

Load shedding is an extreme measure to be adopted when the stability of the grid can be compromised due to severe contingencies: faults, generators disconnections, lines tripping [147]. However, firm load shedding is a severe measure for the disconnected customers and incurs considerable costs [148]. The ST can decrease the consumed load active power by controlling the voltage in the LV grid in accordance with load sensitivity, thus realizing a softer load reduction. The accuracy of this method depends on the knowledge of the load active power dependence on voltage. In order to guarantee to the TSO and DSO a pre-specified load reduction, an accurate analysis of the load sensitivity is needed. The On-Line Load Identification can perform this analysis and provide accurate data on load composition, and thus an accurate load reduction when needed.

The On-line Load Identification and Control is represented with more details in Figure 6.2. At each time step, the controller measures current and voltage from the ST filter and performs

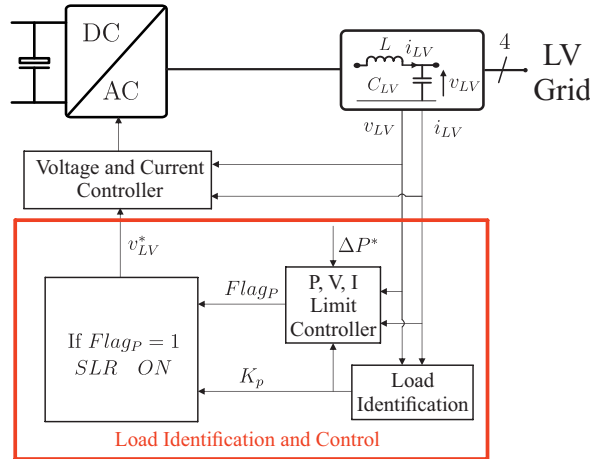


Figure 6.2: Load Identification and Control scheme: the limit controller triggers the Soft Load Reduction (SLR) depending on the external signal coming to ST and the ST internal constraints (e.g., current).

a first security check on the power, voltage and current limits. If the ST receives the request of load reduction, the limit controller triggers the Soft Load Reduction control. Respecting the voltage and current limit, the Soft Load Reduction algorithm applied the requested voltage change. If the security current limit of ST is exceeded (here fixed at 95 % of the maximum current), ST limit controller overrides any control action and triggers the Voltage-Based OVC (see Chapter 5). The ST performs load identification every 20 s (in a real application this could be every 5 – 10 minutes) and evaluates in real time the amount of voltage drop to be applied for achieving a 5 % reduction of the load. A significant source of variability regarding voltage sensitivity is the varying power injection from uncontrolled DG. Thus, in order to introduce variability in the grid, the PV active power curves shown in Figure 4.12 have been implemented in the two photovoltaic power plants in Figure 4.11, both shown in Chapter 4.

The ramp voltage adopted in this study case to measure load sensitivity is -0.02 p.u. over a time window of 0.5 s and the total voltage disturbance lasts 2 s. As shown in Figure 6.3, at $t = 100$ s the ST receives the signal from the TSO/DSO to reduce the load by 5 % for 100 s. The ST uses the active power sensitivities to voltage evaluated in the previous time interval (Figure 6.3a) and applies a reduction of 8 % of the voltage (Figure 6.3b). The green line in Figure 6.3b is the bus 8 voltage profile, representing the lowest voltage in the grid during the load reduction. It is shown how the voltage is kept near 0.90 p.u., still acceptable considering the emergency request of load reduction by the TSO/DSO. Note that the load is less sensitive to voltage variation in this case than a constant current load ($K_P < 1$). As can be noticed from Figure 6.3c,d, the average of the load shed is about 4.6 % for the the entire time window. The voltage and the load active power are restored to the nominal value when the load reduction is not needed any longer.

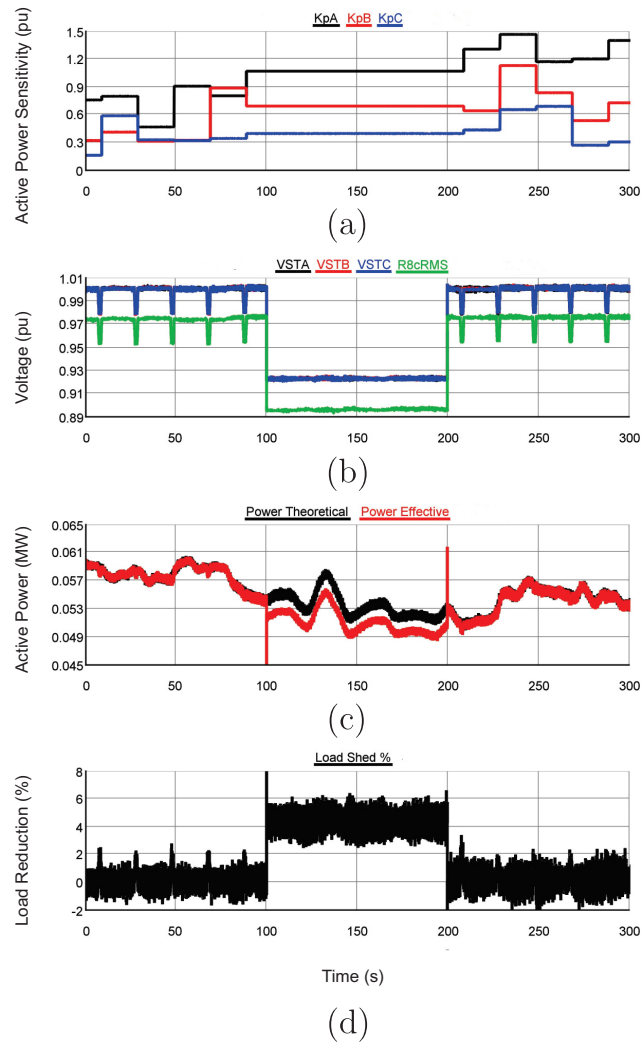


Figure 6.3: Soft Load Reduction: (a) active power exponential coefficients evaluated in real time, (b) ST voltages and bus 8 voltage (green line), (c) Three-phase active power at 1 p.u. voltage (black line) and when the 5 % load reduction is applied (red line), (d) load reduction in %.

6.2 ST transmission grid frequency regulation

An increasing integration of DERs, mostly renewable-based, and a higher demand variability, stress the transmission grid that must cope with the customers and producers requests, as well as with market rules. Under these conditions an unexpected event (e.g., fault, generator disconnection, or line tripping) challenges the stability of the system. A violation of the power quality standard (under- or over-voltage/frequency violations) can occur, and in extreme cases it may trigger a cascade of failures that leads to regional or national blackouts. In recent history a particular case in the European grid involving frequency stability occurred: the Italy blackout in 2003. In the Italian case a series of interconnection lines tripping leaved the system with a generation deficit of 6400 MW, causing the generator breakers opening due to under-frequency conditions [149][150]. Currently, the European Transmission System Operators (TSOs) are not able to give a definitive explanation to this phenomenon. Final

considerations shown in [149] concluded that a proper load shedding scheme could have saved the system from the collapse, mostly if it would have acted promptly.

The Smart Transformer (ST) can offer frequency regulation services to the HV grid, exploiting its feature to control the active power consumption in the LV grid. When the OLLI method [J5] is implemented in a ST, the load active power response to voltage and frequency variation can be evaluated in real time. From this analysis a proper corrective control action can be applied to offer frequency regulation services to the transmission grid.

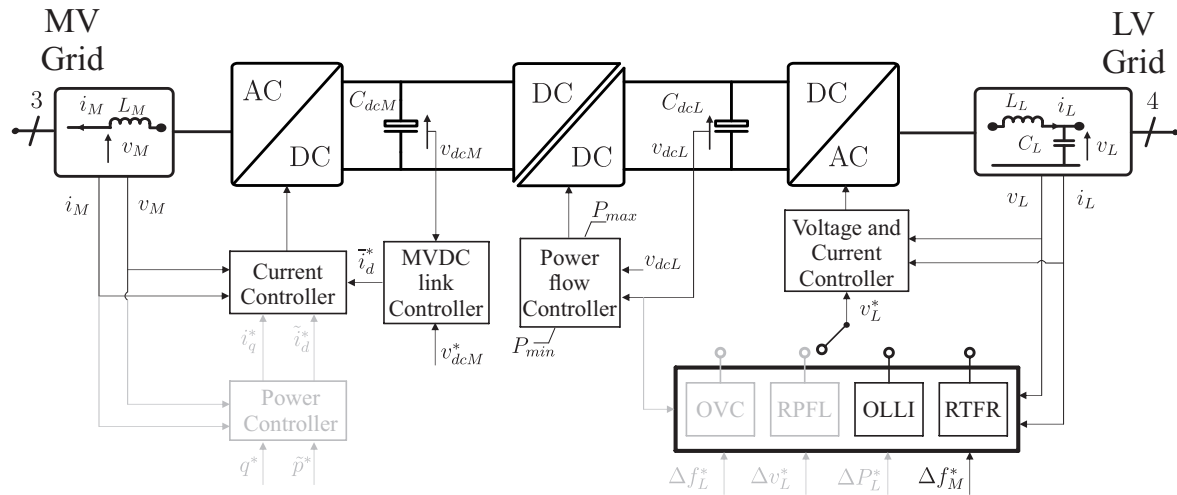


Figure 6.4: Smart Transformer Real Time Frequency Regulation (RTFR) controller scheme.

The real time frequency controller represented in the more general Figure 6.4 is described in more details in Figure 6.5. If a variation of frequency is measured in the ST MV grid side, the ST sets the power modulation ΔP^* following the droop characteristic shown in Figure 6.6:

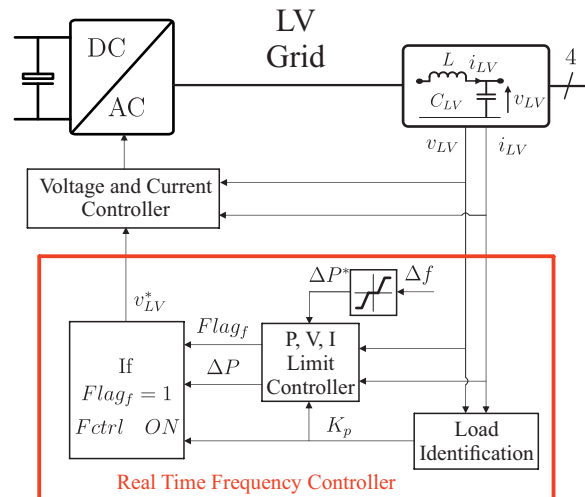


Figure 6.5: Real time frequency controller scheme

The power modulation request ΔP^* is checked by a limit controller, that sets the power variation request ΔP . Every few minutes the load sensitivity evaluation algorithm estimates the new K_P for each of the three phases and, if the ST measures a frequency deviation, it applies the voltage variation in order to control the load consumption. If the ST receives the

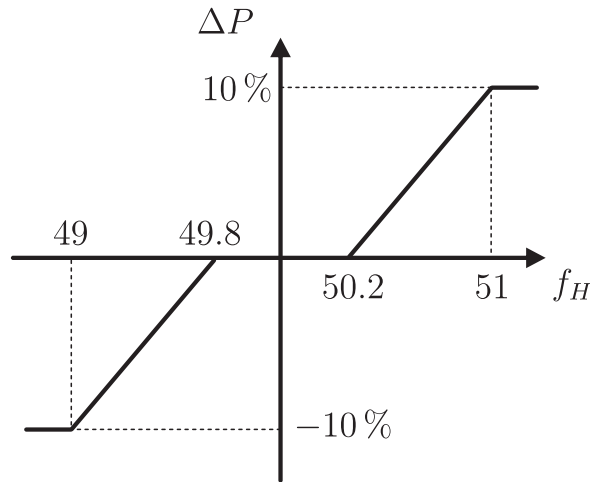


Figure 6.6: Frequency/power characteristic implemented in the RTFR controller.

request to modify the active power consumption in LV grid to compensate the transmission grid frequency variation, the on-line control algorithm applies relation (6.5). To be set, the voltage must be constrained within the minimum and the maximum voltage limit. In order to limit the power quality impact on the LV grid, the ST restores the voltage nominal value after the frequency transient ends and the frequency value is inside the controller dead-zone.

Equivalent HV system model

In order to emulate the behavior of the high voltage grid, the equivalent system shown in Figure 6.7 has been considered. This system consists of a governor, a turbine (reheat steam system), the rotor inertia and load damping contribution. The governor is represented with a droop characteristic that adjusts the power output in the turbine linearly with the frequency deviation from the nominal value. The governor dynamic is simulated with a first-order low pass filter with time constant T_G . The transfer function of the turbine depends on the reheater time constant T_{RH} , the fractional power of the high pressure section of the turbine F_{HP} , and the time constant of the main inlet volume T_{CH} . R_G is the governor droop characteristic. The output of the turbine is the mechanical power variation ΔP_m . The equilibrium of the system is reached when the mechanical power variation is zero or is exactly equal to the electrical power variation ΔP_e . The HV system has an inertia M_I created by the rotating machines present in the grid, that links the frequency deviation to the power imbalance. A load damping factor D_L has been added to emulate the load frequency dependency [114]. When the two powers are not balanced, the system output $\Delta\omega_r$, that is the frequency deviation from the nominal value, becomes non-zero. It means that the frequency varies in the system and the generators and their governors must provide the active power needed for restoring the $\Delta\omega_r$ to zero. The equivalent system parameters have been taken from [114], as described for the case of reheat turbine governor. It can be argued that several turbines with different time constants and transients behavior can be chosen, obtaining smoother or more oscillating results. However, the frequency support control impact will not differ substantially from case to case.

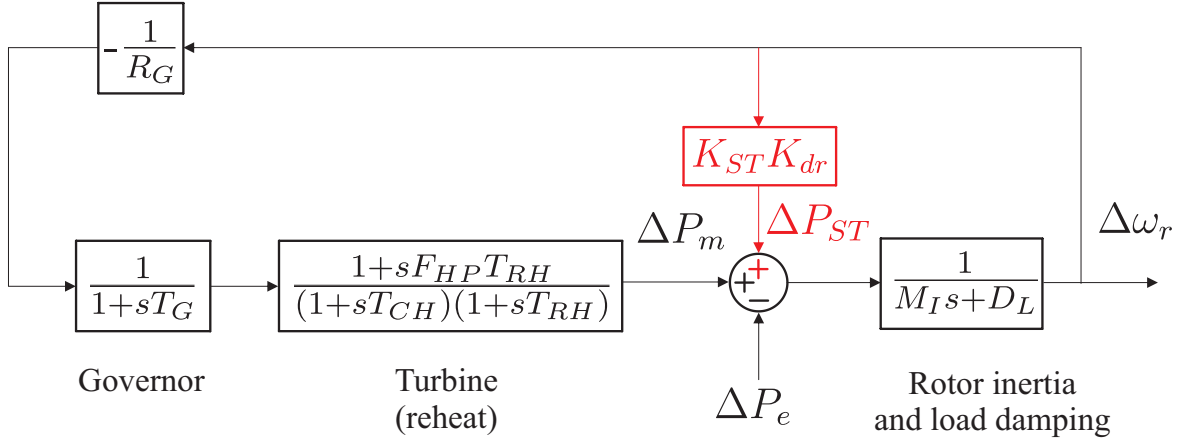


Figure 6.7: Equivalent HV system model

In Figure 6.7, the contribution of the ST is highlighted in red. The ST, spread in the distribution grid, contributes to the system stability with the power variation ΔP_{ST} . The ST power variation is decided by means of the droop curve described in Figure 6.6 and linearized in this scheme with the droop coefficient K_{dr} . The parameter K_{ST} describes instead the distribution of ST in the grid. This parameter varies between 0 and 1, and indicates the penetration of the ST-fed load in the grid. The HV system parameters are listed in Table 6.1.

Table 6.1: Equivalent HV system parameters

Parameter	Value	Parameter	Value
R_G	0.05	T_G	0.2 s
T_{CH}	0.2 s	F_{HP}	0.3
T_{RH}	7 s	M_I	10 s
D_L	1	K_{dr}	-6.25

To understand the contribution of the ST control, the loop in Figure 6.7 has to be analyzed. Let us consider the contribution to the frequency control by the equivalent generator equal to:

$$E_{Gen}(s) = -\frac{1}{R_G} \frac{1}{1+sT_G} \frac{1+sF_{HP}T_{RH}}{(1+sT_{CH})(1+sT_{RH})} \quad (6.6)$$

where the contribution of governor and turbine are summed up. The total contribution of generator and ST is then:

$$E_{Gen,ST}(s) = K_{ST}K_{dr} + E_{Gen}(s) \quad (6.7)$$

and considering the system inertia and load damping factor

$$I_d(s) = \frac{1}{M_I s + D_L} \quad (6.8)$$

the response of the system frequency following an electrical power variation is described by the transfer function:

$$G_{\Delta P_e}(s) = -\frac{I_d(s)}{1 + I_d(s)E_{Gen,ST}(s)} \quad (6.9)$$

The contribution of the ST RTFR controller is visible in the root locus in Figure 6.8. Increasing the participation of the ST, the poles tend to move toward the real axis and moving away from the imaginary axis. The result is in a more damped system than in the case without ST RTFR control.

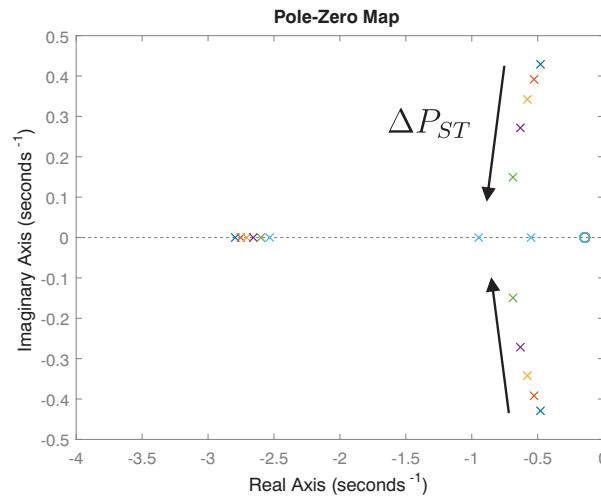


Figure 6.8: Rootlocus under variable penetration of Smart Transformer.

This behavior is clearer if the step response of the system is shown. As depicted in Figure 6.9a. Under a variation of 100 % of electrical load, the HV system has a variation equal to -0.11 pu in the frequency, reaching in a 50 Hz grid the minimum frequency of 44.5 Hz. With the implementation of STs in the grid, the frequency variation decreases, till reaching -0.08 pu (46 Hz peak) in case of 50 % of ST-fed grid power share. The behavior of the equivalent generator changes as well in presence of ST. The RTFR algorithm supports the generator during the transient, reducing and damping the generator power response (Figure 6.9a).

In the previous case, a system inertia $M=10$ s has been chosen. However, with the increasing integration of power electronics-based generators the inertia can decrease sensibly. The cases with different system inertia are shown in Figure 6.10. The inertia is varied from 2 s to 10 s and the step response of the system has been evaluated. Two cases are evaluated: (a) no ST control in the grid (Figure 6.10a); and (b) ST-fed load equal to 20 % of the total load and RTFR control active (Figure 6.10b). Two effects are noticeable: the RTFR control reduces the negative frequency variation under any inertia values, and the system is damped, mostly if the inertia is low, such as $M=2$ s (light blue lines in pictures).

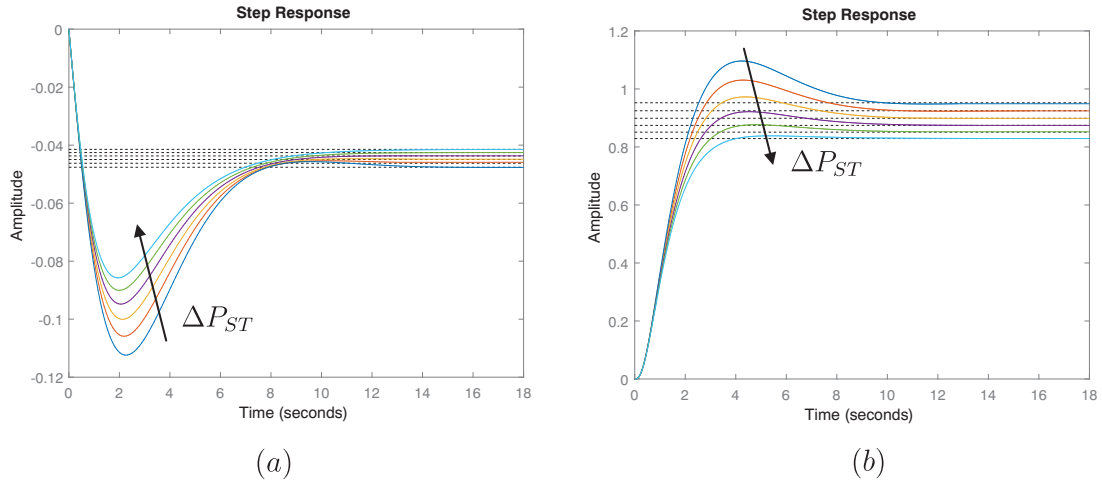


Figure 6.9: Step response of the HV system to a negative variation of electrical power ΔP_e : (a) Frequency variation in per-unit; (b) Generator response in per-unit.

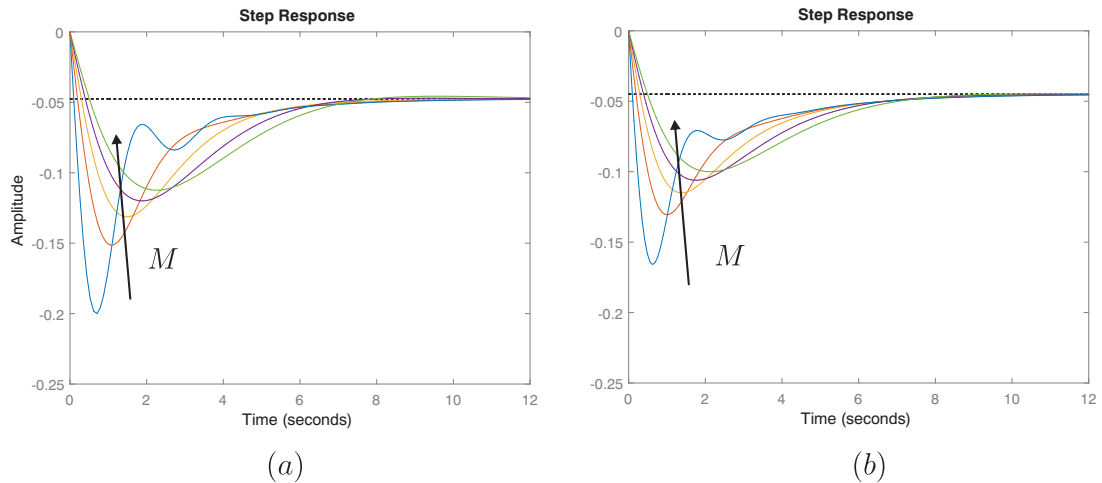


Figure 6.10: Frequency variation under different system's inertia: (a) no ST contribution; (b) ST contributes to 2% of the total power.

6.3 Power Hardware In Loop evaluation

The evaluation of the real time frequency support controller has been verified by means of PHIL evaluation. The PHIL scheme, already described in Chapter 3, has been modified in this study as shown in Figure 6.11. The Hardware under Test, in this case the ST, controls the voltage v_L on the filter capacitor. The measurement system measures the voltage and sends the measurement signals v_L to the RTDS software, RSCAD. Here the voltage is applied directly in the ST-fed grid by means of an ideal controlled voltage source. The current demanded by the grid i_g^* is sampled in RTDS and sent to a current controller, that controls the current injection i_g of the linear power amplifier in order to reproduce accurately the grid current i_g^* , closing the loop. Between the simulated grid and the ST hardware, a current scale factor of 100 has been introduced in the current to cope with the limited power capability of the hardware in lab. It means that 1 kW power change in the hardware side corresponds to

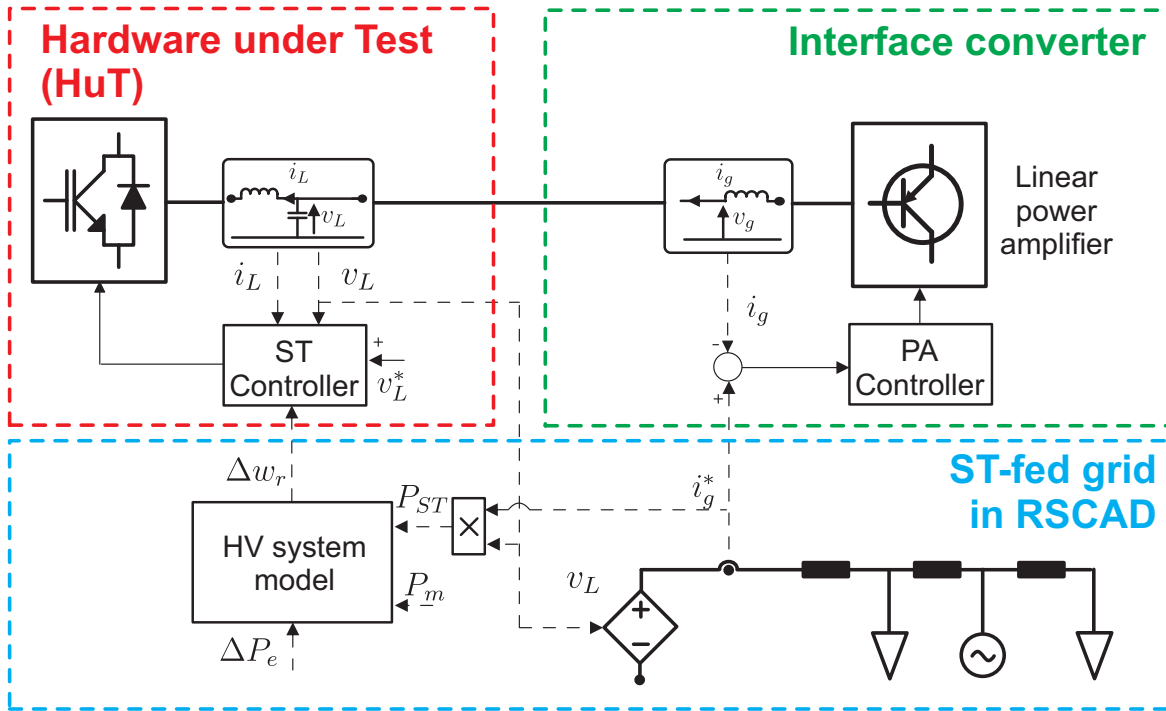


Figure 6.11: PHIL: Hardware under Test (HuT) (red frame), Hardware of the PHIL setup (green frame), Software of the PHIL setup (RSCAD) (blue frame).

100 kW power change in RSCAD.

To simulate the transmission grid, the HV system equivalent model, shown in the previous section, is realized in RSCAD. This model emulates the grid transient behavior during disturbances. It receives, as input, the ST power measurement P_{ST} from the LV grid simulated in RSCAD and the machines mechanical power P_m and electrical power variation ΔP_e from an external set point. The output of the HV system model is the frequency deviation that is sent to the ST real time frequency support controller. The parameters of the ST setup are specified in Table 5.6 in chapter 3.

This work applies a modified version of the CIGRE European LV distribution network benchmark described in Chapter 3 and depicted in Figure 6.12. The LV grid has been implemented in RSCAD and simulated with a time step of $45 \mu s$, in the range of the typical time steps used for PHIL applications [100]. The CIGRE grid has been realized under the following assumptions: 1) the three-phase loads have been considered as constant impedance model and balanced, and 2) the photovoltaic power plants *A* and *B* are both injecting 20 kW, with power factor $\cos(\phi)=1$. Table 6.2 itemizes the load power consumption and the position in the grid, while Table 6.3 itemizes the location and power injection of the two PV power plants.

The PHIL evaluation has been performed applying a electrical power variation ΔP_e to the equivalent system in order to create an under-frequency and over-frequency conditions in the HV system. In order to assess the influence of the ST frequency support to the HV grid, 5 different test cases have been considered: the base case, where no RTFR control has been applied; and the following 4 cases where the ST-fed load controlled via RTFR increases

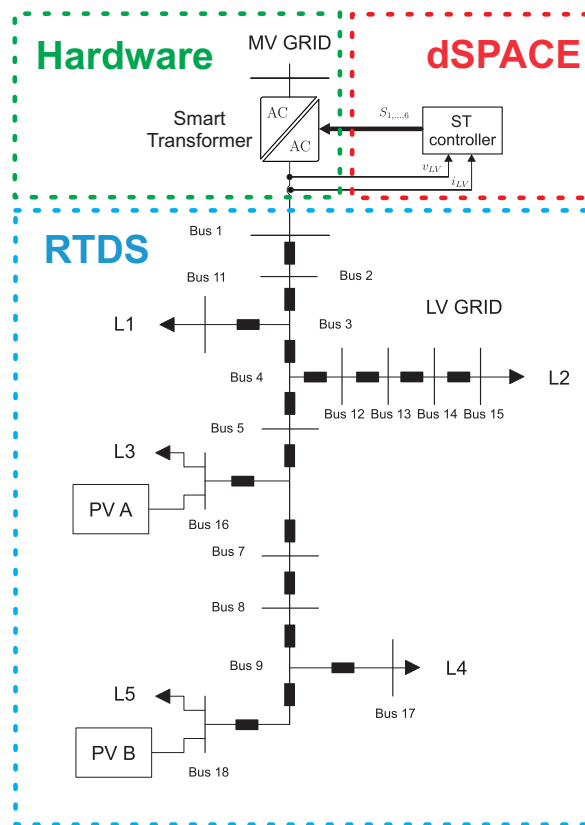


Figure 6.12: modified CIGRE European LV distribution network benchmark implemented in RSCAD.

Table 6.2: Load Data

Load	Bus	Active Power (kW)	Reactive Power (kVAr)
L_1	11	25	10
L_2	15	50	30
L_3	16	45	20
L_4	17	5	5
L_5	18	20	5

Table 6.3: PV Data

DER	Bus	Active Power (kW)	$\cos\phi$
PV A	16	20	1.00
PV B	18	20	1.00

respectively to 10 %, 20 %, 30 %, and 50 % of the total load. In this evaluation, a maximum controllable active power of 10 % has been assumed for each ST. This limitation is done in order to avoid large voltage excursions in LV grid due to the RTFR controller action.

Two events are considered in the PHIL evaluation: an under-frequency case, created by an increase of the load power request of 20 %; and an over-frequency case, caused by a decrease

of the load power equal to 20 %.

Under-frequency event

To create an under-frequency event, the grid electrical power P_e has been increased with a step of 20 %. This contingency can be referred to the lost of a big power plant or the disconnection of an area supplying the transmission system under investigation. From the Figure 6.13 plotted in RSCAD, it can be seen how without any control the frequency tends to decrease below 49 Hz.

Increasing the presence of ST in the grid two important effects can be noticed. Firstly, the frequency negative peak is reduced introducing more ST-based grids. With 20 % ST presence in the grid, the frequency peak is reduced of 100 mHz, while with the futuristic case of half load controlled by ST (50 % case), the frequency peak is reduced of more than 200 mHz.

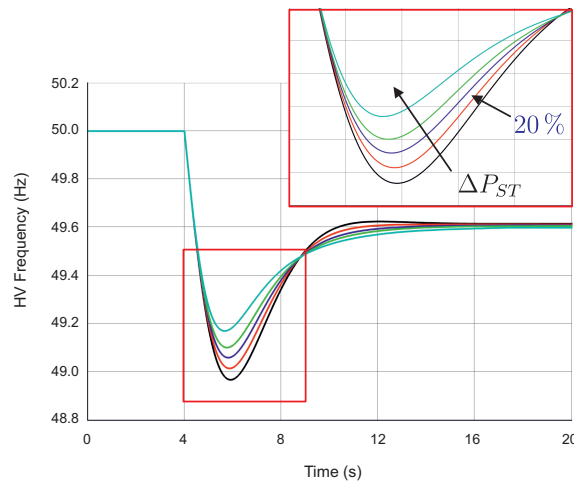


Figure 6.13: HV frequency during under-frequency condition

Secondly, the ST shows a faster control action than the HV system (governor and turbine). In Figure 6.14, it can be noted how the ST presence helps to reduce the mechanical power variation peak ΔP_m , from 23 % to 20.5 % in case of 20 % ST-fed load, till to reach an over-damped behavior in case of 50 % of controlled load. Two major effects are achieved: the system power oscillations are more damped than the case without any control; the STs reduces the generator effort to reestablish a constant frequency value.

To depict the operation of the real time frequency controller in LV grid, the test case of 20 % ST-fed controlled load has been chosen. Applying the on-line load sensitivity identification, the grid K_P has been found equal to 1.25 pu. During the power variation in the HV grid, and the following under-frequency conditions, the ST reduces the voltage set-point in the grid up to 0.92 pu (Figure 6.15). The grid experiences an under-voltage condition, with the buses farther from the ST slightly below 0.9 pu. However, this condition is found still acceptable due to short duration of the under-voltage condition. The control, after a 20 second transient, restores the voltage nominal value in order to not affect the LV grid power quality.

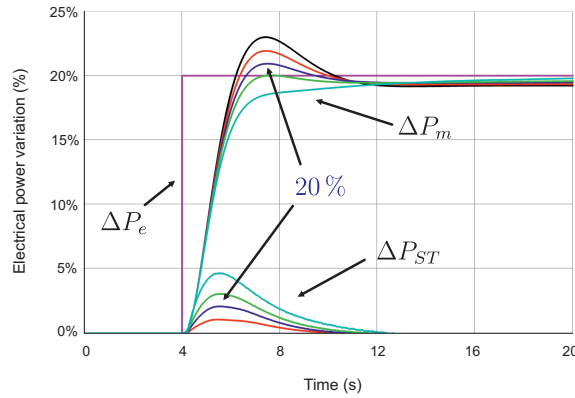


Figure 6.14: HV system power during under-frequency condition

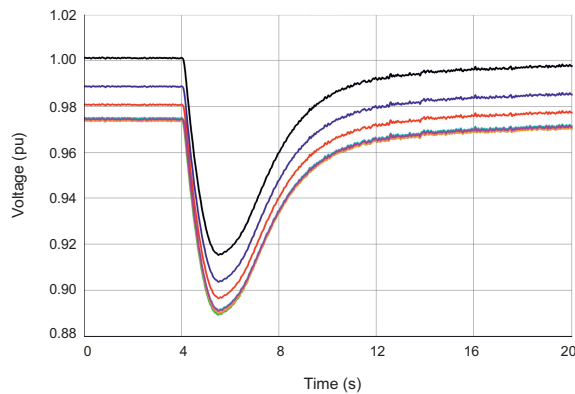


Figure 6.15: Voltage profile in the LV grid during the frequency controller operations, (Test Case C).

In Figure 6.16 the ST measured powers have been plotted. The first graph shows the measured active power in the hardware side, instead in the second graph the LV grid active (black line) and reactive (red line) power have been plotted. As can be noticed, there is a factor 100 between the measured power in hardware and software side. During the frequency transient, the frequency reaches almost 49 Hz. Following the droop characteristic in Figure 6.6, it corresponds to a power variation of 10%. The ST converter in the hardware side, varies the active power from 1.05 kW to 0.95 kW during the frequency negative peak, as expected from the droop characteristic. Where, in the RSCAD side, the LV grid power consumption varies from 105 kW to 95 kW. This demonstrates the accuracy of the on-line load sensitivity identification algorithm.

Over-frequency event

Analogously to the under-frequency case, the ST is able to support the transmission grid during over-frequency transients. As can be noted in Figure 6.17, the real time frequency controller of ST is able to reduce of 100 mHz or 200 mHz the frequency deviation in the 20% and 50% controlled load case, respectively. In terms of active power contribution, the ST contribution is similar to under-frequency case (Figure 6.18). Increasing the presence of ST, the power contribution from the transmission grid generators ΔP_m is more damped.

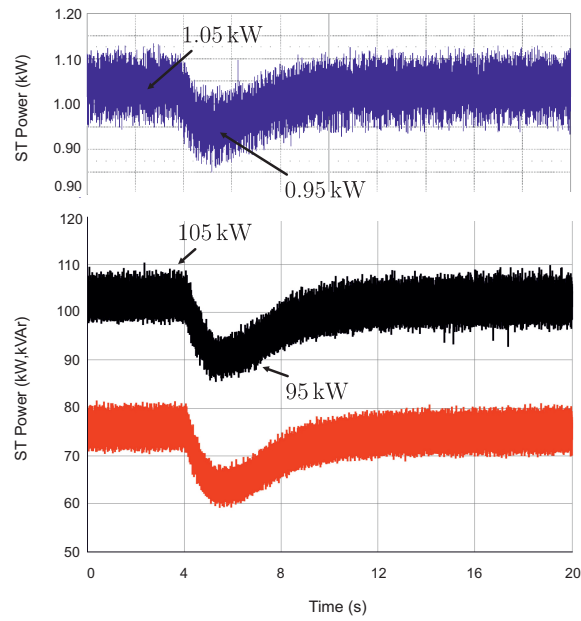


Figure 6.16: ST (HuT) active power (blue line), ST (RSCAD) active (black line) and reactive (red line) power, (Test Case C).

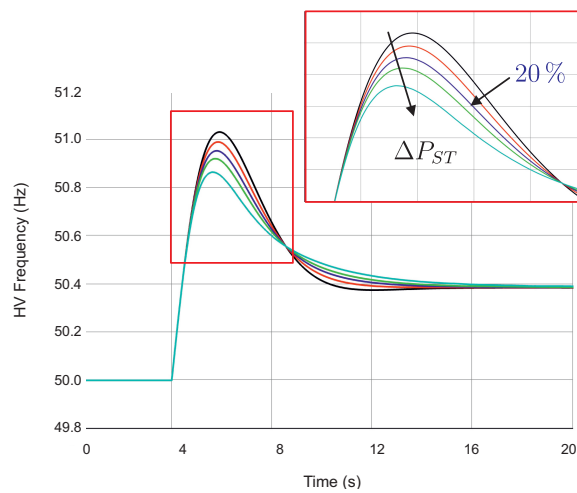


Figure 6.17: HV frequency during over-frequency condition

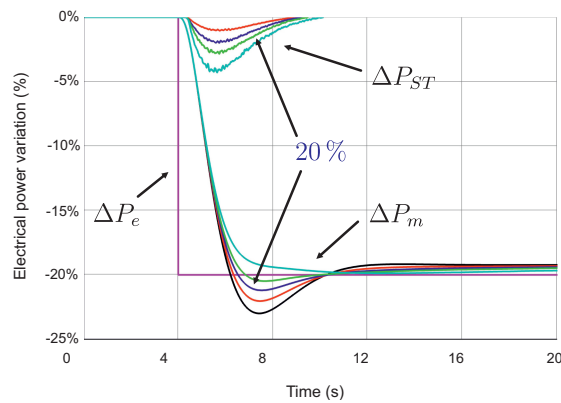


Figure 6.18: HV system power during over-frequency condition

A substantial difference compared to the under-frequency case can be noticed in the LV-grid voltage behavior Figure 6.19. The maximum voltage deviation is limited to 7% and it is related to ST bus. Instead in the under-frequency case (Figure 6.15), the voltage deviation reaches 11% in the farther bus in the grid. This is caused by the fact that the grid is absorbing power from the ST, and thus the voltage drop is positive. It can be concluded that the power availability of the single ST depends also on the grid composition and power injection of the DG. In case of limited DG power injection, the real time frequency controller has more capability upwards (over-frequency case) than downwards (under-frequency case), and vice-versa in case of high DG power production.

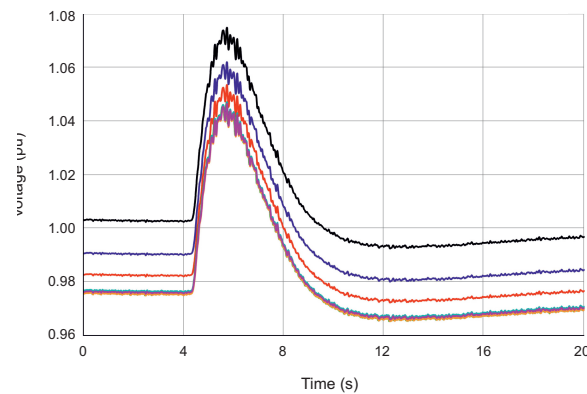


Figure 6.19: Voltage profile in the LV grid during the frequency controller operations, (20% ST-fed controlled load).

6.4 Conclusions

The control of the load offers new flexibility in the grid management due to the fast response in changing the power following an input signal. The ENTSO-E, in several reports has underlined that the load can provide ancillary services (frequency regulation, generator ramp rate support) to the transmission grid. The ST can provide this services controlling the load in the ST-fed grid, varying the voltage set-point, and thus the the power consumption of the ST-fed grid. If the transmission grid operators requests a power modulation, both downwards and upwards, the ST adapts the power consumption by means of voltage control. Two services have been explored in this chapter: the soft load reduction, and the transmission grid frequency regulation. The first service represents an alternative to the firm under-frequency load shedding. If the ST receives a power reduction request coming from the TSO, it adapts the voltage set-point in the ST-fed grid to reduce instantaneously the load consumption of the desired quantity. On the opposite of the load shedding strategies, the ST does not disconnect any load in the grid, but it reduces the power consumption, restoring it after the TSO request is cleared. The second service modulates the power consumption of the load in order to provide frequency regulation services to the transmission grid. During perturbations, the frequency deviates from the nominal value, and in extreme cases (e.g. below 47.5 Hz or above 51.5 Hz [121]) it may trigger the generators under- or over-frequency protections. The ST,

controlling the load, can support the frequency regulation during these phenomena. Measuring the frequency deviation in the MV side, the ST decreases the load consumption in case of under-frequency events, and viceversa, increases the consumption if an over-frequency condition is met. It has been proved in this chapter that a 20 % of ST-controlled load is sufficient to decrease the frequency variation of 100 mHz in the HV grid.

7 Summary, conclusion and future research

7.1 Summary and conclusion

A change in the production and transmission of electrical energy is undergoing in the electrical grid. The generators share is moving from few big power plants concentrated in the transmission system to many small distributed generators installed in the distribution grids. These resources, if from one side help to increase the system reliability and to decrease the transmission losses, on the other side challenge the grid management due to their characteristics: intermittent energy production feature (valid for renewables), low contribution to the system inertia (if converter-connected to the grid), and spread and not pre-planned presence in the grid (e.g., photovoltaics) in opposition with the studied connection points of big power plants. These characteristics can lead to several issues in the distribution grid, in case of high integration share of distribution generation: reverse power flow and consequent voltage violations, decreased system inertia and subsequent higher impact of disturbances in the grid (e.g., frequency deviation), fast power variations in the grid, followed by fast voltage transients. In the first chapter, device-based and system-level solutions have been described, together their approach to address these issues. However, all these solutions aim to solve specific issues and not to deal with the grid management independently from the grid issues.

This thesis addresses the Smart Transformer technology, that represents an actuator of system level strategies, aiming to solve the grid challenges. The ST, a power electronics-based transformer [J10], does not aim simply to replace the conventional transformer in adapting the voltage from the MV grid to LV grid, but to offer additional services to the distribution and transmission grids. Chapter 2 is dedicated to the description of the ST system, as well as its controllers. The topology chosen by this work is the three-stage one, and each stage is depicted in this chapter, with particular focus on the tuning of each stage controllers, taking in account the grid needs and the possible services it can offer.

To evaluate the ST performances in the distribution grid, simulation tests can be performed. However, simulating in details each ST component can be challenging in terms of computational time, mostly if referred to power system studies with large and complex grids, and it can lead to an oversimplification of the system and its constraints. Chapter 3 addresses the issue of validating the ST performances by means of experimental setups. Three solutions are proposed: a hardware solution, composed by a microgrid setup, aimed for tests where all hardware dynamics and constraints must be included (e.g., harmonics or components parameters variability); a controller solution, that is the Control-Hardware-In-Loop, targeting the validation of a particular controller that will be employed in ST industrial applications; a "hybrid" solution, including the previous two, that is the Power-Hardware-In-Loop, allowing the ST hardware performances evaluation in a large scale distribution grid. The grid, simulated in a Real Time Digital Simulator, is interfaced with the ST hardware by means of a linear power amplifier. The last solution has been studied thoroughly, focusing in partic-

ular on the stability of the loop and the accuracy in reproducing in hardware the software variables (i.e., grid current).

As mentioned above, the ST can offer additional services to the grid, than simply transforming the voltage in the MV/LV substation. An innovative service is to identify the load active and reactive power sensitivities to voltage and frequency. In Chapter 4 the "On-Line Load sensitivity Identification" algorithm is presented, enabling the possibility to evaluate algebraically the response of the net load consumption to voltage and frequency variations. The algorithm is described and validated by means of simulations and experimental tests. Furthermore, analysis over the accuracy of the algorithm in case of low power conditions (power exchange in MV grid near to 0), and influence of the DG power production in the ST-fed grid for the sensitivities calculation have been presented.

The ST controls the voltage waveform in the ST-fed grid. This gives the possibility to vary the voltage amplitude and frequency in order to interact with the voltage-sensitive loads and the droop controller-equipped generators. The voltage/frequency control in ST-fed grid is described in Chapter 5, where two services are described: the reverse power flow limitation and the ST overload control. The first one is a service for the MV grid, aiming to avoid the high voltage conditions in MV grid, limiting the power flow reversal in the MV/LV substation. The second one, is a protection service that the ST offers to itself. Interacting with loads and generators with the voltage/frequency control, the ST can handle high power consumption situations, reducing the power demand from the grid. Eventually, an frequency-variable voltage controller, named Fractional-Order Repetitive Controller, is described, able to maintain high control standard during variable frequency conditions.

The idea to control the load consumption can target also services for the MV and HV grids. Knowing the voltage sensitivities by means of the OLLI algorithm shown in Chapter 4, in Chapter 6 two services are offered: the Soft Load Reduction, where the voltage is varied to guarantee the desired power reduction in the ST-fed grid, creating an alternative to the firm load shedding; the Real Time Frequency Regulation, that controls the load consumption in order to support the HV grid during frequency deviation, and thus enabling control dynamics faster than the generators ones.

7.2 Research contribution

Contribution to the ST modeling

- A three-stage ST average model has been developed for power systems studies purpose, considering variations to be adopted in case of different converter topologies.
- ST controllers for each of the three stages have been described, suggesting a tuning fitted to provide grid services, such as rejection of disturbances.

Contribution in the ST experimental testing

- Comparison between different experimental testing setups (microgrid, CHIL, and PHIL) are given, taking into account the evaluation goals. Advantages and disadvantages of each solution have been provided.
- Development of a current-type Power-Hardware-In-Loop evaluation for ST applications. Mathematical studies of loop stability and accuracy have been provided, considering the models of the ST and interface hardware, and not simply assuming their equivalent impedance.

Contribution to the ST controllers development for providing services to the distribution grids

- Introduction of the voltage and frequency controllers in ST-fed grids to control the load consumption and power generation for increasing the controllability of distribution and transmission grids.
- Identification of such ancillary services to be offered, considering the control constraints in the ST-fed grid (e.g., minimum and maximum voltage).
- Development of an innovative methodology to calculate in real time the load active and reactive power sensitivities to voltage and frequency.
- Development of an overload controller based on the current sensitivities evaluation to guarantee the ST safety during load power consumption higher than its own capacity.

7.3 Future Research

The Smart Transformer offers new control possibilities to optimize the distribution grid management and to offer new services. This work has illustrated new strategies and approaches to increase the controllability of the grid.

In the author's opinion, the current challenges that the future research must address are:

- The ST has been thought to replace the conventional transformer. However, this is only a possible application of the ST. It can indeed support the conventional transformer working in parallel. This reduces the ST size, not being involved the entire peak load demand, but it allows several degree of freedom in controlling the grid and optimizing its operations. Studies must be performed to demonstrate the advantages and to understand the control limitations that this solution offers instead of the ST replacement of the conventional transformer.
- The voltage/frequency control is based on the load sensitivity to voltage and frequency variation. New power electronics-based devices are controlled in order to not to be sensitive to such variations. Moreover, their integration in the distribution grids is increasing steadily, substituting the directly grid-connected machines. This implies to a decreased load controllability by the voltage/frequency controller. A comprehensive study has to be carried out in order to understand if a "load constant power-based" grid can be a possible future scenario and with which extend the ST will be able to interact with the local loads and generators.
- It has been demonstrated that the DG active and reactive power injection impacts in the sensitivity evaluation. In this work, it has been analyzed mathematically only in simplified cases, to demonstrate the main concept. Further studies have to derive mathematically this impact, taking in account the dynamics of the DG controllers (e.g., presence of a governor, or not constant power injection), and the complexity of the grid in case of reactive power injection (i.e. the different cables impedance along the line).
- The services to be provided to the HV and MV grid in terms of load controllability have to be further expanded, due to the unique potential of ST to modify the load power consumption without disconnecting any customer. Particular focus has to be given on the possibility to modify the power consumption upwards (i.e. increasing the load demand) by means of voltage increment. Analysis must be developed to carefully assess the voltage limits worldwide, and how varying the voltage may affect the customers (e.g., billing, safety of equipments).
- The ST, despite the additional advantages that it brings, its costs are higher than the conventional solutions (e.g., transformer with LTC). Studies are needed to quantify the remuneration of the ancillary services offered by the ST, and put it in the relation with the initial investment in installing the ST instead of the conventional transformer. Further considerations must be made on the ST sizing considering costs and services to be offered.

8 References

- [1] Barker, P.P. and Mello, R.W. de: *Determining the impact of distributed generation on power systems. i. radial distribution systems*. In *Power Engineering Society Summer Meeting, 2000. IEEE*, volume 3, pages 1645–1656 vol. 3, 2000.
- [2] Coster, E.J., Myrzik, J.M.A., Kruimer, B., and Kling, W.L.: *Integration issues of distributed generation in distribution grids*. *Proceedings of the IEEE*, 99(1):28–39, Jan 2011, ISSN 0018-9219.
- [3] Hart, E. K., Stoutenburg, E. D., and Jacobson, M. Z.: *The potential of intermittent renewables to meet electric power demand: Current methods and emerging analytical techniques*. *Proceedings of the IEEE*, 100(2):322–334, Feb 2012, ISSN 0018-9219.
- [4] Weekes, T., Molinski, T., and Swift, G.: *Transient transformer overload ratings and protection*. *IEEE Electrical Insulation Magazine*, 20(2):32–35, March 2004, ISSN 0883-7554.
- [5] Tielens, Pieter and Hertem, Dirk Van: *The relevance of inertia in power systems*. *Renewable and Sustainable Energy Reviews*, 55:999 – 1009, 2016, ISSN 1364-0321. <http://www.sciencedirect.com/science/article/pii/S136403211501268X>.
- [6] Hasheminamin, M., Agelidis, V. G., Salehi, V., Teodorescu, R., and Hredzak, B.: *Index-based assessment of voltage rise and reverse power flow phenomena in a distribution feeder under high pv penetration*. *IEEE Journal of Photovoltaics*, 5(4):1158–1168, July 2015, ISSN 2156-3381.
- [7] Pillai, J.R., Thogersen, P., Moller, J., and Bak-Jensen, B.: *Integration of electric vehicles in low voltage danish distribution grids*. In *IEEE Power and Energy Society General Meeting*, pages 1–8, July 2012.
- [8] Ayres, H.M., Freitas, W., Almeida, M.C. de, and Silva, L.C.P. da: *Method for determining the maximum allowable penetration level of distributed generation without steady-state voltage violations*. *IET Generation, Transmission Distribution*, 4(4):495–508, April 2010, ISSN 1751-8687.
- [9] Hoke, A., Butler, R., Hambrick, J., and Kroposki, B.: *Steady-state analysis of maximum photovoltaic penetration levels on typical distribution feeders*. *IEEE Transactions on Sustainable Energy*, 4(2):350–357, April 2013, ISSN 1949-3029.
- [10] Clement-Nyns, K., Haesen, E., and Driesen, J.: *The impact of charging plug-in hybrid electric vehicles on a residential distribution grid*. *IEEE Transactions on Power Systems*, 25(1):371–380, Feb 2010, ISSN 0885-8950.
- [11] Putrus, G. A., Suwanapingkarl, P., Johnston, D., Bentley, E. C., and Narayana, M.: *Impact of electric vehicles on power distribution networks*. In *2009 IEEE Vehicle Power and Propulsion Conference*, pages 827–831, Sept 2009.

-
- [12] Masoum, M.A.S., Moses, P.S., and Hajforoosh, S.: *Distribution transformer stress in smart grid with coordinated charging of plug-in electric vehicles*. In *IEEE PES Innovative Smart Grid Technologies (ISGT)*, pages 1–8, Jan 2012.
- [13] Rutherford, M.J. and Yousefzadeh, V.: *The impact of electric vehicle battery charging on distribution transformers*. In *26th Annual IEEE Applied Power Electronics Conference and Exposition (APEC)*, pages 396–400, March 2011.
- [14] Fu, Weihui, McCalley, J. D., and Vittal, V.: *Risk assessment for transformer loading*. *IEEE Transactions on Power Systems*, 16(3):346–353, Aug 2001, ISSN 0885-8950.
- [15] Liu, R., Dow, L., and Liu, E.: *A survey of pev impacts on electric utilities*. In *ISGT 2011*, pages 1–8, Jan 2011.
- [16] Verzijlbergh, R. A., Grond, M. O. W., Lukszo, Z., Sloopweg, J. G., and Ilic, M. D.: *Network impacts and cost savings of controlled ev charging*. *IEEE Transactions on Smart Grid*, 3(3):1203–1212, Sept 2012, ISSN 1949-3053.
- [17] Shahnia, Farhad, Majumder, Ritwik, Ghosh, Arindam, Ledwich, Gerard, and Zare, Firuz: *Voltage imbalance analysis in residential low voltage distribution networks with rooftop {PVs}*. *Electric Power Systems Research*, 81(9):1805 – 1814, 2011, ISSN 0378-7796.
- [18] Leemput, N., Geth, F., Van Roy, J., Delnooz, A., Buscher, J., and Driesen, J.: *Impact of electric vehicle on-board single-phase charging strategies on a flemish residential grid*. *IEEE Trans. on Smart Grid*, 5(4):1815–1822, July 2014, ISSN 1949-3053.
- [19] *Recommended practice for monitoring electric power quality*. *IEEE Std 1159-2009* (Revision of IEEE Std 1159-1995), pages c1–81, June 2009.
- [20] Duarte, S.X. and Kagan, N.: *A power-quality index to assess the impact of voltage harmonic distortions and unbalance to three-phase induction motors*. *IEEE Trans. on Power Delivery*, 25(3):1846–1854, July 2010.
- [21] Faiz, J., Ebrahimpour, H., and Pillay, P.: *Influence of unbalanced voltage on the steady-state performance of a three-phase squirrel-cage induction motor*. *IEEE Trans. on Energy Conversion*, 19(4):657–662, Dec 2004, ISSN 0885-8969.
- [22] Pillay, P. and Manyage, M.: *Loss of life in induction machines operating with unbalanced supplies*. *IEEE Trans. on Energy Conversion*, 21(4):813–822, Dec 2006, ISSN 0885-8969.
- [23] Liu, Changjin, Xu, Dehong, Zhu, Nan, Blaabjerg, F., and Chen, Min: *Dc-voltage fluctuation elimination through a dc-capacitor current control for dfig converters under unbalanced grid voltage conditions*. *IEEE Trans. on Power Electronics*, 28(7):3206–3218, July 2013, ISSN 0885-8993.

-
- [24] Passey, Robert, Spooner, Ted, MacGill, Iain, Watt, Muriel, and Syngellakis, Katerina: *The potential impacts of grid-connected distributed generation and how to address them: A review of technical and non-technical factors*. Energy Policy, 39(10):6280 – 6290, 2011, ISSN 0301-4215. Sustainability of biofuels.
- [25] Woyte, A, Van Thong, Vu, Belmans, R., and Nijs, J.: *Voltage fluctuations on distribution level introduced by photovoltaic systems*. IEEE Transactions on Energy Conversion, 21(1):202–209, March 2006, ISSN 0885-8969.
- [26] *Technische Richtlinie Erzeugungsanlagen am Mittelspannungsnetz (Richtlinie für Anschluss und Parallel-betrieb von Erzeugungsanlagen am Mittelspannungsnetz)*, 2007.
- [27] Yan, Ruifeng and Saha, T.K.: *Investigation of voltage stability for residential customers due to high photovoltaic penetrations*. IEEE Transactions on Power Systems, 27(2):651–662, May 2012, ISSN 0885-8950.
- [28] Delille, G., Francois, B., and Malarange, G.: *Dynamic frequency control support by energy storage to reduce the impact of wind and solar generation on isolated power system's inertia*. IEEE Transactions on Sustainable Energy, 3(4):931–939, Oct 2012, ISSN 1949-3029.
- [29] Appen, J. von, Braun, M., Stetz, T., Diwold, K., and Geibel, D.: *Time in the sun: The challenge of high pv penetration in the german electric grid*. Power and Energy Magazine, IEEE, 11(2):55–64, March 2013, ISSN 1540-7977.
- [30] Mortazavi, H., Mehrjerdi, H., Saad, M., Lefebvre, S., Asber, D., and Lenoir, L.: *A monitoring technique for reversed power flow detection with high pv penetration level*. IEEE Transactions on Smart Grid, 6(5):2221–2232, Sept 2015, ISSN 1949-3053.
- [31] Levi, Victor, Kay, Mike, and Povey, Ian: *Reverse power flow capability of tap-changers*. In *18th International Conference and Exhibition on Electricity Distribution, CIRED*, pages 1–5, June 2005.
- [32] Cipcigan, L.M. and Taylor, P.C.: *Investigation of the reverse power flow requirements of high penetrations of small-scale embedded generation*. IET Renewable Power Generation, 1(3):160–166, September 2007, ISSN 1752-1416.
- [33] Thomson, M.: *Automatic voltage control relays and embedded generation. i*. Power Engineering Journal, 14(2):71–76, April 2000, ISSN 0950-3366.
- [34] Liu, Y., Bebic, J., Kroposki, B., Bedout, J. de, and Ren, W.: *Distribution system voltage performance analysis for high-penetration pv*. In *IEEE Energy 2030 Conference*, pages 1–8, Nov 2008.
- [35] Liu, Yutian, Zhang, Peng, and Qiu, Xizhao: *Optimal reactive power and voltage control for radial distribution system*. In *Power Engineering Society Summer Meeting*, volume 1, pages 85–90 vol. 1, 2000.

-
- [36] Turitsyn, K., Sulc, P., Backhaus, S., and Chertkov, M.: *Options for control of reactive power by distributed photovoltaic generators*. Proceedings of the IEEE, 99(6):1063–1073, June 2011, ISSN 0018-9219.
- [37] Muttaqi, K.M., Le, A.D.T., Negnevitsky, M., and Ledwich, G.: *A coordinated voltage control approach for coordination of OLTC, voltage regulator and DG to regulate voltage in a distribution feeder*. In *Industry Applications Society Annual Meeting, IEEE*, pages 1–8, Oct 2013.
- [38] Reese, C., Buchhagen, C., and Hofmann, L.: *Voltage range as control input for OLTC-equipped distribution transformers*. In *Transmission and Distribution Conference and Exposition (TD), IEEE PES*, pages 1–6, May 2012.
- [39] Gao, C. and Redfern, M.A.: *A review of voltage control techniques of networks with distributed generations using on-load tap changer transformers*. In *45th International Universities Power Engineering Conference (UPEC)*, pages 1–6, Aug 2010.
- [40] Liu, Xiaohu, Aichhorn, A., Liu, Liming, and Li, Hui: *Coordinated control of distributed energy storage system with tap changer transformers for voltage rise mitigation under high photovoltaic penetration*. IEEE Trans. on Smart Grid, 3(2):897–906, June 2012, ISSN 1949-3053.
- [41] Virayavanich, S., Seiler, A., Hammer, C., and Weck, K. H.: *Reliability of on-load tap changers with special consideration of experience with delta connected transformer windings and tropical environmental conditions*. In *Cigré*, 1996.
- [42] Carvalho, P.M.S., Correia, Pedro F., and Ferreira, L.A.F.: *Distributed reactive power generation control for voltage rise mitigation in distribution networks*. Power Systems, IEEE Transactions on, 23(2):766–772, May 2008, ISSN 0885-8950.
- [43] Li, K., Liu, J., Wang, Z., and Wei, B.: *Strategies and operating point optimization of statcom control for voltage unbalance mitigation in three-phase three-wire systems*. IEEE Transactions on Power Delivery, 22(1):413–422, Jan 2007, ISSN 0885-8977.
- [44] Ghosh, A. and Ledwich, G.: *Compensation of distribution system voltage using dvr*. IEEE Transactions on Power Delivery, 17(4):1030–1036, Oct 2002, ISSN 0885-8977.
- [45] Hill, C. A., Such, M. C., Chen, D., Gonzalez, J., and Grady, W. M.: *Battery energy storage for enabling integration of distributed solar power generation*. IEEE Transactions on Smart Grid, 3(2):850–857, June 2012, ISSN 1949-3053.
- [46] Teleke, S., Baran, M. E., Huang, A. Q., Bhattacharya, S., and Anderson, L.: *Control strategies for battery energy storage for wind farm dispatching*. IEEE Transactions on Energy Conversion, 24(3):725–732, Sept 2009, ISSN 0885-8969.
- [47] Yoshimoto, K., Nanahara, T., and Koshimizu, G.: *New control method for regulating state-of-charge of a battery in hybrid wind power/battery energy storage system*. In *2006 IEEE PES Power Systems Conference and Exposition*, pages 1244–1251, Oct 2006.

- [48] Bevrani, Hassan, Ise, Toshifumi, and Miura, Yushi: *Virtual synchronous generators: A survey and new perspectives*. International Journal of Electrical Power & Energy Systems, 54:244 – 254, 2014, ISSN 0142-0615. <http://www.sciencedirect.com/science/article/pii/S0142061513003062>.
- [49] Short, J. A., Infield, D. G., and Freris, L. L.: *Stabilization of grid frequency through dynamic demand control*. IEEE Transactions on Power Systems, 22(3):1284–1293, Aug 2007, ISSN 0885-8950.
- [50] Yao, E., Samadi, P., Wong, V. W. S., and Schober, R.: *Residential demand side management under high penetration of rooftop photovoltaic units*. IEEE Transactions on Smart Grid, 7(3):1597–1608, May 2016, ISSN 1949-3053.
- [51] Ziadi, Z., Taira, S., Oshiro, M., and Funabashi, T.: *Optimal power scheduling for smart grids considering controllable loads and high penetration of photovoltaic generation*. IEEE Transactions on Smart Grid, 5(5):2350–2359, Sept 2014, ISSN 1949-3053.
- [52] Liu, X., Aichhorn, A., Liu, L., and Li, H.: *Coordinated control of distributed energy storage system with tap changer transformers for voltage rise mitigation under high photovoltaic penetration*. IEEE Transactions on Smart Grid, 3(2):897–906, June 2012, ISSN 1949-3053.
- [53] Hatta, H., Asari, M., and Kobayashi, H.: *Study of energy management for decreasing reverse power flow from photovoltaic power systems*. In *2009 IEEE PES/IAS Conference on Sustainable Alternative Energy (SAE)*, pages 1–5, Sept 2009.
- [54] *Prescrizioni relative ai servizi di rete e ai distacchi per la generazione distribuita*, August 2014.
- [55] ENTSOE-WGAS: *Survey on ancillary service procurement, balancing market design 2015*. Technical report, 2016.
- [56] Palensky, P. and Dietrich, D.: *Demand side management: Demand response, intelligent energy systems, and smart loads*. IEEE Transactions on Industrial Informatics, 7(3):381–388, Aug 2011, ISSN 1551-3203.
- [57] Wang, Z. and Wang, J.: *Review on implementation and assessment of conservation voltage reduction*. IEEE Transactions on Power Systems, 29(3):1306–1315, May 2014, ISSN 0885-8950.
- [58] Strbac, Goran: *Demand side management: Benefits and challenges*. Energy Policy, 36(12):4419 – 4426, 2008, ISSN 0301-4215. <http://www.sciencedirect.com/science/article/pii/S0301421508004606>, Foresight Sustainable Energy Management and the Built Environment Project.
- [59] Atzeni, I., Ordóñez, L. G., Scutari, G., Palomar, D. P., and Fonollosa, J. R.: *Demand-side management via distributed energy generation and storage optimization*. IEEE Transactions on Smart Grid, 4(2):866–876, June 2013, ISSN 1949-3053.

-
- [60] Ruiz, N., Cobelo, I., and Oyarzabal, J.: *A direct load control model for virtual power plant management*. IEEE Transactions on Power Systems, 24(2):959–966, May 2009, ISSN 0885-8950.
- [61] Huang, Kun Yuan and Huang, Yann Chang: *Integrating direct load control with interruptible load management to provide instantaneous reserves for ancillary services*. IEEE Transactions on Power Systems, 19(3):1626–1634, Aug 2004, ISSN 0885-8950.
- [62] Lasseter, R.H.: *Microgrids*. In *IEEE Power Engineering Society Winter Meeting*, volume 1, pages 305–308 vol.1, 2002.
- [63] Kroposki, B., Lasseter, R., Ise, T., Morozumi, S., Papathanassiou, S., and Hatziargyriou, N.: *Making microgrids work*. IEEE Power and Energy Magazine, 6(3):40–53, May 2008, ISSN 1540-7977.
- [64] Katiraei, F., Iravani, R., Hatziargyriou, N., and Dimeas, A.: *Microgrids management*. IEEE Power and Energy Magazine, 6(3):54–65, May 2008, ISSN 1540-7977.
- [65] Guerrero, J. M., Vasquez, J. C., Matas, J., Vicuna, L. G. de, and Castilla, M.: *Hierarchical control of droop-controlled ac and dc microgrids; a general approach toward standardization*. IEEE Transactions on Industrial Electronics, 58(1):158–172, Jan 2011, ISSN 0278-0046.
- [66] Krause, T., Andersson, G., Frohlich, K., and Vaccaro, A.: *Multiple-energy carriers: Modeling of production, delivery, and consumption*. Proceedings of the IEEE, 99(1):15–27, Jan 2011, ISSN 0018-9219.
- [67] Geidl, M., Koeppel, G., Favre-Perrod, P., Klockl, B., Andersson, G., and Frohlich, K.: *Energy hubs for the future*. IEEE Power and Energy Magazine, 5(1):24–30, Jan 2007, ISSN 1540-7977.
- [68] Bozchalui, M. C., Hashmi, S. A., Hassen, H., Canizares, C. A., and Bhattacharya, K.: *Optimal operation of residential energy hubs in smart grids*. IEEE Transactions on Smart Grid, 3(4):1755–1766, Dec 2012, ISSN 1949-3053.
- [69] Geidl, M. and Andersson, G.: *Optimal power flow of multiple energy carriers*. IEEE Transactions on Power Systems, 22(1):145–155, Feb 2007, ISSN 0885-8950.
- [70] Ipakchi, A. and Albuyeh, F.: *Grid of the future*. IEEE Power and Energy Magazine, 7(2):52–62, March 2009, ISSN 1540-7977.
- [71] Brook, J. L., Staab, R. I., Bowers, J. C., and Niehaus, H. A.: *Solid state regulated power transformer with waveform conditioning capability*, 1980.
- [72] McMurray, William: *Power converter circuits having a high frequency link*, 1968.
- [73] Dujic, D., Mester, A., Chaudhuri, T., Coccia, A., Canales, F., and Steinke, J. K.: *Laboratory scale prototype of a power electronic transformer for traction applications*. In *Proceedings of the 2011 14th European Conference on Power Electronics and Applications*, pages 1–10, Aug 2011.

-
- [74] Huber, J. E. and Kolar, J. W.: *Volume/weight/cost comparison of a 1mva 10 kv/400 v solid-state against a conventional low-frequency distribution transformer*. In *2014 IEEE Energy Conversion Congress and Exposition (ECCE)*, pages 4545–4552, Sept 2014.
- [75] Huang, A. Q., Crow, M. L., Heydt, G. T., Zheng, J. P., and Dale, S. J.: *The future renewable electric energy delivery and management (freedm) system: The energy internet*. *Proceedings of the IEEE*, 99(1):133–148, Jan 2011, ISSN 0018-9219.
- [76] She, X., Yu, X., Wang, F., and Huang, A. Q.: *Design and demonstration of a 3.6-kv: 120-v/10-kva solid-state transformer for smart grid application*. *IEEE Transactions on Power Electronics*, 29(8):3982–3996, Aug 2014, ISSN 0885-8993.
- [77] Huang, A. Q.: *Solid state transformer and freedm system power management strategies*. <https://www.freedm.ncsu.edu/wp-content/uploads/2016/11/FREEDM-Seminar-Series-4-Power-Management-with-SSTs-by-Alex-Huang.pdf>.
- [78] She, Xu, Huang, A.Q., and Burgos, R.: *Review of solid-state transformer technologies and their application in power distribution systems*. *IEEE Journal of Emerging and Selected Topics in Power Electronics*, 1(3):186–198, Sept 2013, ISSN 2168-6777.
- [79] Kumar, C. and Liserre, M.: *Operation and control of smart transformer for improving performance of medium voltage power distribution system*. In *Power Electronics for Distributed Generation Systems (PEDG), 2015 IEEE 6th International Symposium on*, pages 1–6, June 2015.
- [80] Kumar, C. and Liserre, M.: *A new prospective of smart transformer application: Dual microgrid (dmg) operation*. In *IECON 2015 - 41st Annual Conference of the IEEE Industrial Electronics Society*, pages 004482–004487, Nov 2015.
- [81] Teodorescu, R., Liserre, M., and Rodriguez, P.: *Grid Converters for Photovoltaic and Wind Power Systems*. WILEY, 2011.
- [82] Hahn, F., Andresen, M., Buticchi, G., and Liserre, M.: *Thermal analysis and balancing for modular multilevel converters in hvdc applications*. *IEEE Transactions on Power Electronics*, PP(99):1–1, 2017, ISSN 0885-8993.
- [83] Akagi, H., Watanabe, E. H., and Aredes, M.: *Instantaneous Power Theory and Applications to Power Conditioning*. Wiley - IEEE Press, 2007.
- [84] Qin, H. and Kimball, J. W.: *Solid-state transformer architecture using ac 2013;ac dual-active-bridge converter*. *IEEE Transactions on Industrial Electronics*, 60(9):3720–3730, Sept 2013, ISSN 0278-0046.
- [85] Alonso, A. Rodríguez, Sebastian, J., Lamar, D. G., Hernando, M. M., and Vazquez, A.: *An overall study of a dual active bridge for bidirectional dc/dc conversion*. In *2010 IEEE Energy Conversion Congress and Exposition*, pages 1129–1135, Sept 2010.

-
- [86] Huber, J., Miniboeck, J., and Kolar, J.: *Generic derivation of dynamic model for half-cycle dcm series resonant converters*. IEEE Transactions on Power Electronics, PP(99):1–1, 2017, ISSN 0885-8993.
- [87] Costa, L., Buticchi, G., and Liserre, M.: *Highly efficient and reliable sic-based dc-dc converter for smart transformer*. IEEE Transactions on Industrial Electronics, PP(99):1–1, 2017, ISSN 0278-0046.
- [88] Schweizer, M. and Kolar, J. W.: *Design and implementation of a highly efficient three-level t-type converter for low-voltage applications*. IEEE Transactions on Power Electronics, 28(2):899–907, Feb 2013, ISSN 0885-8993.
- [89] Andresen, M., Costa, L. F., Buticchi, G., and Liserre, M.: *Smart transformer reliability and efficiency through modularity*. In *2016 IEEE 8th International Power Electronics and Motion Control Conference (IPEMC-ECCE Asia)*, pages 3241–3248, May 2016.
- [90] Edrington, C.S., Steurer, M., Langston, J., El-Mezyani, T., and Schoder, K.: *Role of power hardware in the loop in modeling and simulation for experimentation in power and energy systems*. Proceedings of the IEEE, 103(12):2401–2409, Dec 2015, ISSN 0018-9219.
- [91] Lauss, G., Faruque, M.O., Schoder, K., Dufour, C., Viehweider, A., and Langston, J.: *Characteristics and design of power hardware-in-the-loop simulations for electrical power systems*. IEEE Transactions on Industrial Electronics, 63(1):406–417, Jan 2016, ISSN 0278-0046.
- [92] Bokhari, A., Alkan, A., Dogan, R., Diaz-Aguiló, M., León, F. de, Czarkowski, D., Zabar, Z., Birenbaum, L., Noel, A., and Uosef, R. E.: *Experimental determination of the zip coefficients for modern residential, commercial, and industrial loads*. IEEE Transactions on Power Delivery, 29(3):1372–1381, June 2014, ISSN 0885-8977.
- [93] Lampropoulos, I., Vanalme, G. M. A., and Kling, W. L.: *A methodology for modeling the behavior of electricity prosumers within the smart grid*. In *2010 IEEE PES Innovative Smart Grid Technologies Conference Europe (ISGT Europe)*, pages 1–8, Oct 2010.
- [94] Panwar, M., Lundstrom, B., Langston, J., Suryanarayanan, S., and Chakraborty, S.: *An overview of real time hardware-in-the-loop capabilities in digital simulation for electric microgrids*. In *2013 North American Power Symposium (NAPS)*, pages 1–6, Sept 2013.
- [95] Jeon, J. H., Kim, J. Y., Kim, H. M., Kim, S. K., Cho, C., Kim, J. M., Ahn, J. B., and Nam, K. Y.: *Development of hardware in-the-loop simulation system for testing operation and control functions of microgrid*. IEEE Transactions on Power Electronics, 25(12):2919–2929, Dec 2010, ISSN 0885-8993.
- [96] Mueller, S. C., Georg, H., Nutaro, J. J., Widl, E., Deng, Y., Palensky, P., Awais, M. U., Chenine, M., Kuch, M., Stifter, M., Lin, H., Shukla, S. K., Wietfeld, C., Rehtanz, C.,

- Dufour, C., Wang, X., Dinavahi, V., Faruque, M. O., Meng, W., Liu, S., Monti, A., Ni, M., Davoudi, A., and Mehrizi-Sani, A.: *Interfacing power system and ict simulators: Challenges, state-of-the-art, and case studies*. IEEE Transactions on Smart Grid, PP(99):1–1, 2016, ISSN 1949-3053.
- [97] Manbachi, M., Sadu, A., Farhangi, H., Monti, A., Palizban, A., Ponci, F., and Arzandpour, S.: *Real-time co-simulation platform for smart grid volt-var optimization using iec 61850*. IEEE Transactions on Industrial Informatics, 12(4):1392–1402, Aug 2016, ISSN 1551-3203.
- [98] Kotsampopoulos, P.C., Lehfuss, F., Lauss, G.F., Bletterie, B., and Hatziargyriou, N.D.: *The limitations of digital simulation and the advantages of phil testing in studying distributed generation provision of ancillary services*. IEEE Transactions on Industrial Electronics, 62(9):5502–5515, Sept 2015, ISSN 0278-0046.
- [99] Huerta, F., Gruber, J. K., Prodanovic, M., and Matatagui, P.: *Power-hardware-in-the-loop test beds: evaluation tools for grid integration of distributed energy resources*. IEEE Industry Applications Magazine, 22(2):18–26, March 2016, ISSN 1077-2618.
- [100] Ren, W., Steurer, M., and Baldwin, T.L.: *Improve the stability and the accuracy of power hardware-in-the-loop simulation by selecting appropriate interface algorithms*. IEEE Transactions on Industry Applications, 44(4):1286–1294, July 2008, ISSN 0093-9994.
- [101] Aristidou, P., Valverde, G., and Van Cutsem, T.: *Contribution of distribution network control to voltage stability: A case study*. IEEE Transactions on Smart Grid, PP(99):1–1, 2015, ISSN 1949-3053.
- [102] Douglass, P. J., Garcia-Valle, R., Østergaard, J., and Tudora, O. C.: *Voltage-sensitive load controllers for voltage regulation and increased load factor in distribution systems*. IEEE Transactions on Smart Grid, 5(5):2394–2401, Sept 2014, ISSN 1949-3053.
- [103] Farrokhbadi, M., Cañizares, C. A., and Bhattacharya, K.: *Frequency control in isolated/islanded microgrids through voltage regulation*. IEEE Transactions on Smart Grid, PP(99):1–10, 2015, ISSN 1949-3053.
- [104] Price, W.W., Wirgau, K.A., Murdoch, A., Mitsche, James V., Vaahedi, E., and El-Kady, M.: *Load modeling for power flow and transient stability computer studies*. IEEE Transactions on Power Systems, 3(1):180–187, Feb 1988, ISSN 0885-8950.
- [105] Tang, X. and Milanovic, J. V.: *Assessment of the impact of demand side management on power system small signal stability*. In *2017 IEEE Manchester PowerTech*, pages 1–6, June 2017.
- [106] Schneider, Kevin P, Fuller, J, Tuffner, F, and Singh, Ruchi: *Evaluation of conservation voltage reduction (cvr) on a national level*. Pacific Northwest National Laboratory report, 2010.

-
- [107] Ballanti, A., Ochoa, L. F., and Turnham, V.: *Monte carlo assessment of customer voltage constraints in the context of cvr schemes*. In *23rd International Conference on Electricity Distribution CIGRE 2015*, pages 1–5, 2015.
- [108] Ballanti, A. and Ochoa, L. N. F.: *Voltage-led load management in whole distribution networks*. *IEEE Transactions on Power Systems*, PP(99):1–1, 2017, ISSN 0885-8950.
- [109] Milanovic, J.V., Yamashita, K., Martinez Villanueva, S., Djokic, S.Z., and Korunovic, L.M.: *International industry practice on power system load modeling*. *IEEE Transactions on Power Systems*, 28(3):3038–3046, Aug 2013, ISSN 0885-8950.
- [110] *Load representation for dynamic performance analysis [of power systems]*. *IEEE Transactions on Power Systems*, 8(2):472–482, May 1993, ISSN 0885-8950.
- [111] *Standard load models for power flow and dynamic performance simulation*. *IEEE Transactions on Power Systems*, 10(3):1302–1313, Aug 1995, ISSN 0885-8950.
- [112] Strunz, K., Abbasu, E., Fletcher, R., Hatzigiorgiou, N. D., Iravani, R., and Joss, G.: *Benchmark system for network integration of renewable and distributed energy resources c06.04.02*. Technical report, CIGRE, 2014.
- [113] Stojanovic, Dobrivoje P., Korunovic, Lidija M., and Milanovic, J.V.: *Dynamic load modelling based on measurements in medium voltage distribution network*. *Electric Power Systems Research*, 78(2):228 – 238, 2008, ISSN 0378-7796. <http://www.sciencedirect.com/science/article/pii/S0378779607000272>.
- [114] Kundur, P.: *Power System Stability and Control*. Electric Power Research Institute, 1994.
- [115] Regulski, P., Vilchis-Rodriguez, D. S., Djurovi?, S., and Terzija, V.: *Estimation of composite load model parameters using an improved particle swarm optimization method*. *IEEE Transactions on Power Delivery*, 30(2):553–560, April 2015, ISSN 0885-8977.
- [116] Han, Dong, Ma, Jin, He, Ren mu, and Dong, Zhao yang: *A real application of measurement-based load modeling in large-scale power grids and its validation*. *IEEE Transactions on Power Systems*, 24(4):1756–1764, Nov 2009, ISSN 0885-8950.
- [117] Hajagos, L.M. and Danai, B.: *Laboratory measurements and models of modern loads and their effect on voltage stability studies*. *IEEE Transactions on Power Systems*, 13(2):584–592, May 1998, ISSN 0885-8950.
- [118] *VSC Valves and Breakers, RTDS manual*.
- [119] Callaway, D. S. and Hiskens, I. A.: *Achieving controllability of electric loads*. *Proceedings of the IEEE*, 99(1):184–199, Jan 2011, ISSN 0018-9219.
- [120] Ballanti, A., Ochoa, L. N., Bailey, K., and Cox, S.: *Unlocking new sources of flexibility: Class: The world’s largest voltage-led load-management project*. *IEEE Power and Energy Magazine*, 15(3):52–63, May 2017, ISSN 1540-7977.

-
- [121] *Reference technical rules for the connection of active and passive users to the lv electrical utilities*, Dec. 2012. <http://www.ceiweb.it/doc/norme/12333.pdf>.
- [122] Gupta, S. C.: *Phase-locked loops*. Proceedings of the IEEE, 63(2):291–306, Feb 1975, ISSN 0018-9219.
- [123] Rodriguez, P., Pou, J., Bergas, J., Candela, J.I., Burgos, R.P., and Boroyevich, D.: *Decoupled double synchronous reference frame pll for power converters control*. IEEE Transactions on Power Electronics, 22(2):584–592, March 2007, ISSN 0885-8993.
- [124] Limited, Energex: *Energex distribution annual planning report - volume 1*. Technical report, 2015.
- [125] Carr, J., Wang, Zhenyuan, Bhattacharya, S., Hatua, K., and Madhusoodhanan, S.: *Overloading and overvoltage evaluation of a transformerless intelligent power substation*. In *2013 IEEE Power Energy Society General Meeting*, pages 1–5, July 2013.
- [126] Rocabert, J., Luna, A., Blaabjerg, F., and Rodríguez, P.: *Control of power converters in ac microgrids*. IEEE Transactions on Power Electronics, 27(11):4734–4749, Nov 2012, ISSN 0885-8993.
- [127] Zhang, X., Wang, Y., Yu, C., Guo, L., and Cao, R.: *Hysteresis model predictive control for high-power grid-connected inverters with output lcl filter*. IEEE Transactions on Industrial Electronics, 63(1):246–256, 2016.
- [128] Han, Y., Xu, L., Khan, M. M., Chen, C., Yao, G., and Zhou, L. D.: *Robust deadbeat control scheme for a hybrid apf with resetting filter and adaline-based harmonic estimation algorithm*. IEEE Transactions on Industrial Electronics, 58(9):3893–3904, 2011.
- [129] Timbus, A. V., Ciobotaru, M., Teodorescu, R., and Blaabjerg, F.: *Adaptive resonant controller for grid-connected converters in distributed power generation systems*. In *IEEE Applied Power Electronics Conference and Exposition (APEC)*, pages 1–6, March 2006.
- [130] Hara, S., Yamamoto, Y., Omata, T., and Nakano, Michio: *Repetitive control system: a new type servo system for periodic exogenous signals*. IEEE Transactions on Automatic Control, 33(7):659–668, Jul 1988, ISSN 0018-9286.
- [131] Zou, Z., Zhou, K., Wang, Z., and Cheng, M.: *Fractional-order repetitive control of programmable ac power sources*. IET Power Electronics, 7(2):431–438, February 2014, ISSN 1755-4535.
- [132] Yang, Y., Zhou, K., and Blaabjerg, F.: *Enhancing the frequency adaptability of periodic current controllers with a fixed sampling rate for grid-connected power converters*. IEEE Transactions on Power Electronics, 31(10):7273–7285, Oct 2016, ISSN 0885-8993.

-
- [133] Escobar, G., Catzin-Contreras, G.A., and Lopez-Sanchez, M.J.: *Compensation of variable fractional delays in the $6k\pm 1$ repetitive controller*. IEEE Transactions on Industrial Electronics, 62(10):6448–6456, Oct 2015, ISSN 0278-0046.
- [134] Zhou, Keliang and Wang, Danwei: *Digital repetitive controlled three-phase pwm rectifier*. IEEE Transactions on Power Electronics, 18(1):309–316, Jan 2003.
- [135] Laakso, T.I., Valimaki, V., Karjalainen, M., and Laine, U.K.: *Splitting the unit delay [fir/all pass filters design]*. IEEE Signal Processing Magazine, 13(1):30–60, Jan 1996, ISSN 1053-5888.
- [136] Wang, Yigang, Wang, Danwei, Zhang, Bin, and Zhou, Keliang: *Fractional delay based repetitive control with application to pwm dc/ac converters*. In *IEEE International Conference on Control Applications (CCA)*, pages 928–933, Oct 2007.
- [137] Energy Regulators, Agency for the Cooperation of: *Recommendation of the agency on the regulatory response to the future challenges emerging from developments in the internal energy market*. Technical report, 2014.
- [138] Commiteee, Power System Dynamic Performance: *Contribution to bulk system control and stability by distributed energy resources connected at distribution network*. Technical report, IEEE, 2017.
- [139] Kroposki, B., Johnson, B., Zhang, Y., Gevorgian, V., Denholm, P., Hodge, B. M., and Hannegan, B.: *Achieving a 100renewable grid: Operating electric power systems with extremely high levels of variable renewable energy*. IEEE Power and Energy Magazine, 15(2):61–73, March 2017, ISSN 1540-7977.
- [140] Lalor, G., Mullane, A., and O’Malley, M.: *Frequency control and wind turbine technologies*. IEEE Transactions on Power Systems, 20(4):1905–1913, Nov 2005, ISSN 0885-8950.
- [141] Margaris, I. D., Papathanassiou, S. A., Hatziaargyriou, N. D., Hansen, A. D., and Sorensen, P.: *Frequency control in autonomous power systems with high wind power penetration*. IEEE Transactions on Sustainable Energy, 3(2):189–199, April 2012, ISSN 1949-3029.
- [142] You, Haibo, Vittal, V., and Yang, Zhong: *Self-healing in power systems: an approach using islanding and rate of frequency decline-based load shedding*. IEEE Transactions on Power Systems, 18(1):174–181, Feb 2003, ISSN 0885-8950.
- [143] Pulendran, S. and Tate, J. E.: *Energy storage system control for prevention of transient under-frequency load shedding*. IEEE Transactions on Smart Grid, PP(99):1–10, 2015, ISSN 1949-3053.
- [144] Ramtharan, G., Ekanayake, J. B., and Jenkins, N.: *Frequency support from doubly fed induction generator wind turbines*. IET Renewable Power Generation, 1(1):3–9, March 2007, ISSN 1752-1416.

-
- [145] Denholm, P., Ela, E., Kirby, B., and Milligan, M.: *The role of energy storage with renewable electricity generation*. Technical report, National Renewable Energy Laboratory, 2010.
- [146] Navid, N. and Rosenwald, G.: *Market solutions for managing ramp flexibility with high penetration of renewable resource*. IEEE Transactions on Sustainable Energy, 3(4):784–790, Oct 2012, ISSN 1949-3029.
- [147] Taylor, C. W.: *Concepts of undervoltage load shedding for voltage stability*. IEEE Transactions on Power Delivery, 7(2):480–488, Apr 1992, ISSN 0885-8977.
- [148] Industrial, IEEE and Committee, Commercial Power Systems: *Report on reliability survey of industrial plants, part ii: Cost of power outages, plant restart time, critical service loss duration time, and type of loads lost versus time of power outages*. IEEE Transactions on Industry Applications, IA-10(2):236–241, March 1974, ISSN 0093-9994.
- [149] Corsi, S. and Sabelli, C.: *General blackout in italy sunday september 28, 2003, h. 03:28:00*. In *Power Engineering Society General Meeting, 2004. IEEE*, pages 1691–1702, June 2004.
- [150] Andersson, G., Donalek, P., Farmer, R., Hatziargyriou, N., Kamwa, I., Kundur, P., Martins, N., Paserba, J., Pourbeik, P., Sanchez-Gasca, J., Schulz, R., Stankovic, A., Taylor, C., and Vittal, V.: *Causes of the 2003 major grid blackouts in north america and europe, and recommended means to improve system dynamic performance*. IEEE Transactions on Power Systems, 20(4):1922–1928, Nov 2005, ISSN 0885-8950.

9 Attachments

9.1 Journal publications related to this thesis

- J1 L. F. Costa, G. De Carne, G. Buticchi, M. Liserre. "The Smart Transformer: A solid-state transformer tailored to provide ancillary services to the distribution grid" *IEEE Power Electronics Magazine*, 4 (2), 2017: 56-67.
- J2 M. Andresen, K. Ma, G. De Carne, G. Buticchi, F. Blaabjerg, M. Liserre. "Thermal stress analysis of medium-voltage converters for Smart Transformers" *IEEE Transactions on Power Electronics*, 32 (6), 2017: 4753-4765.
- J3 G. De Carne, G. Buticchi, Z. Zou, M. Liserre. "Reverse power flow control in a ST-fed distribution grid" *IEEE Transactions on Smart Grid*, Early Access, 2017.
- J4 R. Zhu, G. De Carne, F. Deng, M. Liserre. "Integration of large photovoltaic and wind system by means of Smart Transformer" *IEEE Transactions on Industrial Electronics*, Early Access, 2017.
- J5 G. De Carne, M. Liserre, C. Vournas. "On-line load sensitivity identification in LV distribution grids" *IEEE Transactions on Power Systems*, 32 (2), 2017: 1570-1571.
- J6 G. De Carne, Z. Zou, G. Buticchi, M. Liserre, C. Vournas. "Overload control in Smart Transformer-fed grids" *Applied Sciences*, 7 (2), 2017: 56-67.
- J7 Z. Zou, G. De Carne, G. Buticchi, M. Liserre. "Frequency-Adaptive Control of Smart Transformer-fed distribution grid" *IEEE Transactions on Industrial Electronics*, Early Access, 2017.
- J8 G. De Carne, G. Buticchi, M. Liserre, C. Vournas. "Load control using sensitivity identification by means of Smart Transformer" *IEEE Transactions on Smart Grid*, Early Access, 2017.
- J9 G. Buticchi, D. Barater, M. Liserre, G. De Carne, Z. Zou. "Analysis of the frequency control of a master/slave micro-grid", *IET Renewable Power Generation*, 10 (10), 2016: 1570-1576.
- J10 M. Liserre, G. Buticchi, M. Andresen, G. De Carne, L. F. Costas, Z. Zou. "The Smart Transformer: impact on the electric grid and technology challenges", *IEEE Industrial Electronics Magazine*, 10 (2), 2016: 46-58.

9.2 Conference publications related to this thesis

- C1 X. Gao, G. De Carne, M. Liserre, C. Vournas. "Voltage control by means of smart transformer in medium voltage feeder with distribution generation", *IEEE PowerTech*, Manchester, 2017, 1-6.

-
- C2 G. De Carne, M. Langwasser, X. Gao, G. Buticchi, M. Liserre. "Power-Hardware-In-Loop setup for power electronics tests", PCIM Europe, 2017, 1-7.
- C3 G. De Carne, G. Buticchi, T. Kerekes, M. Liserre. "Power-Hardware-In-Loop harmonic analysis of a Smart Transformer-fed distribution grid", 42nd Annual Conference of the Industrial Electronics Society, IECON, 2016, 7004-7009.
- C4 G. De Carne, Z. Zou, G. Buticchi, M. Liserre. "Variable frequency voltage control in a ST-fed grid by means of a Fractional-Order Repetitive Control", 25th International Symposium on Industrial Electronics (ISIE), 2016, 1230-1235.
- C5 X. Gao, G. De Carne, M. Liserre, C. Vournas. "Increasing integration of wind power in medium voltage grid by voltage support of Smart Transformer", Wind Europe, 2016, 1-7.
- C6 G. De Carne, G. Buticchi, M. Liserre, P. Marinakis, C. Vournas. "Coordinated frequency and voltage overload control of Smart Transformers", IEEE PowerTech, Eindhoven, 2015, 1-5.
- C7 G. De Carne, G. Buticchi, M. Liserre, C. Vournas. "Frequency-based overload control of smart transformers", IEEE PowerTech, Eindhoven, 2015, 1-5.
- C8 G. De Carne, G. Buticchi, M. Liserre, C. Yoon, F. Blaabjerg. "Voltage and current balancing in low and medium voltage grid by means of smart transformer", IEEE Power and Energy Society General Meeting, 2015, 1-5.
- C9 M. De Cristofaro, N. Femia, G. Petrone, G. Buticchi, G. De Carne, M. Liserre. "The effect of a constant power load on the stability of a smart transformer", IEEE 13th International Conference on Industrial Informatics (INDIN), 2015, 1605-1610.
- C10 S. Brueske, G. De Carne, M. Liserre. "Multi-frequency power transfer in a smart transformer based distribution grid", 40th Annual Conference of the Industrial Electronics Society, IECON, 2014, 4235-4331.
- C11 G. De Carne, M. Liserre, K. Christakou, M. Paolone. "Integrated voltage control and line congestion management in active distribution networks by means of Smart Transformers", 23rd International Symposium on Industrial Electronics (ISIE), 2014, 2613-2619.

9.3 Candidate resume

Name:

Giovanni De Carne

Date of birth:

26.07.1988

Place of birth:

Noci (BA)

Nationality:

Italian

Education

High school diploma, Liceo Scientifico Gaetano Salvemini, Bari, 2007.

Course of study:

2007-2011: Bachelor degree in Electrical Engineering, Politecnico di Bari.

2011-2013: Master degree in Electrical Engineering, Politecnico di Bari.

Work Experience:

2013-Present: Scientific staff member at the chair of power electronics at the Christian-Albrechts Universitaet zu Kiel.